SCUOLA DI DOTTORATO
UNIVERSITÀ DEGLI STUDI DI MILANO–BICOCCA

Department of *Materials Science*

PhD program in *Chemical, Geological and Environmental Sciences*, XXX Cycle
Curriculum in *Chemical Sciences*

Ab initio modeling of the physical and (photo)chemical properties of realistic TiO_2 nanoparticles in vacuum and in aqueous environment

PhD Candidate: Gianluca **Fazio**
Matr. 726017

Supervisor: Prof. Cristiana **Di Valentin**
Coordinator: Prof. Maria Luce **Frezzotti**

Academic Year 2016/2017

La science a-t-elle promis le bonheur?
Je ne le crois pas. Elle a promis la vérité,
et la question est de savoir
si l'on fera jamais du bonheur avec de la vérité.

Emile Zola

To think is to forget a difference,
to generalize, to abstract.

Jorge Luis Borges

Contents

1 Introduction **7**

1.1 Photon energy conversion 8
1.2 Titanium dioxide materials 11
1.2.1 Synthesis of TiO_2 nanoparticles: size and shape control 12
1.2.2 Mechanism of TiO_2 photocatalysis 14
1.3 State of the art of computational studies on anatase TiO_2 16
1.3.1 Bulk and flat surfaces 16
1.3.2 Nanoparticles 20
1.3.3 Interface with water 22
1.4 Outline of the PhD thesis 23

2 Theoretical Background **26**

2.1 Elements of Quantum Chemistry 26
2.1.1 The Schrödinger Equation 26
2.1.2 The Variational Principle 27
2.1.3 The Hartree-Fock Approximation 28
2.1.4 Electron correlation 30
2.1.5 Basis sets 30
2.1.6 Periodic Systems 32
2.2 Density-Functional Theory 34
2.2.1 The Hohenberg-Kohn Theorems 34
2.2.2 The Kohn-Sham Equations 35
2.2.3 Exchange-Correlation Functionals 36
2.2.4 Hybrid functionals 37
2.2.5 Electronic properties 38
2.3 Density-Functional Tight-Binding approach 42
2.3.1 First-order DFTB method 45
2.3.2 Self-consistent charge extension 46
2.4 Geometry optimization techniques 47
2.4.1 Local minimum search 49

2.4.2 Global minimum search . . . 49
2.4.3 Transition state search . . . 50
2.5 Molecular Dynamics . . . 51
2.5.1 Non-natural ensembles . . . 52

3 Ground State Properties of Anatase TiO_2 Nanocrystals versus Nanospheres 54
3.1 Introduction . . . 54
3.2 Computational Details . . . 55
3.3 Structural Properties . . . 57
3.3.1 Nanoparticles shapes . . . 57
3.3.2 Size and Morphology . . . 58
3.3.3 Simulated EXAFS . . . 62
3.3.4 Surface Energies . . . 66
3.4 Electronic Properties . . . 69
3.4.1 Band Gaps . . . 69
3.4.2 Frontier Orbitals . . . 72
3.4.3 Total and projected density of states . . . 77
3.5 Global optimization of TiO_2 Nanospheres . . . 81
3.5.1 Simulated Annealing . . . 83
3.5.2 Structural Analysis . . . 85
3.5.3 Electronic Structure . . . 90
3.6 Conclusions . . . 94

4 Photoexcited Carriers Recombination and Trapping in Anatase TiO_2 Nanocrystals versus Nanospheres 97
4.1 Introduction . . . 97
4.2 Computational Details . . . 99
4.3 Free/trapped exciton and recombination . . . 101
4.3.1 Experimental background . . . 101
4.3.2 Bulk system . . . 102
4.3.3 Nanoparticles . . . 103
4.4 Separate carriers trapping . . . 110
4.4.1 Experimental background . . . 110
4.4.2 Electron trapping . . . 112
4.4.3 Hole trapping . . . 122
4.4.4 Distorsion due to the nanosize and trapping . . . 131
4.5 Effect of water on the hole trapping ability . . . 134
4.5.1 Vibrational analysis . . . 135

4.5.2 Hole trapping mechanism 142
4.6 Conclusions 150

5 Water Multilayers at the Interface with Anatase TiO_2 Nanoparticles 152
5.1 Introduction 152
5.2 Computational Details 154
5.3 Assessment of a DFTB-based method 159
5.3.1 Water dimer and bulk water properties 159
5.3.2 Bulk anatase TiO_2 162
5.3.3 Water/(101) anatase interface 162
5.3.4 Molecular dynamics of water multilayers on (101) anatase 166
5.3.5 Energy barrier for water dissociation 174
5.4 Water/anatase TiO_2 spherical nanoparticle interface 175
5.4.1 Single site coverage 176
5.4.2 Monolayer coverage 178
5.4.3 Multilayer coverage 187
5.5 Conclusions 191

6 Summary and Conclusions 194

Bibliography 196

List of Publications 206

School participations, Oral presentations 208

1 Introduction

One of the most important scientific and technological challenges of the 21^{st} century concerns the transition from a fossil fuel based economy to a sustainable and carbon-neutral one, based on renewable energy sources, such as solar and wind power. Nowadays, although the ongoing trends show a growing share of carbon-free energy and an increase in attention to energy storage, the large majority (> 75 %) of the global energy consumption is still provided by fossil fuels with a very small fraction of solar and wind energy (< 2 %). [1]

This present large-scale use of carbon-based energy sources is currently increasing the global concentration of CO_2, which recently crossed the point of no return of 400 ppm. [2,3] Carbon dioxide is one of the main *greenhouse* gases, the principal cause of the global warming, whose consequences are already affecting the climate of planet Earth, with more intense precipitations and more frequent droughts. [4] In order to avoid the most serious consequences of the climate change in the next decades and to meet the increasing energy demand of the growing global population, a more and more consistent share of carbon-free energy will be required. [5]

In order to increase the contribution of solar energy to the future energy supplies, its cost must be strongly reduced to be competitive or even more convenient than fossil fuels. To reach this goal and provide inexpensive solar fuels and electricity, groundbreaking advances not only in the applied, but also in the fundamental science of photon energy conversion are necessary. In fact, light energy can be already efficiently harvested and converted to electrical or chemical energy by a vast array of photomaterials. [6] However, in order to meet the above mentioned requirements, the cost/efficiency ratio of such technologies has to be improved.

A promising strategy to enhance the performances of energy materials is to investigate and control them at the atomic-scale. This idea, anticipated by R. Feynman fifty years ago in his famous talk "There is plenty of room at the bottom", [7] is at the basis of the fields of *nanoscience* and *nanotechnology*, which made giant leaps forward in the last decades. As a matter of fact, the physical and chemical behaviour of a nanostructured material can be very different from the extended one, because of the quantum confinement and/or the higher surface-to-bulk ratio. These peculiar features that emerge at the nanoscale can be very useful for the fine control of the properties for a specific application.

Besides energy-related issues, the manipulation of matter at the nanoscale can be

extremely useful in many other fields, for example in biomedical applications. In fact, the complex and elegant molecular machinery of life, which regulates cell functioning, is mainly composed of biomolecules, e.g. proteins and nucleic acids, that have similar lenght scale of a nanoparticle. Thus, biological molecules and nanomaterials can be integrated into hybrid nanoconjugates, providing, for instance, innovative targeting drug delivery systems and powerful nanoparticle-based tools for biomolecular sensing and cancer therapies. These technologies are collectively referred to as *nanomedicine*, which is one of the fastest-growing field in nanoscience and is poised to revolutionize future healthcare and medicine. [8]

In the following, I will first provide an introduction on the materials for light energy conversion and their applications in the energy, environmental and biomedical fields. Subsequently, I will focus the attention on one of the most studied photomaterial, titanium dioxide (TiO_2). In particular, I will discuss the strategies to control the synthesis of TiO_2 nanomaterials and the fundamental physical and chemical processes at the basis of its photoactivity. Finally, I will briefly review part of the literature regarding the computational studies on TiO_2 and define the objectives of the present PhD project.

1.1 Photon energy conversion

Upon irradiation of any material, a portion of light energy is transfered to it and converted into another form of energy. Light photons are easily converted into heat, whilst the conversion into chemical energy or electricity, which is more technologically relevant, is a challenging task.

In this regard, semiconductors are the best-suited materials for the efficient conversion of light energy. In fact, when the incident light photon has an energy equal or higher than the band gap of the semiconductive material, an electron (e^-) is excited into the conduction band, leaving an electron hole (h^+) in the valence band, as shown in the left side of Figure 1.1.

When the photogenerated charges are directly employed to produce an electrical current, enabling the production of electric energy from sunlight, we refer to *photovoltaic* applications. Instead, when the photoinduced charges promote a chemical reaction, we refer to *photocatalytic* applications.

Concerning the field of *photovoltaics*, silicon or other inorganic semiconductors are still the most spread materials for light-to-electricity conversion, even though they present several limitations, such as the high production cost and the low diffuse light absorption. More advanced solar technologies are the hybrid organic-inorganic solar cells, such as dye-sensitized solar cells (DSSCs), which hold promises to overcome the issues of silicon-based photovoltaics. DSSCs are photoelectrochemical devices, developed by Grätzel et al. in 1991, [10] that exploit light-harvesting dye molecules adsorbed on a layer of sintered semiconductive nanoparticles, usually titanium dioxide (TiO_2). Photoexcited electrons from the dye molecules are injected into the semiconductor conduction band, leaving the dyes in the oxidized state. Subsequently, the electrons flow through an external circuit, generating an electrical current towards the counterelectrode, where they are collected by a redox couple solvated in the elec-

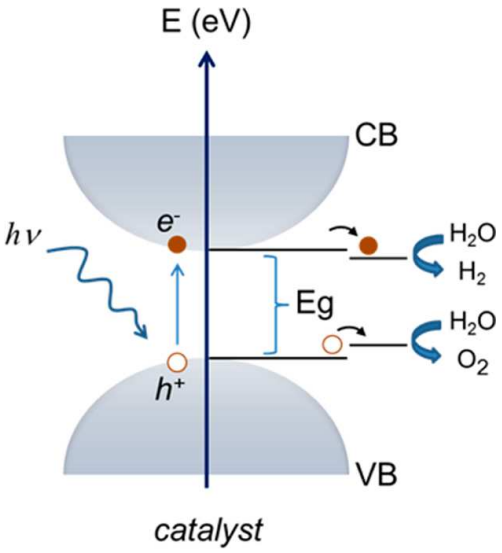

Figure 1.1 – Scheme of the typical light-induced water splitting: (i) hydrogen is produced by the reduction of the protons by the electrons in the conduction band (CB) and (ii) oxygen evolves via the oxidation assisted by the photoinduced holes in the valence band (VB) of the photocatalytically active semiconductor. Reprinted with permission from ref. [9]. Copyright 2014 American Chemical Society.

trolyte, usually triiodide ions, which regenerates the oxidized dye. Recently, with the introduction of lead halide perovskite as light-absorbing material, [11] this technology has reached efficiencies up to 22.1%, [12] becoming extremely attractive for the commercial energy market.

In the case of *photocatalysis*, the semiconductor is used to convert light into chemical energy. As a matter of fact, the photoexcited charges can migrate to the surface of the material and trigger a series of redox processes, as shown in the right side of Figure 1.1 for the photoelectrolysis of water, which leads to the concomitant production of hydrogen and oxygen. Thus, a photocatalytic semiconductive material can effectively exploit solar energy to generate clean fuels, such as hydrogen, contributing to the growing global demand of energy vectors.

Nevertheless, in general, the efficiency of the photocatalytic processes is rather low, and this depends on a series of factors.

First of all, the relative positions of the band edges need to be compatible with the reduction and oxidation electrochemical potentials. This means that the conduction band minimum (CBM) needs to be higher in energy than the reduction potential of the catalyzed reaction (about 0 eV vs NHE for the $H^+ \rightarrow H_2$ semireaction) and the valence band maximum (VBM) lower than the oxidation potential (about 1.23 eV vs NHE for the $H_2O \rightarrow O_2$ semireaction).

Actually, many semiconductors meet this requirement, as reported in Figure 1.2. However, most of them are not applicable as photocatalyst because of one or more of

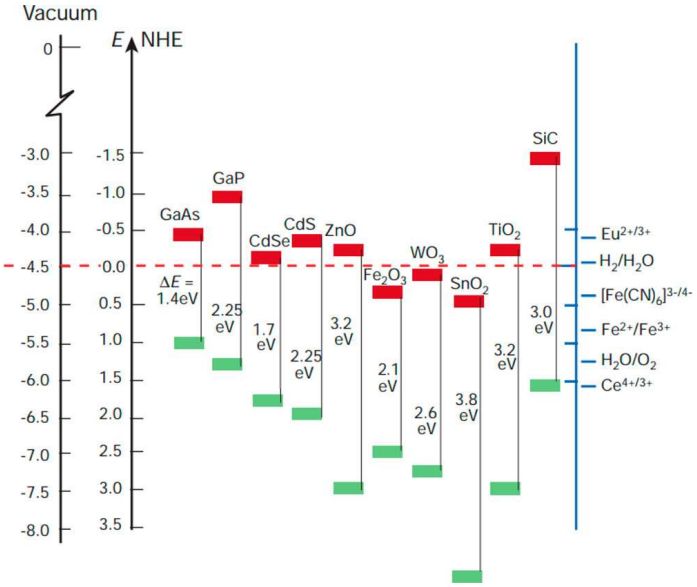

Figure 1.2 – Energy band positions for some selected semiconductors in contact with an aqueous environment at pH = 1 with respect to the normal hydrogen electrode (NHE). Conduction band minimum (red) and valence band maximum (green) are represented together with the band gap. The energy scale is shown in eV with respect both to the vacuum and to the normal hydrogen electrode (NHE). On the right, several electrochemical potential of relevant redox couples are given against the NHE potential. Reprinted with permission from ref. [13]. Copyright 2001 Nature Publishing Group.

the following reasons: [13–19]

- a too rapid electron–hole recombination, which prevents the migration of the photoinduced charges to the surface and, thus, the redox processes;
- instability of the semiconductor to light, as in the case of CdS, or to the aqueous environment, as in the case of ZnO;
- difficulties to engineer band gap and the relative positions of the band edges.

Among the available semiconductors, TiO_2 shows the highest performances, thanks to its stability to light and water, along with a relatively long lifetime of the electron–hole pairs. This ability of TiO_2 to efficiently convert light photons into chemical energy was demonstrated forty years ago by the pioneering work of Honda and Fujishima on light-induced water splitting. [20] Since then, titanium dioxide has been extensively studied by the scientific community for advanced applications in many modern research fields, [9, 21–23] and it still is considered the reference material in photocatalysis.

In fact, besides solar hydrogen generation, [20,21] TiO_2 has been shown to catalyze many photochemical processes of interest in energy and environmental applications,

such as the reduction of CO_2 to methane, [24], water [25] and air [26] purification, and even biomass reforming. [21]

More recently, TiO_2 materials have attracted also interest in the biomedical field. [27] Indeed, photoinduced charge carriers can react with the aqueous solution and dissolved oxygen to form of a variety of reactive oxygen species (ROS), such as hydroxyl radicals ($OH^{\bullet}$), superoxide anions ($O_2^{\bullet -}$) and hydrogen peroxide (H_2O_2). The cytotoxicity of ROS species can be exploited to kill specific cells in the so-called *photodynamic therapy*, which is a promising noninvasive treatment for cancer. [28]

Given the central role of titanium dioxide in the research fields of photovoltaics and photocatalysis, the physical and (photo)chemical properties of this semiconductor have been widely investigated by the scientific community. In the next section, the fundamental knowledge on TiO_2 materials will be presented.

1.2 Titanium dioxide materials

Titanium dioxide (TiO_2) is a low-cost and chemically inert semiconductive oxide with a large refractive index, high photostability and strong ultraviolet (UV) light filtering. Owing to these properties, it has been largely utilized as a white pigment for paints, food coloring, sunscreens and cosmetics. [29]

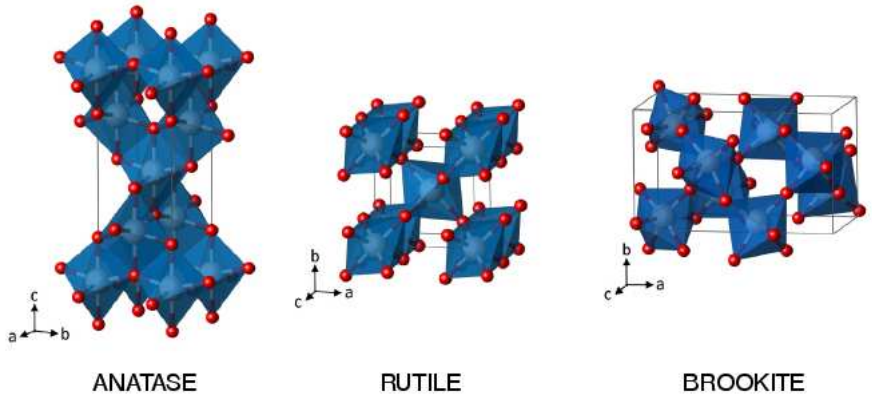

Figure 1.3 – Main polymorphs of titanium dioxide: anatase, rutile and brookite. Oxygen atoms are shown in red, titanium atoms in grey and the TiO_6 octahedra are represented by blue polyhedral shapes. Reprinted and adapted with permission from ref. [30]. Copyright 2012 IOP Publishing.

TiO_2 exists in nature in one of its three phases, *anatase*, *rutile* and *brookite*. As depicted in Figure 1.3, the basic building blocks of these structures are TiO_6 octahedra, where each Ti^{4+} cation is coordinated by six O^{2-} anions. The three polymorphs are characterized by a different distortion of the TiO_6 octahedra and a diverse connectivity between the octahedral units. For technological applications, anatase and rutile are the most studied polymorphs: at ambient conditions, the former has an *indirect*

band gap of 3.2 eV, whereas the latter has a *direct* band gap of 3.0 eV.

The wide band gap is one of the biggest drawbacks of titanium dioxide, since pure TiO_2 is primarly active in the ultraviolet region, which constitutes less than 5 % of the solar light spectrum. In regard to this, many efforts have been made to extend the light absorption of TiO_2 in the visible region. The most efficient strategies include band gap engineering, through the introduction of cationic or anionic impurities, and surface sensitization with other light active material, e.g. an organic dye molecule.

In addition to visible light sensitization, nanostructruring is crucial to improve the performances of the material for advanced applications. In fact, the use of TiO_2 nanoparticles as building blocks, thanks to their high surface-to-bulk ratio, is key to increase the surface area and, thus, the amount of available reactive surface sites for dye adsorption or photocatalytic processes.

Furthermore, the properties of TiO_2 at the nanoscale can be different from the bulk material and the investigation of these effects can give useful insights for the reduction of the reoccuring electron–hole recombination, which affects the efficiency of all its applications. As a matter of fact, the characteristic time scale of the photocatalytic processes can be strongly influenced by the size and morphology of the TiO_2 nanoparticle, leading to peculiar effects on the photoactivity. [23, 31]

Finally, the phase of the TiO_2 material has been found to play a prominent role on the performances. In particular, it is well-accepted by the scientific community that anatase is more photoactive than rutile and brookite. [32,33] Therefore, since anatase is the most photocatalytically active polymorph and also the most common phase of nano-TiO_2, as it will be discussed in the next section, from now on we will focus our attention only on anatase TiO_2 materials.

1.2.1 Synthesis of TiO_2 nanoparticles: size and shape control

Several methods are available for the preparation of TiO_2 nanoparticles and they can be classified in two main categories: physical and chemical methods. In the physical methodologies, small structures are produced from larger ones in a top-down approach. On the contrary, chemical methods rely on a bottom-up approach starting from molecular precursors. These methods are generally more precise and suitable to synthetize small structures (< 100 nm). [34]

Specifically, solution-phase approaches, i.e. *hydrothermal* or *sol-gel* synthesis, are best suited to attain the finest control of the size, morphology of the nanostructures for advanced applications. These methods usually employ an organic or inorganic titanium precursors, such as titanium alcoxides [35] or halides ($TiCl_4$ and TiF_4), [36] which are hydrolyzed in contact with water, leading to the formation of $Ti(OH)_4$ and its subsequent condensation to give Ti–O–Ti chains. For instance, in the case of a titanium tetrachloride precursor, the first steps of the synthesis would proceed as follows:

$$\begin{aligned} \textit{Hydrolysis:}\ & TiCl_4 + 4H_2O \rightarrow Ti(OH)_4 + 4HCl \\ \textit{Condensation:}\ & 2\ Ti(OH)_4 \rightarrow (OH)_3Ti\text{–}O\text{–}Ti(OH)_3 + H_2O. \end{aligned} \tag{1.1}$$

The condensation process is generally pH–dependent and, when the solution is concentrate enough, leads spontaneously to the nucleation and growth of the nanopar-

ticles. However, small TiO_2 nanoparticles (< 50 nm) are typically unstable in solution, hence the use of surfactants and capping ligands, e.g. carboxylic acids, alcohols, amines or phosphonic acids, is necessary to avoid the agglomeration. Furthermore, these protecting agents are critical in determining the morphology of the final nanoparticle, since they can favor the growth of certain facets with respect to others. Similarly, also the presence of anions, e.g. Cl^- and F^- ions coming from the hydrolysis of the precursors, can lead to a stabilization of high energy facets in both anatase and rutile cases. [37]

Overall, the choice of the type of capping agents, precursors, as well as the temperature and pH of the solution, allows for the control of the size and morphology of the synthetized TiO_2 nanoparticles. In fact, various well-faceted shapes, such as TiO_2 nanocrystals, nanorods and nanoplatelets, can be synthetized, [34,37] as shown in Figure 1.4 (b, c, d).

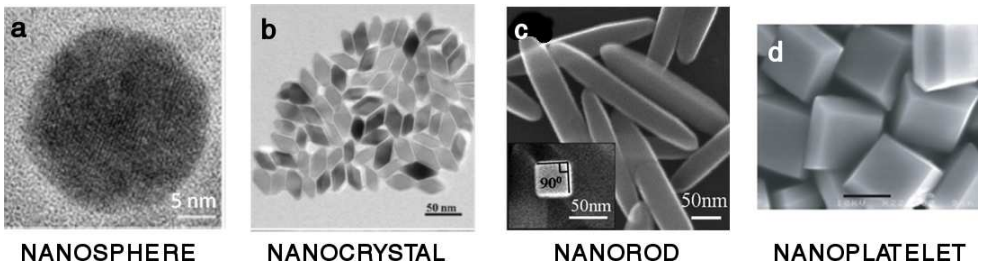

Figure 1.4 – TEM (a,b) and SEM (c,d) images anatase TiO_2 nanoparticles with different size and shape. Adapted with permission from refs. [38–41].

Another crucial factor is the density of particles during synthesis: an excessive dilution may lead to a partial dissolution of titania nanocrystals and the formation of spherical nanoparticles (see Figure 1.4a). These systems, similarly to nanotubes and nanorods, are characterized by a highly curved surface, which is expected to be particularly rich of undercoordinate sites, resulting in enhanced chemical binding properties. [31] In fact, nanoparticles with exposed curved surfaces are attracting major attention for photocatalytic applications and specific synthetic protocols for the production of such systems have been developed. [42,43]

Concerning the size of the synthetized TiO_2 nano-objects, their dimension can be tailored from hundreds down to 2 nm, [44–47] with the ones of 4–5 nm in diameter commonly investigated for practical applications. [48–52]

As regards the phase of the synthetized TiO_2 nanostructure, even though rutile is the most stable allotrope at ambient conditions, the relative stability of the different polymorphs is found to be dependent on the particle size, with anatase being thermodynamically favored at sizes below 14 nm. [53] This size-dependent phase transition favors the synthesis of highly pure anatase TiO_2 nanocrystals [54,55], hence anatase is very common in nanostructured TiO_2 samples.

The possibility to finely tailor the size and the shape of the titanium dioxide nanoparticles is crucial to tune the properties of the material and improve the overall performances for a specific application. In fact, the physical and chemical properties

of TiO_2 are expected to be influenced by the nanoscale dimension and the morphology, due to the quantum confinement and differences in the surface structure and reactivity. Even the photocatalytic activity of TiO_2, whose mechanisms will be briefly described in the next section, can be affected by the nanostructuring. [56]

1.2.2 Mechanism of TiO_2 photocatalysis

A deep knowledge of the photocatalytic processes, inside and at the surface of TiO_2, is of utmost relevance for the understanding of reaction mechanisms and, consequently, for the design of better photocatalysts. In Figure 1.5 is reported an overview of the main events that happen in the time scale from femtosecond to milliseconds in an irradiated TiO_2 sample. [23]

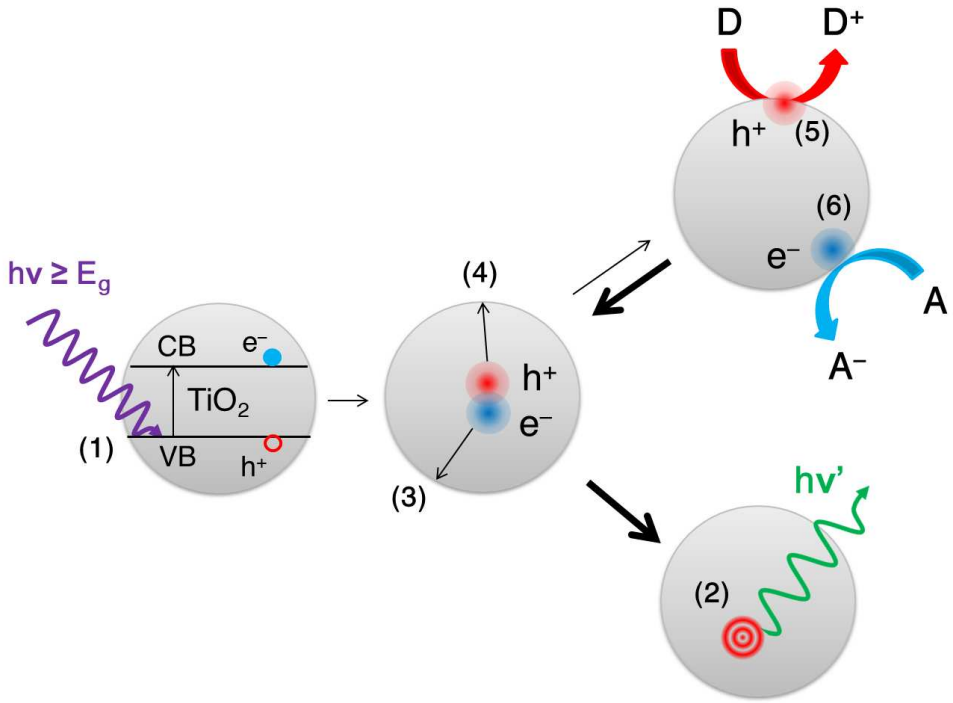

Figure 1.5 – Schematic representation of the photocatalytic processes in TiO_2 materials: (1) generation of charge carriers by photon absorption; (2) thermal or irradiative recombination of the electron–hole pair; (3) migration and trapping of conduction band electrons at a titanium sites and (4) of valence band holes to oxygen sites at the surface; (5) oxidative ($D \rightarrow D^+$) and (6) reductive ($A \rightarrow A^-$) reactions initiated by trapped holes and electrons, respectively.

Before discussing the photoinduced processes, it is important to underline that, in a semiconductor in contact with the vacuum, surface states may be formed with drastic consequences on the electronic structure. This is not the case for stoichiometric TiO_2,

since flat bands have been observed. [57] Nonetheless, if the surface contains defects or is functionalized with adsorbed molecules, an upward or downward bending of the valence and conduction bands can be induced, according to the amount of defects or to the electronegativity of the adsorbates. [58, 59] This band bending creates electric fields in the vicinity of the surface that can facilitate charge carriers separation.

When a TiO_2 material is exposed to illumination with a photon energy larger than the band gap ($h\nu \geq E_g$), electron–hole pairs are generated in the time of femtoseconds. At this stage, recombination of the photogenerated electron–hole couples can already happen, limiting the photocatalytic activity of TiO_2. This phenomenon can occur nonirradiatively with the release of heat, which is generally deemed to be the most frequent recombination channel, or irradiatively with the emission of a light photon. [47] The characteristic time scale of this process may extend from the picosecond to the millisecond, depending on the TiO_2 sample, the temperature and light intensity. [23]

If the photoinduced charges succeed to separate, they can become trapped at lattice sites. There are two main categories of charge trap: shallow traps are characterized by a partial delocalization of the charge and a rather small energy gain for the trapping process; on the contrary, deep traps induce a full localization of the charge on a single site with a large energy gain. As regards photoinduced electrons, they can become trapped in shallow traps in the bulk within 100–260 fs and, on a longer time scale (50 ps), they can eventually trap deeply on a single Ti^{4+} site of the (sub)surface, resulting in a reduced Ti^{3+} ion. [23] As regards photogenerated holes, they can deeply trap on single O sites within 200 fs, which means that deep trapping is significantly faster for holes than for electrons. Generally, it is assumed that holes can be trapped either by bridging O_{2c} atoms or by surface OH groups, forming bridging $O^{-\bullet}$ or terminal $OH^{\bullet}$ species. [23]

Once that electrons and holes are trapped, the interfacial charge transfer to a substrate, such as water, molecular oxygen or organic molecules, may occur, driving the redox activity. Specifically, the time scale of the oxidation processes, i.e. $h^+_{tr} + D \rightarrow D^+$, is in the order of hundreds of picoseconds, whereas the reduction processes, i.e. $e^-_{tr} + A \rightarrow A^-$, are generally slower, up to 100 μs.

According to the mechanism discussed above, the overall photocatalytic efficiency is determined by two critical factors. First, the competition between charge–carriers recombination and their separation and trapping, followed by the competition between trapped carriers recombination and surface redox reactions. Thus, higher efficiencies are expected when the recombination is suppressed or the interfacial charge transfer is accelerated.

In this regard, the water environment can play a crucial role on the light-induced processes by promoting electron or hole trapping and by generating surface electric fields. In general, the molecular-level understanding of the interaction between nano-TiO_2 and water is a fundamental aspect to be addressed, since most of the applications of titanium dioxide are performed in aqueous medium or humid environment. [58]

1.3 State of the art of computational studies on anatase TiO_2

Molecular simulations, in particular first-principles calculations, are an extremely precious tool for the investigation and rationalization of the observed properties of titanium dioxide. Being the most widely used material in photocatalysis, it is not surprising that a tremendous number of theoretical and computational studies on its physical and chemical properties are present in the literature.

The majority of the theoretical investigations are based on density functional theory (DFT), since this methodology can describe structural and electronic properties of medium size systems ($\sim$ 100 atoms) with a good balance between accuracy and computational cost (for more information on the methods, see Chapter 2). Furthermore, it was proved to be quite successful in the prediction of the properties and the explanation of experimental observations.

In this section, I will provide a brief overview of the state of the art of computational studies on TiO_2, focusing mainly on defect-free stoichiometric anatase TiO_2, the most common polymorph in titanium dioxide nanomaterials, which are the object of the present PhD project. For a more exhaustive and general review see Ref. [60].

1.3.1 Bulk and flat surfaces

Most of the computational first-principle studies are devoted to either bulk of surface slabs of TiO_2, since quantum chemical calculations on such systems are relatively affordable in terms of computational effort and many experimental data are available for the comparison of the theoretical results.

Bulk anatase

Bulk anatase is characterized by a tetragonal lattice ($P4_2/mnm$, D_{2d} point symmetry) with four TiO_2 units per unit cell, which is given in Figure 1.6a. Within the TiO_6 octahedra, the two axial Ti–O bond distances (exp. 1.98 Å) are slighly longer than the four equatorial ones (exp. 1.93 Å). [61] The bonding character of this crystalline solid is found to be largely ionic, with some covalent contribution. [62]

Concerning the electronic properties of bulk anatase, as it is in general for semiconducting oxides, the band gap is one of the most critical quantity to be reproduced. The band structure of anatase TiO_2, as calculated by standard DFT (GGA–PBE), is reported in Figure 1.6b. The band gap is correctly predicted to be *indirect*: the bottom of the conduction band (CB) is at Γ point of the Brillouin zone, whereas the top of the valence band is close to the X point. However, due to the self-interaction issue inherent in DFT, the band gap is significantly underestimated with respect to the experimental value of 3.4 eV. [63] In contrast, hybrid functional DFT typically overestimates the band gap by 0.4–0.5 eV [64] and the use of more sophisticated screened-Coulomb hybrid functionals only partially solves the issue. [65, 66] As regards DFT+U methods, unphysical U values (U = 6 eV) are necessary to reproduce the experimental band gap. [66]

Given the small size of the bulk anatase cell, quasiparticle GW calculations are

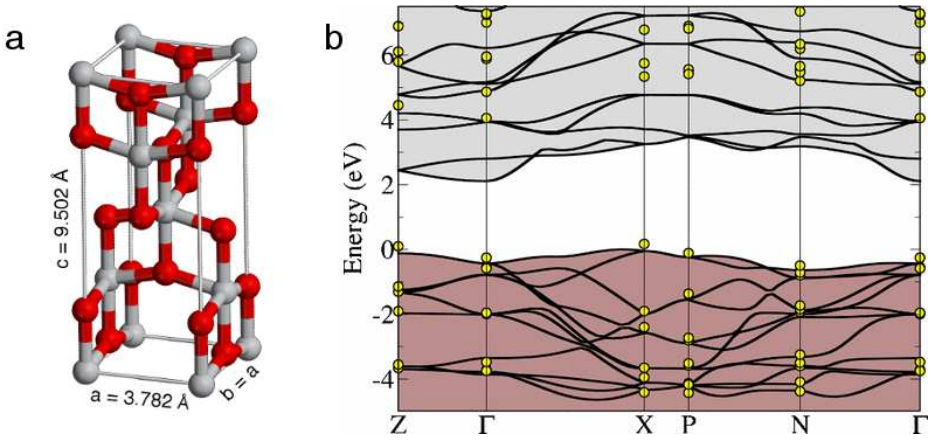

Figure 1.6 – (a) Bulk anatase unit cell and parameters. Oxygen atoms and titanium atoms are shown in red and grey, respectively. (b) Band structure of bulk anatase along the high symmetry directions of the first Brillouin zone. Black lines indicate the GGA–PBE calculations, yellow dots indicate the eigenvalues obtained after G_0W_0 corrections. Reprinted with permission from ref. [67]. Copyright 2016 American Physical Society.

feasible. In general, when standard DFT is used as starting point, they overestimate the band gap, [67–69] as shown by yellow dots in Figure 1.6, while better results are obtained starting from hybrid DFT or DFT+U. [30, 70]

Another critical issue is the alignment of the valence and conduction band edges with respect to the vacuum. Recently, this has been evaluated with a QM/MM cluster model, by computing the bulk anatase ionization potential (IP). [71, 72] Considering the value of the band gap of anatase, the electron affinity (EA) has been estimated to be 5.1 eV, in agreement with the experimental results.

As regards charge carriers in TiO_2, an important question is whether they behave like free electrons and holes or they couple with the lattice to form polarons, i.e. charge-induced distortions. This aspect can be elucidated only by introducing some self-interaction correction, like in DFT+U or in hybrid functionals, because standard DFT tends to overdelocalize electrons.

The polaronic nature of the electron–hole couple (exciton) has been demonstrated using the hybrid B3LYP functional in a bulk anatase supercell (96-atoms), by atomic relaxation of the triplet exciton. [73] The triplet exciton is highly localized on next-neighboring Ti^{3+}_{6c} and O^{-}_{3c} sites, inducing a structural reorganization with an energy gain associated with this process of 0.6 eV. The computed photoluminiscence (PL) of 2.6 eV satisfactorily agrees with the experimental one.

As regards the behaviour electrons and holes in TiO_2 once they are separated, it can be described by polaron theory. [74]

Electron polarons are usually identified as Ti^{3+} species, where the electron is trapped on a single Ti site, causing a local elongation of the Ti–O bonds. The use of hybrid functionals [73] or DFT+U [75, 76] is required to describe the polaronic nature

of extra electrons in bulk anatase, even though the size of the polaron cannot be easily established, being dependent on the method employed. Using B3LYP functional, 76% of the electron is localized on a single Ti site and most of the remaining is confined within a sphere of 6 Å in radius. [73] The electron trapping energy is computed to be 0.23 eV, suggesting that the electron is weakly bound to the bulk anatase lattice. Concerning electron transport, the activation barrier for polaron hopping from one site to the other has been evaluated to be ∼0.3 eV using DFT+U calculations. [75]

Self-trapping of the hole can be described by hybrid functionals [73] and also by DFT+U [76–78], even though unphysical values of U are necessary to localize an electron hole. [79] Using the B3LYP functional, the energy gain associated to hole trapping is computed to be 0.74 eV. The hole is found to be highly localized on an O_{3c} (85%) and its midgap state is deeper than that of the electron. The calculated values of the EPR hyperfine coupling constants with ^{17}O for the trapped hole are in fair agreement with the experiments. [80] Concerning hole transport, hopping barriers along different directions have been estimated to fall between 0.5 and 0.6 eV by DFT+U. [79]

Clean anatase surfaces

In the last two decades, stimulated by the development of novel growth techniques and atomic-scale surface science studies, many theoretical works on TiO_2 surfaces have appeared in literature.

Surface energy is the focus of a large number of investigations, because it is a quantity which is hard to measure experimentally and has a central role in the thermodynamic, structural and chemical properties of metal oxide surfaces. In fact, it is fundamental for understanding the relative stabilities of the different exposed facets and, consequently, for the construction of the size-dependent phase diagram of nanocrystalline TiO_2.

Surfaces are usually modeled as few layers slabs with periodic boundary conditions in the plane of the surface. Surface energies are obtained from the total energy difference, normalized for the surface area, between the slab and an equal number of bulk TiO_2 units. In both standard and hybrid DFT studies, [81–86] structural relaxation was found to have an important role in surface energetics, since it can reduce the surface energy by more than 50%. All the studies agree on the sequence of stability of low-index surfaces (101) < (100) < (001) < (110), which nicely correlates with the density of undercoordinated exposed atoms. This sequence is consistent with the observed predominance of (101) facets in most anatase samples.

Given the surface energies, the equilibrium morphology of a macroscopic anatase crystal can be obtained via the standard Wulff construction. [88] As found in natural samples, the equilibrium shape in vacuum is a truncated bipyramid, shown in Figure 1.7c, exposing mainly (101) facets and a minority of (001) ones. [81–83] Considering the surface energies for anatase and rutile, as obtained by DFT, it is possible to predict the anatase vs rutile phase stability as a function of the nanoparticle size. In vacuum, the predicted phase transition from anatase to rutile occurs at a particle diameter greater or equal to 9.3 nm. [83] This value and the ratio of the exposed facets have been found to be influenced by adsorbed species, such as hydrogen or

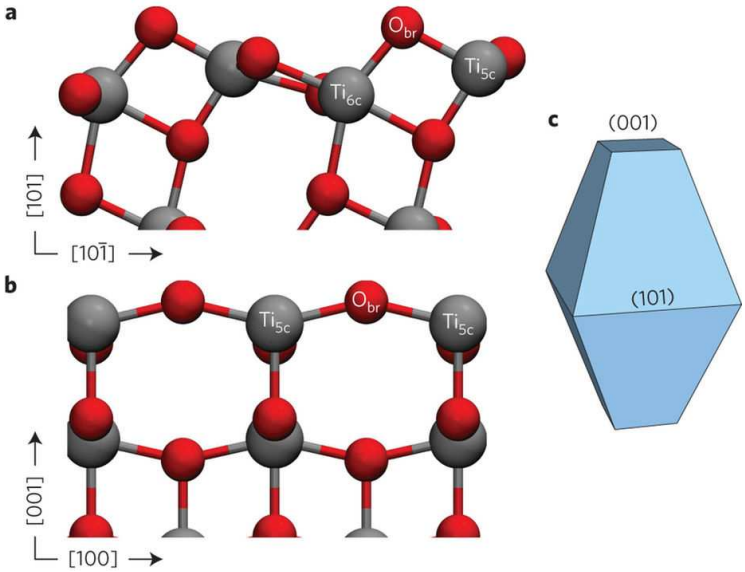

Figure 1.7 – Ball-and-sticks representation of the (101) anatase (a) and (001) anatase (b) surfaces. Coordination patterns of the exposed superficial atoms are indicated. (c) Calculated Wulff shape in vacuo; a similar shape is found also for hydrated anatase. Reprinted with permission from ref. [87]. Copyright 2016 Nature Publishing Group.

oxygen, [83] water environment and acid-base surface chemistry. [89, 90]

The clean anatase (101) surface, depicted in Figure 1.7a, has a 1×1 periodicity with a characteristic sawtooth profile when viewed from the [010] direction. The exposed atoms are five-fold (Ti_{5c}) and six-fold (Ti_{6c}) coordinated Ti atoms, as well as bridging oxygen atoms (O_{br} or O_{2c}) and three-fold coordinated (O_{3c}) O species. Upon structural relaxation, a significant displacement of surface atoms from bulk-like positions is observed. [81–84] In particular, Ti–O bonds between Ti and O_{2c} atoms are ∼5–10% shorter than in the bulk, resulting in a rather rigid relaxed surface.

The bulk-terminated anatase (001) surface exposes undercoordinated Ti_{5c}, bridging O_{2c} and fully coordinated O_{3c} atoms, as shown in Figure 1.7b. Upon relaxation, one of the two bonds formed by each O_{2c} atom with its neighboring Ti_{5c} species becomes shorter (1.8 Å), whereas the other elongates (2.2 Å). [81] The surface energy does not change significantly after relaxation, indicating that a more stable surface structure may exist. One of the proposed surface reconstruction is given by the "ad-molecule" (ADM) model: [91] the [100] rows of bridging O_{2c} atoms of the unreconstructed 1×1 surface are replaced by rows of TiO_3 species with a 1×4 periodicity. The resulting surface energy is nearly half of that of the unreconstructed surface and this structure is consistent with the experimental STM images of anatase (001) films grown epitaxially. [92] However, considering that such reconstruction implies a considerable mass transport, it is unlikely that this process can happen at the relatively low temperature employed during the synthesis of TiO_2 nanoparticles. Thus, the (001) surfaces of

anatase nanoparticles in an aqueous environment can be well described by a hydrated 1×1 unreconstructed (001) model. [93]

Regarding the behaviour of charge carriers at the surface, the polaron self-trapping energy of electrons and holes is computed to be larger than in the bulk, according to B3LYP calculations on anatase (101) slab models. Specifically, electrons are found to be preferentially trapped at Ti_{5c} sites with an energy gain of 0.6 eV, whereas holes localize at bridging O_{2c} sites with a considerable energy gain of 1.4 eV. [73]

1.3.2 Nanoparticles

Although anatase TiO_2 nanoparticles lie at the heart of many technological applications, only a limited number of computational studies devoted to them are present in the literature, due to the computational effort required to describe such large systems. Moreover, these are often based on classical interatomic potentials, [94–100] which cannot provide any information on the interplay between size, shape and electronic structure. Semiempirical and molecular orbital studies on TiO_2 nanoparticles were reported, [101–103] but they can reach only a limited level of accuracy. Only very recently, thanks to the advances of modern high-performance computing, accurate first-principles investigations of realistic TiO_2 nanosystems of few nm in size have become feasible, though still very computationally demanding.

All the DFT-based studies recently appeared in the literature have dealt with faceted TiO_2 nanoparticles, [104–109] whereas none has focused on highly reactive spherical ones yet.

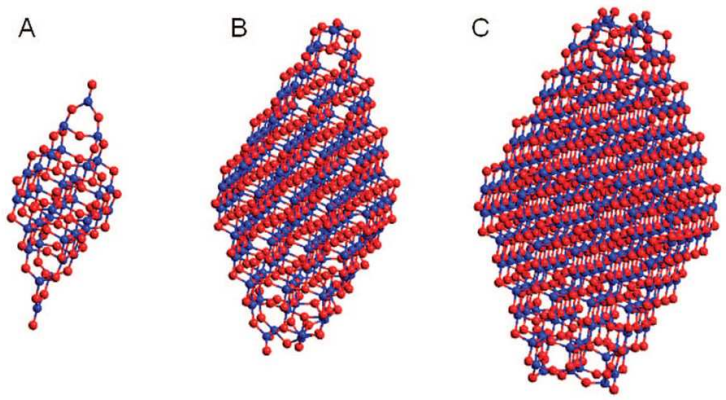

Figure 1.8 – Energy minimized TiO_2 nanoparticle models: (A) 1 nm anatase, (B) 2 nm anatase, (C) 3 nm anatase. Titanium atoms are shown in blue, oxygen atoms in red. Adapted with permission from ref. [104]. Copyright 2009 American Chemical Society.

One of the first investigations of realistic faceted anatase nanoparticles was performed by Hummer et al., [104] who employed stoichiometric decahedral $(TiO_2)_n$ models with n up to 272, reported in Figure 1.8. The models have been preliminary optimized with classical force fields and then relaxed with a standard DFT (PBE)

method and a plane-wave basis set. These calculations evidenced a significant difference between the total surface particle energy and the summed energies of constituent facets, demonstrating the considerable contribution of edges and corners to surface energy for nanoparticles with size below 3 nm. However, Hummer et al. have not taken into account that highly undercoordinated atoms on the surface of the nanoparticle are expected to be saturated with hydrogen in a humid environment.

A series of TiO_2 anatase $(TiO_2)_n$ nanoparticles with different size (n = 58–449) and truncated bipyramidal shape were employed by Li and Liu [106] to investigate the first proton removal step in the oxygen evolution reaction. Highly undercoordinated surface atoms (Ti_{4c} and O_{1c}) were saturated by dissociated water molecules. The effect of the solvent was considered through a continuum solvation model and the nanoparticles were optimized at a full GGA-PBE level using numerical atomic orbitals and norm-conserving pseudopotentials. This study revealed that for particles larger than 2 nm the band gap and the HOMO/LUMO energies rapidly converge to the ones of extended (101) and (001) surfaces, proving that quantum size effects apply only for very small TiO_2 nanosystems. In addition, the HOMO and LUMO orbitals of the nanoparticles are found to be spatially separated.

Nunzi et al. [105, 108] used differently sized models of anatase nanocrystals, i.e. $(TiO_2)_n$ (n = 161–918), saturated with hydrogen on the (001) facets, to study the nature and distribution of electronic trap states close to the edge of the conduction band. First, geometrical optimizations with an approximate-DFT method (SCC-DFTB) were carried out and, then, single-point electronic structure calculations were performed using standard DFT methods with a plane wave basis set and hybrid DFT with localized basis functions. Similarly to the work by Li and Liu, a different spatial distribution of the HOMO and LUMO levels was observed.

Electronic structure, polaronic trapping and TD-DFT absorption spectra of anatase TiO_2 nanocrystals have been recently investigated by Hubbard-U corrected DFT with a plane wave basis set in a small size model (265 atoms). [107] HOMO and LUMO levels were computed to be both delocalized in the central belt of the nanocrystal. Excess electrons were found to coexist both as small polarons at Ti^{3+} sites and band-like carriers, whereas only deep trapping at O_{2c} sites was observed for holes.

Although commonly synthetized and studied for many applications, [31] spherical TiO_2 nanoparticles have been theoretically investigated only by molecular dynamics (MD) simulations with force field approaches, [94–96, 98] hence no information about the electronic structure and chemical reactivity of such systems is available in the literature. Generally, the Matsui-Akaogi force field, [110] composed by an attractive van der Waals term and an electrostatic contribution, is employed.

Naicker et al. [94] performed MD simulations of spherical anatase, brookite and rutile TiO_2 nanoparticles with a size in the range between 2 and 6 nm. No phase transformation was observed during the simulation time (3 ns), even though very high temperature (2000 K) have been explored. Interestingly, four-fold and five-fold coordinated Ti atoms on the surface showed shorter Ti–O bonds with respect to fully coordinated Ti atoms.

Other investigations were devoted to the study of the sintering process between spherical TiO_2 nanoparticles. [95,96] Molecular dynamics trajectories for two colliding TiO_2 nanoparticles with a size of ∼3 nm were collected for 1 ns with a temperature

as high as 2000 K, considering different relative orientations for the collision.

1.3.3 Interface with water

Water on flat anatase surfaces

In the last decades, the interaction between TiO_2 surfaces and water has been object of countless theoretical investigations, [111] since it is relevant for most of the TiO_2-based technologies, which are normally performed in an aqueous or humid environment.

On the defect-free anatase (101) surface, a single water adsorbs molecularly forming a dative bond with the undercoordinated surface Ti_{5c} atom. This adsorption mode was predicted theoretically by standard DFT [112] and supported by experimental observations, such as atomic-scale STM images. [113, 114] The dissociation of water is an unfavorable process on the (101) surface and its activation barrier is computed to be $\sim$0.52 eV using a DFT+U method. [115]

Water multilayer adsorption on anatase has been the subject of a number of first-principles molecular dynamics simulations. [116–119] In these studies, no water dissociation was registered in rather long simulations for a water monolayer (ML), bilayer (BL) and trilayer on the defect-free (101) anatase surface. The position of water molecules in these layers has been found to be vertically and laterally ordered and this has been related to a complex and delicate interplay between surface roughness, water-titania and water-water interactions. [117] The first layer of water molecules are directly adsorbed to the Ti_{5c} atoms, whereas the second layer establishes strong H-bonding with the O_{2c} atoms and the water molecules in the first layer. These two layers form a stable bilayer with short H-bonds between them, as analyzed in detail by Mattioli et al. [120] Instead, the third layer has been found to be less bound and more mobile.

In contrast, a single water molecule was reported to exothermically dissociate on the unreconstructed anatase (001) surface. [112] The dissociative adsorption is associated with a significant reorganization: water cleaves one of the surface Ti–O bonds and two facing H-bonded hydroxyls are formed, releasing part of the tensile stress of the bulk-terminated surface. At monolayer coverage, a mixed molecular-dissociated monolayer, where only 25% of the water molecules are dissociated, has been computed to be stable using a large 2×4 slab supercell model. [121]

As a further step, several computational studies have addressed the oxidation of water on various TiO_2 surfaces. [122–124] Similar mechanisms for the oxygen evolution reaction are found on the (101) and (001) surfaces, whereas the energetics is sensitive to the relative position of the valence band maximum. [124] In all cases, the rate determining step of the reaction is the first proton removal. The kinetics of this step on a (101) surface has been analyzed in detail in a recent first-principles molecular dynamics investigation. [125] In this study, liquid water is described explicitly and the energy profile for the proton transfer is determined by hybrid DFT calculations. The results indicate that the proton transfer occurs before the electron transfer of the hole initially, that is initially trapped on a surface oxygen atom. However, the mechanism of water photooxidation on TiO_2 surfaces is still controversial, since recent static DFT calculations have reported a concerted proton/hole transfer to form $OH^{\bullet}$

radicals from adsorbed water and a hole trapped at an O_{2c} site. [126]

Concerning the influence of the water environment on electron trapping, recently Car-Parrinello molecular dynamics (CP-MD) simulations on (101) and (001) anatase surfaces in liquid water revealed that excess electrons have a tendency to avoid the surface and stay inside the slab. [87] Moreover, an extra electron on the aqueous (101) tends to become trapped into a stable Ti^{3+}–$O_{br}H$ complex, derived from the dissociation of an adsorbed water molecule.

Water on anatase nanoparticles

The computational investigation of the interface between water and a realistic TiO_2 nanoparticle is a particularly challenging task, given the large size of the metal oxide system and the liquid nature of water, which requires the recourse to molecular dynamics techniques. For this reason, very few computational studies are reported in the literature.

Early studies were based on classical force field, such as the Matsui-Akaogi potential. [110] Koparde et al. [98] reported a molecular dynamics simulations at room temperature (300 K) and hydrothermal conditions (523 K and 50 kbar) for 2.5–4.0 nm spherical anatase nanoparticles immersed in explicit water. In this study, an increase in crystallinity of the particles in water with respect to the vacuum has been observed. Two hydration layers solvate the nanoparticles and in the first one water is highly oriented.

More recently, a reactive force field (ReaxFF) has been developed to describe Ti–O–H interactions in the TiO_2/water systems. [127] In this kind of approaches, the interatomic potential is parametrized to DFT references on the basis of the bond order between atoms, hence this method can model bond breaking and formation in large systems. Using this methodology, the reactivity towards water solvent of small TiO_2 nanoparticles ($\sim$ 1 nm) has been investigated, finding a remarkable dissociative behaviour of interfacial water molecules. [100]

However, in order to have a description of the electronic structure and an accurate picture of the reactivity of a TiO_2 nanoparticle in a water environment, even more sophisticated methods are necessary. First-principles molecular dynamics simulations, based on standard DFT, for a $(TiO_2)_n$ cluster ($n = 30$) in contact with a small number of water molecules have been reported. [128] In this case, even though the methodology is highly accurate and can provide a quantum insight, the model can be hardly representative of a realistic nanoparticle. A compromise between accuracy and size of the model has to be reached for a meaningful theoretical investigation of the water/TiO_2 nanoparticle interface.

1.4 Outline of the PhD thesis

The aim of this PhD project is the first-principles investigation of anatase TiO_2 nanoparticles with different morphologies and a realistic size in vacuum and in water environment, focusing on various aspects relevant for technological applications.

For this study we employed state-of-the-art computational methods and massively parallelized codes in order to perform highly accurate calculations of such large sys-

tems in a reasonable time. Most of the calculations were based on density functional theory (DFT), using hybrid functionals and localized basis sets, which is a well-suited approach for the description of titanium dioxide. An approximate-DFT method, namely the self-consistent charge density-functional tight-binding (SCC-DFTB), has been considered for the study of the largest systems and of the dynamical behaviour of water/titania interfaces. An overview of the theoretical methodologies employed in this PhD work is provided in Chapter 2.

The first part of the work was devoted to the construction of the models of stoichiometric anatase TiO_2 nanoparticles and the investigation of their ground state structural and electronic properties as a function of the size (1.5 to 4.4 nm in diameter) and the morphology (spherical vs faceted), as discussed and described in Chapter 3. As regards the structural properties, we focused on the surface-to-bulk ratio, the type and number of undercoordinated surface atoms, lattice distortions with respect to the bulk and surface energies. As regards the electronic properties, we have analyzed the band gaps, electronic affinities, ionization potentials and the electronic density of states. We dedicated particular efforts for the description of the complex structural features of spherical TiO_2 nanoparticles, which have been modeled with a multistep/scale approach. Specifically, we employed the computationally efficient SCC-DFTB method to perform a global optimization of the geometries, which have been then relaxed at a full hybrid DFT level of theory. Moreover, we compared the computed properties at the two levels of theory in order to assess the ability of SCC-DFTB to describe TiO_2 large systems.

Subsequently, we focused the attention on the effect of size, shape and of additional water molecules on charge carriers dynamics in TiO_2 nanoparticles, as reported in Chapter 4. First, we modeled the electron/hole pairs formation, their recombination and separation in bare spherical vs faceted anatase nanoparticles. Then, we described the self-trapping process of isolated charge carriers in different portions of the nanoparticles, highlighting the best trapping sites for electron and holes. In this regard, the role of corners, edges and surface curvature, which are peculiar features of nanostructured TiO_2 and are not present in flat surfaces, has been evidenced. We corroborated this detailed computational analysis by the comparison with the available experimental data from electron paramagnetic resonance (EPR) and transient absorption (TA) spectroscopies. Lastly, on the basis of a combined theoretical/experimental approach, in collaboration with research groups in Japan, we demonstrated that water adsorption assists the hole trapping only for spherical TiO_2 nanoparticles and not for well-faceted ones. The different water adsorbates on the surface of the nanoparticles have been identified by comparing the computed vibrational structure with water-coverage controlled infrared spectra. Then, we calculated the hole trapping ability of the nanoparticles as a function of the water content in order to explain the shape-dependent behaviour observed in the TA spectra of the TiO_2 samples.

Finally, we tackled the study of the complex water/TiO_2 nanoparticle interface, as detailed and discussed in Chapter 5. First, we developed a novel computational approach, based on the computationally efficient SCC-DFTB method, to accurately describe this important solid–liquid interface. We assessed the reliability of this new methodology for the separated components (bulk TiO_2 and water) and for the prototypical water/(101) anatase interface with respect to DFT and experimental data.

As a further step, we employed this novel approach, in parallel with hybrid DFT, for the investigation of water adsorption on a realistic spherical TiO_2 nanoparticle up to monolayer coverage. In particular, we showed the prefered adsorption mode of single water molecules and of a full water monolayer as well as the effect of the water surrounding on the structural and electronic properties. Finally, multilayer water coverage has been simulated via a SCC-DFTB-based molecular dynamics run, which is analyzed in terms of water density profile from the surface and O–H bond orientation.

2 Theoretical Background

The first-principles modeling of semiconductive oxides nanoparticles is a complex and computationally demanding task, especially when complex systems with many degrees of freedom and the interaction with light are involved. On the one hand, one should aim to be accurate, but highly sophisticated methods are not feasible when the system contain hundreds of atoms. On the other hand, one may employ inexpensive molecular mechanics approaches, but they cannot provide any information on the electronic structure and the excited states, which are fundamental for the study of a photocatalytically active semiconductor material.

To reach a good compromise between accuracy and computational effort, it is necessary to apply smart approaches, i.e. efficient approximations to the fundamental equations of quantum physics. However, one should know in detail the theoretical background of these approaches in order to understand which information is left behind and to assess the validity of the results.

This chapter is devoted to the discussion on the fundaments of quantum chemistry, the main concepts of density-functional theory (DFT) and its approximation in the density functional tight-binding (DFTB) method. Moreover, we will present the algorithms for geometry optimization and for molecular dynamics (MD) simulations. Note that this is only an introduction to the methodologies used in this thesis, whereas a detailed description of the computational details will be reported in a specific section of each Chapter.

2.1 Elements of Quantum Chemistry

In this section some of the fundametal aspects of the electronic structure theory will be recalled as the theoretical foundations for the following discussion of density-functional theory (DFT) and approximate-DFT methods.

2.1.1 The Schrödinger Equation

A quantum mechanical description of a molecular system of N electrons and M nuclei is provided by the time-independent non-relativistic Schrödinger equation:

$$\hat{H}\Psi(\mathbf{x}_1, \mathbf{x}_2, \ldots, \mathbf{x}_N, \mathbf{R}_1, \mathbf{R}_2, \ldots, \mathbf{R}_M) = E\Psi(\mathbf{x}_1, \mathbf{x}_2, \ldots, \mathbf{x}_N, \mathbf{R}_1, \mathbf{R}_2, \ldots, \mathbf{R}_M) \quad (2.1)$$

where Ψ is the wavefunction, E is its total energy and $\hat{H}$ is the Hamiltonian operator defined in absence of magnetic or electric fields. $\hat{H}$ is a differential operator that, when applied to Ψ, gives the total energy E as a sum of kinetic energy of electron and nuclei and potential energy of the nucleus-nucleus, nucleus-electron and electron-electron Couloumb interactions. The wave function Ψ contains all the possible information to be known about the system and is a function of the $3N$ spatial coordinates of the electrons $\{\mathbf{r}_i\}$ and their N spin coordinates, collectively termed $\{\mathbf{x_i}\}$, and the $3M$ spatial coordinates of the nuclei $\{\mathbf{R}_\alpha\}$.

Due to the complexity and the correlated motion of the particles, the exact solution of the Schrödinger equation is feasible only for system with very few electrons, e.g. H or He atoms. [129]

In order to study more complicated systems, such as the ones of interest in materials science, mathematical approximations of this equation are necessary. One of these is the *Born–Oppenheimer* approximation, which takes advantage of the much slower motion of nuclei with respect to the electrons due to the significant differences of mass (e.g. a carbon nucleus is about 20000 times heavier than an electron). Therefore, we can approximately consider that electrons move in the field of fixed nuclei, so that the Hamiltonian operator can be reduced to

$$\hat{H}_{elec} = -\frac{1}{2}\sum_{i=1}^{N}\nabla_i^2 - \sum_{i=1}^{N}\sum_{\alpha=1}^{M}\frac{Z_\alpha}{r_{i\alpha}} + \sum_{i=1}^{N}\sum_{j=1}^{N}\frac{1}{r_{ij}} = \hat{T} + \hat{V}_{Ne} + \hat{V}_{ee} \quad (2.2)$$

where indices i and j run over all the N electrons and α refer to each of the M nuclei of the system. The corresponding Schrödinger equation depends only parametrically on the nuclear coordinates $\{\mathbf{R}_\alpha\}$

$$\hat{H}_{elec}\Psi_{elec}(\mathbf{x_1}, \mathbf{x_2}, \ldots, \mathbf{x_N}; \{\mathbf{R}_\alpha\}) = E_{elec}\Psi_{elec}(\mathbf{x_1}, \mathbf{x_2}, \ldots, \mathbf{x_N}; \{\mathbf{R}_\alpha\}) \quad (2.3)$$

In other words, only Ψ_{elec} for a certain fixed molecular geometry has to be calculated and the total energy E_{tot} of the system is then given by the sum of E_{elec} and the constant nuclear Coulombic repulsion term $E_{nn} = \sum_{\alpha\beta} Z_\alpha Z_\beta / R_{\alpha\beta}$.

2.1.2 The Variational Principle

Unfortunately, except few trivial exceptions, equation 2.3 can not be solved analytically. Nevertheless, the *variational principle* provide a recipe to systematically approach the wave function of the ground state, Ψ_0, i.e. the lowest energy state. This principle states that the expectation value of the Hamiltonian operator from any well-behaved trial function Ψ_{trial} will be an upper bound to the true energy of the ground state E_0, i.e.

$$\langle\Psi_{trial}|\hat{H}|\Psi_{trial}\rangle = E_{trial} \geq E_0 = \langle\Psi_0|\hat{H}|\Psi_0\rangle \quad (2.4)$$

Therefore, the Ψ_{trial} which gives the lowest energy will be the ground state wavefunction, whose energy is the true ground state energy E_0. In the everyday practice, since it is obviously not possible to try all the eligible functions, the variational principle is applied on subsets of them.

To sum up, once the number of electrons N and the positions of the nuclei $\{\mathbf{R}_\alpha\}$ are defined, a Hamiltonian $\hat{H}$ can be written and, then, Ψ_0, E_0 and all the related properties are determined using the minimization process.

2.1.3 The Hartree-Fock Approximation

To deal with the electron-electron repulsion in Eq. 2.2 other approximations are necessary for any system with more than one electron. The *Hartree-Fock (HF) approximation* is one of those and not only it is a corner stone of almost all the wave function based methods, but it has also a conceptual relevance. Some fundamental concepts that are relevant for our study are intimately connected with this approximation, such as locality, exchange, self-interaction, electron correlation and self-consistency.

As discussed in the previous section, a suitable and manageable subset of wave function has to be defined to apply equation 2.4. In the Hartree-Fock scheme the complicated many-electron wave function is approximated as an product of N one-electron functions $\chi_i(\mathbf{x_i})$, called *spin orbitals*:

$$\Psi_0 \approx \Phi_{SD} = \frac{1}{\sqrt{N!}} \begin{vmatrix} \phi_1(\mathbf{x}_1) & \phi_2(\mathbf{x}_1) & \dots & \phi_N(\mathbf{x}_1) \\ \phi_1(\mathbf{x}_2) & \phi_2(\mathbf{x}_2) & \dots & \phi_N(\mathbf{x}_2) \\ \vdots & \vdots & & \vdots \\ \phi_1(\mathbf{x}_N) & \phi_2(\mathbf{x}_N) & \dots & \phi_N(\mathbf{x}_N) \end{vmatrix} \tag{2.5}$$

The product is expressed in the form of determinant (*Slater determinant* Φ_{SD}) so that the *antisymmetry* of the electrons is respected, because the sign changes upon exchange of two columns. The spin orbitals, usually chosen to be orthonormal, are composed of a spatial orbital $\phi_i(\mathbf{r})$ and a spin function, $\alpha(s)$ or $\beta(s)$.

$$\phi_i(\mathbf{r}, s) = \phi(\mathbf{r})\sigma(s), \quad \sigma = \alpha, \beta \tag{2.6}$$

Now we can use the variational principle to find the Slater determinant with the lowest energy (E_{HF}).

$$E_{HF} = \min_{\Phi_{SD} \to N} \langle \Phi_{SD} | \hat{H} | \Phi_{SD} \rangle \tag{2.7}$$

The spin orbitals $\{\phi_i\}$ into Φ_{SD} are varied until the minimum is reached and orthonormality constraints must be satisfied during the minimization, introducing the *Lagrangian multipliers* ϵ_i in the resulting equations. These equations are the *Hartree-Fock equations*, whose solutions are the 'best' spin orbitals to attain the lowest value of E_{HF}.

$$\hat{f}(\mathbf{x}_1)\phi_i(\mathbf{x}_1) = \epsilon_i \phi_i(\mathbf{x}_1), \quad i = 1, 2, \dots, N. \tag{2.8}$$

In these N eigenvalue equations, the Langrangian multipliers ϵ_i and $\phi_i(\mathbf{r}_1)$ are the eigenvalues and the eigenfunctions of the *Fock operator* $\hat{f}(\mathbf{r}_1)$, respectively. Although

the $\{\epsilon_i\}$ have been introduced only to respect the orbitals orthonormality, the *Koopmans' Theorem* [130] proofed that they are an approximation of minus the ionization energy associated with the removal of the i-th electron:

$$\epsilon_i \approx E_N - E^i_{N-1} = -IE(i) \tag{2.9}$$

Thus, the $\{\epsilon_i\}$ have a physical interpretation and may be compared with the experimental ionization potential.

The Fock operator is an effective one-electron operator defined as

$$\hat{f}(\mathbf{x}_1) = \overbrace{-\frac{1}{2}\nabla^2}^{\hat{T}} \overbrace{- \sum_A^M \frac{Z_A}{r_{1A}}}^{\hat{V}} + V^{HF}(\mathbf{x}_1) = \hat{h} + V^{HF}(\mathbf{x}_1). \tag{2.10}$$

In addition to the kinetic energy of the electrons and their interaction with the nuclei, the Fock operator contains the *Hartree-Fock* potential V^{HF}, which is the average repulsive potential experienced by the electron in the $\phi_i(\mathbf{x}_1)$ spin-orbital due to the remaining N−1 electrons. This operator, where the electron-electron repulsion is taken into account only in an average way, replaces the two-electron operator $1/r_{ij}$ in equation 2.2. The Hartree-Fock potential V^{HF} is composed by two terms:

$$V^{HF}(\mathbf{x}_1) = \sum_j^N (\hat{J}_j(\mathbf{x}_1) - \hat{K}_j(\mathbf{x}_1)). \tag{2.11}$$

The Coulomb operator $\hat{J}$, defined as

$$\hat{J}_j(\mathbf{x}_1) = \int |\phi_j(\mathbf{x}_2)|^2 \frac{1}{r_{12}} d\mathbf{x}_2, \tag{2.12}$$

describes the Coulomb repulsive potential experienced by an electron at $\mathbf{x}_1$ due to the average charge distribution of another electron in the spin orbital ϕ_j. This is a *local* operator, because the application of $\hat{J}_j(\mathbf{x}_1)$ on a spin orbital $\phi_i(\mathbf{x}_1)$ depends only on the value of ϕ_i at the coordinates $\mathbf{x}_1$. The second term appearing in the Hartree-Fock potential is the exchange operator $\hat{K}$, that can only be defined when it is applied on a spin-orbital:

$$\hat{K}_j(\mathbf{x}_1)\phi_i(\mathbf{x}_1) = \phi_j(\mathbf{x}_1) \int \phi^*_j(\mathbf{x}_2) \frac{1}{r_{12}} \phi_i(\mathbf{x}_2)\, d\mathbf{x}_2 \tag{2.13}$$

This operator causes an exchange of the variables in the two spin orbitals, since $\mathbf{x}_2$ goes into ϕ_i and $\mathbf{x}_1$ goes into ϕ_j. Additionally, the results of the application of $\hat{K}_j(\mathbf{x}_1)$ on $\phi_i(\mathbf{x}_1)$ depends on the value of ϕ_i on all points in the integration space, since ϕ_i appears now in the integrand function. Therefore, the exchange potential is called *non-local*. Due to the orthonormality of spin-orbitals, the exchange contributions are different from zero only when electrons have the same spin.

Noteworthy, in the case i is equal to j, the Coulomb operator in equation 2.12 describes the interaction of the charge distribution of one electron with itself. This is the *self-interaction* and it is clearly unphysical. In the framework of Hartree-Fock,

the issue of the self-interaction is elegantly solved by the exchange operator $\hat{K}$ which is identical to $\hat{J}$ when $i = j$, so they perfectly cancel each other out in equation 2.11. In other approaches, such as density-functional theory, this issue constitutes a major obstascle to be overcome.

Finally, one should note that the Hartree-Fock potential in Eq. 2.11 depends on the spin orbitals, i.e. on the solution of the eigenvalue problem to be solved. Therefore, the solution has to be found iteratively through a *self-consistent field* (SCF) procedure: starting from a 'guess' of the orbitals, the HF equations are solved obtaining a new set of orbitals; this set is used to define a new HF potential in the next iteration, resulting in another set of orbitals; this cycle is repeated until convergence, i.e. the energy and/or the spin orbitals no longer change up to a defined threshold.

Once that the spin-orbitals have been computed, the Hartree-Fock total energy can be calculated as:

$$E^{HF} = \sum_i \langle \phi_i | \hat{T} + \hat{V} | \phi_i \rangle + \sum_{i,j} \langle \phi_i \phi_j | 1/r_{ij} | \phi_i \phi_j \rangle - \sum_{i,j} \langle \phi_j \phi_i | 1/r_{ij} | \phi_i \phi_j \rangle \qquad (2.14)$$

where the last two terms are the so-called Coulomb and exchange series.

2.1.4 Electron correlation

Although it generally captures most of the features of a molecular system, a single Slater determinant Φ_{SD} is still an approximation and never corresponds to the exact wave function. Thus, due to the variational principle, E_{HF} is less negative than the exact ground state energy (within the Born-Oppenheimer approximation and ignoring relativistic effects), and their difference is called *correlation energy* (E_C^{HF}).

$$E_C^{HF} = E_0 - E_{HF} \qquad (2.15)$$

This term is always negative and it contains what it is not covered by the effective HF potential, that is the *dynamical* and the *static* electron correlation. The former type of correlation is related to the instantaneous repulsion of the individual electrons, which is not taken into account in the average HF electrostatic potential. This means that in the Hartree-Fock approach electrons will be closer to each other than in the real wave function, causing a larger Coulomb repulsion overall. The dynamical correlation is connected to the $1/r_{12}$ term in the Hamiltonian and is known to be short-range.

The latter type of correlation, often refered as *left-right* correlation, depends on the fact that in special circumstances a single Slater determinant is not enough to describe the exact ground state due to the existence of other Slater determinants with comparable energy. In this case, the recourse to multi-reference approaches, such as configuration-interaction (CI) methods, is needed for the correct description of the system.

2.1.5 Basis sets

For convenience, the one-electron wavefunctions ϕ_i are usually expanded in a linear combination of functions $\{\chi_i\}$, called *basis set* functions, whose analytical form

is known. In the computational practice, the summation is truncated to a certain number M of basis functions:

$$\phi_i(\mathbf{r}) = \sum_{\nu=1}^{M} c_{i\nu}\chi_i(\mathbf{r}) \tag{2.16}$$

The number M must be at least equal to the number of electrons N. Adding new functions to the basis set increases the quality of the ϕ_i and lowers the total energy, due to the variational principle, until the complete basis set limit ($M \to \infty$), also known as the *Hartree-Fock limit*, is reached. In practical calculations, the number M is determined as a balance between accuracy and computational cost. Using the expansion in Eq. 2.16, the Hartree-Fock equations (Eqs. 2.8) can be written in matrix notation as follows

$$\begin{aligned} &\mathbf{F}\,\mathbf{C} = \mathbf{S}\,\mathbf{C}\,\epsilon \\ &F_{\alpha\beta} = \langle\chi_\alpha|\hat{f}|\chi_\beta\rangle \\ &S_{\alpha\beta} = \langle\chi_\alpha|\chi_\beta\rangle \end{aligned} \tag{2.17}$$

where $S_{\alpha\beta}$ are the overlap integrals between basis functions and $F_{\alpha\beta}$ are the elements of the Fock matrix $\mathbf{F}$. The latter are the sum of the one-electron Hamiltonian elements and the contribution from the Coulomb and exchange integrals:

$$F_{\alpha\beta} = \langle\chi_\alpha|\hat{h}|\chi_\beta\rangle + \langle\chi_\alpha|\hat{J}|\chi_\beta\rangle - \langle\chi_\alpha|\hat{K}|\chi_\beta\rangle \tag{2.18}$$

The choice of the basis functions depends on the physics of the problem and on the computational convenience. The functional form may be exponential (Slater-type orbitals, STOs), Gaussian (Gaussian-tupe orbitals, GTOs), plane waves, etc. The use of exponential functions may seem to be the natural choice for atom-centered basis sets, since they describe the correct behaviour for $\mathbf{r} = 0$ and the decay at large distances. However, Gaussian functions are much easier for calculating multi-center integrals in Eq. 2.18, resulting in an overall computational efficiency higher than with STOs. The radial part of a Gaussian-type orbital is defined as:

$$\chi_n^{GTO} = r^{2(n-1)}\exp(-\alpha r^2) \tag{2.19}$$

where α controls how compact (large α) or diffuse (small α) is the basis function. In order to better reproduce the correct behaviour, a contracted Gaussian functions, composed by the linear combination of k GTOs, such as $\chi_n = \sum_k a_n\chi_k^{GTO}$ may be used.

Since the atomic behaviour is mostly determined by valence electrons, *split-valence* basis sets are generally employed, where the core orbitals are described by only one contracted Gaussian function and the valence shell is instead represented by two or more set of contracted GTOs. A split-valence basis set is indicated with the string N–KLG, where N, K and L are the number of GTO in the contraction of the core and valence Gaussian functions. Moreover, polarised functions (symbolized by a "*"), i.e. orbitals with higher angular momentum, and diffuse functions (symbolized by a "+"), characterized by small α exponents, may be added to the basis set to improve its quality.

In this thesis, a Gaussian-type split-valence basis set with polarized functions has been routinely employed. In some specific cases, the addition of a diffuse function to the basis set has been tested to check the convergence of the results.

2.1.6 Periodic Systems

The quantum chemical formalism described in the previous sections can also be applied to *periodic systems*, where the electrostatic potential due to the nuclei is a periodic function. In periodic systems, due to the translational symmetry, a *unit cell*, defined by the $\mathbf{a}_1$, $\mathbf{a}_2$ and $\mathbf{a}_3$ lattice vectors, can be identified in the crystal lattice. Given the lattice vectors in the direct space, the corresponding *reciprocal lattice vectors* in the reciprocal space, $\mathbf{b}_1$, $\mathbf{b}_2$ and $\mathbf{b}_3$, are obtained applying the orthonormality condition $\mathbf{a}_i\mathbf{b}_j = 2\pi\delta_{ij}$, where δ_{ij} is the Kronecker delta. The equivalent of the unit cell in reciprocal space is the (first) *Brillouin zone*, which is shown for graphene in Figure 2.1b.

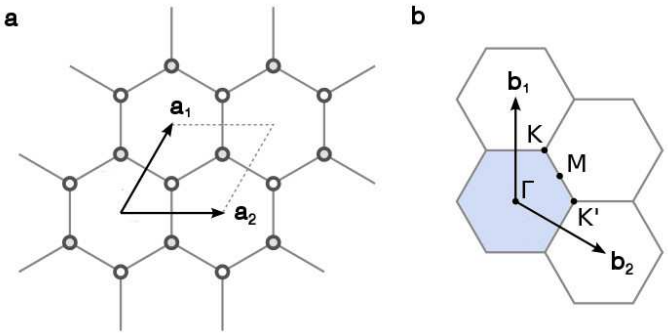

Figure 2.1 – (a) Direct lattice, unit cell and cell vectors of graphene. (b) Reciprocal lattice, first Brillouin zone (BZ, in light blue), reciprocal cell vectors and critical points of the BZ.

The Hamiltonian operator of the electrons in a periodic potential is periodic itself, since the external potential $\hat{V}_{Ne}(\mathbf{r}_i)$ must obey to the periodicity of the lattice:

$$V(\mathbf{r} + N_j a_j) = V(\mathbf{r}), \;\; j = 1, 2, 3 \tag{2.20}$$

where a_j are the lattice vectors and the N_j are arbitrary integer numbers. The *Bloch theorem* [131] shows that the eigenfunctions of such periodic Hamiltonian can be factorized in a plane-wave $e^{i\mathbf{kr}}$ and a periodic function $u_\mathbf{k}(\mathbf{r}_i)$, called *Bloch* or *crystalline orbital*:

$$\psi_\mathbf{k}(\mathbf{r}_i) = e^{i\mathbf{kr}} u_\mathbf{k}(\mathbf{r}_i) \tag{2.21}$$

where $\mathbf{k}$ is the reciprocal space vector, which is the equivalent of the direct space vector $\mathbf{r}$. The Bloch orbital can be expanded into a basis set of plane wave functions (χ^{PW}) or atom-centered (Gaussian) basis functions (χ^{GTO}), see Section 2.1.5. The electronic structure problem has now been substantially simplified because only the

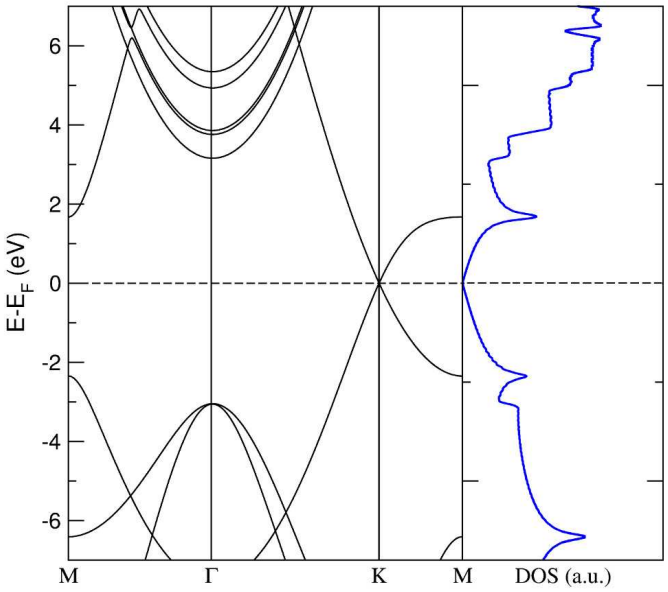

Figure 2.2 – Energy bands of graphene along the path $\Gamma - M - K$ and total density of states (DOS).

electrons within the unit cell have to be considered. However, the eigenvalue problem will now also depend on the $\mathbf{k}$ vector within the first Brillouin zone:

$$\mathbf{F}^{\mathbf{k}}\mathbf{C}^{\mathbf{k}} = \mathbf{S}^{\mathbf{k}}\mathbf{C}^{\mathbf{k}}\epsilon^{\mathbf{k}} \tag{2.22}$$

The resulting eigenfunctions are continuous function of $\mathbf{k}$, varying in a range of energy called *bands*. As an example, the dispersion of the bands in graphene is shown in Figure 2.2. The density of energy levels for any given energy is the *density of states* (DOS), which is also reported in Figure 2.2.

The DOS is an informative way to describe the electronic structure of an extended system since several important properties are directly shown by it, such as the band gap and band widths.

The total energy of the system per unit cell is given by the integration of the occupied bands, i.e. below the Fermi level (E_F), over all the $\mathbf{k}$ space. Nevertheless, for non-metallic systems, the integration can be done numerically with few $\mathbf{k}$ points. Moreover, when the unit cell of the system is large enough (and thus the BZ is small enough) the total energy can be already converged at the origin of the $\mathbf{k}$-space (i.e. Γ point). In general, for periodic calculations in this work, the Brillouin zone has been sampled using an uniform grid of $\mathbf{k}$ points, generated via the Monkhorst-Pack algorithm. [132]

2.2 Density-Functional Theory

The theoretical framework shown in the previous section, based on the wave function Ψ or an approximate version of it, presents a severe problem. Increasing the dimension of the system, the wave function would rapidly reach very large size and complexity, since it depends on $4N$ variables, three spatial and one spin coordinate for each of the N electrons. Thus, any wave-function approach would be unmanageable for large quantum systems, such as the TiO_2 nanoparticles under study in this PhD work.

An alternative idea is to focus on the electron density function $\rho(\mathbf{r})$ of the many-electron system, instead of the hard-to-compute wavefunction. The electron density $\rho(\mathbf{r})$ is a non negative function defined as the probability of finding an electron in the region of space $d\mathbf{r}$:

$$\rho(\mathbf{r}) = N \int \Psi^* \Psi ds_1 d\mathbf{x}_2 \dots d\mathbf{x}_N \tag{2.23}$$

This quantity is dependent *only* on the three spatial coordinates and, unlike Ψ, it is also a physical observable, measurable through X-ray diffraction. [133] Early attempts to express the total energy of the system using the electron density have been done by Thomas and Fermi in the 1920s. [134, 135] However, the foundations of density functional theory (DFT), one of the most successfull computational tool of the last three decades, relies on the work by Hohenberg, Kohn and Sham in the 1960s.

2.2.1 The Hohenberg-Kohn Theorems

In 1964, P. Hohenberg and W. Kohn showed that the ground state properties are uniquely determined by the electron density $\rho(\mathbf{r})$. [136] The first point to be proven is related to the external potential $V = \sum_{i=1}^{N} v(\mathbf{r}_1)$: it is fairly obvious that V determines Ψ and then $\rho(\mathbf{r})$ through the Schrödinger equation, but the fundamental question is whether it is true the opposite, i.e. that the electron density defines univocally the external potential. This has been demonstrated by the **First Hohenberg-Kohn Theorem**.

Theorem 1 *The external potential $v(\mathbf{r})$ of a system is univocally determined, within a trivial additive constant, by the electron density $\rho(\mathbf{r})$.*

The proof of this theorem is based on the variational theorem. Therefore, the ground state energy of the system can be expressed as a *functional* of the electron density

$$E_0[\rho] = F[\rho] + \int d\mathbf{r} v(\mathbf{r}) \rho(\mathbf{r}) \tag{2.24}$$

where $F[\rho]$ is the *universal* functional, whose analytical expression is unknown but the existence has been proven. The **Second Hohenberg-Kohn Theorem** introduces a variational principle applicable to the density functionals.

Theorem 2 *Considering the relation $\rho(r)_1 \Longleftrightarrow v_1$ from the first HK theorem, and assuming that there is a $\rho(r)_2$, such that $\rho(r)_2 \geq 0$, then: $E_{v1} \leq E_{v2}$.*

Also the proof of the second theorem is again based on the variational theorem, thus density functional theory is only applicable to non-degenerate ground states. Therefore, the ground state energy of a many-electron system corresponds to the minimum value of $E[\rho]$ for all the possible electron densities. However, this is true only when the exact universal F functional is used. In the common practice, the density functional is approximated, hence DFT may not be always supported by the variational principle.

2.2.2 The Kohn-Sham Equations

In order to apply the Hohenberg and Kohn theorems, a practical yet efficient form of the unknown universal functional has to be formulated. First, the density functional $F[\rho]$ in Eq. 2.24 can be decomposed as:

$$F[\rho(\mathbf{r})] = T[\rho(\mathbf{r})] + E_H[\rho(\mathbf{r})] + E_{xc}[\rho(\mathbf{r})] \tag{2.25}$$

where $T[\rho]$ is the kinetic energy functional, $E_H[\rho]$ is the mean field interaction and $E_{xc}[\rho]$ is the correction to the mean field part, due to exchange and electron correlation effects. Among these terms only the mean field interaction is known, but the main problem arises from the definition of the kinetic energy, because the analytical form of the wavefunction is needed. In 1965, Kohn and Sham [137] developed a clever way to overcome this issue, introducing a fictitious non-interacting system and expressing the electron density with auxiliary functions. In the Kohn-Sham DFT (KS-DFT) scheme, the electron density is expanded in a set of single particle wavefunctions $\phi_i(\mathbf{r}, s)$:

$$\rho(\mathbf{r}) = \sum_{i}^{N} \sum_{s} \phi_i(\mathbf{r}, s)^* \phi_i(\mathbf{r}, s) \tag{2.26}$$

these auxiliary functions are known as the *Kohn-Sham (KS) orbitals*. It is then possible to define a *non-interacting reference system* with the same exact density as the real one formed by the Slater determinant of these N KS orbitals. In such a system, the kinetic energy can be exactly calculated through the expression:

$$T_S[\rho] = \sum_{i}^{N} \langle \phi_i | -\frac{1}{2}\nabla^2 | \phi_i \rangle \tag{2.27}$$

Clearly, this kinetic energy $T_S[\rho]$ is not equal to the true kinetic energy of N interacting electrons, i.e. $T_S[\rho] \neq T[\rho]$. Kohn and Sham solved this issue including the residual part of the kinetic energy ($T_C[\rho]$) in the definition of the *exchange-correlation energy*, so that the total energy functional can be written as

$$E[\rho(\mathbf{r})] = T_S[\rho(\mathbf{r})] + E_H[\rho(\mathbf{r})] + E_{Ne} + E_{xc}[\rho(\mathbf{r})] \tag{2.28}$$

where

$$E_{xc}[\rho(\mathbf{r})] = T_C[\rho(\mathbf{r})] + E_{ncl} \tag{2.29}$$

In other words, E_{xc} not only contains the non-classical effects (E_{ncl}), i.e. the self-interaction correction, exchange and correlation, but also the correction of the error in the kinetic energy evaluation.

Analogously to the Hartree-Fock approach, we now minimize $E[\rho]$ with respect to the KS orbitals, under the orthonormality constraint. [138] The resulting one-electron equations are the *Kohn-Sham equations*:

$$\left(-\frac{1}{2}\nabla^2 + V_{\text{eff}}(\mathbf{r_1})\right)\phi_i = \epsilon_i\phi_i \tag{2.30}$$

where

$$V_{\text{eff}}(\mathbf{r_1}) = \int \frac{\rho(\mathbf{r}_2)}{r_{12}}\, d\mathbf{r}_2 + V_{xc}(\mathbf{r}_1) - \sum_A^M \frac{Z_A}{r_{1A}} \tag{2.31}$$

As well as it is not available an exact expression of the exchange-correlation energy E_{xc}, even the explicit form of the related potential V_{xc} is unknown. Thus, V_{xc} is defined as the functional derivative of E_{xc} with respect to ρ:

$$V_{xc} = \frac{\delta E_{xc}}{\delta \rho} \tag{2.32}$$

Similarly to the HF equations, the KS potential is dependent on the initially unknown KS orbitals. For this reason, the KS equations are solved iteratively, through a self-consistent field (SCF) procedure, already described in section 2.1.3.

2.2.3 Exchange-Correlation Functionals

If the exact analytical form of $V_{xc}[\rho]$ were known, the DFT total energy would be exactly equal to the eigenvalue of the Schrödinger equation, i.e. the solution to the electronic structrure problem. For this reason, most of the methodological work that has been done after the formulation of the Kohn-Sham equations concerned the definition of a reasonable and efficient exchange-correlation potential V_{xc}. Although there are few physical constraints that a functional has to fulfill, the search for better functionals is largely based on mathematical intuition and 'trial and error'. [129]

One of the first ideas to approximate $E_{xc}[\rho]$ is the *Local Density Approximation* (LDA). This approach is based on the physics of the *uniform electron gas*, i.e. a system of N electrons in a positive background of charge. Within this approximation, the exchange-correlation (xc) energy functional depends only on the value of the electron density $\rho(\mathbf{r})$ in each point of the space:

$$E_{xc}^{LDA}[\rho] = \int \rho(\mathbf{r})\epsilon_{xc}(\rho(\mathbf{r}))d\mathbf{r}, \tag{2.33}$$

where $\epsilon_{xc}(\rho(\mathbf{r}))$ is the xc energy of the electron gas per particle. This quantity can be further decomposed into the individual contributions,

$$\epsilon_{xc}(\rho(\mathbf{r})) = \epsilon_x(\rho(\mathbf{r})) + \epsilon_c(\rho(\mathbf{r})). \tag{2.34}$$

The explicit form of ϵ_x for the homogeneous electron gas can be derived from the Hartree-Fock exchange. [139] No analytical form of the correlation part ϵ_c is known, but highly accurate expressions based on interpolation are available and one of the most used is by Vosko, Wilk and Nusair (VWN). [140, 141]

The homogeneous electron gas model is clearly different from the real situation in molecules where the density changes abruptly from point to point. For this reason, the LDA functionals have been found to work fine for metals and some solids, but they do not produce chemically accurate results with a clear tendency to overbind molecules (by ≈ 1 eV). [142, 143]

A higher degree of accuracy can be reached with the *generalized gradient approximation* (GGA), in which the information from the gradient of the electron density, $\nabla\rho(\mathbf{r})$, is included. [129] Thanks to this contribution, the functional would better account for the inhomogeneities of the real electron density. Similarly to LDA, E_{xc}^{GGA} is generally split into its components, E_x^{GGA} and E_c^{GGA}. Prominent implementation are the Perdew, Burke and Ernzerhof (PBE) functional [144], for both the exchange and correlation parts, and the widely used, Lee, Yang and Parr (LYP) correlation functional, [145] which is not based on the correlation energy of the electron gas but on the exact one for the helium atom. The GGA functionals are largely employed in computational chemistry and materials science, since errors on the energies are usually lower than 0.3 eV, approaching the chemical accuracy (0.1 eV). [142, 143]

2.2.4 Hybrid functionals

As discussed in section 2.1.3, in the Hartree-Fock (HF) theory the exchange energy can be computed exactly and, when $i = j$, the Coulomb integrals are equal to the exchange ones, solving completely the self-interaction issue. In order to exploit these features of HF exchange, *hybrid functionals* replace a fraction of the GGA exchange with the Hartree-Fock exact exchange, so that the exchange-correlation functional is formulated as follows

$$E_{xc}^{hyb} = E_{xc}^{GGA} + \lambda(E_x^{HF} - E_x^{GGA}) \tag{2.35}$$

where λ is the fraction of HF exchange calculated using the exchange operator in equation 2.13 and the Kohn-Sham orbitals $\{\phi_i\}$

$$E_x^{HF} = -\frac{1}{2}\sum_{i,j,\sigma}^{occ}\int d\mathbf{r}\int d\mathbf{r}'\frac{\psi_{i\sigma}^*(\mathbf{r})\psi_{j\sigma}^*(\mathbf{r}')\psi_{i\sigma}(\mathbf{r}')\psi_{j\sigma}(\mathbf{r})}{|\mathbf{r}-\mathbf{r}'|}. \tag{2.36}$$

The introduction of a portion λ of exact exchange improves the overall description of the exchange-correlation energy and the accuracy of the method. [142, 143, 146] Moreover, it partially corrects the self-interaction error, giving more accurate results for band gaps and electron localization/delocalization. The most popular hybrid functional is the B3LYP, [145, 147] whose functional form is the following:

$$E_{xc}^{B3LYP} = (1-a)E_x^{LDA} + aE_x^{HF} + bE_x^{B88} + cE_c^{LYP} + (1-c)E_c^{LDA} \tag{2.37}$$

where E_x^{B88} is a GGA exchange functional and a, b and c are empirical parameters fitted to reproduce thermodynamic data, such as atomization and ionization potentials, proton affinities, and total atomic energies. This fitting procedure resulted in $a = 0.20$, $b = 0.72$ and $c = 0.81$. Although this functional was initially developed to investigate the electronic structure of molecules, it showed surprisingly good performances in many other chemical applications, including transition-metal chemistry and condensed-phase systems. This functional is routinely used in this work, because the correction to the self-interaction, albeit partial, is particularly important for the description of the band gap and charge carriers in TiO_2 systems. [148–150]

However, the introduction of a portion of exact exchange into the energy functional influences also the asymptotic behaviour of the electron-electron repulsion, that is lower than it should ($-1/r$ for $r \to \infty$). For this reason, *range-separated hybrid functionals*, where the Coulomb operator is split into a short- and a long-range part, have been developed. In this way, the amount of HF exchange can be tuned as a function of the interelectronic distance, recovering the correct asymptotic limit. In this work, the range-separated Heyd-Scuseria-Ernzerhof functional (HSE06) has been tested for TiO_2 systems, since it was reported to predict the band gaps of semiconductors with errors as small as 0.2 eV. [151]

It is important to underline that hybrid functionals introduce a *non-local* contribution in the total energy due to the exact exchange. This means that the energy functional in a specific point is not only dependent on the value of the density (and/or its gradient) at that point as in *local* LDA or GGA approximation, but also on the Kohn-Sham orbitals, which are not local quantities but delocalized in all the integration space.

2.2.5 Electronic properties

Energy Gaps

The energy gaps, such as the HOMO–LUMO gap in molecules and the band gap in extended materials, are one of the most important properties defining the electronic structure of a system. Commonly, they are distinguished in *fundamental* and *optical* gaps. The fundamental gap E_g is defined as the energy difference between the first ionization potential (IP) and the first electron affinity (EA) and it can be measured by several techniques, for instance photoemission spectroscopy. Instead, the optical gap corresponds to the difference in energy between the ground state and the first excited state of the system and it is usually determined by UV-vis spectroscopy.

In a ground state theoretical framework, such as the one of DFT, it is common practice to approximate the fundamental gap E_g to the Kohn-Sham gap E_{gKS}, since IP and EA are connected to the N-th and $(N+1)$-th Kohn-Sham orbital energies, i.e. ϵ_N and ϵ_{N+1} via the following equation: [152]

$$\begin{aligned} IP(N) &= -\epsilon_N(N-\delta) \\ EA(N) &= -\epsilon_{N+1}(N+\delta) \end{aligned} \tag{2.38}$$

where δ is an infinitesimal variation of the integer electron number. However, it is well-known that a standard Kohn-Sham DFT calculation is equivalent to approaching

the integer electron number from below, [153] i.e. it provides $\epsilon_{N+1}(N-\delta)$. However, the two values of ϵ_{N+1} approaching from below or from above are not equal and they differ by exactly the derivative discontinuity in E_{xc} (DD or Δ_{xc}). Therefore, the fundamental gap can be evaluated as follows:

$$E_g = IP - EA = \epsilon_{N+1} - \epsilon_N + DD \tag{2.39}$$

Standard LDA or GGA functionals do not have a derivative discontinuity of the exchange-correlation energy, therefore the Kohn-Sham gaps obtained with these approaches are lower than the fundamental gap. [154] On the contrary, for hybrid functionals, since they are orbital-dependent potentials, the above derivative discontinuity argument does not apply. Therefore, hybrid functionals can yield more accurate predictions of the band gaps, although the performances depends on the choice of the functional. [155, 156] Among them, the B3LYP functional is capable to predict the band gap of a wide range of solids with an error lower than 10 %. [149]

Excited states

Density-functional theory has been largely used to study ground state properties such as total and binding energies, bond lenghts and angles, lattice constants and also dipole moments and polarizabilities, with a degree of accuracy significantly higher than Hartree-Fock, even more if hybrid functionals are employed. [146, 157, 158]

Nonetheless, especially when light-matter interaction is involved, one is interested in the properties of excited states of the molecular system. Remarkably, information on these states can be extracted from DFT, even though is a ground state theory.

One widely spread approach is to use the *time-dependent* extension of DFT (TD-DFT), a general scheme to follow the dynamic response of the electron density to time-dependent potentials, like the oscillating external electric fields of light. In addition to the vertical excitation energies, directly comparable to UV-Vis spectroscopy, TD-DFT can provide also the excited state properties, such as its energy, forces and geometry. [159]

Another common approach derives from solid-state physics, where the electronic excited state in a bulk material is often described as an *exciton*, i.e. an excited electron and hole couple. In the DFT framework, accurate calculations of the energy level of the non-interacting electron and hole can be derived using the Green's function formalism within the GW approach [160], whose results are directly comparable to X-ray photoabsorption energies or work function measurements. Moreover, when the electron/hole Coulomb interaction is screened enough by the lattice, the GW results are already a good approximation of the excitation energy. However, in many cases, the interaction between the electron/hole pair, namely the *excitonic effects*, is relevant and can be taken into account with the *Bethe-Salpeter* equation (BSE), [161] providing accurate prediction of the electronic transitions energy.

However, for systems with hundreds of atoms, TD-DFT and Green's function based calculations become extremely demanding from a computational point of view. A viable, though not always applicable, solution for large molecules is to use a *time-independent* approach, such as the ΔSCF-DFT method, that allows to compute excited state energies and forces at the cost of a plain DFT calculation. This methodol-

ogy employs non-Aufbau electronic configurations to converge the Kohn-Sham SCF equations to an excited state. In the case that the excited state is the lowest-energy state with that symmetry, the SCF is guaranteed to converge to the right solution, otherwise it may collapse to a lower-energy state.

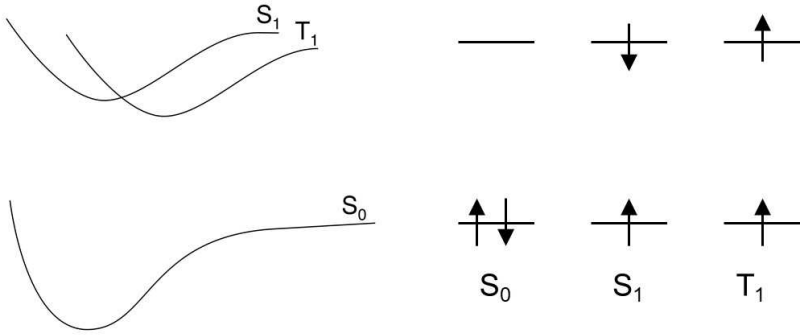

Figure 2.3 – Potential energy surface for the ground state S_0 and first excited states S_1 and T_1.

For example, considering the case shown in Figure 2.3, the double radical singlet state S_1 would be very difficult to converge, since the electronic structure would easily collapse to the S_0 state. Instead, the excited triplet state T_1 is easily accessible, being a ground state for the triplet spin configuration. In this work, a ΔSCF approach will be used to model photoexcited carriers in TiO_2 systems.

Transition Levels

In the case of semiconductor materials, point defects in the regular lattice significantly affect the electronic properties. In fact, they may introduce levels within the band gap (deep state) or near the band edges (shallow state). These states can be probed experimentally through several spectroscopies, such as transient absorption (TA) spectroscopy. All these techniques involve a variation in the charge state of the defect, which cannot be described accurately by the single-particle Kohn–Sham eigenvalues. A better approximation of these kind of electronic transitions can be obtained with the transition energy levels computation. [162–164]

The formation energy of a defect D with a charge q is defined as:

$$\Delta H_{D,q}(E_F, \mu) = [E_{D,q} - E_H] + q[E_v + E_F] + \sum n_i \mu_i \tag{2.40}$$

where the charge q is dimensionless (e.g. $+1$, 0, -1), $E_{D,q}$ and E_H are the total energies of the host+defect and the host-only systems, respectively, E_v is the valence band maximum (VBM) energy, E_F is the Fermi level with respect to the VBM, n_i is the number of added ($n_i > 0$) or removed ($n_i < 0$) atoms to create the defects, and μ_i is the chemical potential of the defect species. In this PhD work, we are interested in

the levels of self-trapping states of TiO_2 charge carriers, where the chemical potential contribution is zero, since no other chemical species are added or removed.

The transition level $\varepsilon(q/q')$ is defined as the value of the Fermi level where the charge states q and q' have the same formation energy,

$$\Delta H_{D,q}(E_F = \varepsilon(q/q'), \mu) = \Delta H_{D,q'}(E_F = \varepsilon(q/q'), \mu). \tag{2.41}$$

From Eq. 2.41 it follows that:

$$[E_{D,q} - E_H] + q[E_v + \varepsilon(q/q')] = [E_{D,q'} - E_H] + q'[E_v + \varepsilon(q/q')] \tag{2.42}$$

thus:

$$\varepsilon(q/q') = \frac{E_{D,q'} - E_{D,q}}{q - q'} - E_v \tag{2.43}$$

The $\varepsilon(q/q')$ corresponds to the vertical transition between the q and q' charge state and are thus labeled as optical transition levels, $\varepsilon^{opt}(q/q')$. In the specific case of self-trapping charge states two cases can be distinguished:

- one negative charge (electron, e^-) is added to the system, inducing the formation of a negatively charged trap state with a level in the gap below the conduction band.
- one positive charge (hole, h^+) is added to the system, inducing the formation of a positively charged trap state with a level in the gap above the valence band.

Conventionally, the q' corresponds to the defect, i.e. a charge trap (TRAP) in this case, with one electron more (q + 1 e^-), thus q' is -1 in the case of the electron trap defect, 0 in the case of the hole trap defect. Therefore, the transition level, i.e. the position in the band gap of electron and hole trap states can be computed as:

$$\begin{aligned} \varepsilon(0/-1) &= \frac{E_{TRAP,0} - E_{TRAP,-1}}{-1-0} - E_v = E_{TRAP,-1} - E_{TRAP,0} - E_v \\ \varepsilon(+1/0) &= \frac{E_{TRAP,+1} - E_{TRAP,0}}{0-1} - E_v = E_{TRAP,0} - E_{TRAP,+1} - E_v \end{aligned} \tag{2.44}$$

The transition levels of an electron and an hole trap in the gap are schematically represented in Figure 2.4.

During a transient absorption experiment, as shown by the arrows in Figure 2.4, the electron and hole traps experiences a $-1 \rightarrow 0$ and a $+1 \rightarrow 0$ transitions, respectively. Thus, the optical transition between the electron trap state and the conduction band can be computed as follows:

$$\varepsilon^{opt}(-1/0; e) = E_c - \varepsilon^{opt}(0/-1) = E_{TRAP,0} - E_{TRAP,-1} + E_c \tag{2.45}$$

where $E_{TRAP,0}$ and $E_{TRAP,-1}$ are the neutral and charged total energies of the system in the atomic structure where the electron is self-trapped, and E_c is the energy

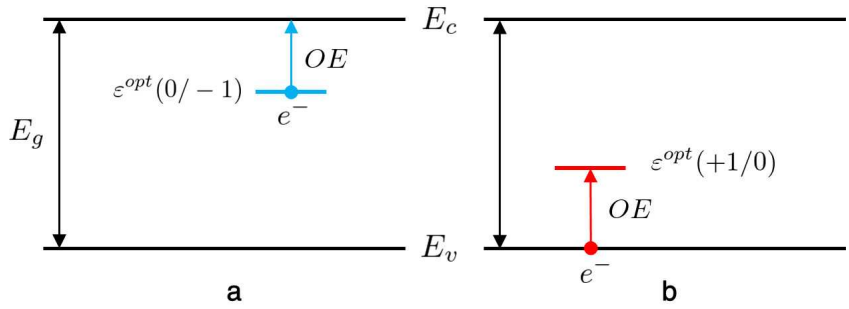

Figure 2.4 – Schematic representation of the transient ab sorption process (optical excitation, OE) for electron (a) and hole (b) charge trap states. The position in the gap (E_g) of the corresponding transition levels $\varepsilon(0,-1)$ and $\varepsilon(+1,0)$ are also represented.

of the bottom of the conduction band. The conduction band bottom can be estimated by the vertical electron affinity of the system ($E_c \approx -\text{EA}$).

Similarly, the optical transition between the valence band and the hole trap level is given by:

$$\varepsilon^{opt}(+1/0;h) = \varepsilon^{opt}(+1/0) = E_{TRAP,0} - E_{TRAP,+1} - E_v \tag{2.46}$$

where the energy of the top of the valence band, E_v, can be evaluated by the computed vertical ionization potential ($E_v \approx -\text{IP}$). Since in this PhD work we treat large finite systems, the total energies are directly accessible by charged calculations, because no periodic boundary conditions and consequently no background of charge is needed.

2.3 Density-Functional Tight-Binding approach

In the last three decades, the Kohn-Sham DFT scheme has been proved to be an efficient tool for the prediction of the properties of molecular and condensed phase systems. However, the system size and the time scales accessible with DFT are still limited to few hundreds of atoms and few picoseconds, as sketched in Figure 2.5. Less demanding calculations using classical or reactive force fields allow for very large scale simulations, but the predictivity is limited and they can not provide a quantum insight. Semiempirical quantum-chemical methods (SE-QM) recover the quantum description at a lower cost than HF or DFT, even though they employ empirical parameters with little physical meaning, limiting their application only to simple organic molecules. [165]

A good compromise for the investigation of systems in the nanoscale is the tight-binding (TB) approximation of the KS-DFT theory, namely density-functional tight binding (DFTB). As a matter of fact, in terms of applicability and predictivity, this method sets in between DFT and molecular mechanics methodologies, allowing for accurate calculations of thousands of atoms and simulation time in the order of hun-

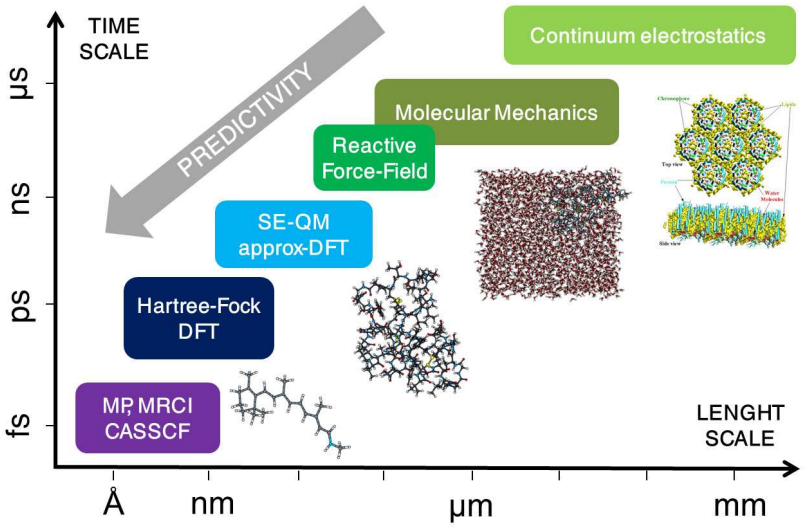

Figure 2.5 – Typical time and size range of applicability for commonly used molecular and atomistic calculations methods.

dreds of picoseconds. Noteworthy, this method contains only a small number of rather transferable parameters, improving the transferability with respect to SE-QM approaches.

The main concept of "tight-binding" is to calculate the electronic structure of the many-body system from a parametrized Hamiltonian matrix, whose elements are usually set in order to reproduce experiments or band structures. This is the basic idea of the Hückel theory [166] for aromatic molecules, which was extended to periodic solids by Slater and Koster in 1954. [167] In any TB approach, the total energy of the system is defined as the sum of an attractive (E_{el}) and repulsive (E_{rep}) term [168]:

$$E_{TB} = E_{el} + E_{rep} = \sum_{i}^{N} \epsilon_i + \frac{1}{2} \sum_{\alpha \neq \beta}^{M} v^{\alpha,\beta}(|\mathbf{R}_\alpha - \mathbf{R}_\beta|) \tag{2.47}$$

where ϵ_i are the eigenvalues of the parametrized Hamiltonian and $v^{\alpha,\beta}$ is a two-body repulsive potential. In the following, I will deliver an introduction to the TB scheme derived from density-functional theory. A deeper discussion on the method and its derivation can be found in Refs. [165], [169] and [170].

Approximate density functional theory

As discussed in section 2.2, the DFT total energy of a system can be written as

$$E_{tot}[\rho(\mathbf{r})] = T_S[\rho(\mathbf{r})] + E_{Ne}[\rho(\mathbf{r})] + \overbrace{\frac{1}{2}\int\int \frac{\rho(\mathbf{r})\rho(\mathbf{r}')}{|\mathbf{r}-\mathbf{r}'|}d\mathbf{r}d\mathbf{r}'}^{E_H} + E_{xc}[\rho(\mathbf{r})] + \sum_{\alpha,\beta}\overbrace{\frac{Z_\alpha Z_\beta}{R_{\alpha\beta}}}^{E_{nn}} \tag{2.48}$$

Through the solution of the corresponding Kohn-Sham equations, the KS orbitals ϕ_i and the electron density ρ of the system can be obtained. Given this quantities, the DFT total energy can be rewritten as

$$E_{tot}[\rho] = \sum_i^{occ} \langle\phi_i|\hat{h^0}|\phi_i\rangle - \frac{1}{2}\left[\int V_{\text{eff}}\rho d\mathbf{r} - \int V_{Ne}\rho d\mathbf{r}\right] + E_{xc}[\rho] - \frac{1}{2}\int V_{xc}\rho d\mathbf{r} + E_{nn} \tag{2.49}$$

where the effective one-electron Hamiltonian ($\hat{h}^0$, defined in equation 2.30) is followed by a series of terms to correct the double counting into the eigenvalues summation and E_{nn} is the nuclear repulsion.

Being E_{tot} variational with respect to density variations, the total energy may be calculated also using an approximate electron density ρ_0, which is considered the reference one and should be close to the exact density ρ. The reference density ρ_0 is usually defined as the superposition of the neutral atomic densities: $\rho_0 = \sum_\alpha \rho_\alpha^0$.

Then, to improve the description of the electron density, we include an appropriate density fluctuation $\delta\rho$, so that $\widetilde{\rho} = \rho_0 + \delta\rho$. Using a Taylor expansion up to the second order, E_{tot} may be written as follows:

$$\begin{aligned} E[\rho(\mathbf{r})] &= \underbrace{\sum_i^{occ}\langle\phi_i|\hat{h}[\rho_0]|\phi_i\rangle}_{1} + \underbrace{E_{xc}[\rho_0]}_{2} - \underbrace{\frac{1}{2}\int V_H[\rho_0]\rho_0'\, d\mathbf{r}'}_{3} \\ &- \underbrace{\int \rho_0 V_{\text{xc}}[\rho_0]d\mathbf{r}'}_{4} + \underbrace{E_{nn}}_{5} \\ &+ \underbrace{\frac{1}{2}\int \delta\rho V_H[\delta\rho]d\mathbf{r}'}_{6} + \underbrace{\frac{1}{2}\int\int \left.\frac{\delta^2 E_{xc}}{(\delta\rho)^2}\right|_{\rho_0} (\delta\rho)^2 d\mathbf{r}'}_{7} + o(\delta\rho^3) \end{aligned} \tag{2.50}$$

where $\hat{h}[\rho_0]$ is an approximate one-electron Hamiltonian given by the kinetic energy operator and the sum of the effective potential of neutral atoms:

$$\hat{h}[\rho_0] = \frac{1}{2}\nabla^2 + \sum_\alpha V_{\text{eff},\alpha}^0 \tag{2.51}$$

The different DFTB approaches are characterized by the order of the charge fluctuation that is taken into account: first-order DFTB or DFTB1 considers only terms 1–5; self-consistent charge DFTB (SCC-DFTB or DFTB2) includes also terms 6–7; DFTB3 introduces even the third-order effects ($o(\delta\rho^3)$) in the calculation.

2.3.1 First-order DFTB method

The traditional first-order DFTB approach treats only the ρ_0-dependent terms of eq. 2.50, i. e. terms 1–5. In particular, term 1 can be decomposed into the contributions by valence and core electrons:

$$\sum_{i}^{occ} \langle\phi_i|\hat{h^0}|\phi_i\rangle = \sum_{i}^{valence} \langle\phi_i|\hat{h^0}|\phi_i\rangle + \sum_{i}^{core} \langle\phi_i|\hat{h^0}|\phi_i\rangle = \sum_{i}^{valence} n_i\epsilon_i + \sum_{i}^{core} n_i\epsilon_i \quad (2.52)$$

It can be demonstrated (see ref. [165]) that terms 2–5, together with the summation on the core orbital energies, behave like a short-range repulsive potential that rapidly goes to zero for large interatomic distances. In the DFTB methodology, this short-range potential is modeled as a sum of pairwise distance-dependent repulsive energy, so that the total energy assumes the typical tight-binding form shown in Eq. 2.47:

$$E^{DFTB1} = E_{el} + E_{rep} = \sum_{i}^{valence} n_i\epsilon_i + \frac{1}{2}\sum_{\alpha\neq\beta}^{M} v^{\alpha,\beta}(R_{\alpha\beta}). \quad (2.53)$$

The Kohn-Sham eigenvalues $\{\epsilon_i\}$ and eigenvectors $\{C_i\}$ are obtained by solving a generalized eigenvalue problem

$$\mathbf{H}\,\mathbf{C} = \mathbf{S}\,\mathbf{C}\,\epsilon \quad (2.54)$$

where KS orbitals are expanded in a minimal basis of optimized Slater-type functions $\{\chi_i\}$. The elements of the Hamiltonian ($\mathbf{H}$) and overlap ($\mathbf{S}$) matrixes are computed as follows

$$\begin{aligned} S_{\mu\nu} = &\quad \langle\chi_\mu|\chi_\nu\rangle \\ H^0_{\mu\nu} = &\quad \begin{cases} \epsilon_\mu^{free-atom} & \mu = \nu \\ \langle\chi_\mu^\alpha|\hat{T} + V_0^\alpha + V_0^\beta|\chi_\nu^\beta\rangle & \alpha \neq \beta \\ 0 & otherwise \end{cases} \end{aligned} \quad (2.55)$$

where indexes μ and ν run on the basis set functions and α and β refer to atoms. In other words, the matrix elements are limited to one- and two-center integrals, computed via atomic or diatomic LDA or GGA density-functional theory calculations. The energy functional in these DFT methods is purely local, thus these integrals can be calculated in advance and stored in tables, i.e. in the so-called Slater-Koster (SK) files, as a function of the interatomic distance.

The repulsive pairwise potential $v^{\alpha,\beta}(R_{\alpha\beta})$ is instead fitted to DFT calculation using a set of reference structures.

$$v^{\alpha,\beta}(R_{\alpha\beta}) = \left\{ E^{\mathrm{SCF}}_{\mathrm{LDA/GGA}}(\mathbf{R}) - \sum_{i}^{occ} n_i\epsilon_i(\mathbf{R}) \right\}\Bigg|_{\text{reference structure}} \quad (2.56)$$

As an example, we report the fitting procedure for the carbon-carbon potential, which usually consider acetylene, ethylene and ethane as reference molecules:

1) for each C–C bond distance in a defined range, the proper molecule is chosen and its C–C bond is set to a specific value.

2) the corresponding full DFT total energy (E_{DFT}) and the DFTB E_{el} in Eq. 2.53 are computed.

3) the repulsive energy E_{rep} for that specific C–C bond lenght is $E_{DFT} - E_{el}$

4) steps 1–3 are repeated with a different C–C distance and the values of E_{rep} as a function of the distance are fitted with a polynomial function, whose coefficients are stored in the Slater-Koster file.

Once that the integrals and repulsive potentials for each atomic pair in the systems are known, the DFTB total energy is computed according to Eq. 2.53.

2.3.2 Self-consistent charge extension

The above described methodology works fine as long as the electron density of the neutral atoms is a good approximation of the real electron density. This is not the case for heteronuclear molecules or polar semiconductors, where the charge-transfer between atoms is significant. In order to treat the long-range electrostatic interaction of the induced charges and increase the overall accuracy of the first-order DFTB, an improved scheme called self-consistent charge DFTB (SCC-DFTB) has been developed [171].

In this new procedure, terms 6 and 7 of Eq. 2.50 are approximated through a multipole expansion, truncated at the monopole order:

$$E_{2nd} = \frac{1}{2}\int \delta\rho V_H[\delta\rho]d\mathbf{r}' + \frac{1}{2}\int\int \left.\frac{\delta^2 E_{xc}}{(\delta\rho)^2}\right|_{\rho_0} (\delta\rho)^2 d\mathbf{r}d\mathbf{r}' \approx \frac{1}{2}\sum_{\alpha,\beta}^{N} \gamma_{\alpha\beta}\Delta q_\alpha \Delta q_\beta \quad (2.57)$$

where Δq_i are the induced charges on the atoms and $\gamma_{\alpha\beta}$ is a Coulombic-like interaction potential, that accounts for the Hartree and exchange-correlation. In the original formulation of the SCC-DFTB method, the $\gamma_{\alpha\beta}$ function is composed by two terms

$$\gamma_{\alpha\beta} = \frac{1}{R_{\alpha\beta}} - S_{\alpha\beta} \quad (2.58)$$

in which $S_{\alpha\beta}$ is an exponetially decaying short-range correction between the two nuclei α and β. Later, it has been shown that this function is crucial for the description of hydrogen-bonded systems, [172, 173] which are object of study in this work. For these cases, a modified hydrogen bonding damping (HBD) function $\gamma_{\alpha H}$ has been introduced to describe the interaction between the atom α and hydrogen:

$$\begin{aligned} \gamma_{\alpha\beta} &= \frac{1}{R_{\alpha\beta}} - S_{\alpha\beta} \times f_{\alpha H}, \\ f_{\alpha H} &= \exp\left[-\left(\frac{U_\alpha + U_H}{2}\right)^{\zeta} r_{\alpha H}^2\right]. \end{aligned} \quad (2.59)$$

where U_α and U_H are the Hubbard parameters, which are linked to the corresponding chemical hardness of α and hydrogen atom. The additional ζ parameter in the exponential is usually determined by fitting to *ab initio* calculations of H-bond energies.

Finally, the SCC-DFTB total energy is then defined as

$$E^{SCC-DFTB} = \sum_{i}^{valence} n_i \epsilon_i + \frac{1}{2} \sum_{j \neq k}^{M} E_{rep}(R_{\alpha\beta}) + \frac{1}{2} \sum_{\alpha,\beta}^{N} \gamma_{\alpha\beta} \Delta q_\alpha \Delta q_\beta. \tag{2.60}$$

The induced charges Δq_i depend on the one-electron wave-functions ϕ_i through the Mulliken population analysis, thus a self-consistent procedure is needed to calculate the total energy. Indeed, the two-center Hamiltonian matrix elements in Eq. 2.55 are modified by the induced charges as follows

$$H^0_{\mu\nu} = \langle \chi^\alpha_\mu | \hat{T} + V^\alpha_0 + V^\beta_0 | \chi^\beta_\nu \rangle + \frac{1}{2} \sum_{K}^{atoms} (\gamma_{\alpha K} + \gamma_{\beta K}) \Delta q_K. \tag{2.61}$$

Therefore, the total energy is obtained by solving the eigenvalue problem in Eq. 2.54 iteratively until convergence of the induced charges Δq_i.

The first derivatives of the (SCC-)DFTB total energy, which are necessary for the optimization and molecular dynamics runs, can be calculated analytically through the following formula:

$$\begin{aligned} F_\alpha = & - \sum_{i}^{occ} n_i \sum_{\mu \in \alpha} c_{\mu i} c_{\nu i} \left[\frac{\partial H^0_{\mu\nu}}{\partial \mathbf{R}_\alpha} - \left(\epsilon_i - \frac{H^1_{\mu\nu}}{S_{\mu\nu}} \right) \frac{\partial S_{\mu\nu}}{\partial \mathbf{R}_\alpha} \right] \\ & - \Delta q_\alpha \sum_{\xi}^{N} \frac{\partial \gamma_{\alpha\xi}}{\partial \mathbf{R}_\alpha} \Delta q_\xi - \frac{\partial E_{rep}}{\partial \mathbf{R}_\alpha} \end{aligned} \tag{2.62}$$

2.4 Geometry optimization techniques

As discussed in section 2.1.1, in the Born-Oppenheimer approximation the nuclear and electronic motion are considered independent and it is possible to write a nuclear Schrödinger equation:

$$[\hat{T}_N(\mathbf{R}_\alpha) + E_{elec}(\mathbf{R}_\alpha) + V(\mathbf{R}_\alpha)] \Phi(\mathbf{R}_\alpha) = E_{tot} \Phi(\mathbf{R}_\alpha) \tag{2.63}$$

where E_{elec} is the electronic energy, obtained solving Eq. 2.3 for the geometry $\{\mathbf{R}_\alpha\}$, and V is the nuclear repulsion. The sum of these two contribution defines the *potential energy surface* (PES) in which the N nuclei moves. Neglecting the translational and rotational degrees of freedom, the PES is a complex hypersurface with $3N - 6$ internal coordinates.

On the potential energy surface there are a number of geometries called *critical* or *stationary* points, evidenced in Figure 2.6, which are particularly important for the

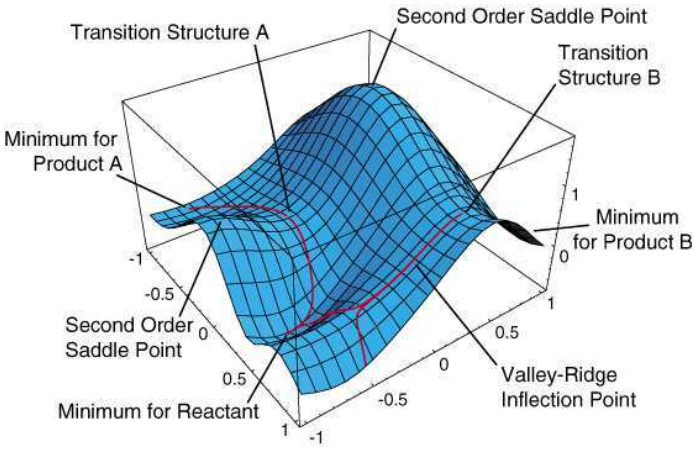

Figure 2.6 – The critical points on a multi-dimensional potential energy surface. [174]

description of the structural and chemical properties of the system. In correspondence to these points all the first derivatives of the energy with respect to each degree of freedom, i.e. the gradient $\mathbf{g}$, are zero:

$$\mathbf{g} = \left(\frac{\delta E}{\delta \mathbf{R}_1}, \frac{\delta E}{\delta \mathbf{R}_2}, \ldots, \frac{\delta E}{\delta \mathbf{R}_M} \right) = \mathbf{0} \tag{2.64}$$

The points on the PES with a clear relevance are the minima, which correspond to stable or metastable geometries. A multi-dimensional potential energy surface often contain more than one minima: the lowest energy one is the *global* minimum, whereas all the others are *local* minima. In many cases, the *first-order saddle points* are also important, because they represent the transition state structures between two minima and are related to the dynamical behaviour of the system.

The characterization of the critical points is performed through the study of the curvature of the potential energy surface. This information can be derived from the *Hessian matrix* $\mathbf{H}$, i.e. the matrix of the second derivatives along the allowed degrees of freedom. A related quantity is the force constants matrix $\mathbf{F}$, which introduces the *mass-weighted* cartesian coordinates $q_\alpha = \sqrt{m_\alpha}\Delta R_\alpha$ and is more informative than $\mathbf{H}$:

$$\mathbf{H} = \begin{bmatrix} \frac{\partial^2 E}{\partial R_1^2} & \cdots & \frac{\partial^2 E}{\partial R_1 R_M} \\ \vdots & \ddots & \vdots \\ \frac{\partial^2 E}{\partial R_M R_1} & \cdots & \frac{\partial^2 E}{\partial R_M^2} \end{bmatrix} \quad \mathbf{F} = \begin{bmatrix} \frac{\partial^2 E}{\partial q_1^2} & \cdots & \frac{\partial^2 E}{\partial q_1 q_M} \\ \vdots & \ddots & \vdots \\ \frac{\partial^2 E}{\partial q_M q_1} & \cdots & \frac{\partial^2 E}{\partial q_M^2} \end{bmatrix} \tag{2.65}$$

As a matter of fact, the eigenvalues and the eigenvectors, obtained by the diagonalization of the $\mathbf{F}$ matrix, are the vibrational frequencies ω_i in the harmonic approximation and the normal modes Q_i of vibration of the molecular system, respectively. In the case of a minimum on the potential energy surface, all the eigenvalues will be

positive, whereas a saddle point will present all positive values except one.

Geometry optimization techniques, such as the ones discussed in the following sections, are algorithm to systematically locate the stationary points. Most of them perform a local optimization, i.e. they determine the *nearest* stationary point to the starting geometry. Instead, the global minimum search, as well as the identification of the first-order saddle points, are usually more complex and demanding tasks, for which more sophisticated approaches have been developed.

2.4.1 Local minimum search

Local methods can be classified on the basis of the maximum order of the energy derivatives that are used in the algorithm: the higher the order of the derivative, the more efficient is the method, although more calculations are necessary. In this section, we will specifically discuss a common second-order algorithm which have been routinely employed during this work: the second-order *(pseudo-)Newton–Raphson* method.

In Newton–Raphson methods, the function $f(\mathbf{x})$ to be optimized, i.e. the potential energy surface, is expanded around the initial point $\mathbf{x}_0$.

$$f(\mathbf{x}) = f(\mathbf{x}_0) + \mathbf{g}^T(\mathbf{x} - \mathbf{x}_0) + \frac{1}{2}(\mathbf{x} - \mathbf{x}_0)^T\mathbf{H}(\mathbf{x} - \mathbf{x}_0) \tag{2.66}$$

The step towards the minimum is derived imposing the first derivative of $f(\mathbf{x})$ to be zero.

$$(\mathbf{x} - \mathbf{x}_0) = -\mathbf{H}^{-1}\mathbf{g} \tag{2.67}$$

Since Eq. 2.66 is an approximation, the step would not directly result in a stationary point, but the procedure can be repeated iteratively until convergence. However, this basic approach has a major problem, related to the computational cost to compute the second derivatives in the Hessian matrix $\mathbf{H}$.

In order to avoid this computational load, an *updating* scheme starting from an approximated Hessian $\mathbf{H}_0$ can be employed. The first steps are computed through a *first-order* technique and after few steps the updated Hessian is a good approximation in the direction towards the stationary point. Since an approximated Hessian is used, these methods are known as *pseudo-Newton–Raphson* methods. Many updating scheme are available and the *Broyden–Fletcher–Goldfarb–Shanno* (BGFS) [175,176] is the one used in this work, as it usually keeps the Hessian positive definite, performing better for minimum optimizations.

2.4.2 Global minimum search

Finding the global minimum is a particularly difficult task because the number of possible geometry configurations, and thus minima, typically increases exponentially with the number of atoms. Therefore, a systematic search exploring all the possible degree of freedom on a grid, is feasible only for small molecules. [146] To tackle the global minimum problem for larger systems, such as the ones under study, a tool to explore the conformational space in a smart way is needed. Many techniques have

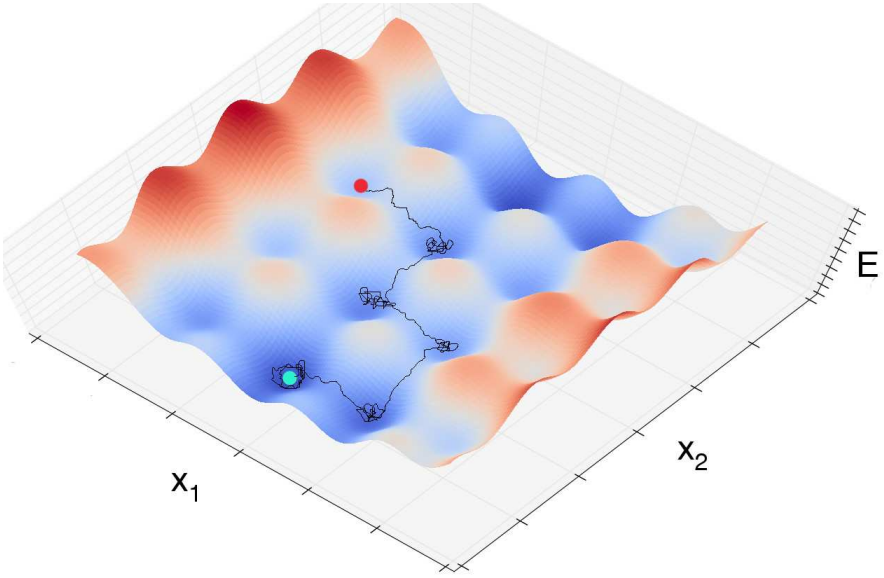

Figure 2.7 – A successful simulated annealing process from a local minimum (red dot) to the global one (cyan dot) in a multi-minima potential energy surface.

been developed for this scope and they are usually based on *molecular dynamics* (MD), *stochastic or Monte Carlo* methods or *genetic algorithms* (GA) approaches.

In molecular dynamics methods, which will be discussed in section 2.5, the molecular system is given a certain kinetic energy and allowed to evolve in time, so that energy barriers can be overcome. Thus, many energy minima will be explored and the lowest energy structures can be optimized, providing a reasonable sampling of the conformational space.

However, in order to reach structures that are very different from the starting ones, a long and computationally expensive simulation time may be needed. To this end, a more efficient approach is the *simulated annealing* (SA). [177] In this method, sketched in Figure 2.7, the temperature of the molecular dynamics is set to a very high value (up to 1000 K) and then it is gradually decreased to 0 K during the simulation. At the end of the simulation, the system will be hopefully "trapped" in the global energy minimum. The SA approach is the one applied in this work to find the global minimum structure of the TiO_2 nanoparticles.

Unfortunately, none of these configurational sampling techniques can guarantee to find the true global minimum but they may generate a local minimum that is more stable and close in energy to the global one.

2.4.3 Transition state search

The localization of the first-order saddle points on the potential energy surface is not conceptually different from the identification of an energy minima. However, there

are no general methods that are guaranteed to work, except for small molecules where a systematic approach can be applied.

A first strategy implies the knowledge of a very good guess of the transition state (TS) structure: in this case a local optimization method should be able to localize the saddle point if it is the nearest critical point.

In most of the cases, however, only a crude estimate of the TS is available and *interpolation methods* can help to find a structure much closer to the saddle-point. [146] The interpolation may be between only three points (reactant, product and guessed TS), such as in *linear* or *quadratic synchronous transit* methods or between many intermediate structures, as in the popular *nudged elastic band* (NEB) method. [178]

The NEB approach requires to generate a number of images between the reactant ($\mathbf{R}$) and the product ($\mathbf{P}$). Then, a target function (the "elastic band") is defined as the sum of the energies of the images plus a penalty term to favor the even distribution of the points along the reaction path:

$$T_{\mathrm{NEB}}(\mathbf{R}, \mathbf{I}_1, \ldots, \mathbf{I}_M, \mathbf{P}) = \sum_{i=1}^{M} E(\mathbf{x}_i) + \sum_{i=1}^{M-1} \frac{1}{2} k(\mathbf{x}_{i+1} - \mathbf{x}_i)^2 \tag{2.68}$$

where k is the spring constant of the "elastic band". Finally, the T_{NEB} function is minimized "nudging" the elasting band, i.e. considering only the component of the spring force *parallel* to the path in the calculation of the target function and the *perpendicular* one to perform the optimization steps.

2.5 Molecular Dynamics

At a finite temperature, a molecular system will explore the part of the potential energy surface with energies lower than the kinetic energy $k_B T$. Molecular dynamics (MD) is one of the way of simulating this dynamical behaviour, [146] allowing the evolution of the system according to the relevant equation of motion. Commonly, this technique is also used as a configuration space sampling tool, enabling the evaluation of macroscopic properties from the average of microscopic configurations. This implies the assumption that the time evolution is *ergodic*, i.e. it respects the *ergodic principle*. [179] This principle states that the time average of an observable over infinite time is equal to the average on all the possible configurations in the phase space.

A straightforward MD approach is the Born-Oppenheimer molecular dynamics (BO-MD), where the N nuclei of a molecular system are considered to behave, to a good approximation, as classical particles. Thus, their time evolution can be described integrating over time the Newton's second equation:

$$-\frac{\delta V}{\delta \mathbf{R}_\alpha} = m_\alpha \frac{\delta^2 \mathbf{R}_\alpha}{\delta t^2}, \quad \alpha = 1, \ldots, M \tag{2.69}$$

where m_α and $\mathbf{R}_\alpha$ are mass and position of the i nucleus, respectively. The left-hand side is the negative of the first derivative of the potential energy V with respect to the atomic coordinates $\{\mathbf{R}_\alpha\}$, also called forces $\mathbf{F}_\alpha$. Since the potential energy

is generally known only for a given geometry, the Newton's equations are integrated numerically step by step.

The most used numerical methods are based on the *Verlet* algorithm. [180] First, the positions of the nuclei after a small time step Δt are given by a Taylor expansion:

$$\begin{aligned} \mathbf{R}_{i+1} &= \mathbf{R}_i + \frac{\delta \mathbf{R}_i}{\delta t}(\Delta t) + \frac{1}{2}\frac{\delta^2 \mathbf{R}_i}{\delta t^2}(\Delta t)^2 + \dots \\ \mathbf{R}_{i+1} &= \mathbf{R}_i + \mathbf{v_i}(\Delta t) + \frac{1}{2}\mathbf{a_i}(\Delta t)^2 + \dots . \end{aligned} \tag{2.70}$$

Second, the positions a Δt *earlier* in time are obtained by substituting Δt with $-\Delta t$ in Eq. 2.70:

$$\mathbf{R}_{i-1} = \mathbf{R}_i - \mathbf{v_i}(\Delta t) + \frac{1}{2}\mathbf{a_i}(\Delta t)^2 - \dots \tag{2.71}$$

Combining Eqs. 2.70 and 2.71 the positions at the next time step $\mathbf{R}_{i+1}$ can be derived, given the current and previous positions and the current acceleration $\mathbf{a}_i$ from Eq. 2.69:

$$\mathbf{R}_{i+1} = (2\mathbf{R}_i - \mathbf{R}_{i-1}) + \mathbf{a}_i(\Delta t)^2 + \dots \tag{2.72}$$

At the first step, the previous positions are not known, but they are estimated by a first-order approximation from the initial velocities, i.e. $\mathbf{R}_{-1} = \mathbf{R}_0 - \mathbf{v}_0 \Delta t$.

Evaluating the first-derivatives of the energy and consequently the acceleration, the atomic positions can be propagated in time and generate a trajectory. The time step Δt is an important parameter for a MD simulation. As a matter of fact, the validity of the trajectory is higher and higher the smaller is the time step, even though a very small time step would increase largely the computational effort.

The potential V in Eq. 2.59 can be computed with electronic structure methods, such as density-functional theory, or using parametrized force fields. In the former case a Born-Oppenheimer dynamics requires a very tight convergence of the wave function in each time step in order to satisfy the energy conservation over long simulation time and avoid spurious electronic friction terms, making the procedure too computationally demanding in certain circumstances. [181]

An elegant solution to this issue has been formulated by Car and Parrinello (CP-MD), [182], introducing the evolution of the wave function coefficient simultaneously with the nuclear motion, so that is not necessary anymore to fully converge the electronic structure. This can be achieved by assigning "fictive masses" in the order of few hundreds of a.u. to the electrons, i.e. the wave function orbital coefficients, and adding to the total energy the kinetic energy of the orbitals. Even though in the "real" system there is no orbital kinetic energy, in this way the total energy is conserved and realistic results can be obtained keeping this energy contribution relatively small.

2.5.1 Non-natural ensembles

A molecular dynamics simulation will naturally generate a NVE ensemble, where the temperature and pressure fluctuate and the number of atoms, the volume and energy

are conserved. Nonetheless, it is possible to generate NVT or NPT ensembles by scaling at each time step the velocities or positions.

A robust methodology to perform this is to couple the system to a *heat bath*, often called *thermostat*, which gives or substract energy to the system with a certain time constant. The kinetic energy of the system is then modified by scaling the velocities with an heat transfer rate that depends on the coupling parameter τ.

$$v_{scale\text{-}factor} = \sqrt{1 + \frac{\Delta t}{\tau}\left(\frac{T_{\text{desired}}}{T_{\text{actual}}} - 1\right)} \tag{2.73}$$

Such a method will not produce a canonical ensemble and this means it will provide the correct average but incorrect fluctuations of the properties. In *Nosé–Hoover* thermostats, [183] fictitious dynamical variables, i.e. a degree of freedom s, a mass Q and a potential energy $(n+1)k_B T_{desired}\ln(s)$, are assigned to the energy reservoir. In this way, the heat flow and, consequently, the energy oscillations are regulated by the parameter Q. This thermostat may produce a non-ergodic ensemble and this property can be recovered using a series of *Nosé–Hoover chains*. [184]

Similarly, the pressure can be held almost constant by coupling to a "*pressure bath*". In this case, the volume of the system is scaled periodically as follows:

$$R_{scale\text{-}factor} = \sqrt[3]{1 + \kappa\frac{\Delta t}{\tau}\left(\frac{P_{\text{desired}}}{P_{\text{actual}}} - 1\right)} \tag{2.74}$$

where κ is the system compressibility. Analogously to thermostats, this simple kind of *barostat* do not generate correct ensembles and the recourse to a Nosé–Hoover chain approach recover the ergodicity.

3 Ground State Properties of Anatase TiO_2 Nanocrystals versus Nanospheres

In this chapter,[†] realistic models of the TiO_2 nanoparticles (TiO_2 NPs) with faceted and spherical shapes are defined and their structural and electronic properties are computed by means of hybrid density functional theory and self-consistent charge density-functional tight-binding (SCC-DFTB) approach.

From the structural point of view, we focus on the surface-to-bulk ratio, the surface coordination pattern, the atomic displacements due to the surface rearrangements and surface energies. Concerning the electronic properties, we investigate band gaps, electron affinities, ionization potentials, frontier orbitals and electronic densities of states.

3.1 Introduction

Understanding the role of the size and the shape of titanium dioxide nanoparticles is of paramount importance for an effective design of TiO_2-based nanosystems for a specific technological application. As a matter of fact, the structural and electronic properties of the nanoparticles and consequently their functionalities may change dramatically due to quantum confinement or surface defectivity.

As discussed in Chapter 1, TiO_2 nanoparticles size and shape can be efficiently and successfully tailored. The decahedral shape is the most stable for nanocrystallites, but also nanoparticles with curved surfaces, such as nanospheres, nanorods and nanotubes, can be synthetized. It is important to recall that below 14 nm in size, the anatase phase of TiO_2, which is considered to be the most photoactive, [32, 33] is thermodynamically prefered.

At the size of few nanometers, the fraction of surface atoms compared to bulk ones is significant and may depend on the shape. The distribution and the amount of undercoordinated surface sites are expected to be highly affected by the size and

[†]The results described in this Chapter have been reported in: G. Fazio, L. Ferrighi, C. Di Valentin, *J. Phys. Chem. C* **2015**, *119*, 20735–20746; D. Selli, G. Fazio, C. Di Valentin, *J. Chem. Phys.* **2017**, *147*, 164701.

the shape of the nanoparticles. In particular, spherical TiO_2 nanoparticles (NPs) are characterized by very high density of reactive 4-fold coordinated Ti atoms, which are excellent binding sites for organic molecules to form (bio)inorganic nanoconjugates. [31]

However, unlike faceted nanoparticles, TiO_2 nanospheres presents very complex structures and surfaces, making their experimental characterization at the atomistic resolution extremely difficult. To this end, quantum chemical calculations can help to investigate and rationalize the surface structure and the relation with the observed physico-chemical properties.

Therefore, the first aim of this work is to systematically investigate by hybrid DFT the structural and electronic properties of faceted and spherical anatase nanoparticles of different size and to highlight the differences between these two representative TiO_2 nanoparticle shapes. In this part of the work, we will consider "as-carved" nanocrystals/nanospheres diameter sizes up to 3 nm. In order to accurately describe the electronic structure, the range-separated hybrid functional HSE06, which is deemed to be well suited for semiconductive oxides, [151] will be employed and compared to the popular B3LYP functional.

Then, the second aim of this work is to model more finely the structural rearrangement of spherical TiO_2 nanoparticles through a global optimization procedure. In this case, TiO_2 nanospheres with size from 1.5 to 4.4 nm, that contain from 300 to almost 4000 atoms, have been considered. For such systems, global minimization algorithms are not affordable at the DFT level, so we performed a global optimization procedure (simulated annealing) based on the SCC-DFTB method, that at a reduced computational effort provides an accuracy comparable to DFT. Additionally, through the comparison of the computed structural and electronic properties at the DFT and DFTB levels, we performed a benchmark of the DFTB method for the accurate description of TiO_2 nanosystems.

In this chapter, first, the methodological details of the calculations will be presented (Section 3.2); then, the discussion will focus on the structural (Section 3.3) and electronic (Section 3.4) properties of both faceted and spherical nanoparticles; finally, the global optimization of the TiO_2 nanospheres and the benchmark of the SCC-DFTB method will be discussed (Section 3.5).

3.2 Computational Details

In this section, we will specify the computational methods, the models and the settings that have been used for the calculations presented in this Chapter. For a detailed discussion on the theoretical approaches see Chapter 2.

All the DFT calculations were performed using the CRYSTAL14 code, [185] in which the Kohn–Sham orbitals are expanded in atom-centered Gaussian functions. An all-electron basis sets for O 8-411(d1), Ti 86-411 (d41) and H 511(p1) has been used. In some test calculations, a diffuse function has been added to the basis set of all the surface atoms and hydrogen atoms [Ti diffuse 86-411(d411), O diffuse 8-4111(d1), H diffuse 5111(p1)]. The HSE06 [151] and B3LYP [145, 147] hybrid functionals have been used throughout this work.

The Coulomb and exchange series/sums of integrals appearing in the SCF equation (see Eq. 2.14) were truncated according to a threshold of 10^{-7} for Coulomb overlap tolerance, 10^{-7} for Coulomb penetration tolerance, 10^{-7} for exchange overlap tolerance, 10^{-7} for exchange pseudo-overlap in the direct space, and 10^{-14} for exchange pseudo-overlap in the reciprocal space. The condition for the convergence of the SCF cycle was set to 10^{-6} a.u. on the total energy difference between two subsequent cycles.

The forces with respect to atomic coordinates are computed analytically. The local minimum structures on the potential energy surface are determined by using a quasi-Newton algorithm with a BFGS Hessian updating scheme, see Section 2.4.1 for more details. Convergence in the geometry optimization process is checked on the root-mean-square (RMS) and the maximum absolute value of both the forces and nuclear displacements. The default thresholds for geometry optimization within the CRYSTAL14 code are the following: maximum and RMS on the forces have been set to 0.000450 and 0.000300 a.u., and maximum and RMS on the atomic displacements to 0.001800 and 0.001200 a.u., respectively. However, for the 4.4 nm spherical nanoparticle, forces were relaxed to less than 0.010000 a.u. to limit the computational effort.

Vertical (IP^v) and adiabatic (IP^{ad}) ionization potentials are obtained by removing one electron from the model of the nanoparticle in its original geometry and by performing a subsequent full geometry optimization, respectively:

$$\mathbf{NC/NS} \rightarrow \mathbf{NC}^+/\mathbf{NS}^+ + 1e^-(\Delta \mathrm{E} = \mathrm{IP}). \tag{3.1}$$

Vertical (EA^v) and adiabatic (EA^{ad}) electron affinities are computed by adding one electron to the model of the nanoparticle in its original geometry and by performing a subsequent full geometry optimization, respectively:

$$\mathbf{NC/NS} + 1e^- \rightarrow \mathbf{NC}^-/\mathbf{NS}^-(-\Delta \mathrm{E} = \mathrm{EA}). \tag{3.2}$$

For the simulation of the total and projected densities of states (DOS and PDOS) of the nanoparticles the value of σ for the Gaussian peaks in the convolution was set to 0.01 eV.

The DFTB+ code [186] has been employed for all the SCC-DFTB calculations. From now on, DFTB will be used as shorthand for SCC-DFTB. The "matsci-0-3" set of Slater–Koster parameters has been used, being well-suited for anatase and its surfaces, as reported in Ref. [187]. For structural optimizations, the threshold on the charges in the self-consistent charge (SCC) cycles was set to 10^{-4} a.u. and forces were relaxed to less than 10^{-6} a.u. For the **k**-point sampling in bulk anatase calculations within the DFTB methodology, we used a $16 \times 16 \times 16$ Monkhorst–Pack grid. The lattice vectors of the bulk anatase unit cell were optimized using the lattice optimization algorithm implemented in the DFTB+ code.

The lattice parameters for anatase, as obtained with the HSE06 and B3LYP functional and DFTB approach, as well the experimental values, [61] are given in Table 3.1.

The anatase (101) surface has been modeled with a ten triatomic layers slab with 60 atoms. Periodicity has been imposed along the $[10\bar{1}]$ and [010] directions and not in

Table 3.1 – Experimental and optimized cell parameters a and c in Å, and the a/c ratio for bulk anatase, as computed with the HSE06 and B3LYP functionals and DFTB methodology.

	a	c	a/c
HSE06	3.766	9.663	2.569
B3LYP	3.789	9.777	2.580
DFTB	3.810	9.732	2.554
exp.	3.782	9.502	2.512

the direction perpendicular to the surface. The Brillouin zone has been sampled with a 12×12 Monkhorst-Pack **k**-points net. No periodic boundary conditions have been set for nanoparticles, that have been, thus, considered as molecules in the vacuum.

In order to perform the simulated annealing, Born-Oppenheimer DFTB molecular dynamics has been run within the canonical (NVT) ensemble. The equations of motion were integrated with the Velocity Verlet algorithm and the reversibility was ensured by a relatively small time step of 0.5 fs. A Nóse-Hoover chain thermostat, with a time constant of 0.03 ps, was used to target the desired temperature during the simulated annealing simulations.

3.3 Structural Properties

3.3.1 Nanoparticles shapes

Nanoparticles have been carved from the optimized anatase TiO_2 bulk supercell, as calculated with HSE06 and B3LYP functionals or SCC-DFTB approach (see Table 3.1). In order to keep the D_{2d} point group symmetry of anatase, a Ti atom was set at the origin of the coordinate axis when cutting the nanoparticle.

Faceted nanoparticles or nanocrystals (**NC**) have been cut from the bulk anatase crystal according to the minimum energy decahedral shape predicted by Barnard et al. [83] for TiO_2 nanoparticles below 10 nm. The decahedral crystallite, depicted in Figure 3.1, exposes the (101) and the (001) anatase surfaces, which are the lowest energy ones. The lenght of the decahedron edges is defined by the parameters A and B, with $A > B$. Barnard et al. found that the A/B ratio depends on the nanocrystallite size and it is typically around 0.32 for nanocrystals below 10 nm.

The code to cut the anatase bulk supercell has been written in Python, using the tools available in the Atomic Simulation Environment (ASE) software [188] to build and handle atomic structures: first, a large enough anatase bulk supercell has been generated, then, the ten planes of the nanocrystal have been defined using analytical geometry and, finally, a `for` cycle in the script has been run on all the supercell atoms, so that if the atom was inside all the planes was kept and deleted otherwise.

The resulting nanocrystals showed an excess of oxygen in the stoichiometry and a number of monocoordinated oxygen atoms lying on top of the (001) surfaces. To keep chemical stability and restore the stoichiometry, these oxygen atoms have been saturated with H atoms. This procedure resulted in stoichiometric nanocrystals with few dissociated water molecules on (001) surface, as shown in Figure 3.3a,b: $(TiO_2)_{159}$

• 4 H_2O (**NC**$_S$) and $(TiO_2)_{260}$ • 6 H_2O (**NC**$_L$).

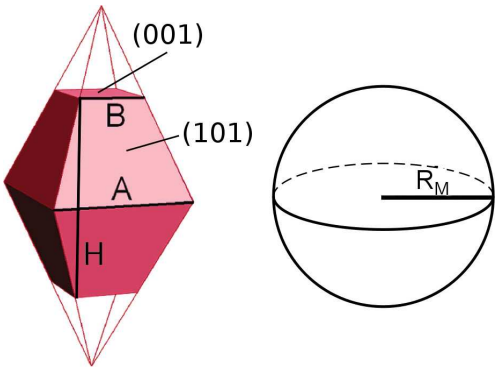

Figure 3.1 – (a) Schematic representation of the Wulff-shape decahedron and its parameters A, B and H. (b) Scheme of a sphere with radius R_M.

Spherical nanoparticles or nanospheres (**NS**) have been obtained following the procedure sketched in Figure 3.2, implemented in a Python ASE script. First, a sphere of arbitrary radius R_M has been carved from bulk anatase supercell. Then, all the two-fold Ti atoms on the surface were removed, because considered too chemically unstable. As done for the nanocrystals, all monocoordinated oxygen atoms were saturated with a number x of hydrogen atoms. A corresponding number x of hydroxyl groups were employed to saturate all the three-fold Ti atoms, considered unstable, and, when necessary to keep stoichiometry, some four-fold Ti atoms. Finally, the process was considered successful if a D_{2d} stoichiometric nanosphere with no Ti_{3c} atoms was built. Otherwise, we changed the radius R_M and repeated the procedure until successful. These operations result in the building of stoichiometric nanospheres saturated with a number x of water molecules, as shown in Figure 3.3c,d: $(TiO_2)_{223}$ • 26 H_2O (**NS**$_S$) and $(TiO_2)_{399}$ • 32 H_2O (**NS**$_L$).

3.3.2 Size and Morphology

The HSE06 optimized structures of the nanocrystals and nanospheres, whose geometrical parameters at the HSE06 and B3LYP level are reported in Table 3.2, are given in Figure 3.3 together with their stoichiometry, number of atoms and percentage of undercoordinated titanium and oxygen atoms. One may notice that the nanoparticles obtained with the B3LYP functional have somewhat larger A, B, H or R_M parameters. For instance, the dimension along the z-axis is slightly elongated, in line with a longer c bulk lattice parameter reported in Table 3.1.

The definition of the surface and, consequently, the volume of a molecular system is not straightforward, since a molecule does not have borders and its electron density ideally extends up to infinity. However, in molecular modeling, surfaces and volumes provide useful information to better understand a system. In this PhD work, we have defined the molecular surface using two approaches: a *geometric surface* or a *Connolly*

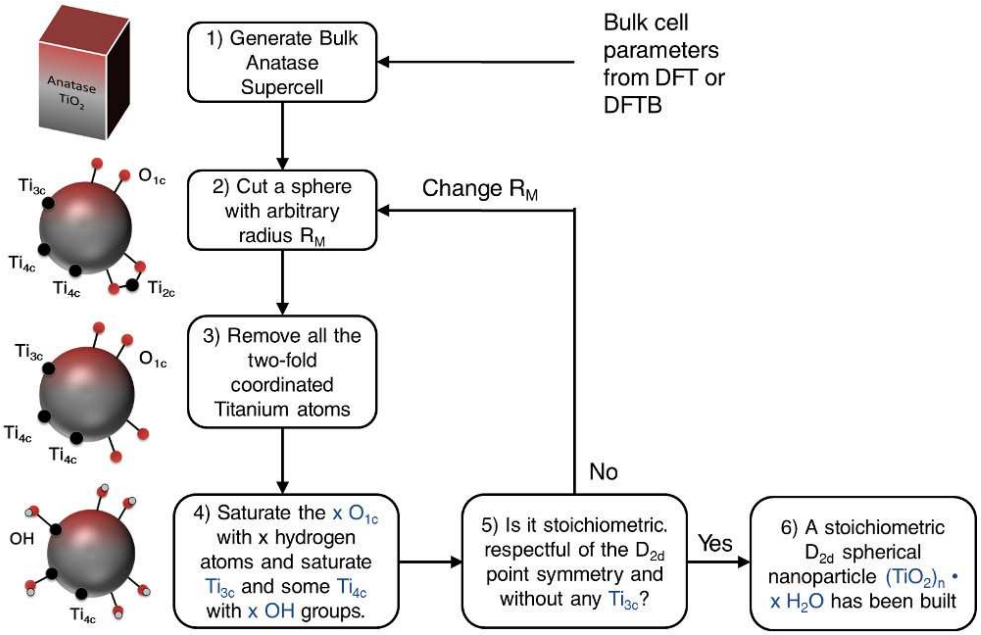

Figure 3.2 – Procedure employed in this work to cut an anatase TiO_2 spherical nanoparticle from bulk anatase supercell.

surface.

For faceted nanoparticles, the geometric surfaces are defined as the smallest Wulff-shape decahedron that contains the nanocrystal, with a specific angle θ between (101) and (001) planes, only determined by the a and c cell parameters ($\theta = \tan^{-1}(c/a)$). We can then extract the values of the parameters A, B and H from the defined solid geometry. Thus, the surface area, S_{geom}, is given by the formula:

$$S_{geom} = 2 \times \left(B^2 + \frac{A^2 - B^2}{\cos\theta} \right) \tag{3.3}$$

For nanospheres, the geometric surfaces are trivially given by the surface of a sphere with radius R_M, the one used to carve the **NS** from the bulk. However, the "geometrical" definition of the surface has two drawbacks: first, the surface areas for **NC** and **NS** models cannot be compared, since they have different definition, and, second, it does not provide any information about the roughness of the surface.

For these reasons we introduced the *Connolly* surface [189, 190] as a general definition of the molecular contour that is also sensitive to the surface corrugation. This approach generates a smooth, three-dimensional surface about a molecule, that represent the surface accessible by the solvent. First, the surface resulting from the superposition of all the atomic Van der Waals spheres is built; then, on this surface a probe sphere of a certain chosen radius, 3.0 Å in this work, is rolled, defining a series of contact points. These are used to form arcs that smooth the holes and cusps of the

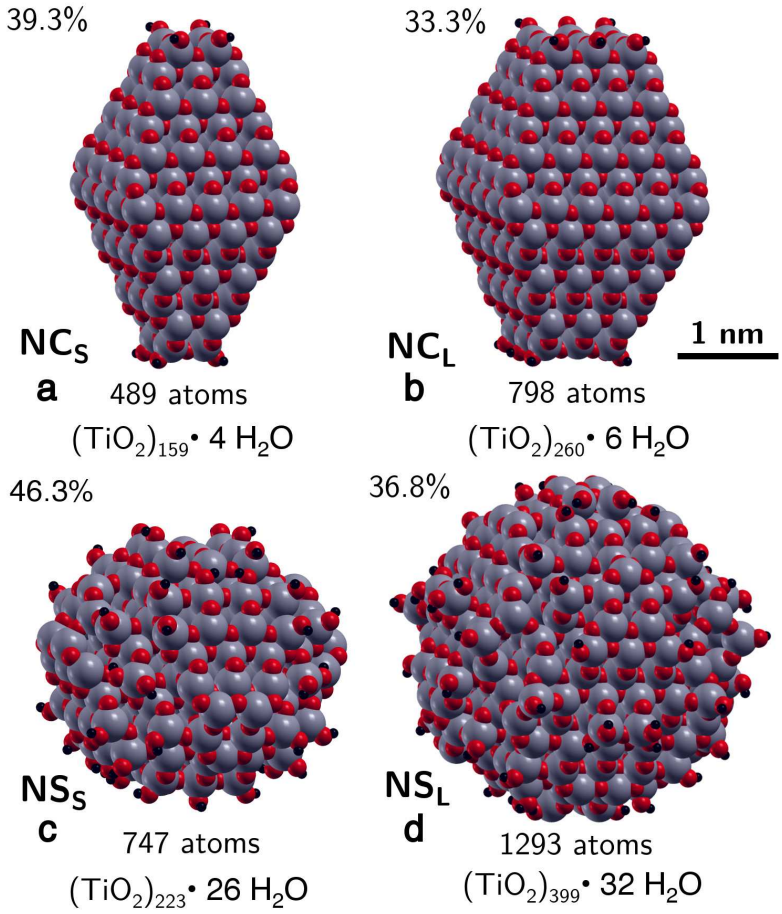

Figure 3.3 – Space-filling representation of the faceted (a, b) and spherical (c, d) anatase nanoparticles, as obtained with the HSE06 functional. The % of undercoordinated sites, the number of atoms and the stoichiometry are also given for each model.

Van der Waals surface, resulting in the Connolly surface.

Using this methodology, we computed the surface of the nanoparticles (S_{Conn}), their volumes (V_{Conn}) and the equivalent diameters (D_{Conn}) of a sphere with the same V_{Conn} of the nanoparticle at hand. The latter parameter allows for a direct comparison between the sizes of **NC** and **NS** models. The resulting data are shown in Table 3.2. One can notice that the size of $\mathbf{NC}_L$ and $\mathbf{NS}_S$ are about the same, comparing the number of atoms and the equivalent diameters D_{Conn}. Finally, the range of size of the nanoparticles under study is between 2 and 3 nm, which is consistent with real small nanocrystallites. [44–47]

Another feature we have analyzed is the coordination sphere around the titanium atoms of the nanoparticles. The coordination/undercoordination of the atomic species

Table 3.2 – Geometrical parameters for the nanoparticles (NPs) shown in Figure 3.3, optimized at the HSE06 and B3LYP level of theory. The decahedron parameters A, B and H, defined in Figure 3.1, are given as well as the B/A ratio for the faceted nanoparticles, whereas the cutting radius R_M is reported for the spherical nanoparticles. The diameter $D_M = 2{\times}R_M$ for nanospheres and the equivalent diameter $D_{eq} = \sqrt[3]{(6V\pi)}$ (where $V = \frac{1}{3}H(A^2+B^2+AB)$ is the geometrical volume of a decahedron) for nanocrystals are also given. S_{Conn} and V_{Conn} are the surface area and the volume estimated with the Connolly method, while D_{Conn} is the equivalent diameter of a sphere with the same Connolly volume. Geometrical parameters are reported in nm, surfaces in nm^2 and volumes in nm^3.

NP	A	B	H	B/A	R_M	D_{eq} (D_M)	S_{Conn}	V_{Conn}	D_{Conn}
HSE06									
$\mathbf{NC}_S$	1.56	0.39	2.83	0.25		1.79	18.4	5.7	2.22
$\mathbf{NC}_L$	1.93	0.77	2.85	0.40		2.19	25.0	9.3	2.61
$\mathbf{NS}_S$					1.22	(2.44)	21.4	8.1	2.49
$\mathbf{NS}_L$					1.50	(3.00)	32.0	14.6	3.03
B3LYP									
$\mathbf{NC}_S$	1.57	0.39	2.87	0.25		1.81	18.7	5.8	2.23
$\mathbf{NC}_L$	1.94	0.78	2.89	0.40		2.21	25.4	9.4	2.62
$\mathbf{NS}_S$					1.23	(2.56)	21.8	8.3	2.52
$\mathbf{NS}_L$					1.51	(3.02)	32.5	15.0	3.06

is a relevant factor in the chemical reactivity of the sites. The coordination number N, reported in the underscript of the site denomination as Nc, is defined as the number of neighbours (Ti or O) within 2.5 Å of distance from the considered site; hydroxyl groups are not considered in the calculation of N and when one or two hydroxyls are bound to the titanium, they are indicated aside.

The coordination pattern of all the atomic species in the designed nanoparticles is graphically reported by colour coding in Figure 3.4 and quantitavely detailed in Table 3.3, in terms of number and percentage of each coordination-type atomic species. For oxygen species, the coordination sphere ranges from O_{3c} to OH, from Ti_{6c} to $Ti_{3c}OH$ for the titanium species.

One can note that the nanocrystals are characterized by a higher percentage of Ti_{5c} atoms (> 40 %) than the nanospheres, with a decreasing trend with size. Instead, the balance between O_{3c} and O_{2c} is not that different when comparing **NC**s with **NS**s. Interestingly, the small nanocrystal ($\mathbf{NC}_S$) has about the same percentage of fully coordinated O atoms than the large nanosphere ($\mathbf{NS}_L$) (70.2% vs 69.2%), indicating that the faceted shape preserves a higher amount of "bulk" structure. The number of hydroxyl groups is higher in the nanospheres, because, in order to ensure the chemical stability, much more hydrogen atoms are required to saturate the undercoordinated atoms resulting from the carving of a spherical surface than a faceted one.

It is noteworthy that nanocrystals have an analogous distribution of atomic species on the surface: considering faceted nanoparticles of different size ($\mathbf{NC}_S$ and $\mathbf{NC}_L$), they present four-fold Ti atoms at corners between the upper and the lower part of the decahedron, five-fold Ti atoms at the edges and on the (101) lateral surface

Table 3.3 – Number of O and Ti atoms with a certain coordination sphere in the HSE06 and B3LYP optimized structures (when different, B3LYP value is in parenthesis) and their percentage with respect to the total number of atoms. The cutoff radius for a Ti–O bond is 2.5 Å.

	$\mathbf{NC}_S$		$\mathbf{NC}_L$		$\mathbf{NS}_S$		$\mathbf{NS}_L$	
	Number	%	Number	%	Number	%	Number	%
O atoms								
OH	8	2.5	12	2.3	52	11.0	64	7.7
O_{2c}	88	27.3	120	22.8	124(128)	26.3	192(200)	23.1
O_{3c}	226	70.2	394	74.9	296(292)	62.7	574(566)	69.2
Ti atoms								
Ti_{4c}	4	2.5	4	1.5	24	10.7	36	9.0
Ti_{5c}	76	47.8	106	40.8	46	20.6	64(72)	16.1
Ti_{6c}	71	44.7	138	53.1	105	47.1	243(235)	60.9
$Ti_{3c}OH$					24	10.8	32	8.0
$Ti_{4c}OH$	8	5.0	12	4.6	8(12)	3.6	16	4.0
$Ti_{5c}OH$					12(8)	5.4		
$Ti_{3c}(OH)_2$							8	2.0
$Ti_{4c}(OH)_2$					4	1.8		

and finally four-fold Ti atoms involving an OH group on the top and bottom (001) surfaces. Spherical nanoparticles ($\mathbf{NS}_S$ and $\mathbf{NS}_L$) are characterized by a considerably larger relative amount of Ti atoms with a coordination number less than 5. These species seem to be randomly distributed on the quasi-spherical surface, giving rise to the colorful representations in the bottom panel of Figure 3.4.

3.3.3 Simulated EXAFS

The distortions with respect to bulk anatase lattice in nanoparticles and in nanospheres are expected to play a crucial role in determining the properties of these nanoobjects. Experimentally, a precious tool to systematically investigate bond lenghts distribution and local environments within a sample is the EXAFS (Extended X-Ray Absorption Fine Structure) spectrum, which is the region of the X-Ray absorption spectrum at energies above the edge of absorption (see left panel of Figure 3.5). Above that limit, which corresponds to the ionization energy of a core electron, the X-ray beam causes the ejection of an electron and the formation of a vacancy in the core shell, which is filled by the decay of an outer shell electron. In this process, an X-ray with an energy equal to the incident light is emitted and this radiation interacts with the one backscattered by neighbour atoms (see right panel of Figure 3.5).

This phenomenon explains the oscillating behaviour in the EXAFS region: given a distance R between the absorbing (A in Figure 3.5) and the neighbour atom (B in Figure 3.5), when the wavelenght of the incident light is such that the interference with the backscattered light is constructive, the detected intensity of absorption increase; otherwise, at a different incident wavelenght, the interference can be destructive and

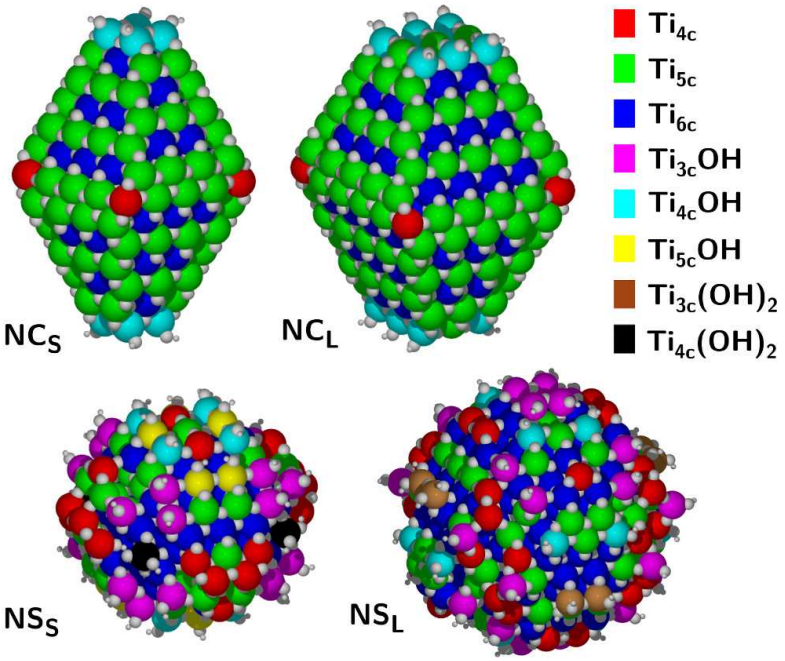

Figure 3.4 – Position of the titanium atoms with a different coordination pattern within the nanocrystals and the nanospheres. The coordination sphere for each site is visually shown by the color coding indicated on the right side.

the intensity decreases. Thus, the oscillations of the X-Ray absorption signal depends on the distance between the absorbing atom and the atoms of the local environment. Then, after some mathematical corrections, the Fourier transform in the frequency space of the signal results in a radial distribution function where the peaks correspond to the average distance of nearest-neighbours.

In this PhD work, we simulated the EXAFS spectra in real space by a convolution of Gaussian peaks ($\sigma = 0.0005$ Å) centred at the distance lenghts between each Ti atom and other atoms (O or Ti) from its first, second and third coordination shells. Taking into account only groups of titanium atoms, we can also compute the projections of the total spectrum onto titanium atoms with the same coordination sphere.

In order to highlight the bond lenght shrinking or stretching with respect to the bulk, we have first simulated the EXAFS peaks of bulk anatase TiO_2 as obtained by relaxing the bulk unit cell with the hybrid functional HSE06 (top panel of Figure 3.6). We investigated a range of distances between 0 and 4 Å, covering three coordination shells around a titanium atom. The first two lines at 1.93 Å and 1.98 Å correspond to the first coordination sphere and they are the Ti–O_{eq} (eq = equatorial) and Ti–O_{ax} (ax = axial) bonds which are different because of a slight tetragonal distortion in the anatase TiO_6 octahedron. Then, the third and fourth line at 3.06 Å and 3.77 Å are

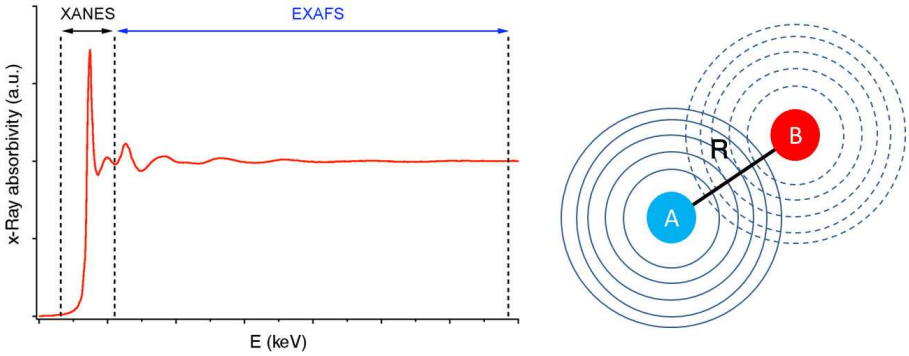

Figure 3.5 – (Left) XANES and EXAFS regions of the X-ray absorption spectrum. (Right) Backscattering of the X-ray radiation between atoms A and B.

the distances between the central Ti atom and the next-neighbouring titanium atoms in the second coordination sphere (Ti$\cdots$Ti). Finally, the fifth line at 3.90 Å is the distance with the oxygen atoms in the third coordination shell (Ti$\cdots$O).

In the case of the nanoparticles under study, the simulated EXAFS spectra is more complex, since, after atomic relaxation, the bond lenghts are distorted due to surface effects and the convolution of the various lines results in broad peaks in the spectrum.

We first focus on the EXAFS spectra of the nanocrystals $\mathbf{NC}_S$ and $\mathbf{NC}_L$ in the second and third panels of Figure 3.6. In the range between 1.7 and 2.6 Å, the Ti–O distance critically depends on the Ti coordination pattern. The main contributions are due to distances between oxygen and Ti_{6c} (green) and Ti_{5c} (blue), which represent more than 90% of the titanium species of $\mathbf{NC}_S$ (see Table 3.3). The Ti_{6c} projection concerns "bulk-like" Ti atoms, since it presents two peaks centered at the bulk anatase equatorial and axial distances. However, the ratio between the Ti–O_{eq} and Ti–O_{ax} contributions is not the typical 4:2 as for Ti_{6c} in the bulk because the number of axial bonds is higher, as a consequence of the nanocrystals shape where H > A, i.e. the decahedron is elongated along the z-axis. The green curve, related to Ti_{5c} distances, shows three features at low bond lenghts (about 1.8 Å), at bulk-like ones (about 2.0 Å) and at high bond (about 2.2 Å) distances. These three-peaks shape is due to the typical relaxation associated to two-fold coordinated oxygen atoms and five-fold coordinated titanium atoms on the mostly exposed (101) surfaces, as previously reported by another theoretical work. [107] Finally, the red projection, associated to the few Ti_{4c} species, presents a low peak at short distances (about 1.8 Å).

Concerning the EXAFS spectra of the spherical nanoparticles $\mathbf{NS}_S$ and $\mathbf{NS}_L$, we noticed a broader variety of projections contributing to the peak of the total EXAFS spectrum in the first coordination sphere, as shown in the bottom two panels of Figure 3.6. For both nanospheres there is a prevalent contribution of Ti_{6c} (blue line), which is more evident for the larger nanosphere because of a higher content of fully coordinated titanium atoms. Noteworthy, the axial and equatorial peaks collapse in a single peak, indicating a higher degree of isotropy in the bulk of the nanospheres.

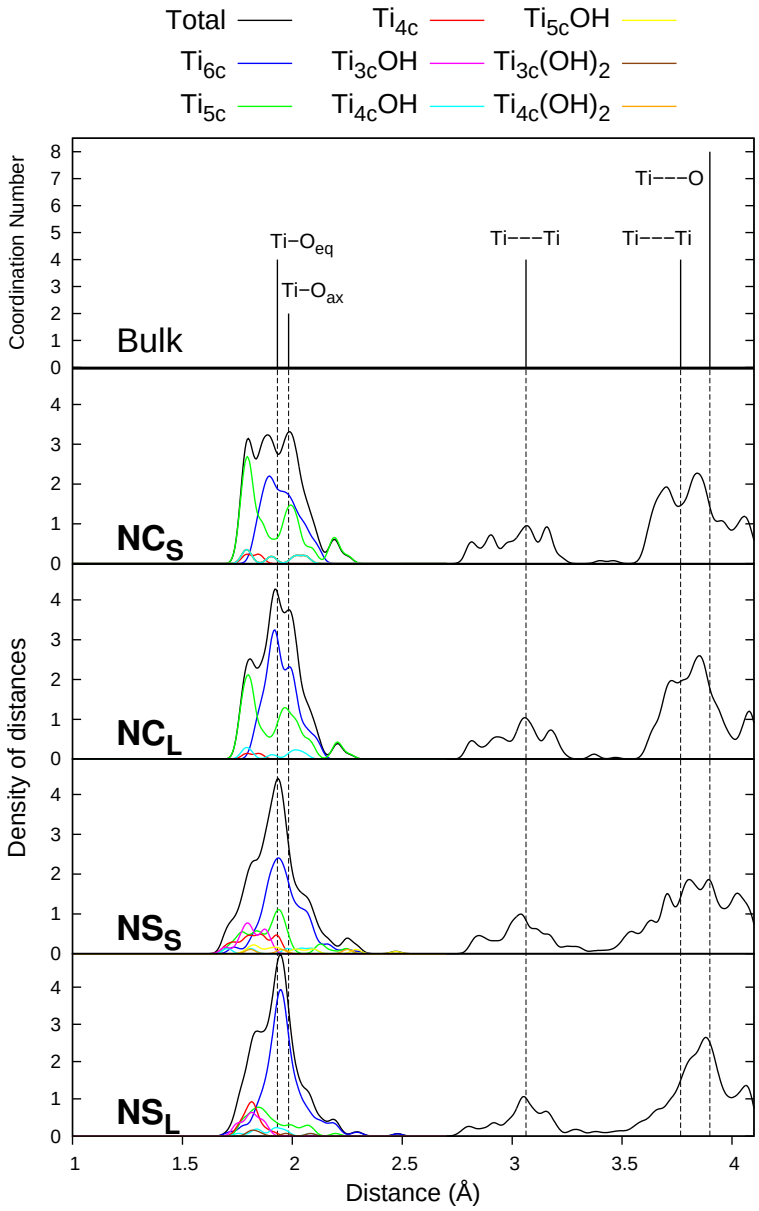

Figure 3.6 – Simulated EXAFS spectra, as obtained with the HSE06 functional, for the anatase bulk (top panel), the nanocrystals $\mathbf{NC}_S$ and $\mathbf{NC}_L$ (central panels) and the nanospheres $\mathbf{NS}_S$ and $\mathbf{NS}_L$ (bottom panels). The total distribution of Ti–O, Ti–Ti and Ti$\cdots$O distances is reported in black, while the distribution of the same distances for each titanium species is color-coded according to the legend on top.

Below 2.0 Å there are various contributions centered at about 1.8 Å due to all the surface species, such as Ti_{4c} and Ti_{5c} or Ti atoms bound to one or more hydroxyl groups.

For both nanocrystals and nanospheres, the Ti$\cdots$Ti feature shows peaks centered at the bulk distance with some broadening and finer structure due to surface, edge and corner species. The faceted nanoparticles are characterized by better defined Ti$\cdots$Ti peaks because of a higher degree of local order with respect to the nanospheres. Moreover, one can notice that the larger the size of the nanoparticles, the more the EXAFS peaks approach the bulk line.

Finally, for the large nanosphere $\mathbf{NS}_L$, which has an average equivalent diameter of about 3 nm, we observe an average compression of the Ti–O bonds connected to a slight average increase of the Ti$\cdots$Ti distances, in line with the experimental EXAFS spectrum observed for anatase TiO_2 nanoparticles of 3 nm in size. [191]

3.3.4 Surface Energies

The cost to form nanoparticles from bulk systems, evaluated by the surface energies, is an important parameter to study the relative stability of different nanostructures. The standard free energy of formation of a nanoparticle (NP) can be decomposed into two contributions, [83] one necessary to form the bulk, one needed to cut the surface:

$$G_{NP}^{0} = G_{NP}^{\text{bulk}} + G_{NP}^{\text{surface}} \tag{3.4}$$

In the case of large faceted nanoparticles, we can assume that the contribution of edges and corners to formation energy is negligible, so that G_{NP}^{surface} can be obtained from the sum of the surface free energy of the exposed facets as follows:

$$G_{NP}^{\text{surface}} = \frac{M}{\rho}(1-e)\left[q\sum_{i}^{\text{facets}} f_i\gamma_i\right] \tag{3.5}$$

where M and ρ are the mass and the density of the material, e is the volume dilation caused by surface tension, q is the surface-to-volume ratio and f_i are the weighting factors of each facet surface free energy γ_i, which is defined as: [83]

$$\gamma_i = \frac{G_i^{\text{surface}}}{S_i} \tag{3.6}$$

where G_i^{surface} and S_i are the free energy of formation of the i-th facet and its surface area, respectively. On the contrary, for small faceted nanoparticles, the free energy contribution due to edges and corners may become significant, hence a correction term to the free energy of the surface has to be included as follows:

$$G_{NP}^{\text{surface}} = G_{NP}^{\text{surfaceonly}} + \Delta G^{\text{edges/corners}} \tag{3.7}$$

The surface free energy G_{NP}^{surface} can be extracted from DFT calculations by considering the total free energy of the nanoparticle, of a bulk TiO_2 unit and the free energy of a water molecule, according to the following expression:

$$G_{NP}^{\text{surface}} = G_{NP} - x \cdot G_{H_2O} - n \cdot G_{\text{bulk}} \tag{3.8}$$

where x and n are the number of absorbed water molecules and TiO_2 units in the nanoparticle, respectively. Nonetheless, free energies calculations are very demanding within DFT, since they require to perform vibrational frequencies or phonons calculations. Thus, in this PhD work, we will approximate total free energies to total electronic energies, as commonly done:

$$G_{NP}^{\text{surface}} \approx E_{NP}^{\text{surface}} \tag{3.9}$$

On this basis, the nanoparticle surface energy γ can be calculated as:

$$\gamma = \frac{E_{NP}^{\text{surface}}}{S_{NP}} \tag{3.10}$$

The concepts exposed above for faceted nanoparticles are valid also for spherical ones, except for the fact that a nanosphere does not present any facets, edges or corner but only a unique quasi-spherical surface. Thus, the surface energies of the **NS**s can be computed by using equations 3.8, 3.9 and 3.10.

The main issue of this general approach is to properly define the surface area of the nanoparticle (S_{NP} in Eq. 3.10). We have employed the two approaches detailed in Section 3.3.2 to define this quantity for nanocrystals and nanospheres. In both cases, hydroxyls groups on the surface were not considered in the definition of the surface because they create artificial protrusions.

In the first approach, the surface is determined by the smallest solid geometry which contains all the atoms of the nanoparticle under study, i.e. the smallest decahedron for nanocrystals and the sphere of radius R_M for nanospheres. Then, the geometrical surface area of the containing solid (S_{geom}) is used as the surface area of the nanoparticle ($S_{NP} = S_{\text{geom}}$). This first method is better suited for the comparison of the surface energies of nanoparticles with the surface energy of regular anatase TiO_2 surfaces, such as the lowest energy (101).

The second approach involves the construction of the Connolly surface [189] that can also account for the roughness of the nanoparticles surface, since it consider the superposition of the Van der Waals volume of each atom. Even if the resulting surface (S_{Conn}) is then smoothed by the Connolly algorithm, it still accounts for the geometrical irregularities, especially in the case of spherical nanoparticles. This is noticeable from the comparison of the the Connolly (in blue) and geometric (in dark red) surfaces in Figure 3.7, as obtained with the above discussed approaches. For nanocrystals, the Connolly surfaces are almost flat on the regular (101) and (001) surfaces of nanocrystals, while they are slightly rippled along the edges. In the case of spherical nanoparticles, as expected, it is wavy all around the nanoparticle due to the superficial roughness of atomic species arranged on a quasi-spherical nanoparticle.

Once the surface area of the nanoparticles is defined, either as $S_{NP} = S_{\text{geom}}$ or $S_{NP} = S_{\text{Conn}}$, the surface energy γ can be computed using Eq. 3.10, obtaining γ_{geom} or γ_{Conn}. All the values of the geometrical and Connolly surface areas and energies are given in Table 3.4 and in Table 3.5, respectively.

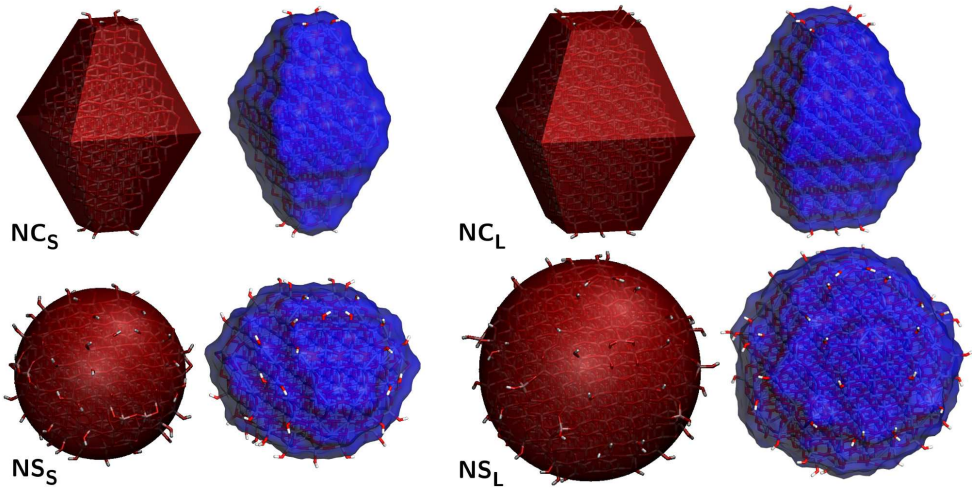

Figure 3.7 – 3D representation of the geometric surfaces (in dark red) and Connolly surfaces (in blue) for all the anatase nanoparticles under study. See Section 3.3.2 for further information on the definition of the surfaces.

In Table 3.4 we compare the surface energies (γ_{geom}) of the various nanoparticles (both **NC**s and **NS**s) with that of the regular (101) anatase surface. Note that the surface energy for this latter system has been calculated using equations analogous to 3.8, 3.9 and 3.10, where the area of the slab model is twice the unit cell area ($2A \times B$, where A and B are the 2D cell parameters). As expected, all the γ_{geom} are higher than the one of a flat surface, in line with what defined in Eq. 3.7. For the larger nanocrystal, since the contribution of edges and corners is smaller, the difference of the surface energy γ_{geom} with respect to the (101) surface is accordingly smaller. It is important to underline that for $\mathbf{NC}_S$ and $\mathbf{NC}_L$ the (101) facets make up the 95-90% of the total geometric surface, respectively, and the presence of highly energetic edges and corners is mitigated by the energy release of the dissociation of water molecules on the (001) facets. In agreement with the Wulff-shape studies, [83] spherical nanoparticles present significantly higher surface energies than faceted nanocrystals. Finally, the results obtained with both the HSE06 and B3LYP functionals are analogous, although HSE06 surface energies of the nanoparticles are systematically larger (by ≈ 0.1 J/m^2) than the B3LYP ones, in line with the difference between the two functionals for the regular (101) surface.

In Table 3.5 surface energies obtained using the Connolly surface (γ_{Conn}) are presented for all the nanoparticles. This approach is better suited to directly compare the values for nanocrystals and nanospheres because exactly the same procedure is used to compute their surface area. Due to surface corrugation, Connolly surface areas are larger than the geometrical ones and consequently all the corresponding surface energies result to be lower. The observed trends of γ_{Conn} are the same as discussed in the previous paragraph for Table 3.4.

Table 3.4 – Surface formation energy terms (in eV), geometrical surface areas (in nm^2) and surface energies (in J/m^2) for the various nanoparticles and for the (101) anatase slab model (computed on 10 triatomic layers), as obtained with the HSE06 and B3LYP functionals.

	$\mathbf{NC}_S$	$\mathbf{NC}_L$	$\mathbf{NS}_S$	$\mathbf{NS}_L$	**Anatase (101)**
HSE06					
$E_{NP}^{surface}$	74.96	97.67	109.62	155.54	
S_{geom}	17.2	23.5	18.7	28.3	
γ_{geom}	0.70	0.67	0.94	0.88	0.634
B3LYP					
$E_{NP}^{surface}$	67.61	87.77	95.68	137.04	
S_{geom}	17.5	23.8	19.0	28.7	
γ_{geom}	0.62	0.59	0.81	0.77	0.544

Table 3.5 – Connolly surface areas (in nm^2) and surface energies (in J/m^2) for the different nanoparticles, as obtained with the HSE06 and B3LYP functionals. The Connolly radius is set to 3.0 Å.

	$\mathbf{NC}_S$	$\mathbf{NC}_L$	$\mathbf{NS}_S$	$\mathbf{NS}_L$
HSE06				
S_{Conn}	18.5	25.0	21.4	32.0
γ_{Conn}	0.65	0.625	0.82	0.78
B3LYP				
S_{Conn}	18.7	25.4	21.8	32.5
γ_{Conn}	0.58	0.55	0.70	0.67

Lastly, in Table 3.6 we report the density of the different surface species for the two nanocrystals and the two nanospheres, in terms of number of undercoordinated atoms or OH groups per unit area (S_{Conn}). This kind of information can help in the rationalization of the trends discussed for the surface energies. As a matter of fact, nanospheres show a higher density of undercoordinated sites than nanocrystals, that justifies the observed higher values of the surface energy. Regarding nanocrystals, one can observe that the density of surface species is about the same in total, but the density of more energetically costly Ti_{4c} is larger in $\mathbf{NC}_S$ than in $\mathbf{NC}_L$. This is one of the reasons of the higher γ_{Conn} found for $\mathbf{NC}_S$ compared to $\mathbf{NC}_L$.

3.4 Electronic Properties

3.4.1 Band Gaps

The comparison of the electronic properties of nanoparticles of different shape with respect to the bulk is of paramount importance for the application of nanoparticles in photocatalysis and photovoltaics. The first fundamental quantity that we discuss is the "band gap", i.e. the energy gap between occupied and unoccupied states.

Table 3.6 – Number of undercoordinated sites per unit area (sites/nm^2) for the nanoparticles and (101) surface, as obtained with HSE06 functional. The surface area is calculated with the Connolly method with a radius equal to 3.0 Å.

Undercoordinated sites per unit area $S_{\mathbf{Conn}}$					
Surface site	**NC**$_S$	**NC**$_L$	**NS**$_S$	**NS**$_L$	**Anatase (101)**
OH	0.43	0.48	2.43	2.00	
O_{2c}	4.77	4.79	5.79	6.00	5.14
Ti_{4c}	0.22	0.16	1.12	1.13	
Ti_{5c}	4.12	4.23	2.15	2.00	5.14
$Ti_{3c}OH$			1.12	1.00	
$Ti_{4c}OH$	0.43	0.48	0.37	0.50	
$Ti_{5c}OH$			0.56		
$Ti_{3c}(OH)_2$				0.25	
$Ti_{4c}(OH)_2$			0.19		
Total	9.97	10.14	13.73	12.88	

Bulk anatase TiO_2 has an indirect band gap, which is estimated, within the present computational setup and by the hybrid functional HSE06, to be 3.65 eV, in agreement with previously reported values. [192] In the case of nanoparticles, although very large, they are still *finite* molecular systems, hence it is not fully correct to refer to band states and, consequently, to band gaps. Therefore, it is necessary to distinguish between very localized states (and refer to molecular orbitals, MOs) and states which are delocalized on several atoms of the nanoparticle and can, thus, be considered as (quasi-)band states.

As regards nanocrystals (**NC**s), the highest occupied state and the lowest unoccupied state, shown in Figure 3.8 and discussed in Section 3.4.2, can be fully considered band states, following the definitions above, therefore the Kohn-Sham band gap of the nanocrystals (E_{gKS}) corresponds to the HOMO-LUMO gap ($\Delta E_{H\text{-}L}$) and is about 0.3 eV larger than for the bulk system (3.94 eV for **NC**$_S$ and 3.90 eV for **NC**$_L$), as reported in Table 3.7.

As regards nanospheres (**NS**s), the highest occupied state is a molecular orbital fully localized on a surface state involving the protruding hydroxyl groups (see next Section 3.4.2 for further information). Thus, the $\Delta E_{H\text{-}L}$ cannot be considered as the band gap of the nanospheres, since the HOMO does not resemble a band state. In order to determine the E_{gKS} for spherical nanoparticles, we need to select a lower energy occupied states which is delocalized on oxygen atoms of the nanoparticle and can be truly considered a "band" state. In this case, we considered the HOMO-4 (see Figure 3.10 for the 3D plots) as the top of the valence band, since it is highest occupied state enough delocalized. Therefore, E_{gKS} values are larger than $\Delta E_{H\text{-}L}$ values, but approaching the bulk band gap (3.69 eV for **NS**$_S$ and 3.67 eV for **NS**$_L$, see Table 3.7).

The convergence of these band gap data has been checked with respect to the basis set dimension adding a diffuse function on each atom of the surface layer of the small nanocrystal **NC**$_S$ (+) and nanosphere **NS**$_S$ (+). We observe just a difference of

Table 3.7 – Relative energy values, with respect to the vacuum level, of the top of the valence band (Top VB), of the HOMO orbital and of the bottom of the conduction band (Bottom CB); energy differences between HOMO and LUMO levels ($\Delta E_{H\text{-}L}$); Kohn-Sham energy gap (E_{gKS}). All HSE06 and B3LYP values are in eV. (+) symbol refers to data obtained with the additional diffuse functions on all the surface atoms (see Section 3.2).

	$\mathbf{NC}_S$	$\mathbf{NC}_S$ (+)	$\mathbf{NC}_L$	$\mathbf{NS}_S$	$\mathbf{NS}_S$ (+)	$\mathbf{NS}_L$	**Bulk**
HSE06							
Top VB	-8.06	-8.23	-8.08	-7.70	-7.88	-7.65	
HOMO	-8.06	-8.23	-8.08	-7.48	-7.65	-7.43	
Bottom CB	-4.12	-4.35	-4.18	-4.01	-4.20	-3.97	
$\Delta E_{H\text{-}L}$	3.94	3.88	3.90	3.47	3.45	3.45	
E_{gKS}	3.94	3.88	3.90	3.69	3.68	3.67	3.65
B3LYP							
Top VB	-8.01	-8.19	-8.03	-7.88	-8.06	-7.68	
HOMO	-8.01	-8.19	-8.03	-7.63	7.83	-7.49	
Bottom CB	-3.91	-4.15	-3.98	-3.92	-4.12	-3.81	
$\Delta E_{H\text{-}L}$	4.10	4.04	4.05	3.71	3.70	3.68	
E_{gKS}	4.10	4.04	4.05	3.96	3.94	3.86	3.81

few hundredths of eV between the results obtained with the two types of basis sets, proving that the convergence is reached.

Lastly, the B3LYP results are fully analogous to the HSE06 ones, although all the energy gaps are systematically larger with the B3LYP functional, as expected from the values of the bulk band gap with the two functionals.

However, the Kohn-Sham band gap is an approximation of the fundamental gap of a molecular system. Therefore, they generally differ from fundamental gaps (E_g), defined as the difference between the ionization potential, IP, and the electron affinity, EA (see Section 2.2.5 for further detail). As discussed in Section 2.2.5, this is related to the derivative discontinuity of the exchange-correlation (xc) functional, i.e. the finite increase in energy of the xc potential when the electron number crosses the integer number of electrons of the system (N).

For extended systems, the use of orbital-dependent functionals, which exhibits a discontinuity as the electron number crosses an integer, leads to meaningful improvements in the prediction of fundamental band gaps from KS gap values. On the contrary, for finite-sized systems, such as molecules or nanoparticles, this is not sufficient because the asymptotic potential, not present in the solids, crucially influences the energy of electron addition or removal. [193] In general, the Kohn-Sham gaps for molecules or nanoparticles, as predicted by hybrid functional calculations, are considerably smaller than fundamental gaps E_g and in arguably better agreement with optical gaps. The difference between the true fundamental gap of a system and its KS gap corresponds to the derivative discontinuity (DD). [194]

All these arguments are fully applicable to the nanoparticles under study. In Table 3.8, the HOMO–LUMO KS gaps can be compared with the fundamental gaps, as obtained from the computed vertical ionization potentials (IP^v) and vertical electron

Table 3.8 – Vertical electronic affinities (EA^v) and ionization potentials (IP^v); fundamental gaps (E_g) and Kohn-Sham ($\Delta E_{H\text{-}L}$) gaps, and their difference, i.e the derivative discontinuity (DD). All values are in eV and given for both the HSE06 and B3LYP functionals. (+) symbol refers to values obtained with additional diffuse functions on all surface (see the text and Section 3.2 for further details).

	HSE06					**B3LYP**				
	EA^v	IP^v	E_g	$\Delta E_{H\text{-}L}$	DD	EA^v	IP^v	E_g	$\Delta E_{H\text{-}L}$	DD
$\mathbf{NC}_S$	3.41	8.93	5.52	3.94	1.58	3.23	8.80	5.57	4.10	1.47
$\mathbf{NC}_S$ (+)	3.64	9.09	5.45	3.88	1.57	3.48	8.98	5.50	4.04	1.46
$\mathbf{NC}_L$	3.52	9.18	5.66	3.90	1.76	3.41	8.78	5.37	4.05	1.32
$\mathbf{NS}_S$	3.39	8.38	4.99	3.47	1.52	3.32	8.41	5.09	3.71	1.38
$\mathbf{NS}_S$ (+)	3.61	8.55	4.94	3.45	1.49	3.54	8.61	5.07	3.70	1.37
$\mathbf{NS}_S$	3.45	8.47	5.03	3.45	1.58	3.30	8.36	5.06	3.68	1.38

affinities (EA^v). Note that the EA^v and IP^v values are calculated as described in the Computational Details in Section 3.2.

As expected, the fundamental gaps (E_g) are always higher than KS gaps (E_{gKS}) by about 1.5 eV, both with HSE06 and B3LYP functionals. The excess electron or the hole, resulting from the removal of the electron, occupy the LUMO and HOMO of the nanoparticle, respectively. Therefore, nanocrystals and nanospheres show similar electron affinities since the LUMO is in all cases a delocalized state involving the Ti atoms in the central portion of the nanoparticle (see next section 3.4.2 for more details). On the contrary, we observe that the ionization potentials are considerably different, with those of the nanospheres being lower than those of the nanocrystals. This arises from the diversity of the HOMO levels in the two cases: in the case of the nanocrystals, it is a delocalized state involving the oxygen atoms in the central portion of the nanoparticle, whereas, in the case of the nanospheres, is a highly localized surface state, as will be discussed in detail in Section 3.4.2. Concerning the size effects, we noticed an increase of EA^v and IP^v of approximately 0.1 eV for both **NC** and **NS** between the large and the small nanoparticles.

Lastly, we have checked the convergence of the fundamental gaps with respect to the basis set extension by performing the same calculations with one additional diffuse function on each atom of the surface layer of the nanoparticles. Although an increase of both the IPs and EAs by more than 0.1 eV has been observed, the values of the fundamental gap are very similar to the ones computed with the smaller basis set.

3.4.2 Frontier Orbitals

In this section we will discuss the frontier orbitals, i.e. the highest occupied molecular orbital (HOMO) and the lowest unoccupied molecular orbital (LUMO), for all the nanoparticles under investigation. Note that in the CRYSTAL14 code it is not possible to plot directly a molecular orbital ϕ_i, but one can plot the electron density projected onto a specific Kohn-Sham eigenstate, i.e. $|\phi_i^2|$. For brevity, we will refer to this quantity as orbital, although no information on the sign of the one-electron

wavefunction is given. The results computed with the two hybrid functionals HSE06 and B3LYP are fully analogous, hence only the HSE06 orbitals will be presented.

First, we focus on the frontier orbitals of the nanocrystals (**NC**), given in Figure 3.8. The HOMOs and LUMOs of $\mathbf{NC}_S$ and $\mathbf{NC}_L$ are perfectly analogous and in agreement with the ones computed in a previous work by Mattioli et al. [107] for nanocrystals of the same size and shape of $\mathbf{NC}_S$. As mentioned in the previous section, the HOMOs of $\mathbf{NC}_S$ and of $\mathbf{NC}_L$ are similar to delocalized band states, mostly involving the 2p atomic orbitals of oxygen of the central belt of the nanocrystals and the contribution of 2p that increase going towards the core of the nanoparticle. Interestingly, there is an alternation of rows of $2p_x$ or $2p_y$, according to the atomic plane of oxygen considered. These layers in the central belt are the ones with the largest xy surface area. Furthermore, going from $\mathbf{NC}_S$ to $\mathbf{NC}_L$ we can notice a significantly lower contribution of the outermost 2p states on undercoordinated O_{2c}.

The LUMOs of $\mathbf{NC}_S$ and of $\mathbf{NC}_L$ resemble again band states, which mostly delocalized on the Ti $3d_{xy}$ states of the central atomic layers of the nanocrystals, which possess the largest xy surface area. Again, going from $\mathbf{NC}_S$ to $\mathbf{NC}_L$ we can notice a lower contribution from the d states centered on surface Ti atoms. Further discussion on the contribution of coordinated/undercoordinated atoms on the frontier states we refer to Section 3.4.3, where total and projected densities of states will be presented and discussed.

The frontier orbitals of the spherical nanoparticles show different features (see Figure 3.9). Also in the case of the $\mathbf{NS}_S$ and $\mathbf{NS}_L$ nanoparticles, the LUMO levels are delocalized states but they involve only the $3d_{xy}$ of fully coordinated bulk atoms. This is more evident for the larger nanosphere, where surface Ti atoms are not involved at all in the LUMO, which is different from what observed for nanocrystals. Even more different is the situation for the highest occupied states. Both in the case of $\mathbf{NS}_S$ and $\mathbf{NS}_L$, the HOMO levels are fully localized on surface hydroxyls. As discussed in Section 3.4.1, this special feature has a relevant effect on the Kohn-Sham gaps. For this reason, deeper states have been studied and the first delocalized state on several O atoms that can be considered a band state and used to compute E_{gKS} is the HOMO-4 (see Figure 3.10).

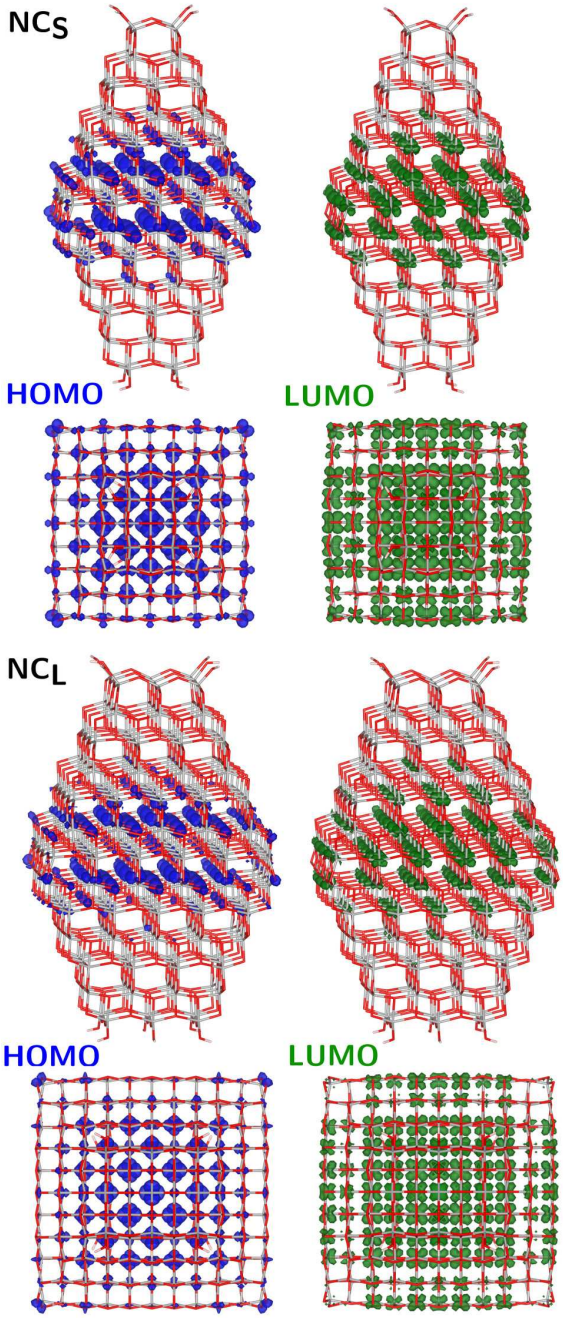

Figure 3.8 – Side (upper) and top (lower) views of the electronic density plot for the frontier orbitals of the two nanocrystals, as obtained with the HSE06 functional and an isosurface value of 0.0005 a.u.

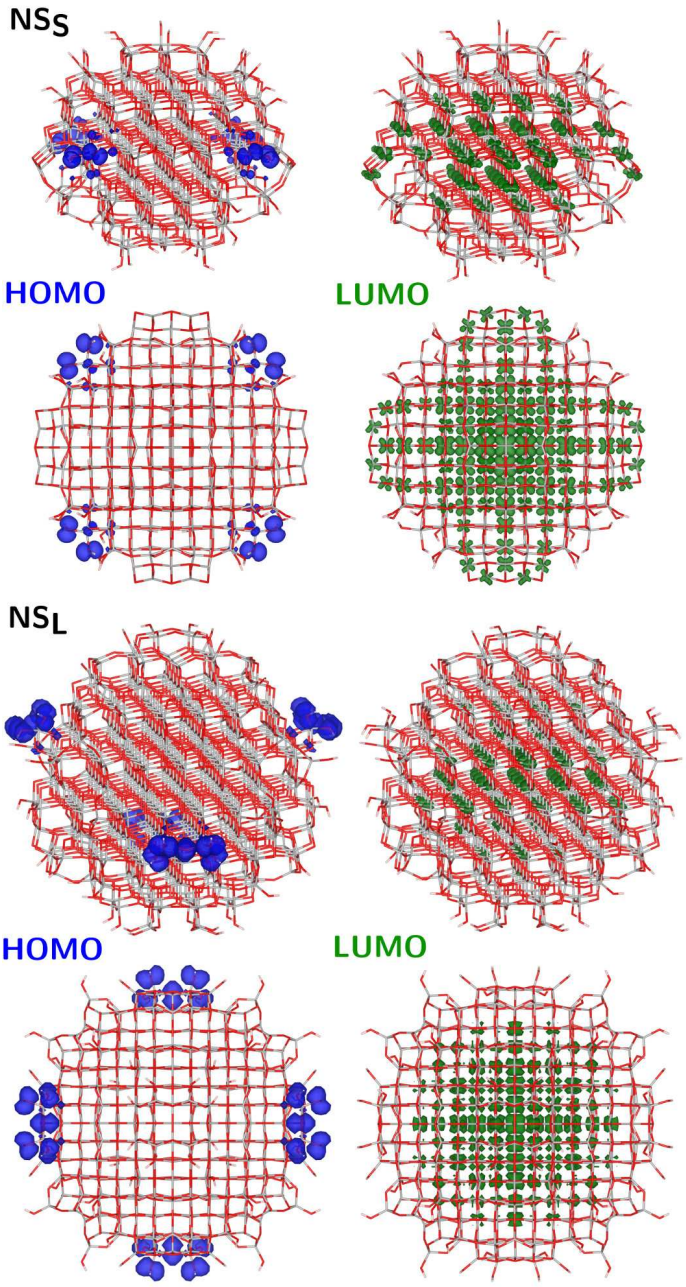

Figure 3.9 – Side (upper) and top (lower) views of the electronic density plot for the frontier orbitals of the two nanospheres, as obtained with the HSE06 functional and an isosurface value of 0.0005 a.u. (0.001 a.u. for the highly HOMO localized states).

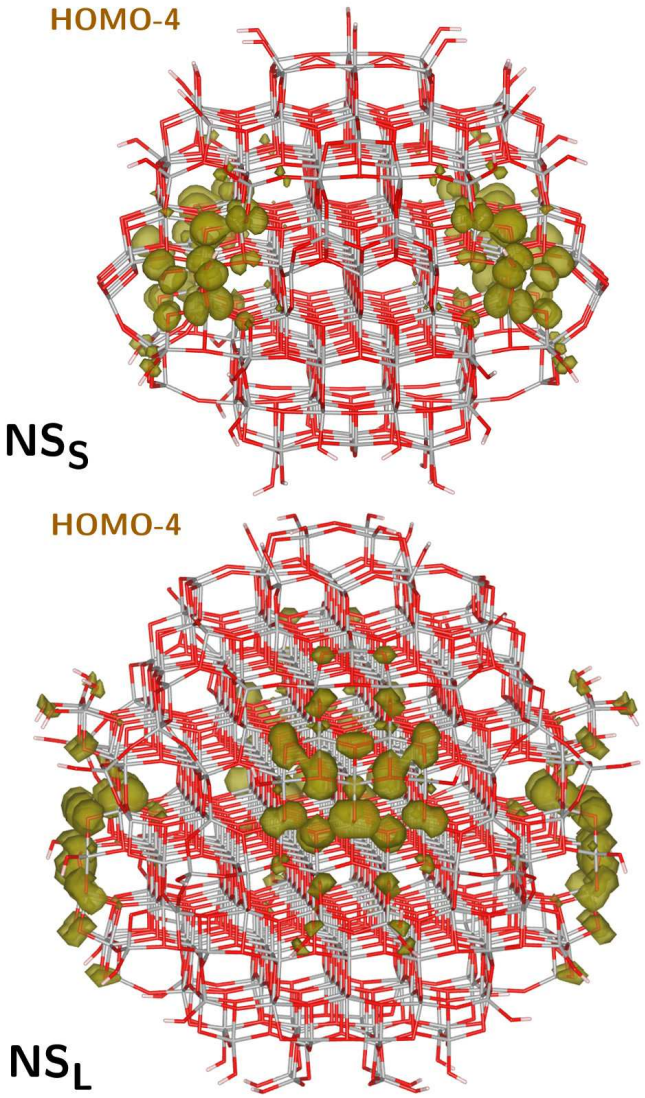

Figure 3.10 – Side views of the electronic density plot for the HOMO-4 orbitals of the two anatase nanospheres, as obtained with the HSE06 functional and an isosurface value of 0.0005 a.u.

3.4.3 Total and projected density of states

Differently from periodic systems discussed in Section 2.1.6, nanoparticles do not possess a continuum of electronic states but discrete energy levels corresponding to a finite number of molecular orbitals. However, for a large enough nanoparticle, the number of these states and their (quasi-)degeneracy is such that to derive the density of states as a function of the energy is more useful than focusing on each of the many eigenstates. Furthermore, the derived density of states of the nanoparticle can be directly compared with the ones of extended systems.

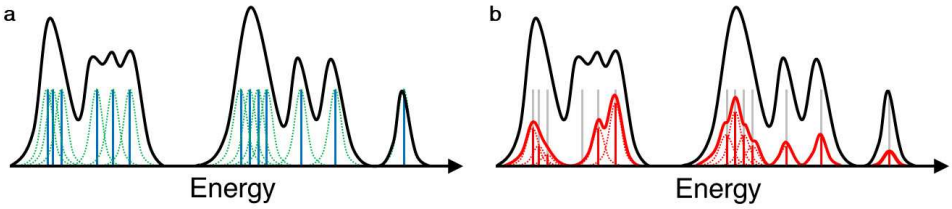

Figure 3.11 – Scheme of the procedure employed for the calculation of the density of states (DOS, a) and projected density of states (PDOS, b).

Throughout this PhD work, we simulated the total density of states (DOS, black curve in Figure 3.11) of the nanoparticle via the convolution of Gaussian peaks (green dashed functions in Figure 3.11a) centered at the Kohn-Sham energy eigenvalue of each orbital (blue lines in Figure 3.11a). We employed normalized Gaussian functions with the following analytical form:

$$f_i(\epsilon) = \frac{1}{\sqrt{2\pi}\sigma} \exp\left(\frac{-(\epsilon - \epsilon_i)}{2\sigma^2}\right) \tag{3.11}$$

where ϵ_i are the discrete Kohn-Sham energy levels and σ is related to the width of the Gaussian function, i.e. the higher is the value of σ, the higher is the broadening of the resulted DOS.

The projections of the density of states have been obtained by using the coefficients in the linear combination of atomic orbitals (LCAO) of each molecular orbital: summing the squares of the coefficients of all the atomic orbitals centered on a specific atomic species results, after normalization, in the relative contribution of each atom type to a specific eigenstate (red bars in Figure 3.11b). Subsequently, each projection (red line in Figure 3.11b) is obtained from the convolution of Gaussian peaks with heights that are proportional to the relative contribution (red dashed functions in Figure 3.11b). Finally, since Kohn-Sham energies are refered to the vacuum level, i.e. the potential energy of an electron at an infinite distance from the molecule, the zero energy for all the DOS is the vacuum one.

The simulated total and projected densities of states (DOS and PDOS) for nanocrystals and nanospheres, as obtained with the HSE06 calculations, are reported in Figure 3.12 and 3.13, respectively. The general features of the density of states for nanoparticles are the same of bulk anatase: [62] the valence band width is about 7 eV and

it is composed mainly by the 2p of the oxygen atoms but not completely, indicating the covalent character of TiO_2; the conduction band is made predominantly by the 3d states of titanium atoms with a small contribution from 2p of oxygen atoms. Besides the already discussed differences in the energy gaps, the DOS and PDOS with the B3LYP functional are fully analogous to the HSE06 ones. We will now focus our attention on the projections on all the different atomic species present in the nanoparticles under study.

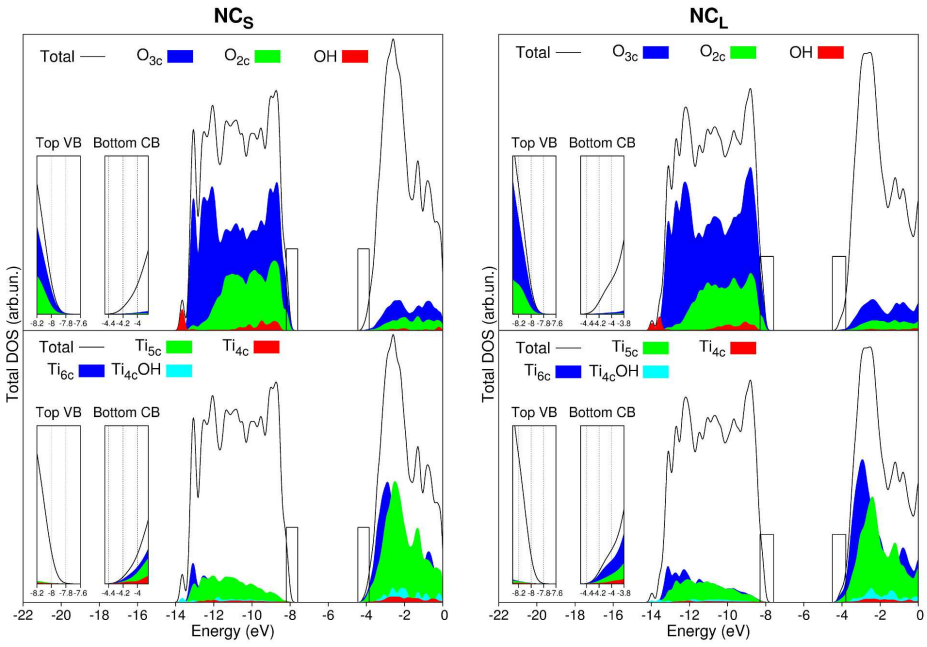

Figure 3.12 – Total (DOS) and projected (PDOS) density of states on different O and Ti atoms of anatase **NC**s, as obtained with the HSE06 functional. Magnified regions of the DOS are shown in the insets. A 0.01 eV Gaussian broadening was used. The zero energy is set to the vacuum level.

Concerning the small nanocrystal $\mathbf{NC}_S$, we observe that: the top of the valence band is basically made by O_{3c} and O_{2c} on the (101) facets (see inset in the upper left panel of Figure 3.12); the bottom of the conduction band is mostly made up by Ti_{6c} and Ti_{5c} (inset in the bottom left panel of Figure 3.12); below the bottom of the valence band a detached peak related to the hydroxyl groups is present. From the comparison of the DOS and PDOS between $\mathbf{NC}_S$ (left panel of Figure 3.12) and $\mathbf{NC}_L$ (right panel of Figure 3.12) one can observe many similarities and only few differences. As one would expect, the projections on fully coordinated O_{3c} and Ti_{6c} species increase in intensity, due to the increase of the bulk-like region of the nanoparticle. Interestingly, the OH peak below the valence band splits in two because, in the larger nanocrystal, two inequivalent types of hydroxyl exist.

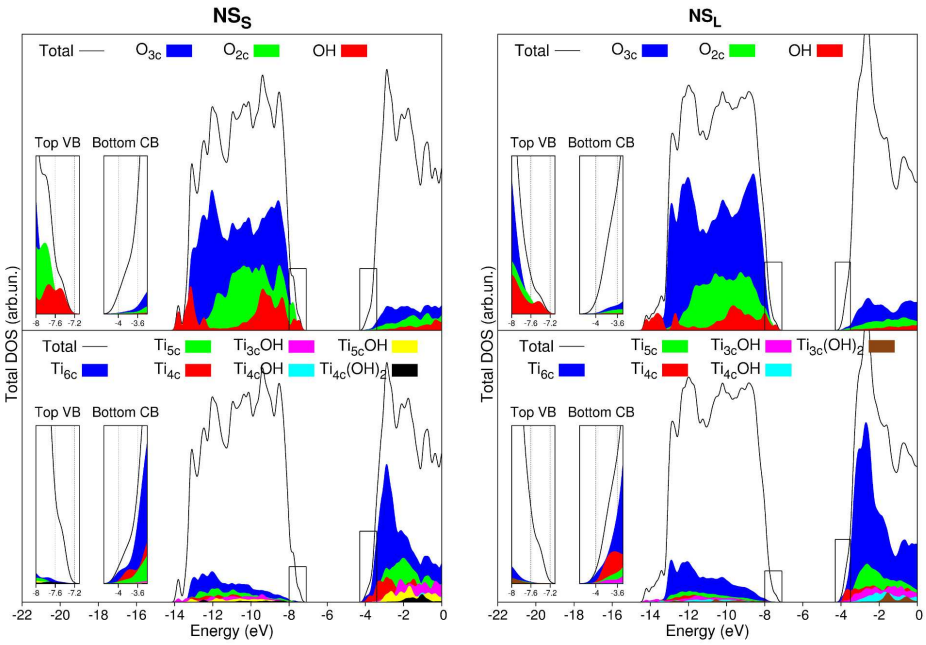

Figure 3.13 – Total (DOS) and projected (PDOS) density of states on different O and Ti atoms of anatase **NS**s, as obtained with the HSE06 functional. Magnified regions of the DOS are shown in the insets. A 0.01 eV Gaussian broadening was used. The zero energy is set to the vacuum level.

As regards the smaller spherical nanoparticle $\mathbf{NS}_S$ (left panel of Figure 3.13), the top of the valence band is prevalently made by the OH groups (inset in the upper left panel of Figure 3.13). At lower energies contributions from 2p states centered on O_{2c} appear and only at even lower energies the O_{3c} projection becomes predominant. The bottom of the conduction band (inset in the bottom left panel of Figure 3.13) is mostly composed by Ti_{6c} with a significant contribution also from Ti_{4c} and Ti_{5c}. Comparing DOS and PDOS for $\mathbf{NS}_S$ with those for $\mathbf{NS}_L$ (left vs right panel of Figure 3.13) some clear trends can be evidenced. Due to the increase in size of the bulk-like core, the O_{2c} to O_{3c} and OH to O_{3c} ratios, as well as the Ti_{5c} to Ti_{6c} ratio, diminish. This impacts also the relative contributions to the top of the valence band (inset in the upper panel on the right of Figure 3.13) in terms of a lower contribution of the O_{2c} and OH species. For the bottom of the conduction band we can observe an increased contribution of Ti_{4c}, even though the Ti_{6c} contribution still is prevalent on the very bottom of the CB (inset in the bottom right panel of Figure 3.13).

In Figure 3.14 we report the projections of the DOS on the OH groups bound to different Ti atoms (Ti_{3c}, Ti_{4c}, Ti_{5c}, $Ti_{3c}OH$ or $Ti_{4c}OH$) for the two nanospheres. In the range between -11 and -7 eV, the peaks in the PDOS are due to the states of the lone pairs of the oxygen atoms of the hydroxyl. Noteworthy, the lone pair on an

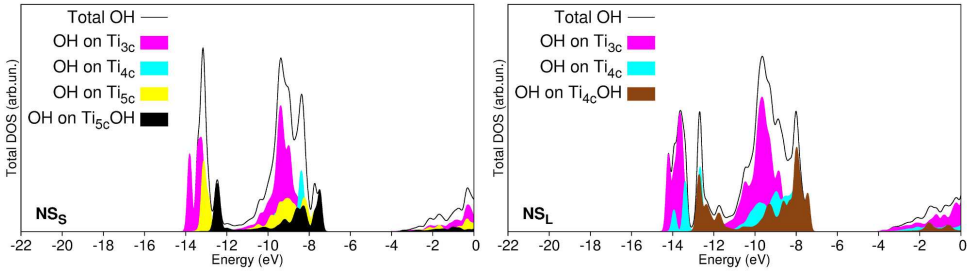

Figure 3.14 – Total (DOS) and projected (PDOS) density of states onto O atoms of different OH groups of anatase nanospheres, as calculated with the HSE06 functional. A 0.01 eV Gaussian broadening has been used. The zero energy is set to the vacuum level.

OH bound to a Ti_{5c} is higher in energy, i.e. more prone to bind an H^+ or trap a hole, than the lone pairs on hydroxyls bound Ti_{4c} or Ti_{3c}.

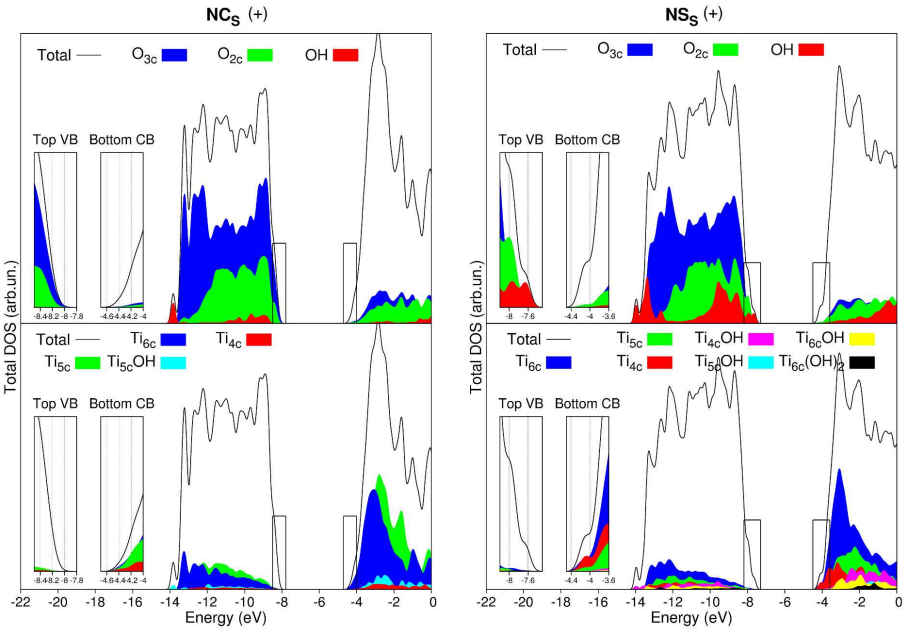

Figure 3.15 – Total (DOS) and projected (PDOS) density of states on different O and Ti atoms of the smallest anatase nanoparticles, as calculated with the HSE06 functional and the addition of diffused functions in the basis set. Magnified regions of the diagram are shown in the insets. A 0.01 eV Gaussian broadening has been used. The zero energy is set to the vacuum level.

Finally, the convergence with respect to the basis set has been checked. The DOS and PDOS for $\mathbf{NC}_S$ and $\mathbf{NS}_S$ resulting from the addition of a diffuse function on the atoms in the external layer of the nanoparticle are given in Figure 3.15. The use of an extended basis set does not cause major variations, except a higher degree of covalency with a larger contribution of titanium atoms to the valence band and a larger contribution of the oxygen atoms to the conduction band.

3.5 Global optimization of TiO_2 Nanospheres

Among all the titania-based nanomaterials, spherical nanoparticles are particularly interesting for the biofunctionalization of TiO_2, thanks to the enhanced binding properties with respect to faceted nanoparticles, caused by the high surface curvature. [31] Quantum chemical simulations can be extremely precious to investigate and rationalize the surface structure of such nano-objects and understand its relation with the observed physico-chemical properties.

In the previous sections, TiO_2 nanospheres have been already modelled carving from anatase bulk a sphere of atoms which results, after saturation with hydrogen atoms, in stoichiometric nanoparticles with a considerable number of intrinsic water molecules included. Then, the models were directly relaxed at the full hybrid DFT level, leading to locally optimized "as-carved" nanoparticles, whose ground state properties were extensively described and compared to the ones of nanocrystals.

However, on the nanospheres built in this unsupervised way there are several hydroxyl groups, which influence the electronic properties (see Section 3.4) and may hide some features of a non-hydrated spherical nanoparticle. For this reason, it is useful to reduce the amount of water as much as possible, trying to keep the global D_{2d} symmetry and the chemical stability of the system, i.e. a minimum of coordination of 4-fold and 2-fold for the Ti and O atoms, respectively. This task is non-trivial and it has been performed manually, removing atom by atom. For the **NS** with a diameter of 2.2 nm ($\mathbf{NS}_S$ in the previous sections) this has been done in two phases, as shown in Figure 3.16.

First, from the $(TiO_2)_{223} \bullet 26\ H_2O$ model (Figure 3.16a) the eight hydroxyl group of the $Ti_{4c}(OH)_2$ have been removed together with eight hydrogen atoms. This means that formally eight water molecules have been subtracted, giving a stoichiometry of $(TiO_2)_{223} \bullet 18\ H_2O$ (Figure 3.16b). The eight hydrogen atoms were removed from eight $Ti_{5c}OH$ species, leaving eight dangling monocoordinated oxygen atoms ($Ti_{5c}O$) that were, in turn, moved to another portion of the **NS**, leaving a Ti_{5c}. In particular, they were moved between two titanium atoms, forming eight new O_{2c} species.

Second, we were able to reduce further the content of water but at the expenses of the global symmetry of the nanosphere. As a matter of fact, other eight water molecules can be removed in a similar way from $Ti_{4c}OH$ species, but only an asymmetric removal is possible, e.g. a hydroxyl group has been removed from one side of the dihedral mirror plane, but not from the other. This led to the stoichiometric nanosphere $(TiO_2)_{223} \bullet 10\ H_2O$, given in Figure 3.16c, which has a lower global symmetry of D_2. Some water molecules still remain on the surface, but this can be truly considered as intrinsic dissociated water modeled in our **NS**s. Indeed, it was reported

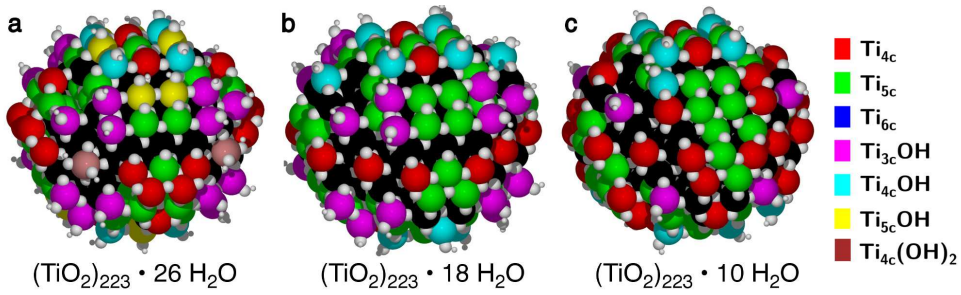

Figure 3.16 – Structures of the 2.2 nm spherical nanoparticle models with a different amount of water on its surface. Oxygen and hydrogen atoms are shown in white, titanium atoms are represented according to their coordination pattern with the color-code on the right part of the figure.

by experimental works that some water adsorbates on spherical nanoparticles cannot be completely removed even after annealing at 600 K. [195]

In addition to the issue of the water content, another problem arises from the fact that the nanosphere may reconstruct towards a more stable and meaningful geometry. To this end, one should apply a global mininum search strategy to a system with more than 500 atoms which is, however, hardly feasible at the DFT level. Therefore, in order to perform this demanding task, we employed the SCC-DFTB methodology, introduced in Section 2.3, which allows for an accuracy comparable to ab initio methods, at a reduced computational cost. [169, 196]

Concerning TiO_2 systems, the SCC-DFTB approach has been already used to accurately calculate properties of periodic systems, such as bulk TiO_2 and TiO_2 surfaces, of both anatase and rutile phases, as well as small TiO_2 clusters and molecules, giving results in good agreement with ab initio (DFT) references. [187, 197–199] This exhaustive list of previous works validates the use of SCC-DFTB as reliable tool for quantum investigations of extended TiO_2 systems.

Several approaches can be employed to explore the potential energy surface and locate the global energy minimum. For instance, one can run a high-temperature molecular dynamics and perform geometry optimization on a large sets of snapshots. This approach allows to partially scan the potential energy surface, but the search of the global minimum is *biased* by the choice of the snapshots.

In this work, in order to obtain an *unbiased* result, we applied the simulated annealing procedure, which has been described in Section 2.4.2, to find the global minima on the potential energy surface of the $\mathbf{NS}_S$ and $\mathbf{NS}_L$ nanospheres. Additionally, we have considered also other two TiO_2 nanospheres, one smaller than $\mathbf{NS}_S$ and the other larger than $\mathbf{NS}_L$, covering the range between 1.5 nm and 4.4 nm of diameter. From now on, the nanospheres will be labeled with their diameter for clarity. Indeed, nanospheres in the size range between ∼2 nm and ∼8 nm have been synthesized and characterized in the last years [56, 80, 200–203] to be used for various applications.

The structures were carved from an anatase bulk supercell following the procedure described in Section 3.3.1 and dehydrated as much as possible. Then, they have been

used as starting point for a series of simulated annealing calculations at different target temperatures. The following results will show that spherical nanoparticles obtained with the annealing processes are in general more stable than the "as-carved" ones, presenting more crystalline core and rearranged surfaces. The most stable structures have been then relaxed at both the SCC-DFTB and hybrid DFT level of theory, even for the largest one of about 4000 atoms. Then, similarly to the previous sections, we performed an analysis of the structural and electronic properties of the globally optimized spherical nanoparticles as obtained with the two levels of theory, with the aim to validate further the SCC-DFTB method for large TiO_2 nanosystems.

3.5.1 Simulated Annealing

For the construction of the nanospheres considered in this study we applied different carving radii in order to obtain nanoparticles with a 1.5 nm, 2.2 nm, 3.0 nm and 4.4 nm diameter size. Once the models were carved, saturated and dehydrated as described above, we have performed a geometry relaxation of the structures at both DFTB and DFT level of theory to obtain a reference total energy for a geometrically constructed nanoparticle (we will refer to them as 0 K or "as-carved" structures).

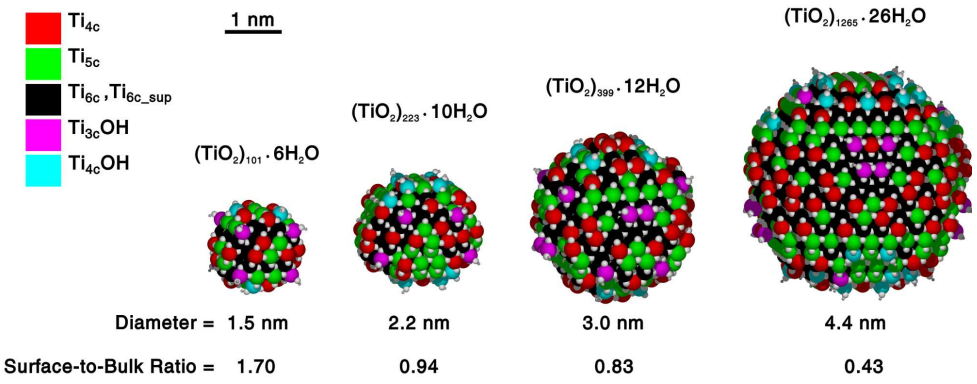

Figure 3.17 – DFT(B3LYP) optimized structures, after simulated annealing, of the different nanospheres under study. For each one, the stoichiometry, the cutting diameter D_M, the surface-to-bulk ratio (as defined in Section 3.5.2) and the position of the Ti atoms with different coordination are reported.

In Figure 3.17 the representation of the most stable DFT globally optimized nanospheres is reported. The color-coding indicating the different coordination pattern of the Ti atoms is slighty different from the one used in Section 3.3.2 and will be discussed exhaustively in Section 3.5.2.

Then, DFTB molecular dynamics simulations have been carried out in order to perform a simulated annealing process, as described in Section 2.4.2. We employed three different target temperatures (300 K, 500 K and 700 K) for the 1.5 nm, 2.2 nm and 3 nm diameter nanospheres, whereas for the largest nanosphere (4.4 nm) the

annealing has been performed only at 500 K. During the molecular dynamics runs the temperature profile has been subdivided in three temporal regions:

I. *Heating period*: heating of the system up to the target temperature in a very short time (1 ps), starting from an initial Boltzmann velocity distribution generated at 150 K.

II. *Equilibration period*: equilibration to the target temperature until the temperature profile is found to be flat.

III. *Cooling region*: gradual cooling down to 0 K (80 K for the 4.4 nm nanosphere) as slow as possible (depending on the size of the nanoparticles considered) in order to end up in the global minimum.

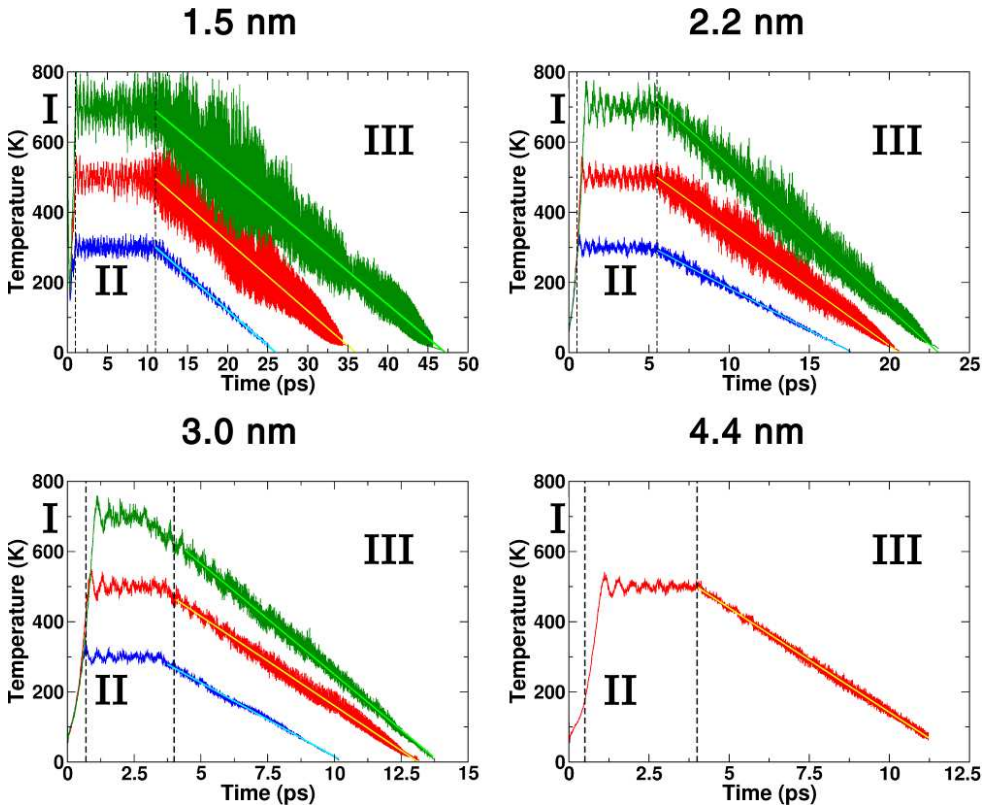

Figure 3.18 – Temperature profiles in the simulated annealing processes for the 1.5 nm, 2.2 nm, 3.0 nm and 4.4 nm nanospheres. Green curves refer to the profile with 700 K of target temperature, red curves refer to the profile with 500 K of target temperature and blue curves refer to the profile with 300 K of target temperature. Heating (I), equilibration (II) and cooling (III) regions have been indicated.

The temperature profiles representations for all the nanoparticles under study are given in Figure 3.18. The permanence time of the nanoparticle in each time region is different and depends mainly on two factors: the target temperature and the size of the nanospheres. Analogously, these two factors rule also the temperature gradient (the average slope of the temperature profile) considered in the heating and the cooling process: the higher is the target temperature and the larger is the **NS**, the higher are the heating and cooling gradients. It is worth noting that the larger is the system, the more attenuated are the temperature fluctuations since, according to statistical physics, their amplitude is proportional to $1/\sqrt{N}$, where N is the number of atoms.

Finally, all the structures produced with different target temperatures have been locally optimized both at the DFTB and DFT(B3LYP) levels of theory. Among them, for each size, we selected the most stable one in terms of energy difference with respect to the not annealed "as-carved" **NS** model (see Table 3.9). The 1.5 nm and 2.2 nm nanospheres resulted to be more stable when annealed at 300 K, because, at higher temperature, some localized amorphous areas form on the surface, causing a loss in stability. For the 3.0 nm nanosphere a similar surface structure has been obtained with all three simulated annealing processes at 300 K, 500 K and 700 K, with the one at 500 K being slightly more stable than the others. For the biggest 4.4 nm **NS**, we used only one target temperature of 500 K to reduce the computational effort. From this analysis we can conclude that larger **NS** models keep crystallinity on the surface up to higher temperature of annealing, whereas this is not true for smaller ones.

Table 3.9 – DFTB and DFT(B3LYP) energy gain (in eV) for the most stable nanospheres obtained from simulated annealing processes with respected to the optimized as carved ones. Note that the as carved NS has not been optimized for the 4.4 nm, thus we could not compute the energy gain and thus this value difference is not available (N.A.).

Diameter (nm)	Target T	ΔE_{DFTB}	$\Delta E_{DFT(B3LYP)}$
1.5	300 K	-1.36	-0.17
2.2	300 K	-4.76	-0.65
3.0	500 K	-6.83	-0.25
4.4	500 K	-10.09	N.A.

Most importantly, the values in Table 3.9 clearly demonstrate that, although the simulated annealing has been performed with the DFTB approach, the global optimization procedure was able to find minima more stable than the "as-carved" ones even at the DFT(B3LYP) level. However, the stabilization at the DFT level is lower than with DFTB, because of the DFTB potential energy surface is an approximation of the DFT(B3LYP) one.

3.5.2 Structural Analysis

Morphology of the nanospheres

The most stable nanospheres at the DFT(B3LYP) level together with a graphical representation of the position of the different Ti species have been already shown in Figure 3.17, where the surface-to-bulk ratio is also reported. This quantity is defined

as the ratio between the number of Ti and O atoms at the NS surface (Ti_{6c}^{sup}, Ti_{5c}, Ti_{4c}, $Ti_{4c}(OH)$, $Ti_{3c}(OH)$, OH, O_{2c}, O_{3c}^{sup}) and the number of fully coordinated Ti and O atoms in the bulk (Ti_{6c} and O_{3c}). Undercoordinated atoms are directly considered to be part of the surface. In analogy to the (101) surface, also fully coordinated atoms may be part of the surface when bound to undercoordinated ones. Thus, fully coordinated Ti (Ti_{6c}^{sup}) are considered to be atoms of the surface (*sup*) when connected to at least one O_{2c}, whereas fully coordinated O (O_{3c}^{sup}) are considered surface (*sup*) atoms when bound to a surface Ti atoms, i.e. Ti_{6c}^{sup}, Ti_{5c}, Ti_{4c}, $Ti_{4c}(OH)$, $Ti_{3c}(OH)$. As one would expect, the larger is the **NS**, the lower the surface-to-bulk ratio, due to the fact that the amount of inner bulk-like atoms increases.

Table 3.10 – Number of Ti atoms with a certain coordination sphere and their percentage with respect to the total number of Ti atoms for all the different size **NS**s geometries optimized with DFTB. Number and percentage of Ti atoms in NSs geometries optimized with DFT(B3LYP) are reported in brackets, when they are different from DFTB.

NS	1.5 nm		2.2 nm		3.0 nm		4.4 nm	
Ti site	Number	%	Number	%	Number	%	Number	%
Ti_{4c}	20 [19]	19.8 [18.8]	36	16.1	53	13.3	106	8.4
Ti_{5c}	20 [21]	19.8 [20.8]	43 [49]	19.2 [22.0]	69 [65]	17.3 [16.3]	159	12.6
Ti_{6c}^{sup}	20	19.8	28 [24]	12.6 [10.8]	72 [75]	18.0 [18.8]	157	12.4
Ti_{6c}	29	28.7	96 [94]	43.1 [42.1]	181 [182]	43.4 [45.6]	791	62.5
$Ti_{3c}OH$	8	7.9	8	3.6	16	4.0	20	1.6
$Ti_{4c}OH$	4	4.0	12	5.4	8	2.0	32	2.5

Concerning the number of different Ti species on the **NS** models, reported in Table 3.10, the data for DFTB and DFT(B3LYP) optimized structures show a good agreement, for the larger **NS**s with surface-to-bulk ratio ≤ 1. Therefore, we may conclude that the DFTB method is able to describe the connectivity within the various NSs with the accuracy of DFT.

Besides the connectivity, the DFTB methodology is even capable to accurately reproduce the atomic positions in the **NS**, since the maximum deviation with respect to the DFT(B3LYP) geometry is in the order of 0.5 Å, as shown in Figure 3.19 for the 2.2 nm model. Similar results are obtained for the 1.5, 3.0 and 4.4 nm spherical nanoparticle models.

Differently from the analogous table in Section 3.3.2, the number of Ti species bound to an OH group is much lower, due to the dehydration step during the building of the models. Furthermore, one may note that, as the size of the nanosphere increases, the percentage of $Ti_{3c}(OH)$ and $Ti_{4c}(OH)$ species, needed to saturate the highly undercoordinated surface Ti atoms, decreases. As one would expect, the number of surface atoms (Ti_{4c}, Ti_{5c}, Ti_{6c}^{sup}) grow roughly quadratically with the radius of the **NS** (since the **NS** surface area is proportional to r^2), whereas bulk Ti_{6c} species grow as

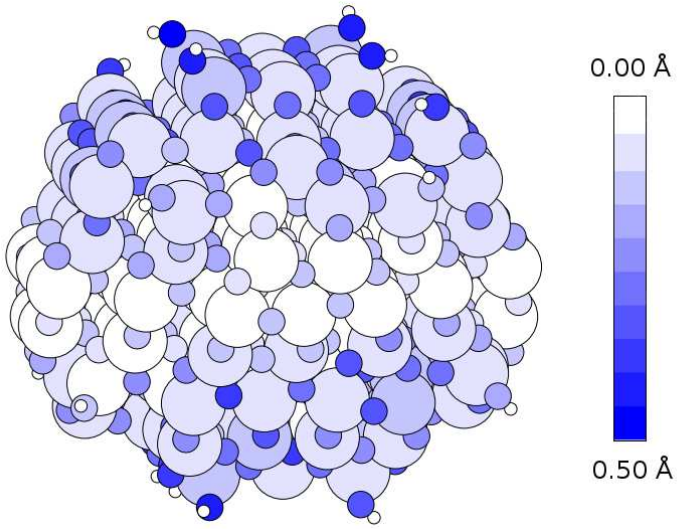

Figure 3.19 – Absolute deviation of the atomic positions between the DFT(B3LYP) and DFTB 2.2 nm spherical nanoparticle models. Atoms are represented by spheres colored according to the absolute deviation, which is color-coded as indicated by the legend on the right. Large, intermediate and small spheres are used for titanium, oxygen and hydrogen atoms, respectively.

the third power of the size (since the **NS** volume is $\propto r^3$). Consequently, approaching the bulk limit, the ratio between surface and bulk atoms clearly tends to zero.

Finally, due to the fact that the 2.2 nm **NS** is the smallest with surface-to-bulk ratio below the value of 1 (see Figure 3.17), we will use it in the next sections as the reference system for further analysis.

Simulated EXAFS

In order to investigate in detail the effect of cutting a spherical surface on the local geometrical environments, we systematically analyze bond lenght modifications with respect to bulk values for the annealed nanospheres using simulated EXAFS spectra, similarly to what has been done for "as-carved" **NC** and **NS** models in Section 3.3.3. The spectra obtained with DFTB and DFT(B3LYP) for the 2.2 nm **NS** as a function of the target temperature are reported in Figure 3.20.

Analogously to Figure 3.6 in Section 3.3.3, the lines shown in the top panels of Figure 3.20 [(a) for SCC-DFTB and (f) for DFT(B3LYP)] are assigned to different coordination spheres of the central Ti atom in bulk anatase TiO_2: the first two lines represent the first coordination sphere, where the Ti–O_{eq} and Ti–O_{ax} bonds are slightly different in a D_{2d} point symmetry (DFTB: Ti–O_{eq} = 1.955 Å and Ti–O_{ax} = 1.995 Å, DFT(B3LYP): Ti–O_{eq} = 1.946 Å and TiO_{ax} = 2.000 Å); then the third and fourth lines (second coordination sphere) are the distances between the

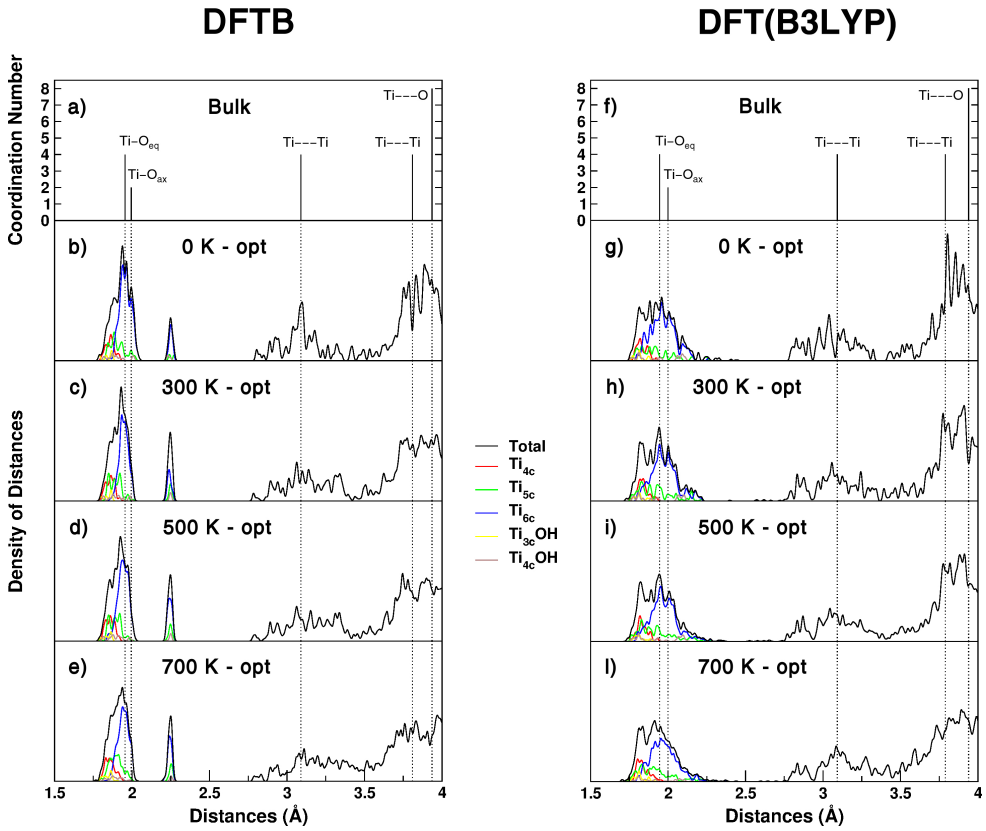

Figure 3.20 – Simulated EXAFS spectra computed with DFTB and DFT(B3LYP) for bulk anatase (top panel (a), (f)), computed with DFTB for 2.2 nm **NS**s produced at different temperature 0 K (b), 300 K (c), 500 K (d), 700 K (e) and computed with DFT(B3LYP) at 0 K (g), 300 K (h), 500 K (i), 700 K (j).

selected central Ti atom and the next-neighboring Ti atoms (Ti$\cdots$Ti) of 3.090 Å and 3.809 Å in the DFTB structure, and 3.092 Å and 3.789 Å in the DFT(B3LYP) one, respectively; finally, the fifth line (third coordination sphere) is the distance between the central Ti atom and O atoms in the third shells (Ti$\cdots$O) of 3.936 Å for DFTB and of 3.939 Å for DFT(B3LYP), respectively.

With respect to the bulk lines, both for the DFTB and DFT(B3LYP), the simulated EXAFS spectra of the nanoparticles show the same qualitative features already discussed in Section 3.3.3 regarding the contributions of the first coordination peak and the position of the Ti$\cdots$Ti and Ti$\cdots$O distances. More interesting in this case is the effect of the target temperature employed for the simulated annealing process: the higher the target temperature, the larger is the broadening of the distribution of distances peaked around the Ti–O_{eq} and Ti–O_{ax} values in the first coordination sphere; furthermore, the contribution of the Ti_{6c} species (blue line) decreases, whereas the

ones from undercoordinated Ti atoms slightly increases. This causes a gradual increment of the population of Ti–O distances around 1.75 Å, which is accompanied with a clear broadening and elongation of the Ti$\cdots$Ti distances in the second coordination sphere. This corroborates what concluded in Section 3.3.3 using the "as-carved" nanospheres about the shrinking of Ti–O distances and the elongation of the Ti$\cdots$Ti, in more evident agreement with the experimental results. [191]

As regards the comparison between the DFTB and DFT(B3LYP) results, we noticed a finer description of the distances in the latter case, in particular the DFT-(B3LYP) structure present a broad and continuous distribution of the Ti–O distances, in the first coordination sphere, that are longer than the Ti–O_{ax} one. In the DFTB spectra, they tend to gather at the same value of about 2.25 Å. In other words, the DFTB optimized **NS** models correctly contain some Ti–O bonds that are longer than 2.05 Å, but, differently from DFT, their equilibrium distance tends to be always about the same ($\sim$2.25 Å). This most likely comes from the DFTB definition of the total energy in Eq. 2.53, which is composed by a repulsive and an attractive term: on the one hand, the pairwise repulsive potential (see Figure 3.21) is exactly the same for all Ti–O pairs, steeply descending until 2.25 Å, where it is almost zero; on the other hand, the attractive term is continuously decreasing with the Ti–O distance until, in the range between 2.05 and 2.25 Å, it is not large enough to compensate for the repulsive term. Consequently, Ti–O bonds longer than 2.25 Å are not favored because of a smaller attractive term and a flat repulsive one, whereas Ti–O bonds shorter than 2.25 Å are not favored because the attractive term is smaller than the repulsive one (at least in the range between 2.05 and 2.25 Å). Clearly, this discrepancy for distances longer than 2.05 Å is a limitation in the description of the fine structural details of the nanoparticles by DFTB method. However, it is not that severe and it will only have a small effect on the electronic structure, as will be discussed below.

Surface Energies

Analogously to "as-carved" **NC**s and **NS**s, we report in Table 3.11 the Connolly surface S_{Conn} and surface energy γ_{Conn} for each globally optimized nanosphere at DFTB and DFT(B3LYP) level of theory.

We observed that, on one side, the Connolly surfaces (S_{Conn}) are very similar for **NS** models optimized with the two methods, in particular the DFT ones are slightly lower than with DFTB. On the other side, DFTB tends to overestimate surface energies ($E_{NP}^{surface}$ in Eq. 3.7), thus resulting γ values are overestimated by approximately 0.5 J/m^2 with respect to the DFT ones.

An interesting result is that with both methods the surface energy does not dependent on the size of the nanosphere. This is due to the compensation of two factors. On the one hand, the larger is the nanoparticle, the lower is the relative amount of highly undercoordinated superficial atoms (see Table 3.10) and so the surface energy should decrease. However, on the other hand, the water molecules we used to saturate the very low coordinated sites (Ti_{3c} and O_{1c}), or intrinsic water molecules, are more abundant in smaller **NS**s (see the percentage of H_2O molecules per TiO_2 units, $n_{H_2O}/\ n_{TiO_2}$, in Table 3.11). This additional water stabilizes the surface energy compensating the higher amount of highly undercoordinated sites, which results in about

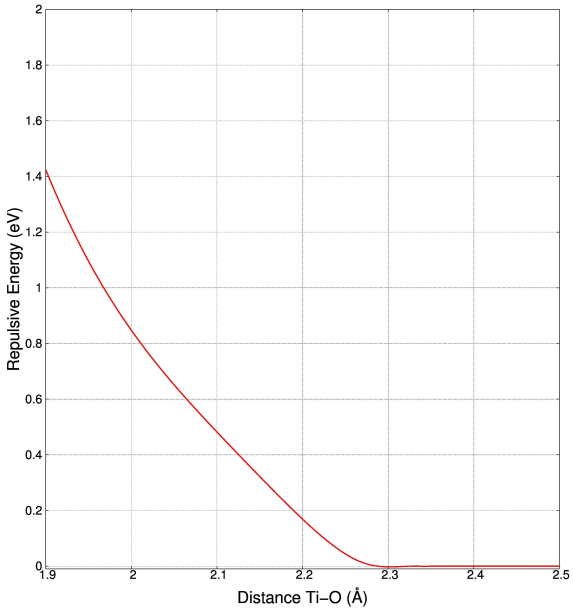

Figure 3.21 – Repulsive potential (E_{rep} in eV) for the Ti–O pair of atoms as a function of the interatomic distance (in Å) in the matsci-0-3 Slater–Koster parameter file.

the same γ_{Conn} for all the **NS**s. A previous work, based on the less accurate force field approach and not considering the intrinsic water, failed in the correct description of the trend of surface energy that was found to increase with the **NS** model dimension. [94]

For a similar reason the surface energy computed for the "as-carved" nanospheres $\mathbf{NS}_S$ and $\mathbf{NS}_L$ in Section 3.3.4 is very similar to the one reported here for dehydrated globally optimized **NS**s, since in the former case there is no stabilizing surface reconstruction but the amount of intrinsic water is higher. In any case, as expected, the surface energy of both "as-carved" and annealed spherical TiO_2 nano-objects is always higher than the one of thermodynamically favored faceted nanoparticles (compare Tables 3.11 and 3.5).

3.5.3 Electronic Structure

Band gaps

In this section we aim, on one side, to evaluate the accuracy of the DFTB method with respect to DFT(B3LYP), in describing the electronic properties of bulk and nanostructured TiO_2. On the other side, we will further analyze the effect of the

Table 3.11 – Connolly surface area (S_{Conn} in nm^2) and surface energy (γ in J/m^2) calculated for different size **NS**s optimized with DFTB and DFT(B3LYP). The number of water molecules per TiO_2 unit is also given. The γ_{Conn} value for the 4.4 nm **NS** is in parenthesis, because it is derived from a partially optimized NS.

NS	1.5 nm		2.2 nm		3.0 nm		4.4 nm	
n_{H_2O}/n_{TiO_2}	5.9 %		4.4 %		3.0 %		2.0 %	
Method	S_{Conn}	γ_{Conn}	S_{Conn}	γ_{Conn}	S_{Conn}	γ_{Conn}	S_{Conn}	γ_{Conn}
SCC–DFTB	13.03	1.23	22.42	1.25	33.13	1.23	70.29	1.27
DFT(B3LYP)	12.76	0.70	22.11	0.72	32.54	0.70	69.48	(0.74)

nanostructuring on the electronic structure, as a continuation of what has been already described in Section 3.4.

As discussed in Section 3.4.1, the band gap is a fundamental property for a material like TiO_2 which finds applications in photocatalysis and photovoltaics. For this reason, many reliable theoretical and experimental data are available for the band gap of this indirect gap semiconductive oxide. In Table 3.12 we reported the DFTB calculated band gap of bulk anatase, together with PBE, [204] PBE0, [70] B3LYP, HSE06, PBE+U [70], G_0W_0 [67] and experimental data measured at temperature close to 0 K. [63]

The band gap obtained with DFTB is in extremely good agreement with the experimental data and Hubbard corrected values, even though it is likely that this is due to error cancellation. [197] As widely known and discussed in Section 2.2.5, GGA methods systematically underestimate band gaps, including the one of anatase TiO_2, while the introduction of some Hartree-Fock exchange in hybrid functionals, such as PBE0, B3LYP or HSE06, provides more accurate values. In particular, band gaps from hybrid DFT methods are slightly overestimated with respect to the experiments, with the HSE06 functional performing better.

Nanoparticles density of states

For the study of the electronic structure of the globally optimized nanospheres, the same considerations already discussed in Section 3.4.1 apply. We distinguish between very localized states (i.e. molecular orbitals, MOs) and states that are delocalized on several atoms of the system (i.e. (pseudo-)band states). Thus, analogously to Section 3.4.1, we defined either the canonical HOMO-LUMO gap ($\Delta E_{H\text{-}L}$) and the Kohn-Sham band gap (E_{gKS}), that is the energy difference between the highest occupied and the lowest unoccupied (pseudo-)band states. However, differently from the "as-carved" nanoparticles, in order to be consistent between the different nanospheres, we employed a more systematic criterion for the definition of the top of the valence (pseudo-)band and the bottom of the conduction one in the calculation of E_{gKS}.

Therefore, we based the definition of a (pseudo-)band state using the maximum squared coefficient ($\max_c = \mathrm{Max}(\{c_i^2\})$) in the linear combination of atomic orbitals (LCAO) for each eigenstate: the first delocalized state, which can be considered a (pseudo-)band state, is the one (in the valence and conduction region, respectively)

Table 3.12 – Bulk anatase TiO_2 electronic band gap (expressed in eV), as obtained from DFTB, standard GGA-DFT, hybrid DFT functionals, GGA-DFT Hubbard corrected (DFT+U), G_0W_0 and experiments.

Method	Band Gap
DFTB this work	3.22
B3LYP this work	3.81
HSE06 this work	3.65
PBE [204]	2.36
PBE0 [70]	4.50
PBE+U [70]	3.27
G_0W_0 [67]	3.83
Exp. [63]	3.4

with a $\max_c$ lower than a threshold of 0.02. In such a way, E_{gKS} is rigorously defined and values for different **NS**s and for different methods can be compared.

Table 3.13 – HOMO-LUMO energy gap ($E_{H\text{-}L}$) and Kohn-Sham electronic gap E_{gKS} (in eV) calculated for different size **NS**s with both DFTB and DFT(B3LYP) approaches.

	$\Delta E_{H\text{-}L}$		E_{gKS}	
NS	DFTB	DFT (B3LYP)	DFTB	DFT (B3LYP)
1.5 nm	3.12	4.23	3.62	4.81
2.2 nm	3.11	4.13	3.55	4.31
3.0 nm	2.95	4.00	3.42	4.13
4.4 nm	2.95	3.90	3.33	3.96

We will first analyze the $\Delta E_{H\text{-}L}$ gaps in Table 3.13. The value of the HOMO-LUMO gap gradually reduce with the size, with the DFT(B3LYP) values being always about $\sim$1.0/1.2 eV higher than the DFTB ones. Most of this difference can be attributed to the intrinsic difference in the prediction of the bulk anatase band gap between the two methods (see Table 3.12) of about 0.6 eV. In addition to this, there is also a significant contribution due to the different equilibrium geometry obtained with the two methods, discussed in Section 3.5.2, which affects the position of the frontier orbitals of the nanospheres associated within the Kohn-Sham band gap, as will be detailed with the analysis of the density of states. As a matter of fact, those states are slightly shifted from the edges of the valence band or the conduction band into the gap, leading to a smaller $\Delta E_{H\text{-}L}$.

As regards Kohn-Sham band gap E_{gKS}, increasing the **NS**s size, its value smoothly decreases approaching the bulk value. Again, the discrepancy between DFTB and DFT(B3LYP) energy gaps can be ascribed to an intrinsic difference and a geometric

factor. Interestingly, even for the larger 4.4 nm nanosphere, the band gap is wider by ∼0.1 eV than in bulk anatase. In fact, on the basis of solid state physics, the quantum confinement effect in a particle with size D causes an increase ΔE_g of the band gap according to the Brus equation: [205]

$$\Delta E_g \approx \frac{2\hbar^2\pi^2}{D^2}\frac{1}{\mu} - \frac{3.6e^2}{\epsilon D} \tag{3.12}$$

where μ is the effective mass of the photoexcited charge carriers (the electron and the hole), ϵ is the dielectric constant. For anatase nanoparticles in the range between 3 and 5 nm, this has been proven experimentally, as reported by Reddy et al. [206] and Liu and collaborators, [200] who measured a band gap enhancement in the order of 0.1-0.2 eV, in line with our DFT and DFTB predictions.

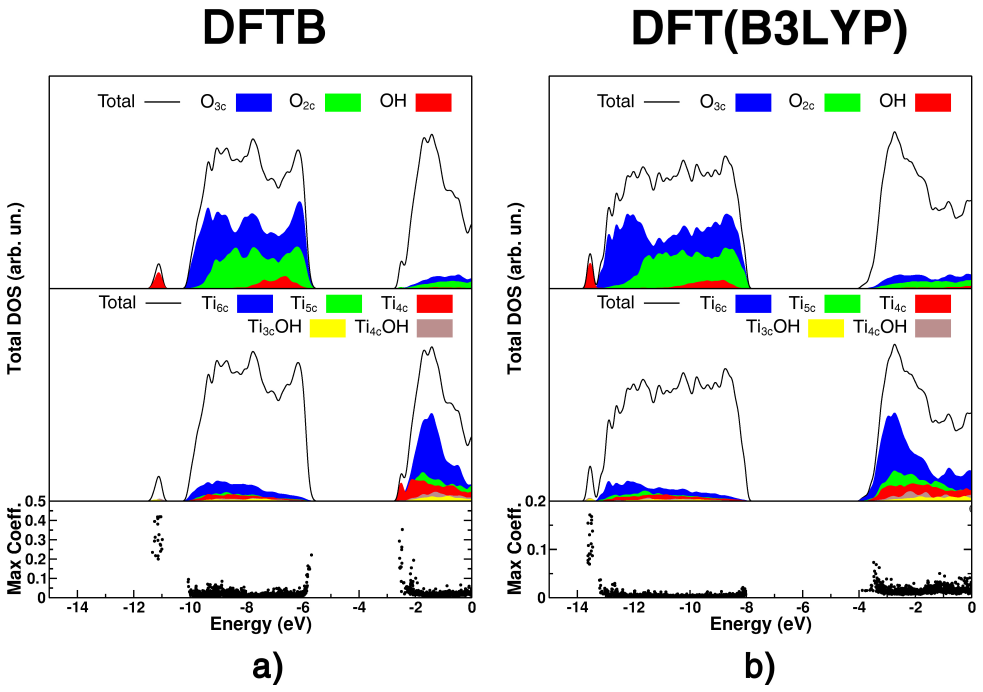

Figure 3.22 – (a) DFTB, (b) DFT(B3LYP) total (DOS) and projected (PDOS) density of states on different coordinated O (upper panel) and Ti (middle panel) atoms of the nanosphere. In the lower panel, the maximum atomic orbital squared coefficients ($\max_c$) of each eigenstate is reported. High values of $\max_c$ indicates localized states while low values correspond to delocalized states.

In Figure 3.22, the DFTB and DFT(B3LYP) total (DOS) and projected (PDOS) densities of states (PDOSs) are reported for the globally optimized 2.2 nm **NS**, along with the value of $\max_c$ for each eigenstate in the DOS.

The features of the DFT(B3LYP) projected density of states in Figure 3.22b are similar to the one already reported in Section 3.4.3 for the corresponding "as-carved"

$\mathbf{NS}_S$ nanosphere, as regard to the main contributions to the valence and conduction band and the detached band of the hydroxyl groups at about –14 eV. An evident difference from the PDOS of the "as-carved" in Figure 3.13 is the strongly reduced component by the OH groups in the valence band, due to the minimal content in water. In such a way, one can clearly observe that the top of the valence band is composed by the 2p orbitals centered on the surface O_{2c}. Instead, the bottom of the conduction band is again made by the d_{xy} orbitals of the Ti_{6c} species, without any influence from the removal of intrinsic water.

The DFTB description of the valence band is consistent with the DFT(B3LYP), except from the fact that the eigenstates at band edge are much more localized (max_c between 0.25 and 0.1) with respect to the DFT(B3LYP) (max_c between 0.1 and 0.02) Regarding the conduction band in the DFTB case, this method tends to overstabilize the states on the Ti_{4c} to the conduction band minimum, in contrast with the DFT(B3LYP) case, where these eigenstates are higher in energy. Besides this notable exception, the DFTB conduction band projections are in good agreement with the DFT(B3LYP) ones.

In Figure 3.23, we report all the total DOS for nanospheres under study, as obtained with both the DFTB and DFT theoretical approaches. Considering the values of max_c from the DFTB calculations, we can confirm the trend of overlocalization of the states at the edge of the band gap for all the **NS**s with respect to DFT(B3LYP). Interestingly, it is worth mentioning that, as the nanosphere size increases, the DFTB description is more and more similar to the DFT(B3LYP) one, since the DOS starts to approach the one of bulk TiO_2.

Furthermore, from this considerations and the shape of DOSs in Figure 3.23, one can find further support, besides the EXAFS analysis in Section 3.5.2, that the DFTB structural description of the TiO_2 **NS**s improves as the dimension of the nanospheres increases. The larger the nanosphere, the less curved is the surface and the more accurate is the description.

3.6 Conclusions

To sum up, in this chapter we have presented a density functional study of the ground state properties of realistic models of faceted and spherical TiO_2 nanoparticles (TiO_2 NPs). Not only different shapes but also different sizes have been considered.

Firstly, the NP models have been built by carving a certain shape from bulk anatase and then saturating highly undercoordinated surface species with hydrogen atoms. The generated small ($\mathbf{NC}_S$) and large ($\mathbf{NC}_L$) nanocrystals are $(TiO_2)_{159} \bullet 4\ H_2O$ and $(TiO_2)_{260} \bullet 6\ H_2O$, respectively; while the small ($\mathbf{NS}_S$) and large ($\mathbf{NS}_L$) nanospheres are $(TiO_2)_{223} \bullet 26\ H_2O$ and $(TiO_2)_{399} \bullet 32\ H_2O$, respectively.

Nanoparticles surfaces and volumes have been computed with the Connolly algorithm, which allows for the direct comparison of differently shaped nanoparticles. Noteworthy, the surface area of a nanocrystal of analogous size of a nanosphere (similar equivalent diameter D_{Conn}) is comparatively larger. As regards surface morphology, nanocrystals are particularly rich of Ti_{5c} species, whereas nanospheres present a broader variety of undercoordinated sites, especially highly reactive 4-fold coordinated

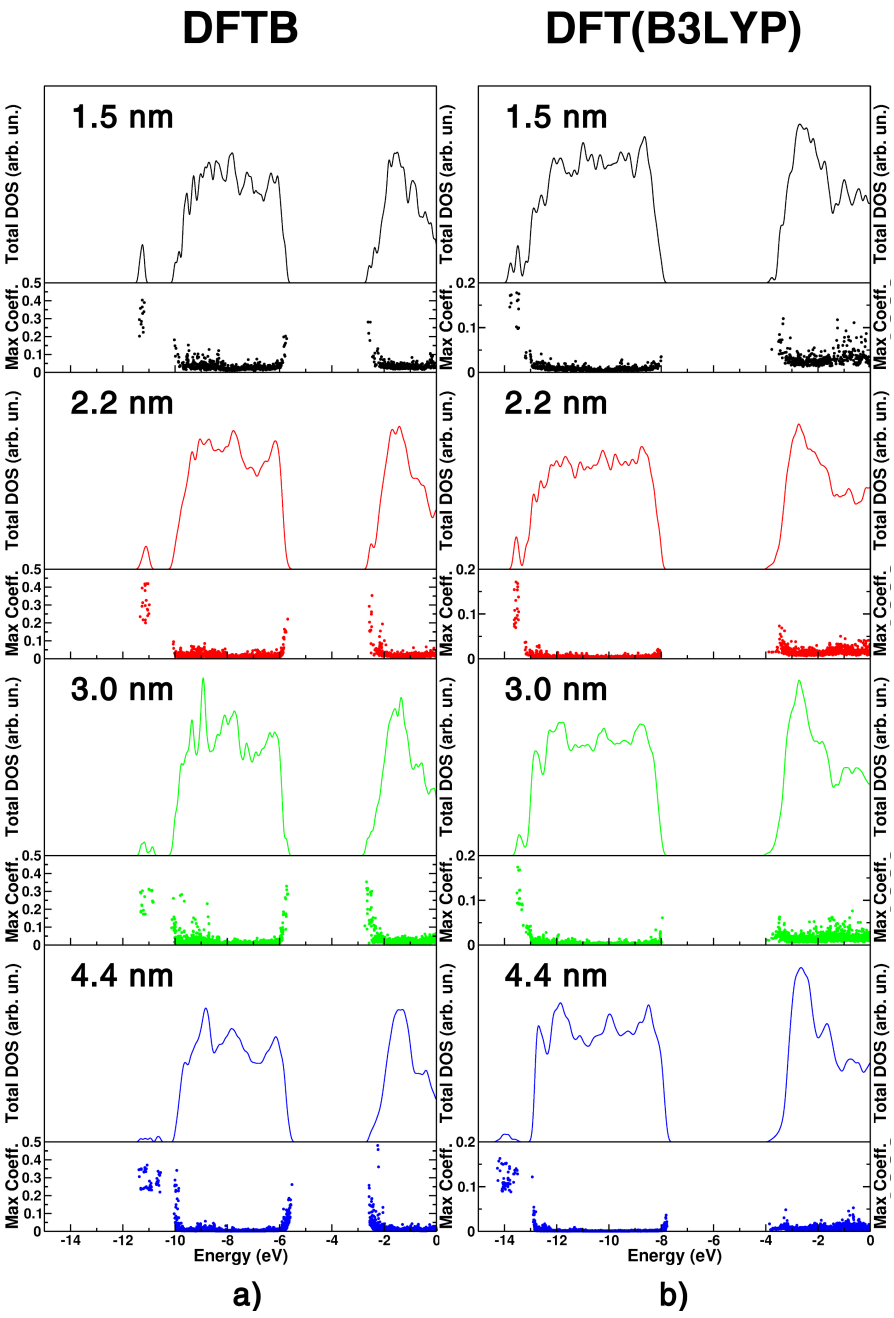

Figure 3.23 – a) DFTB and (b) DFT(B3LYP) total (DOS) density of states for different size nanospheres, 1.5 nm (black), 2.2 nm (red), 3.0 nm (green), 4.4 nm (blue). For each **NS**, the DOS has been normalized to the number of TiO_2 units, to allow the comparison between them. Below each DOS, the squared maximum LCAO coefficient (max_c) of each eigenstate, as a function of the energy, is also graphically shown. High values of max_c correspond to highly localized states, while low values correspond to delocalized states.

ones. Structural distortions of the Ti–O bonds in the nanoparticles have been systematically analyzed by simulated direct-space EXAFS spectra. The peak corresponding to the first coordination sphere is broader for nanospheres than for nanocrystals, confirming a wider variety of undercoordinated species and a more disordered surface for the former. As expected, the larger the nanoparticles size, the more the peaks in the EXAFS spectra approach the bulk system reference lines. The computed surface energies for nanocrystals are higher than for the regular (101) surface, due to edge and corner defects. The ones of the nanospheres are even higher, because of the higher density of undercoordinated sites.

As it is true for all finite molecular systems, also in the case of anatase TiO_2 nanoparticles, Kohn-Sham gaps consistently differ by about 1.5 eV from fundamental gaps obtained from the difference between ionization potentials and electron affinities, as a consequence of the non-zero derivative discontinuity of the exchange-correlation potential.

Secondly, in order to model the structural reconstruction of spherical nanoparticles, we have performed a global optimization procedure (simulated annealing) of TiO_2 nanospheres of increasing diameter (from 1.5 to 4.4 nm) with a minimal amount of intrinsic water. These systems contain between 300 to 4000 atoms, thus the global optimization task is not feasible at the DFT level. For this reason, we employed the computationally efficient SCC-DFTB approach, whose results were also compared to the DFT(B3LYP) ones with the aim to validate this approximate method for titania nanosystems.

The temperature annealing processes lead to structures which are more stable than the original as carved ones. The energy gain in stabilization observed with SCC-DFTB is confirmed by following DFT(B3LYP) optimizations.

Surface energies of the globally optimized nanosphere models are found to be still higher than the ones of faceted nanoparticles. Interestingly, they are not dependent on the **NS**s size, both with SCC-DFTB and DFT(B3LYP) methods, which means the increased cost to make smaller nanosphere is nicely balanced by the increased relative amount of intrinsic dissociated water on the surface.

From the structural point of view, we observed that SCC-DFTB can accurately describe the core part of spherical nanoparticles, with small inconsistencies for some atomic distances at the surface with respect to DFT(B3LYP). The larger the **NS**, the smaller the relative number of surface atoms with respect to core ones. Therefore, SCC-DFTB is progressively more accurate at increasing size.

In conclusion, the detailed analysis, presented in this chapter and briefly summarized above, demonstrates that faceted and spherical nanoparticles present different structural and electronic properties. Moreover, we proved that SCC-DFTB method is a reliable quantum mechanical approach to investigate TiO_2 nanosystems and their structural rearrangements, especially for large systems.

4 Photoexcited Carriers Recombination and Trapping in Anatase TiO_2 Nanocrystals versus Nanospheres

In this chapter,[†] the real-size models for faceted and spherical TiO_2 nanoparticles presented in the previous chapter are employed to investigate the effect of size and morphology and the interaction with water on the life path of energy (excitons) and charge (electrons and holes) carriers by means of hybrid density functional theory calculations.

First, we focus our attention on the photoexcited electron/hole pair formation, separation and radiative recombination in vacuum. Secondly, we analyze the self-trapping processes of separated charges on the different regions of the nanoparticles, in terms of structural distortions, energy gain or cost, charge localization/delocalization and electronic transitions of the trapped electrons or holes.

Lastly, the effect of the water environment on the hole trapping ability of faceted and spherical TiO_2 nanoparticles will be studied in detail with a combined theoretical and experimental approach, in collaboration with experimental research groups in Japan.

4.1 Introduction

Titanium dioxide is still considered the reference material in the modern fields of photocatalysis, photoelectrochemistry and photovoltaics. For the application of TiO_2 in these fields, it is extremely important to understand the processes at the basis of the irradiated light energy conversion into chemical species with intrinsic redox potential. Due to confinement effects or peculiar surface defectivity, these processes may be characterized by shorter or different time scales in nanoparticles, leading to distinctive

[†]The results described in this Chapter have been reported in: G. Fazio, L. Ferrighi, C. Di Valentin, *Nano Energy* **2016**, *27*, 673–689; K. Shirai, G. Fazio, T. Sugimoto, D. Selli, L. Ferraro, K. Watanabe, M. Haruta, B. Ohtani, H. Kurata, C. Di Valentin, Y. Matsumoto "Water-assisted hole trapping at highly curved surface of nano-TiO_2 photocatalyst" *J. Am. Chem. Soc.* **2018**, *140*, 1415–1422.

properties with respect to the extended systems, which may be very interesting for the research community involved in the study and application of nanomaterials.

When a semiconductor material interacts with light, an exciton, i.e. a Coulomb interacting electron/hole pair, is initially formed. [207, 208] The size of the as-formed exciton depends on the dielectric constant of the material and the effective masses of the excited electron and hole. [209] When the exciton strongly couples with lattice vibrations, it may become self-trapped in the lattice, [210] largely reducing its mobility. In this respect, the quantum confinement of an exciton in a nanoparticle of few nanometers size may significantly influence its dimension and localization. [211] Furthermore, it is still an open and critical question whether the close presence of surface defects, such as the ones related to the curvature in nanospheres or facets, edges and corners in nanocrystals, may accelerate the process of excitons separation into electrons and holes or for different reasons, may promote the electron/hole recombination through a strong exciton self-trapping process. [212] Therefore, one may expect that the dynamics of the exciton can be different in spherical with respect to faceted nanoparticles where the surface is mostly composed of flat facets.

Another fundamental question concerns the effect of the aqueous environment, where the photocatalysts are normally employed, on the charge carriers dynamics. Water may be involved in charge trapping process, affecting the overall charge carriers life path. In particular, the rate-determining step in the photocatalytic process is the oxidation of molecules at the surface of the photocatalysts where long-living photogenerated trapped holes play a crucial role. [213] Furthermore, hole trapping enables electrons to live longer, promoting also the reduction reactions. Recent experimental works based on EPR [214] and time-resolved infrared spectroscopy [215] showed that water adsorbates are able to stabilize surface trapped holes and prevent the charge carriers recombination. Nevertheless, the role of interfacing water in charge trapping dynamics is still unclear [125, 126], since most of the experimental studies have been performed either in an ultrahigh vacuum or in an aqueous environment. Bridging the gap between these two experimental conditions is necessary to get a molecular level understanding of the effect of water and clarify how the interaction with water influences the carrier dynamics for designing better TiO_2–based photocatalysts.

The theoretical modeling of all these complex aspects requires the recourse to sophisticated ab initio methods. Spin-polarized density functional theory (DFT) is a viable approach for the large systems under study, since it provides an accurate description at a reasonable computational cost. However, the self-interaction issue present in DFT methods is a severe problem for the correct description of the energetic and degree of localization/delocalization of self-trapped excitons or electrons and holes. [216–219] To this end, some self-interaction correction is necessary as it is present in the more costly hybrid density functional approaches.

In the following, we will first investigate by means of hybrid density functional calculations the life path of light-induced energy carriers (excitons) or charge carriers (electrons and holes) in anatase TiO_2 nanoparticles models, from the exciton formation to the recombination of the photogenerated charge carriers or their trapping. In addition, several relevant quantities have been computed, such as exciton self-trapping energies, photoluminescence emission energies, energy gain associated to charge carrier separation, electron and hole self-trapping energies, EPR parameters and optical

transitions of the self-trapped charges. All these quantities are directly comparable to the experimental data from photoluminescence (PL) measurements, electron paramagnetic resonance (EPR) and transient absorption (TA) spectroscopy. The aim of this part of the work is to get a molecular insight into the processes involving energy (excitons) and charge (electrons and holes) carriers in TiO_2 nanoparticles of various size and shape, given that, as discussed in Section 1.3, the existing literature is still mostly focused on TiO_2 extended model systems, whereas the technological applications are usually based on TiO_2 nanoparticles or nanostructured TiO_2 materials. This part of the study evidences clear trends with size and shape, which can be rationalized in terms of structural distortions of the nanoparticles due to the nanosize.

Secondly, we have tackled the complex problem of the role of water in the charge carrier dynamics through a combined theoretical and computational work. On the one hand, we investigated the adsorption of water and its effect on the hole trapping abilities of TiO_2 nanoparticles with different morphologies through large scale ab initio calculations. On the other hand, in collaboration with experimental groups in Japan led by prof. Yoshihasu Matsumoto from Kyoto University, we compare our theoretical results with steady and transient infrared spectra of TiO_2 nanospheres and nanocrystals, where the water coverage has been gradually increased in a controlled manner. Through this two–dimensional approach, we clearly demonstrate that a hydroxyl group at the curved surface of a spherical TiO_2 nanoparticle is able to trap an electron hole and its trapping ability is significantly enhanced by the adsorption of additional water molecules.

This chapter is organized as follows: first, the computational methods of the calculations (Section 4.2) will be detailed; then the discussion will concern the exciton formation, trapping and recombination (Section 4.3) and the behaviour of the separated photoexcited charge carriers (Section 4.4), together with the relevant experimental data as a reference; finally, the combined theoretical and experimental study on the effect of water adsorption on the hole trapping will be presented (Section 4.5).

4.2 Computational Details

In this section, we will specify the computational methods, the models and the settings that have been used for the calculations presented in this Chapter. For a detailed discussion on the theoretical approaches see Chapter 2.

All the CRYSTAL14 calculations have been performed employing the same computational settings as in Section 3.2, as regards the functionals (B3LYP and HSE06), the basis sets, the thresholds for convergence of the SCF and geometry optimization, as well as the calculations of ionization potentials and electron affinities. However, in this case, the standard B3LYP functional, which has been demonstrated in the previous chapter to provide results similar to the HSE06 potential, will be mainly used.

The TiO_2 anatase bulk was modeled by a large $6\sqrt{2}\times6\sqrt{2}\times1$ bulk supercell with 864 atoms. The k-space sampling for the bulk geometry optimization included a $1\times1\times6$ Monkhorst-Pack net. [132]

Flat anatase crystallographic surfaces were modelled with a three triatomic layers

slab with 108 atoms and a 1×3 periodicity along the [10-1] and [010] directions for the (101) surface and a four triatomic layers with 96 atoms and a 4×2 periodicity along the [100] and [010] directions for the (001) surface; no periodic boundary condition was imposed in the direction perpendicular to the surface. These slab models have been used only to compute the vibrational structure of water adsorbates on the (101) and (001) and hole trapping stabilities on the (001), whereas we have employed the faceted nanoparticle model ($\mathbf{NC}_L$, vide infra) for the calculations of water adsorption. For the k-point sampling of the Brillouin zone, we employed a Monkhorst-Pack net: a $2 \times 2 \times 1$ and a $1 \times 2 \times 1$ mesh ensured convergence of the electronic structure for the (101) and (001) slab models, respectively.

Concerning the models for the nanocrystals, we employed either the small ($\mathbf{NC}_S$, $(TiO_2)_{159} \bullet 4\ H_2O$) and the large ($\mathbf{NC}_L$, $(TiO_2)_{260} \bullet 6\ H_2O$) faceted nanoparticles described in the previous chapter. As regards the spherical nanoparticle model, we mostly used only the 2.2 nm "as-carved" nanosphere (**NS**) in Figure 3.16b with a stoichiometry of $(TiO_2)_{223} \bullet 18\ H_2O$. In one case we carried out calculations also on the larger 3.0 nm nanosphere $(TiO_2)_{223} \bullet 32\ H_2O$ ($\mathbf{NS}_L$ in Figure 3.3).

For the study of water adsorption, vibrational structure and hole trapping on the **NS** model in Section 4.5, we performed a preliminary global optimization procedure to avoid that the structural changes related to water adsorption trigger the nanosphere to relax to another local minimum. Thus, we run a simulated annealing process using the same computational setting based on SCC-DFTB detailed in Section 3.2, with target temperatures of 300 K, 500 K and 700 K. Among the nanospheres obtained after the global optimization, the most stable one is the one annealed at 700 K, that was then further optimized again with the DFT(B3LYP) method.

The binding energies for water molecules on the nanoparticles are defined as the difference between the total energy of the final product of adsorption and the total energy of the isolated systems, i.e. an isolated water molecule and the isolated nanoparticle. Note that, in the case of dissociative mode of water adsorption, the two fragments resulting from the dissociation, i.e. OH and H, were put on opposite sides of the nanoparticles, in order to avoid any spurious interaction effect.

Similarly to the previous chapter, nanoparticles have been treated as large isolated molecules in the vacuum without any periodic boundary conditions. Thus, when an excess charge is introduced in the system, no background of charge is needed. Spin polarization is considered in the case of systems with unpaired electrons. No symmetry constraints were imposed during the geometry optimization run.

Trapping energies (ΔE_{trap}) are defined as the total energy difference between the isolated charge carriers or electron-hole couples in the trapping geometry and the delocalized solution, obtained using the neutral ground state geometry. Distortion energies (ΔE_{dist}) are computed as the difference in total energy between the neutral system in the trapping geometry and the neutral ground-state minimum of that nanoparticle.

In the case of calculations with a different number of atoms, e.g. two nanoparticles with a different number of water molecules adsorbed, a common reference energy is needed to compare charge trapping abilities. Thus, the stability of a hole trap on the surface of the nanoparticles has been computed as the total energy difference between the system with a hole localized on the surface site and the same system with a hole

localized on the innermost O_{3c} atom of the nanoparticle, which has been considered as the reference hole trap.

For molecular systems, vibrational frequencies in the harmonic approximation for an energy minimum structure have been computed by numerical differentiation of the forces. [220, 221] We used a two point formula for the differentiation with 0.003 Å as step. In the case of systems with periodic boundary conditions, second-order derivatives of the total energy are evaluated at Γ point. Furthermore, only for frequency calculations, the convergence threshold on the SCF cycle has been lowered to 10^{-9} a.u., in order to improve the numerical accuracy. All the computed frequencies have been scaled with a scale factor defined as the ratio between the experimental [222] and calculated value for the symmetric stretching mode of a water molecule in gas phase.

The Gaussian09 code [223] was employed to calculate EPR parameters, i.e. g, hyperfine and nuclear quadrupole tensors, for the $(TiO_2)_{29} \bullet 4\ H_2O$ cluster with an excess hole. For these calculations the well-suited EPR-II basis set was used for O and H atoms, whilst for Ti atoms we employed a 6-311+G* basis set when first neighbor to an oxygen atom where the excess hole is trapped and a 6-31G* basis set otherwise.

Simulated total (DOS) and projected (PDOS) densities of states of the nanoparticles have been obtained through the approach described in Section 3.4.3, using a value of 0.001 eV for the σ of the Gaussian peaks in the convolution. In the case of spin polarized systems, (projected) densities of states are computed using the Kohn–Sham eigenvalues of alpha or beta population separately. The reference zero energy for all the DOS is set to the vacuum level, which corresponds to the energy of an electron at an infinite distance from the surface of the nanoparticle.

Electronic transitions from trapping levels to the conduction band or from valence band to trapping levels are estimated by means of the transition level approach, described in Section 2.2.5.

The 3D plots of the bond lenght distortions have been generated by Python scripting on the POV-Ray [224] file. The procedure is the following: first, a raw POV-Ray file, where a single layer or the whole nanoparticle is represented by ball-and-sticks, is generated by the CCDC Mercury program [225]; second, for each cylinder, which represents a Ti–O bond, the difference between the Ti–O distance and the reference is calculated; finally, the color of the cylinder is assigned according to this difference and the reference color-coding.

4.3 Free/trapped exciton and recombination

4.3.1 Experimental background

When, upon irradiation, the photoexcited charges are formed within titanium dioxide, they may radiatively recombine and emit a photon with an energy lower than the absorbed one. This photoluminescence (PL) phenomenon has been observed in anatase single crystals by several experimental works [226–228], which measured a broad band at ∼2.3 eV with a full width of 0.6 eV, assigned to radiative recombination of a self-trapped exciton (STE) localized on a TiO_6 octahedron. Furthermore, a tail of the photoemission band down to 2.0 eV and beyond is often observed. Due

to the competition with non-radiative recombination processes, the intensity of this emission decreases with increasing temperature. The activation energy of this processes is ∼50 meV, [229] thus at room temperature the photoluminescence is almost quenched.

The broad emission peak can be decomposed into three Gaussian bands, [230] centered at 1.95, 2.15 and 2.40 eV, respectively. The lowest energy band should be closely related to the presence of oxygen vacancies since it is also observed in the emission spectrum obtained at lower excitation energies. The other two emissions were both attributed to the exciton (STE) recombination in bulk anatase.

At a sufficiently low temperature, an analogous self-trapped exciton photoluminescence has been observed in the emission spectra of nanoparticles and nanocrystalline films with primary particles size in the range between 4 to 6 nm, [231] 9 to 27 nm [232] and 20 to 130 nm. [233] No significant changes with respect to the emission of anatase single crystals were reported. Noteworthy, the spectrum does not show any variation with the nanocrystals dimension [231, 232] or environment (dispersed water or deposited on a thin film). [234] On the contrary, the dynamics of the photogenerated charges has been found to be affected by size, because of a higher ratio between surface and bulk states for small nanocrystals, causing a faster transfer of photoexcited charges to surface traps. Therefore, the trapping processes, which quenches the photoluminescence, occurs at lower temperature in ∼5 nm nanocrystals than in bulk anatase. [226, 230]

In addition, only for very small nanoparticles (2-9 nm) a band-edge luminescence was reported at room temperature. [200, 235–237] This emission was attributed to the fast radiative recombination of free (delocalized and non trapped) excitons, which is not observed for larger nanoparticles and bulk systems. [232] Lastly, when present, interstitial Ti^{3+} defects give rise to an additional PL peak at lower energies (∼1.8 eV).

In the following, these experimental observations are discussed in the light of the results from the computational models of bulk anatase and faceted and spherical nanoparticles of anatase TiO_2.

4.3.2 Bulk system

We first present the self-trapped exciton (STE) computed for the bulk anatase system, as detailed in a previous work. [73] The excited state is modeled by approximating that the biradical singlet spin state (S_1 curve in Figure 4.1), which is actually formed during the excitation, with the corresponding triplet state (T_1^{eq} curve in Figure 4.1). The only difference between this two states is the spin of the unpaired electron in the conduction band, which is the same of the one in valence band, hence the two wavefunctions should be very similar except from an additional exchange energy contribution.

As expected, in the vertical triplet state (see Figure 4.1b), that is the triplet excited state in the singlet ground state geometry, the exciton is delocalized over the whole bulk supercell: the photoexcited electron is spread on the $3d$ states of the titanium atoms, whereas the photoexcited hole occupies rows of $2p$ of oxygen, with an oscillating pattern of spin density along each row.

When we allow the geometry of the system to relax, we found that the free exciton

becomes spontaneously self-trapped with the electron mostly localized on a single Ti^{4+} ion, which is reduced to Ti^{3+}, and the hole on the equatorial O^{2-} ion, which is oxidized to O^{-}. Starting from a distorted geometry, it has been possible to localize also another solution which differ from the position of the hole trapping O atom (O^{-} species) with respect to the electron trapping Ti atom (Ti^{3+} species). In fact, this can be either in the equatorial (Ti^{3+}–O^{-}_{eq} in Figure 4.1c) or in the axial (Ti^{3+}–O^{-}_{ax} in Figure 4.1d) position of coordination in the TiO_6 octahedron. The two positions are not equivalent, since the axial Ti–O bond is longer by ∼0.05 Å with respect to the equatorial one, as already discussed in Section 3.3.3.

Furthermore, the trapping energy (see Section 4.2 for the definition of this quantity) of the two excitons differs by 0.1 eV in favor of the axial (−0.59 eV vs −0.49 eV, see Table 4.1). The computed photoluminescence energy associated to the decay of these two different STE is 1.99 eV (Ti^{3+}–O^{-}_{ax}) and 2.35 eV (Ti^{3+}–O^{-}_{eq}), respectively. Assuming that these species are equally probable and that relative abundance of the equatorial species is twice that of the axial one, the average emission energy is 2.24 eV. These computed values are in excellent agreement with the broad experimental feature measured for anatase single crystals and the peak decomposition proposed by Sekiya et al., [230] just described in the previous paragraph and centered at 2.3 eV.

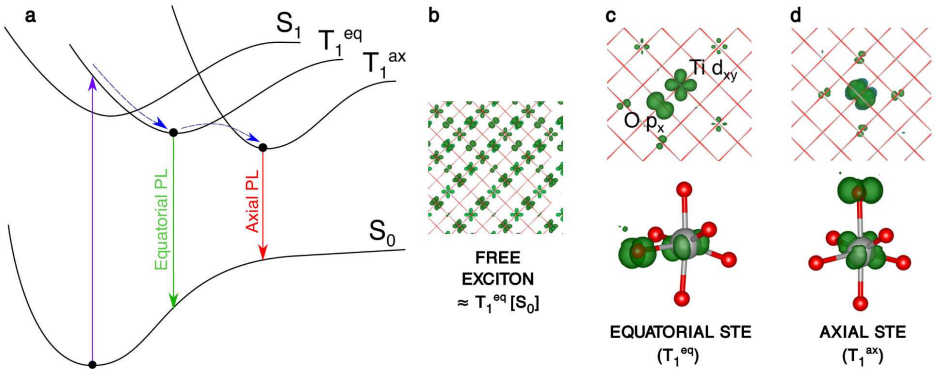

Figure 4.1 – Schematic representation of the processes involving the electron/hole couple: the vertical excitation $S_0 \rightarrow T_1$, the self-trapping relaxation in the bulk structure and the two different photoemissions $T_1^{eq} \rightarrow S_0$ and $T_1^{ax} \rightarrow S_0$. 3D spin density plots of the anatase bulk supercell, as obtained with the B3LYP functional, for the vertical triplet state (b), trapped triplet equatorial (c) and axial (d) exciton in the bulk. The spin density isovalue is 0.01 a.u. (0.0005 a.u. for the vertical triplet).

4.3.3 Nanoparticles

Faceted Nanoparticles

Excitons in nanoparticles may be very different from excitons in the bulk, due to size and/or shape effects. We first present excitons in faceted nanocrystals, considering

the two models of different size designed in Chapter 3: $\mathbf{NC}_S$ with 489 atoms and $\mathbf{NC}_L$ with 798 atoms. These models are shown in Figure 4.2 together with the definition of the main surface sites. In particular, the larger nanocrystal presents an additional (101) layer on four of the eight (101) facets. The comparison between these two nanocrystals will provide information on the effect of size on the excitons.

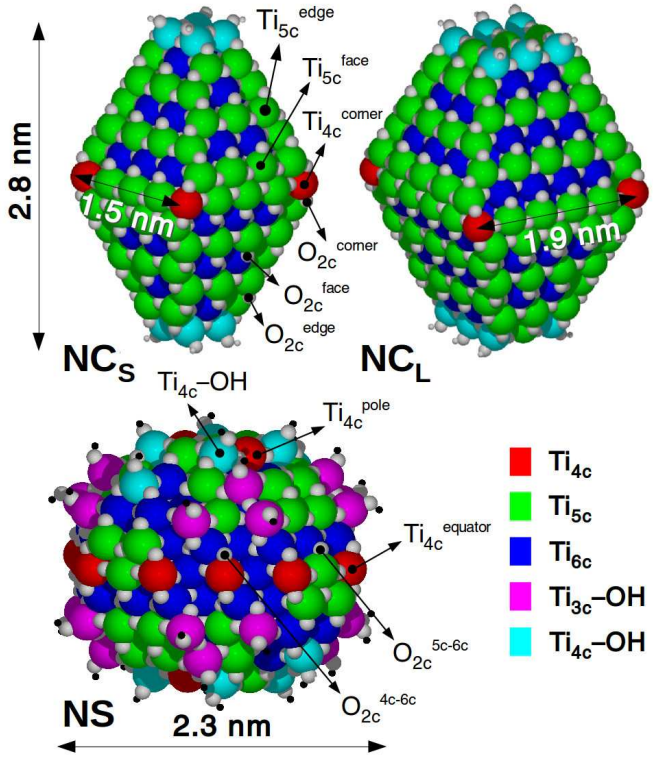

Figure 4.2 – Position of the titanium species with different coordination spheres within the nanoparticle models ($\mathbf{NC}_S$ –$(TiO_2)_{159}$ • 4 H_2O; $\mathbf{NC}_L$ – $(TiO_2)_{260}$ • 6 H_2O; $\mathbf{NS}_S$ $(TiO_2)_{223}$ • 18 H_2O). The coordination number is visually shown by the color coding indicated on the right side. The oxygen and titanium sites that have been considered for charge trapping are labeled as in the tables. Relevant geometric parameter of the nanoparticles are also given.

Analogously to the bulk system, upon excitation of the small nanocrystal ($\mathbf{NC}_S$) a free exciton is formed. Again, this is computationally modeled by calculating the first excited triplet state in the Frank-Condon approximation (i.e. in the ground state geometry), [73] see violet arrow in Figure 4.1. However, in this case, the electron/hole couple (free exciton) is not spread all over the nanoparticle but delocalized in a portion close to the core, see model a in Figure 4.3. Then, if we allow atomic relaxation in the excited state, we may observe the triplet exciton self-trapping (blue arrow in Figure 4.1).

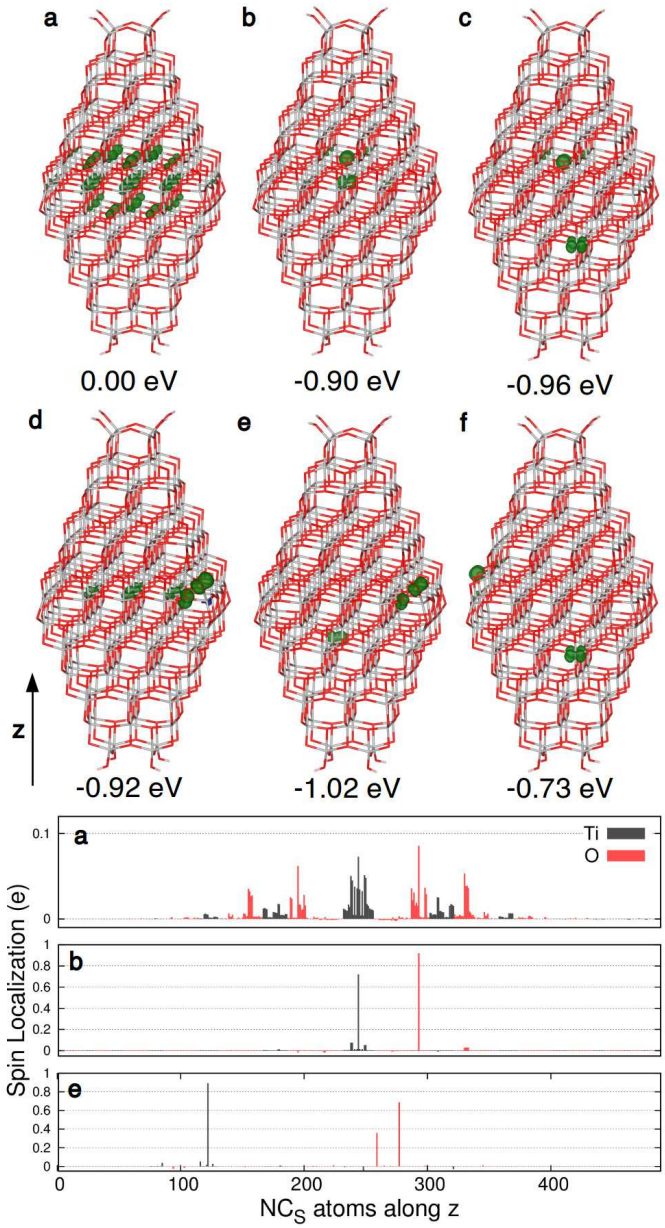

Figure 4.3 – Top panel: 3D spin density plots of $\mathbf{NC}_S$ nanocrystal, as obtained with the B3LYP functional, for the vertical triplet state (a), trapped triplet exciton (axial exciton in Table 4.2, b), triplet state with electron on the surface and hole in the core (c), triplet state with electron in the core and hole on the surface and fully separated charges state with the hole on O_{2c}^{corner} (e) or O_{2c}^{face} (f) and the electron on Ti_{5c}^{face}. The spin density isovalue is 0.01 a.u. (0.002 a.u. for the vertical triplet). Bottom panel: Histogram of the atomic spin on each oxygen or titanium atoms for the a, b and c configurations. The x axis sorts the atoms from bottom to top by their z coordinate.

Table 4.1 – Singlet-Triplet Vertical Excitation Energy $(S_0 \rightarrow T_1)_{vert}$, Trapping Energy ($\Delta E_{trap}$) of the Triplet Exciton and its calculated photoluminescence (PL) in the Axial and Equatorial configuration for bulk anatase as obtained with B3LYP and HSE06 functionals, $\mathbf{NC}_S$ and $\mathbf{NC}_L$ nanocrystals and **NS** and $\mathbf{NS}_L$ nanospheres. All energies are in eV.

		Bulk	$\mathbf{NC}_S$	$\mathbf{NC}_L$	**NS**	$\mathbf{NS}_L$
B3LYP						
$(S_0 \rightarrow T_1)_{vert}$		3.91	3.95	3.95	3.88	
Ti^{3+}–O^-_{ax}	ΔE_{trap}	−0.59	−0.90	−0.80	−0.65	
	PL	1.99	1.71	1.79	1.95	1.96
Ti^{3+}–O^-_{eq}	ΔE_{trap}	−0.49	−0.55			
	PL	2.35	1.80			
HSE06						
$(S_0 \rightarrow T_1)_{vert}$			3.87			
Ti^{3+}–O^-_{eq}	ΔE_{trap}		−0.82			
	PL		1.68			

Indeed, we do, with two possible outcomes, similarly to what observed for the bulk system: the trapping energy (ΔE_{trap} in Table 4.1) for the axial exciton (−0.90 eV), see model b in Figure 4.3, is larger than for the equatorial one (−0.55 eV). The charge localization/delocalization of the exciton can be analyzed in terms of spin density plots and histograms of the atomic spins, given in top and bottom panels of Figure 4.3, respectively. Differently from the free exciton, in the self-trapped exciton, we observe an almost full delocalization of the unpaired electrons on two single Ti (black, 71 %) and O (red, 92 %) atoms, respectively.

The axial self-trapped exciton (model b in Figure 4.3) in the core of the small nanocrystal is a bound exciton, where the electron and the hole localize on a Ti^{4+}–O^{2-} bound pair, i.e. Ti^{3+}–O^-_{ax}. If the electron and the hole have enough energy to overcome the small energy barrier (due to the exciton binding energy) before recombination, the two charges may separate and the system may evolve in several possible final configurations, which are shown in Figure 4.3c-f and detailed in Table 4.2: i) model c, where the electron has migrated to the surface to be trapped on an undercoordinated Ti_{5c} atom on a (101) facet; ii) model d, where the hole has travelled to the surface to be trapped at an O_{2c} site, leaving a delocalized electron in the core of the faceted nanoparticle; iii) models e and f, where both electron and hole have reached the surface to be trapped at a Ti_{5c} and an O_{2c} site, respectively.

It is worth noting that an electron cannot be localized on a single Ti site of the nanocrystal, unless it is bound to the hole in the excitonic pair at the core of the nanocrystal or is trapped at a surface site. Considering the trapping energies of the excitons in model b and e, we can observe that there is a favorable energy gradient for the exciton migration to the surface, where the charges can react with the substrates.

However, configurations c, d, e and f exist if the time scale for migration and trapping at the surface is shorter than that of recombination. Since distances in nanocrys-

tals are short, the surface can be easily reached and, therefore, lower temperatures are needed to quench the photoluminescence, in line with the above mentioned experimental observations. Nonetheless, on the contrary, if the self-trapped exciton of model b recombines before charge migration, the photoluminescence photon energy is estimated by current calculations to be 1.71 eV (see PL in Table 4.1). This value is significantly lower that that of bulk anatase, probably due to the small size of the nanocrystal model employed.

Table 4.2 – Trapping Energy (ΔE_{trap} in eV) of the triplet exciton at different sites with the percentage of charge localization (%electron or %hole) in $\mathbf{NC}_S$ and **NS** anatase nanoparticles, as obtained with the B3LYP and HSE06 functionals. No symmetry constraints are imposed to all the calculations. The sites nomenclature is defined graphically in Figure 4.2.

Model	Position	ΔE_{trap}	%electron	%hole
Electron/Hole pairs in $\mathbf{NC}_S$				
B3LYP				
b	Ti_{6c}^{core} – O_{3c}^{core} (Ti^{3+} – O_{ax}^{-})	−0.90	71%	92%
c	Ti_{5c}^{face} – O_{3c}^{core}	−0.96	89%	91%
d	Ti_{6c}^{core} – O_{2c}^{corner}	−0.92	13%	63%/37%
e	Ti_{5c}^{face} – O_{2c}^{corner}	−1.02	89%	63%/37%
f	Ti_{5c}^{face} – O_{2c}^{face}	−0.73	89%	95%
HSE06				
b	Ti_{6c}^{core} – O_{3c}^{core} (Ti^{3+} – O_{ax}^{-})	−0.82	6%	93%
c	Ti_{5c}^{face} – O_{3c}^{core}	−0.82	6%	73%
e	Ti_{5c}^{face} – O_{2c}^{corner}	−0.82	92%	73%
Electron/Hole pairs in $\mathbf{NC}_L$				
B3LYP				
	Ti_{6c}^{core} – O_{3c}^{core} (Ti^{3+} – O_{ax}^{-})	−0.80	74%	91%
HSE06				
	Ti_{6c}^{core} – O_{3c}^{core} (Ti^{3+} – O_{ax}^{-})	−0.82	6%	93%
Electron/Hole pairs in **NS**				
B3LYP				
	Ti_{6c}^{core} – O_{3c}^{core} (Ti^{3+} – O_{ax}^{-})	−0.65	74%	90%
	$Ti_{6c}^{subsurf}$ – $O_{2c}^{5c\text{-}6c}$	−0.79	86%	90%

Comparing the results obtained for the small ($\mathbf{NC}_S$) and the large ($\mathbf{NC}_L$) in Table 4.2, we may note some clear trends with increasing size. The exciton trapping energy, for the axial model, decreases from −0.90 to −0.80 eV, while the PL emission increases

from 1.71 eV to 1.79 eV (see Table 4.1). This indicates that the larger is the model, the higher is the emission energy. If one considers that the average radius of these two nanocrystals is 1.8 and 2.2 nm (see Table 3.2), one could extrapolate for nanocrystals of 4 nm size, reported in the experimental studies, an emission energy close to 2 eV, similar to that for bulk anatase.

The % of electron-hole localization is pretty high, except for the electron component in the d model. In this case, the hole is far apart on the nanocrystals corner and thus the electron delocalization on several Ti centers is preferred. On the contrary, in model b, where the hole is on the nearest-neighbor axial oxygen atom, the exciton binding energy favors the electron localization on a single Ti site.

As a final remark, we can compare the B3LYP results with a set of HSE06 calculations in Table 4.1 and 4.2. The HSE06 functional provides similar energies for all the types of electron-hole pairs considered, even though the energy gradient for the migration to surface is computed to be equal to zero. Interestingly, the HSE06 calculation for the model b shows a preference for the electron delocalization, even when the hole is localized on the nearest-neighbor axial O atom.

Spherical nanoparticles

We now discuss the excitons in spherical nanoparticles or nanospheres (**NS**), using as reference model that reported in Figure 4.2, where the main surface sites have been highlighted. On this type of nanoparticle there is clearly a wider variety of undercoordinated sites than for well-faceted nanoparticles. Furthermore, spherical nanoparticles contain a larger number of hydroxyl groups required to saturate the Ti atoms to a minimum four-fold coordination, which we have set for the chemical stability of the TiO_2 nanoparticles (see Chapter 3).

The vertical triplet exciton (model a in Figure 4.4), i.e. the exciton in the singlet ground state geometry, is more localized than in the case of nanocrystals. In particular, the electron/hole couple delocalizes over a limited number of oxygen and titanium atoms close to the surface. Interestingly, the singlet-triplet vertical excitation energy $(S_0 \rightarrow T_1)_{vert}$, reported in Table 4.1, is slightly lower for the nanospheres with respect to the bulk and nanocrystal, indicating that a spherical TiO_2 nanoparticle may be photoexcited even at photon energy lower than the bulk band gap, in line with recent experimental observations. [195]

The axial STE (Ti^{3+}–O^{-}_{ax}) in the core of the nanosphere (model b in Figure 4.4) is found to be less trapped than in the faceted models (ΔE_{trap} of -0.65 eV vs -0.90 or -0.80 eV for $\mathbf{NC}_S$ or $\mathbf{NC}_L$, respectively in Table 4.2). This also means that the surface charges are more reactive for the nanospheres than for the nanocrystals. Similarly to what observed for the corresponding model b in $\mathbf{NC}_S$, the electron and hole in the bound exciton are highly localized, as evidenced by the histograms of atomic spins in Figure 4.4 or % of electron/hole localization in Table 4.2.

If the electron and hole have enough energy to overcome the exciton binding, they may migrate to the surface, where they are trapped at single atomic sites. In the case of the nanosphere, we have just considered the most stable configurations for the electron and hole, respectively: the electron localizes on a subsurface Ti_{6c} site (see Figure 4.5 for a definition), while the hole localizes on a surface O_{2c} site. The

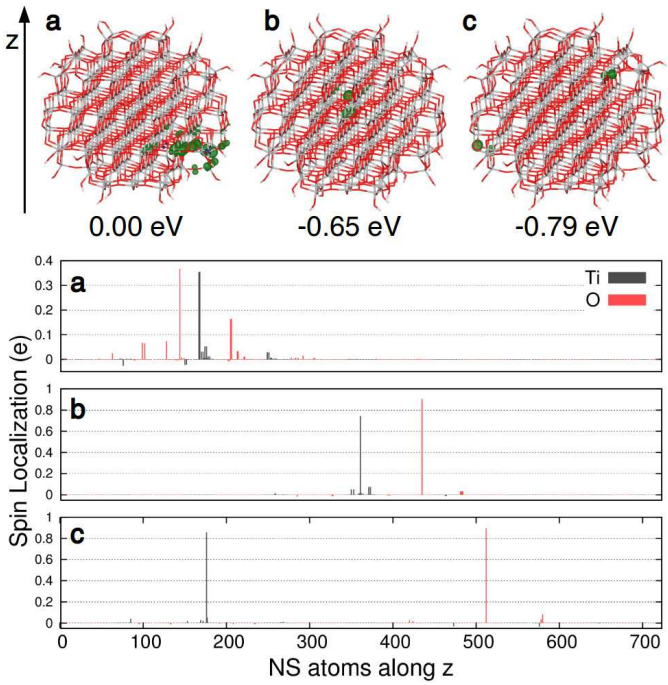

Figure 4.4 – Top panel: 3D spin density plots of **NS** nanosphere, as obtained with the B3LYP functional, for the vertical triplet state (a), trapped triplet exciton (b) and separated charges state (c) with the hole on O_{2c}^{5c-6c} and the electron on $Ti_{6c}^{subsurf}$. Bottom panel: Histogram of the atomic spin on each oxygen or titanium atoms for the a, b and c configurations. The x axis sorts the atoms from bottom to top by their z coordinate.

trapping energy for the electron/hole couple in these sites is bigger and amounts to −0.79 eV, as reported in Table 4.2. This finding confirms that electrons and holes are preferentially trapped closer to or at the surface than in the core of the nanoparticle, regardless of its shape. The computed favorable energy gradient is the driving force of this spontaneous process.

The axial STE in the core of the nanosphere (**NS**) is characterized by a more similar environment to that in bulk anatase than the analogous excitons in the small and large nanocrystals. This is due to the fact that in the **NS** model the central Ti–O pair is surrounded by a larger number of next-neighbouring atoms in the xy plane, i.e. the **NS** model has a larger equivalent diameter in the xy plane than $\mathbf{NC}_S$ and $\mathbf{NC}_L$. For this reason the computed photoluminiscence (PL) energy (1.95 eV) corresponding to the self-trapped exciton in the nanosphere is closer to that obtained for bulk (1.98 eV) than the one calculated for the larger nanocrystal, $\mathbf{NC}_L$ (1.79 eV), in better agreement with the experiments, showing that, at a sufficiently low temperature, photoluminiscence spectra of nanoparticles do not differ much from the one of single crystals. This is further confirmed by using a larger model ($\mathbf{NS}_L$,

described in Chapter 3) with a PL value of 1.96 eV. Given the diameter of **NS** (2.2 nm) and $\mathbf{NS}_L$ (3.0 nm), one can extrapolate that for nanoparticles with a diameter on the xy plane larger than 4 nm, the photoluminiscence energy is already the same of the bulk, in line with the experimental observations by Bieber et al. [231]

4.4 Separate carriers trapping

Once that the electron and hole separate, if they are far apart, they behave like isolated charges. Therefore, as done in previous theoretical study, [73] one can investigate the relative stability of electron and hole traps by adding or removing an electron to the calculation, respectively. Furthermore, the properties of the isolated trapped electrons and holes can be calculated and compared with the available experimental data.

4.4.1 Experimental background

In the experimental literature, two classes of electron traps in anatase powder samples are commonly observed: short-living (< 50 ps) shallow traps, [23, 238] in the range of 50–100 meV below the conduction band [239–242] and long-living deep traps, with trapping energies between 0.4 and 0.6 eV. [243–245] On the contrary, excess holes are found to be deeply trapped in less than 200 fs, [23] so direct measurements of holes in shallow traps are not reported in literature. Charge carriers trapped in the lattice can be probed by spectroscopic techniques, such as electron paramagnetic resonance (EPR) spectroscopy and transient absorption (TA) spectroscopy.

For instance, integrating EPR absorption intensities, Berger et al. determined that just one photogenerated electron/hole pair is present per single UV-irradiated anatase nanoparticle (with an average size of 13 nm), [246] as a consequence of the Coulombic repulsions between excess electrons. Most of the photoexcited electrons (90%) are not detected by EPR, since they are delocalized and, thus, EPR–silent. Only 10% of the electrons are EPR active because they are fully localized at Ti^{3+} sites with an activation barrier for the de-trapping process estimated to be ≈ 26 meV. Photoexcited holes are found to be trapped at the surface of nanoparticles as O^- species, since the EPR signal related to them completely disappears when molecular oxygen, a hole scavenger, is provided. [247]

As regards the source of the EPR signal, the peaks with g values lower than Landé g-factor ($g_e = 2.0023$) are assigned to trapped electrons, whereas g higher than 2.0023 are due to trapped holes. [31] In particular, Chiesa et al. [248] attributed the broad and unfeatured signal (with a g value of about 1.93) to electrons trapped in the external layers of the nanocrystals. All these trapping sites have slightly different local environment, hence slightly different EPR parameters. The other signal ($g = 1.962$, $g = 1.992$) was attributed to Ti^{3+} in regular bulk positions. According to the authors of this work, the corresponding low hyperfine coupling constant with ^{17}O (< 2 MHz) demonstrates that this latter type of unpaired electron is quite delocalized over several lattice sites (electron Bohr radius ≈ 15 Å). Noteworthy, results are found not to depend on the nanoparticles dimension in the range between 6 to 43 nm.

No significant differences in the orthorombic g-tensor of the EPR signal from

trapped holes were observed by Micic et al. [80] for nanoparticles of anatase phase in the range between 2.5 and 30 nm in dimension. Furthermore, these authors concluded that the hydroxyls are not the hole trapping species and that the hole is, instead, trapped to a $O^{\bullet -}$, which is bound to two titanium atoms with inequivalent crystal field splitting. More recently, Brezová et al. [249] measured two distinct axial g-tensor for photoexcited holes in anatase nanoparticles (see Section 4.4.3): O^-_{A1}, which is prevalently present (^{17}O hyperfine coupling constants are available) and O^-_{A2}, which is likely to be closer to more positively charged ions.

Transient absorption (TA) spectroscopy is based on the measurement of the differential absorption of irradiated and non-irradiated material samples. Using this technique it is possible to probe, on one side, the transitions between electron trap levels and conduction bands, or, on the other side, between valence bands and hole trap levels. In general, the estimated amount of electron/hole pairs in these experiments is less than 1–2 per metal oxide nanoparticle, in line with EPR findings.

Recently, TA experiments in the mid-infrared were employed to determine the nature of shallow electron traps in 15–20 nm photoexcited anatase nanoparticles. [250] They were unambiguously assigned to self-trapped electrons in the bulk of the nanoparticles and not to pre-existing defects. The radius of the polaron associated to the electron trap was evaluated to be between 1 and 2 nm in an anatase single crystal. [251]

As regards deep traps, the transient absorption (TA) spectrum in the visible to near-IR range of anatase nanocrystalline films with a grain size between 15 and 20 nm, mainly exposing (101) facets, have been decomposed by Yoshihara et al.: [252] the background spectrum was assigned to free electrons in the conduction band, whereas the broad absorption bands centered at 520 nm (2.38 eV) and 770 nm (1.61 eV) were attributed to trapped holes and electrons, respectively. Again, also the conclusion of these authors are that trapped carriers are at the surface, because they rapidly react with scavengers, whilst free electrons are prefentially trapped in the bulk.

Analogous measurements have been performed by Shkrob et al. [253] but for 4.6 nm aqueous anatase nanoparticles, with a quasi-spherical shape, whose transient holes and electrons were detected at the wavelenghts of 650 nm (1.90 eV) and 900 nm (1.37 eV), respectively. Moreover, they observed that a small subset of holes are located in the interior of the nanoparticles since they cannot be scavenged by adsorbed species.

Also X-Ray absorption spectroscopy (XAS) can be used to probe photogenerated electron traps. Using this technique with a 100 ps time resolution, Rittmann-Frank et al. [254] found two types of photoinduced Ti^{3+} species in 20 nm faceted and 10 nm amorphous nanoparticles under UV irradiation. These were attributed to non-symmetrically distorted six-fold and five-fold coordinated Ti^{3+} sites. More recently, femtosecond time-resolved XAS measurements were performed by Obara et al. [238] on 7 nm anatase nanoparticles in aqueous solution. In these experiments, conduction band electrons were found to localize either on shallow traps in the bulk or deep traps on the five-fold coordinated Ti sites.

4.4.2 Electron trapping

In this section, we investigate the electron trapping process in more detail by describing what happens when a single extra electron is present in the nanoparticles. First, one electron is added to the ground state geometry, then the system is allowed to relax its structure in order to find the closest energy minimum. Finally, the electron trapping of selected sites on the surface of the nanoparticles have been studied by structural optimization of distorted geometries, where all the Ti–O bond lenghts of the TiO_6 octahedron of a specific site have been elongated by about 0.1 Å to favor the localization of the excess electron.

Faceted nanoparticles

In the case of a faceted model ($\mathbf{NC}_S$), the vertically added excess electron is found to be largely delocalized on the majority of the Ti sites (see model a in Figure 4.6), in a quasi-band state. When the atomic relaxation is allowed, the number of Ti sites where the electron is delocalized significantly reduces and only the atoms in the central belt of the nanocrystal are involved (see model b in Figure 4.6). The energy gain, i.e. the trapping energy, associated with the structural relaxation is of −0.21 eV. Finally, the electron trapping on single sites may take place, which is not necessarily more favorable because of a larger positive distortion energy contribution (ΔE_{dist}). Several distinct sites in the nanocrystal have been considered, ranging from a Ti_{4c} on a corner, Ti_{5c} on a (101) face, Ti_{5c} on an edge between two (101) facets, Ti_{6c} subsurface (see Figure 4.2a and Figure 4.5 for the nomenclature). Rather surprisingly, edge and corner Ti sites (see models b and c in Figure 4.7) are not found to be involved in the trapping, since the ΔE_{trap} is significantly less negative than the delocalized solution. This is because only the Ti_{5c} on a (101) face (see model c in Figure 4.6) and the Ti_{6c} in the subsurface (see model a in Figure 4.7) show a larger trapping energy (ΔE_{trap} = −0.28 eV) than the electron delocalized in the layers in the central belt of the nanoparticle ($Core^{deloc}$, −0.21 eV).

In order to analyze the energy contributions to the trapping energy, the value of ΔE_{trap} can be roughly decomposed in an energy cost due to the distortion (ΔE_{dist}) and an energy gain due to the single occupation of a new Kohn-Sham state or SOMO (ϵ_{SOMO}). The best balance between these two quantities is found (see Table 4.3) for the two trapping sites mentioned above. In Figure 4.6c, we represent the Ti_{5c} on a (101) facet (see model c), which can be considered the best electron trapping site, since its electron localization (89% vs 77%) is higher than that of the Ti_{6c} subsurface electron trap, as shown by the spin density plot and by the projected density of states in panel c of Figure 4.8. All the other spin plots of the trapped electron are shown in Figure 4.7.

In the case of the larger faceted model ($\mathbf{NC}_L$), even though trapping energies are systematically lower or even positive due to a more stable and more delocalized reference states, the same considerations described above about the relative stabiity and the localization/delocalization degree of the bulk and surface sites apply. Furthermore, for this larger model, we were able to localize the excess electron on a single titanium ion in the deep core of the nanocrystal (model g in Figure 4.7 or Ti_{6c}^{core} in Table 4.3). However, this electron trap is isoenergetic with the free electron solution

Table 4.3 – Trapping Energy (ΔE_{trap}) for electrons at different sites for the three anatase nanoparticles with B3LYP functional. The reference zero for ΔE_{trap} is obtained by adding one electron with no atomic relaxation. The charge localization (%electron), distortion energy (ΔE_{dist}) and eigenvalue of the unpaired electron state (ϵ_{SOMO}, respect to the bottom of the CB) are also given. Electron Affinity (EA) of one extra electron coming from the vacuum is reported. The potential versus the Standard Hydrogen Electrode (U_{SHE}) has been calculated using the approach in ref. [255] for B3LYP functional. No symmetry constrains are imposed in the calculations. Energies are in eV. The sites nomenclature is defined graphically in Figure 4.2 and Figure 4.5 or in the text.

Position	ΔE_{trap}	%electron	ΔE_{dist}	ϵ_{SOMO}	EA	U_{SHE}
Excess electron in $\mathbf{NC}_S$						
Vertical					3.23	−0.73
Ti_{4c}^{corner}	−0.10	90%	1.26	−1.07	3.33	−0.63
Ti_{5c}^{face}	−0.28	89%	1.10	−1.20	3.51	−0.45
Ti_{5c}^{edge}	−0.12	88%	1.19	−1.03	3.35	−0.61
$Ti_{6c}^{subsurf}$	−0.28	77%	0.64	−0.88	3.51	−0.45
$Core^{deloc}$	−0.21	11%	0.03	−0.24	3.44	−0.52
Excess electron in $\mathbf{NC}_L$						
Vertical					3.42	
Ti_{4c}^{corner}	0.10	90%	1.41	−0.96	3.32	−0.64
Ti_{5c}^{face}	−0.09	89%	1.21	−1.08	3.51	−0.45
Ti_{5c}^{core}	0.00	46%	0.36	−0.42	3.41	−0.55
$Ti_{6c}^{subsurf}$	−0.09	78%	0.77	−0.80	3.51	−0.45
$Core^{deloc}$	−0.04	4%	0.12	−0.11	3.46	−0.50
Excess electron in **NS**						
Vertical					3.15	−0.81
Ti_{4c}^{corner}	−0.09	88%	1.26	−1.07	3.25	−0.71
Ti_{4c}^{pole}	No trapping					
$Ti_{4c}OH$	No trapping					
Ti_{5c}	No trapping					
$Ti_{6c}^{subsurf}$	−0.40	85%	0.85	−1.11	3.55	−0.41
Ti_{6c}^{core}	−0.13	62%	0.47	−0.61	3.28	−0.68
$Core^{deloc}$	−0.11	19%	0.17	−0.26	3.26	−0.70
Excess electron in **Bulk Anatase**						
Bulk	−0.23	80%	0.42	−0.82		

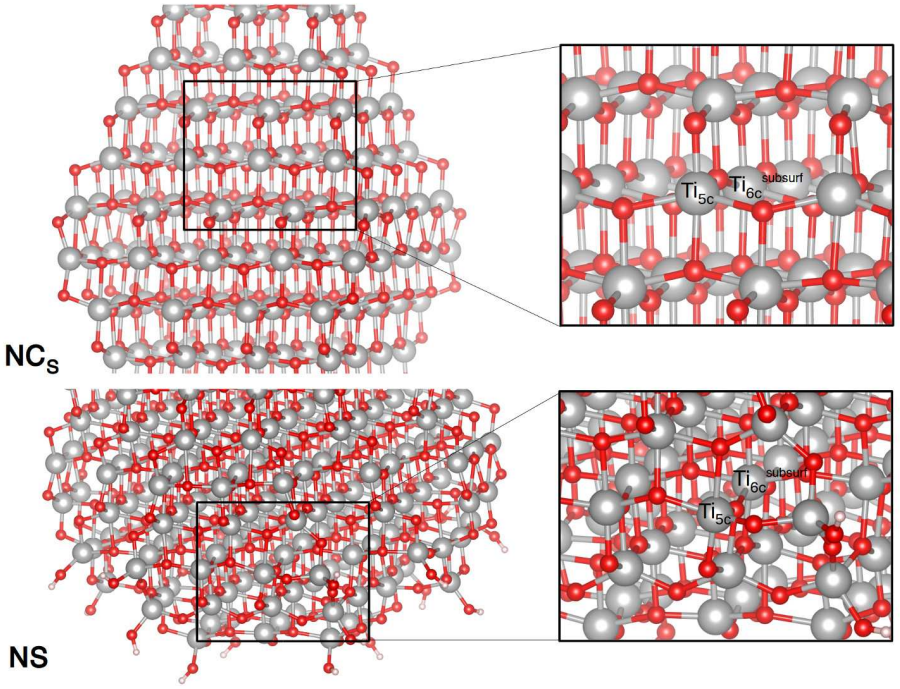

Figure 4.5 – Position of the Ti atoms defined as subsurface Ti_{6c} ($Ti_{6c}^{subsurf}$) in the $\mathbf{NC}_S$ nanocrystal (top panel) and **NS** nanosphere (bottom panel).

(model f in Figure 4.7) and less stable than the one delocalized within the core (model g in Figure 4.7 or $Core^{deloc}$ in Table 4.3).

Therefore, the energetics does not seem to considerably favor the electron trapping on a single site with respect to the electron relaxation in the core of a faceted nanoparticle, which is quite interesting, given that an analogous calculation for a bulk and slab model would favor the single site trapping with respect to full delocalization in a crystal band state by −0.23 eV and −0.62 eV, respectively. [73]

From this analysis of the electron traps in the TiO_2 nanocrystals, we may draw the conclusion that the delocalization of the excess electron within the nanoparticle produces a quite stable large polaron, involving about 3 to 5 titanium atomic layers and extended from the center to the borders of the faceted nanoparticles. This partially localized solution cannot be simply observed in periodic bulk and surface models because of the infinite character of bands. Then, if the electron migrates to the surface, it can be deeply trapped, with a small energy gain with respect to shallow trapping in the core.

Finally, in Table 4.3 the intrinsic redox potentials versus the Standard Hydrogen Electrode (U_{SHE}) are reported for all the electron traps, as computed using the approach by Zhang et al. [255] for B3LYP functional. As one would expect, the higher

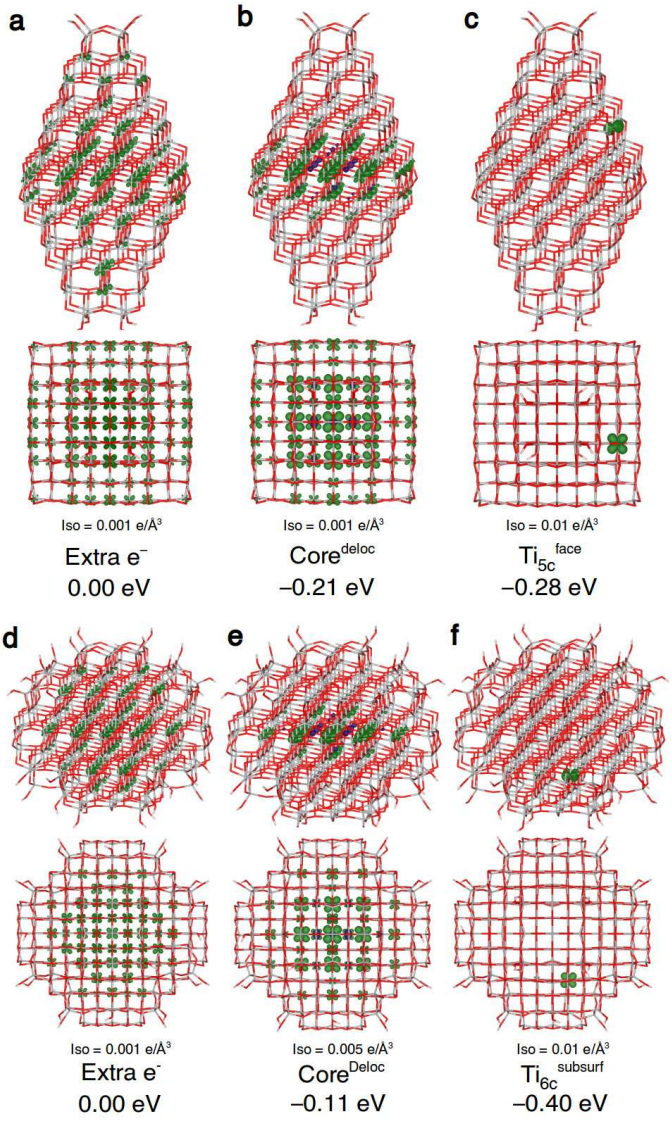

Figure 4.6 – Front and top view of the 3D plots of spin density of trapped electrons in $\mathbf{NC}_S$ nanocrystal (top panel) and in **NS** nanosphere (bottom panel), as obtained with the B3LYP functional. Below each structure the isovalue of corresponding 3D plot and the energy gain (ΔE_{trap}) relative to the vertical addition of an excess charge are given. The sites nomenclature is defined graphically in Figure 4.2 or in the text.

the trapping energy the less negative is the electrode potential, since the trapped electron is less reactive. In all the cases, however, the potential is lower than zero, hence all the Ti^{3+} species would be able to reduce water to hydrogen in an acidic environment.

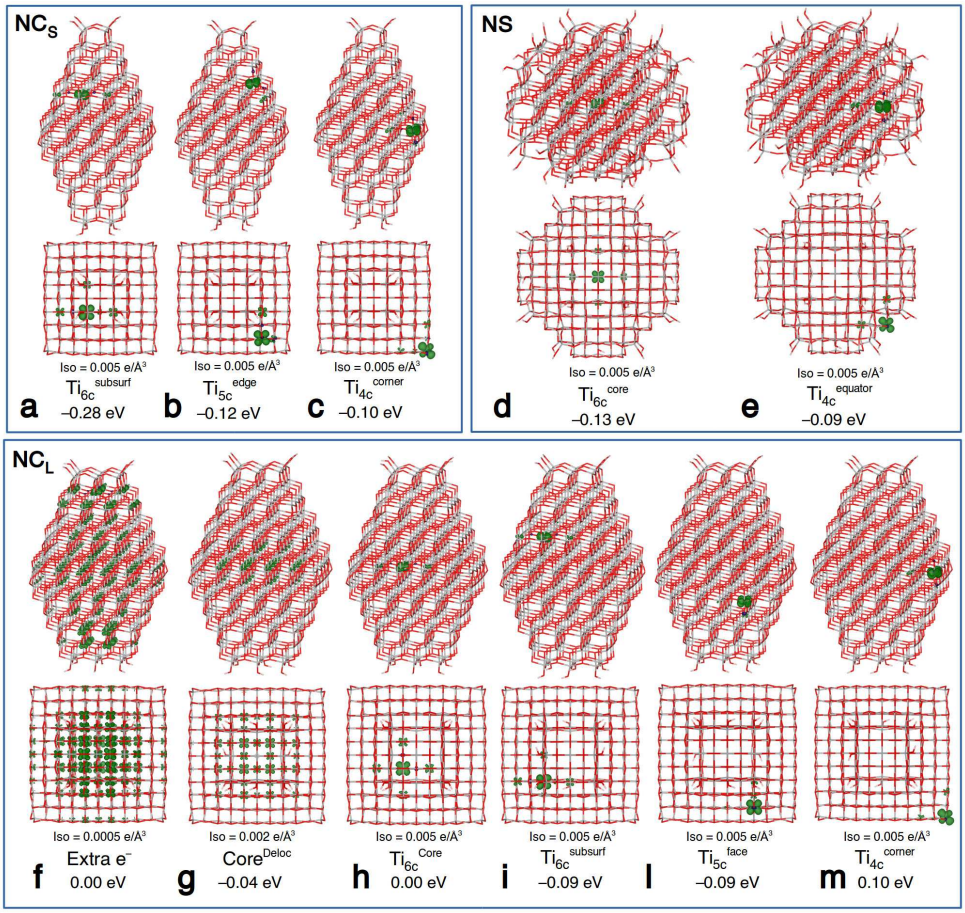

Figure 4.7 – Additional front and top views of the 3D plots of spin density of trapped electrons in $\mathbf{NC}_S$ and $\mathbf{NC}_L$ nanocrystals (top panel left and bottom panel, respectively) and in **NS** nanosphere (top panel right). Below each structure the isovalue of each 3D plot and the energy gain (ΔE_{trap}) relative to the vertical addition of an excess charge are given. The sites nomenclature is defined graphically in Figure 4.2 and Figure 4.5 or in the text.

Spherical nanoparticles

For a spherical nanoparticle (**NS**), the excess electron is found to be fully delocalized on all the titanium atoms, except those in the most external atomic shell. This

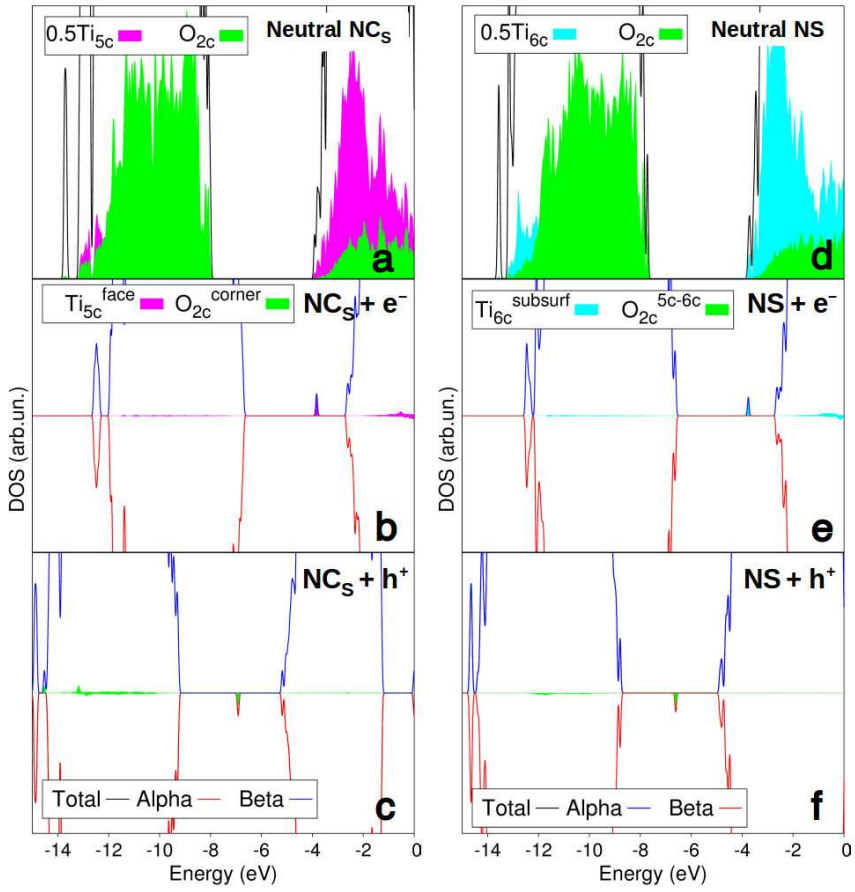

Figure 4.8 – Simulated total (DOS) and projected (PDOS) density of states on different oxygen and titanium atoms, as obtained with the B3LYP functional, of: (a) the neutral $\mathbf{NC}_S$, (b) $\mathbf{NC}_S$ with an additional electron and (c) $\mathbf{NC}_S$ with an additional hole in their best trapping site; (d) the neutral **NS**, (e) **NS** with an extra electron and (f) **NS** with an extra hole in their best trapping site. A 0.001 eV Gaussian broadening has been employed. The zero energy is set to the vacuum level. The sites nomenclature is defined graphically in Figure 4.2 and Figure 4.5 or in the text.

behaviour is different from that of $\mathbf{NC}_S$ and $\mathbf{NC}_L$ and it is clearly described by the comparison between the spin density plot of model a and d in Figure 4.6. When structural relaxation is allowed in the presence of the extra electron, the spin density mainly localizes on three titanium atomic layers, with an associated energy gain of -0.11 eV (see model e in Figure 4.6 and trapping energy for $\text{Core}^{\text{deloc}}$ in Table 4.3).

Lastly, the localization of the extra electron on a single atomic site has also been studied, as reported in Table 4.3 for the **NS** model. Unexpectedly, although several

Ti_{4c} and Ti_{5c} sites were considered, no trapping was observed, except for a tiny trapping energy (−0.09 eV) in the case of a four-fold titanium atom at the equator of the nanosphere (see $Ti_{4c}^{equator}$ in Figure 4.7e). On the contrary, the most favorable trapping site is determined to be a Ti_{6c} in the subsurface of the nanosphere (see model f in Figure 4.6) with a ΔE_{trap} of −0.40 eV. The large electron localization indicated by the atomic spin density at this trap (85%), given in Table 4.3, is corroborated also by the PDOS reported in Figure 4.8. No other trapping site is found to be competitive with this one (see Table 4.3). Interestingly, unlike faceted nanoparticles, in the case of nanospheres the electron delocalization at the core of the nanoparticle (see $Core^{deloc}$ in Figure 4.7 and Table 4.3) seems to be less favorable if compared to full localization on a subsurface site: −0.11 vs −0.40 eV.

Finally, if we focus the attention on the electron affinities (EA) in Table 4.3, we can directly compare electron trapping sites of nanoparticles with different size and shape ($\mathbf{NC}_S$, $\mathbf{NC}_L$ and **NS**), since for EA there is a common reference, which is the vacuum. One can observe that the range of energies of the EA values is rather small: from 3.25 to 3.55 eV, regardless of the dimension and morphology of the nanoparticle, which indicates similar trapping abilities of the three nanoparticles under study.

Trapping centers

In this paragraph, the geometry of the electron trapping site is analyzed and compared to reference sites with the same coordination pattern: a six-fold coordinated Ti atom in the anatase relaxed bulk (Figure 4.9a), a five-fold coordinated Ti atom on the (101) anatase surface (Figure 4.9b) and a four-fold coordinated Ti atom a corner of a nanocrystal (Figure 4.9c). In particular, we focus our attention on bond distances in the reference sites and in the nanoparticle ones once that the electron has been trapped. For both the nanocrystals and nanospheres, we observe that the electron trapping process causes a general elongation of the bond distances in the order of ∼0.1 Å , especially of those bond lenghts in the plane of the titanium *d* orbital hosting the excess electron. On the contrary, variations of the bond angles with respect to the original site are more subtle and the most significant ones are the widenings of the O1–Ti–O3 angle and O2–Ti–O4 angle for the Ti_{5c}^{face} and Ti_{4c} sites, respectively.

Note that the a four-fold Ti trapping sites (right side of Figure 4.9) are present only in nanoparticles, such as $\mathbf{NC}_S$ and **NS**. Here, the angle distortion is more pronounced, whereas the bond elongation is smaller and both effects are caused by the absence of a second coordinating (and repulsive) oxygen atom.

Comparison with the experiments

Regardless of the nanoparticle shape and size, we could always identify energy minima for both shallow (delocalized) and deep (localized) self-trapping states for electrons, which involve d_{xy} states of Ti atoms in the lattice. One should expect to measure high values of electron paramagnetic (EPR) hyperfine coupling constants with the next-neighboring ^{17}O nuclei for deep traps and low values for the shallow ones. As a matter of fact, the isotropic component of the hyperfine interaction is proportional to the density of spin on the *s* functions of the magnetic nucleus according to the following equation:

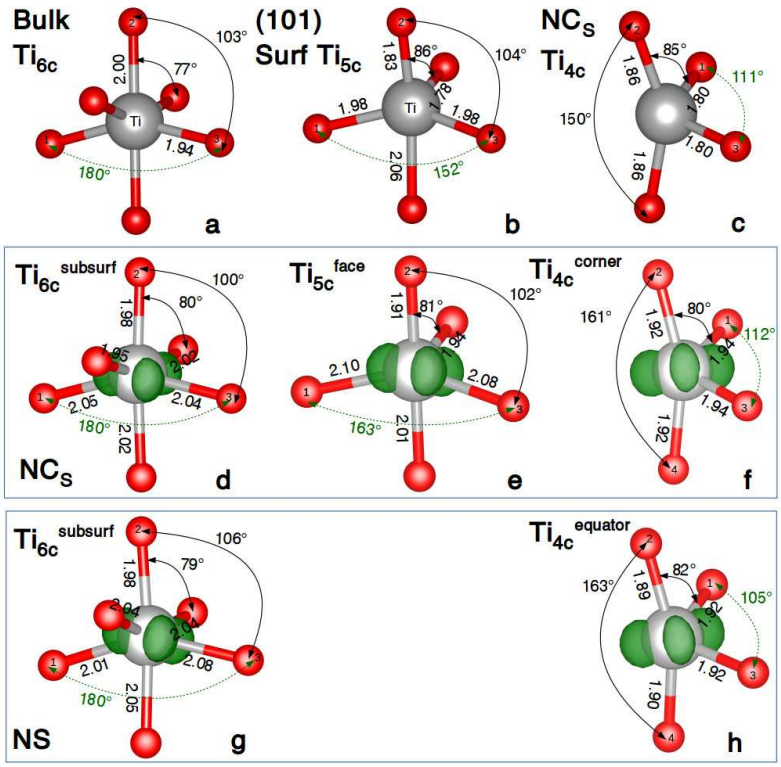

Figure 4.9 – Ball-and-stick representation and spin densities (isovalue = 0.03 a.u) of the principal trapping sites of an extra electron in $\mathbf{NC}_S$ (d, e, f) and **NS** (g and h), together with relevant bond lenghts and angles. As reference, the geometrical parameters for a a) Ti_{6c} of an anatase bulk; b) Ti_{5c} of an (101) anatase slab and c) Ti_{4c} at the corner of $\mathbf{NC}_S$ are shown in the top panel. The dashed green line indicates the dihedral between the planes O3–Ti–O2 and O2–Ti–O1. The nomenclature of the sites is defined graphically in Figure 4.2 and Figure 4.5 or in the text.

$$a_{iso} = 2\frac{\mu_0}{3} g_N \beta_N g_e \mu_B \langle \rho^s \rangle \tag{4.1}$$

where $\langle \rho^s \rangle$ is the electronic density on the nucleus, g_e is the Landé g-factor, g_N is the nuclear g-factor and μ_B and β_N are the Bohr and nuclear magnetons, respectively. The amount of spin on the magnetic ^{17}O nucleus would be higher the more the electron on the next-neighbouring Ti atom is localized.

Indeed, we observe that when the electron is highly localized in a deep trapped, the calculated hyperfine coupling constants with ^{17}O are very similar to those computed for a model $Ti^{3+}(H_2O)_6$, [256] whereas the isotropic coupling constant significantly decreases when the electron is delocalized over many titanium sites, in better agreement with EPR experimental parameters for small anatase nanoparticles ($a_{iso} < 2$ in

Table 4.4).

Table 4.4 – Computed (B3LYP) and experimental hyperfine Fermi contact term with ^{17}O (a_{iso}, in MHz) for $Ti^{3+}(H_2O)_6$ cation and for localized/delocalized models of one extra electron in anatase faceted and spherical nanoparticles. The degree of localization is reported in % of an electron.

	System	Site	Localization	a_{iso}	Reference
Calculated	$Ti^{3+}(H_2O)_6$	-	100%	6.7	[256]
	$\mathbf{NC}_L$	Ti_{6c}^{core}	46%	6.3	This work
		$Core^{deloc}$	4%	1.4	This work
	NS	Ti_{6c}^{core}	62%	6.7	This work
		$Core^{deloc}$	19%	3.9	This work
Experimental	$(Ti^{3+})_{aq}$	-	Localized	7.4	[256]
	Anatase NP	-	Delocalized	<2	[248]

As regards the trapping energies with respect to a free electron in conduction band (CB), the computed values are in line with the experimental values: shallow traps are found to be in the range between 0.04 to 0.20 eV, [239–242] whereas ΔE_{trap} for deep traps can reach 0.40 eV. [243–245] The best sites for electron trapping are surface five-fold coordinated and subsurface six-fold coordinated titanium atoms, in both faceted and spherical nanoparticles, in line with the results from X-Ray absorption spectroscopy. [254]

Lastly, we wish to compare the excitation energies associated with electronic transitions between the electron trap and the CB, as computed with the transition level approach (see Computational Details in Section 4.2), with the experimental absorption energies from transient absorption (TA) spectroscopy. [252, 253] The optical transitions for electrons and holes trapped in the core and on the surface of the nanocrystals and nanospheres are given in Table 4.5.

For faceted nanoparticles, as discussed above, the Ti_{5c}^{3+} is found to be the best trapping site for electrons. The computed transitions from this trap state to the CB minimum are 1.38 and 1.30 eV for $\mathbf{NC}_S$ and $\mathbf{NC}_L$, respectively, which are slightly lower than the experimental transition of 1.61 eV observed with transient absorption spectroscopy (TA) for films of anatase nanoparticles exposing mainly (101) facets. [252] This underestimation may be caused by the fact that the electron is initially trapped in a d_{xy} state (t_{2g} state) and the final states which have the correct symmetry for a permitted transition (e_g) are found to be (see the PDOS in Figure 4.10) at least 0.5 eV above the CB minimum.

For spherical nanoparticles, the best electron trap is the Ti_{6c}^{3+} in the subsurface (see Figure 4.5). The calculated transition from this trap state to the CB minimum is 1.25 eV, which is consistent with the experimental value of 1.37 eV, measured by TA spectroscopy of aqueous spherical TiO_2 nanoparticles. [253]

It is worth noting that the electronic transitions from electron traps in the core or in subsurface layers are characterized by quite low excitation energies, especially in the case of an electron trapped in the core (Ti_{6c}^{core}).

Table 4.5 – Computed (B3LYP) and experimental optical transitions (in eV) between the electron trap levels and the conduction band minimum (CBM), $\varepsilon^{\text{opt}}(-1/0;e)$, and the valence band maximum (VBM) and the hole trap levels, $\varepsilon^{\text{opt}}(+1/0;h)$, for the three anatase nanoparticles under study. Calculated transition for the best trapping electron/hole trapping sites are evidenced in bold. The sites nomenclature is defined graphically in Figure 4.2 and Figure 4.5 or in the text.

Optical Transition	Location	Trapping Site	**NC**$_S$	**NC**$_L$	**NS**
from e$^-$ trap to CBM $\varepsilon^{\text{opt}}(-1/0;e)$	Core	e^- shallow	0.24	0.16	0.28
		$\text{Ti}_{6c}^{\text{core}}$	-	0.37	0.60
	Surface	$\text{Ti}_{6c}^{\text{core}}$	0.91	0.87	**1.25**
		$\text{Ti}_{5c}^{\text{face}}$	**1.38**	**1.30**	-
	Experimental		1.61 [252]		1.37 [253]
from VBM to h$^-$ trap $\varepsilon^{\text{opt}}(+1/0;h)$	Core	$\text{O}_{3c}^{\text{core\_ax}}$	2.44	2.32	2.07
	Surface	O_{2c}^{4c-5c}	**2.65**	**2.69**	2.38
		O_{2c}^{5c-6c}	2.52	-	**2.59**
	Experimental		2.38 [252]		1.90 [253]

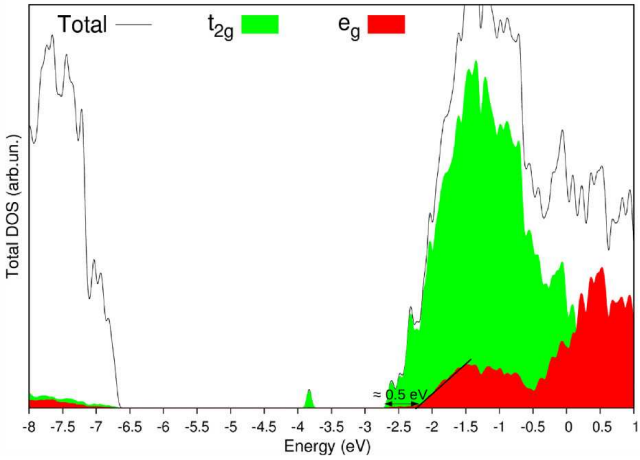

Figure 4.10 – Total (DOS) and projected (PDOS) density of states on Ti t_{2g} and e_g states of the **NC**$_S$ nanocrystal with an extra electron in $\text{Ti}_{5c}^{\text{face}}$ site. The black line shows the inset of the titanium e_g band, which starts about 0.5 eV above the bottom of the conduction band.

4.4.3 Hole trapping

Faceted nanoparticles

The addition of an electron hole, i.e. the removal of an electron, in a faceted nanoparticle ($\mathbf{NC}_S$) results in a delocalized hole within two full oxygen layers at the center of the nanocrystal (see model a in Figure 4.11). However, when atomic relaxation is allowed, the delocalization is completely quenched and the hole fully localizes on a single three-fold coordinated oxygen atom in the core of the nanocrystal in axial position with respect to the innermost Ti atom, with a significant associated energy gain of -0.97 eV (see $O_{3c}^{\text{core\_ax}}$ in Figure 4.11b). In the case that the hole has enough energy to overcome the barrier for diffusion, which was estimated to be of about 0.5 eV, [79] it may migrate to the corner of the nanocrystal (O_{2c}^{corner}) with a further energy gain of -0.11 eV ($\Delta E_{trap} = -1.08$ eV). The spin density of the hole is shared between two oxygen atoms this corner site: an O_{2c} and an O_{3c}, as clearly evidenced by the spin plot in model c of Figure 4.11 and in panel f of Figure 4.13. Other possible, but less effective, oxygen sites for hole trapping have been considered, which are represented in Figure 4.12 and reported in Table 4.6, together with the distortion energies (ΔE_{dist}) and the Kohn-Sham energy of the unoccupied one-electron state corresponding to the electron hole. Similar results are obtained for the larger nanocrystal ($\mathbf{NC}_L$), as given in Table 4.6 and represented in Figure 4.12: the migration of the excess hole is found to be a favorable process also for the larger faceted nanoparticle, but the trapping energies are systematically shifted by $\sim$0.1 eV.

Spherical nanoparticles

For spherical nanoparticles, due to the lower degree of order and crystallinity, the removal of one electron from the neutral ground state structure, i.e. the vertical ionization, involves only a limited portion of the nanoparticle, as shown by the spin density plot of model d in Figure 4.11. This solution cannot be considered a delocalized band-like state and, thus, it should not be used as the zero reference to calculate the trapping energies of the different hole trapping sites (ΔE_{trap}), as was done in the case of faceted nanoparticles. Therefore, in the case of the hole traps for the TiO_2 nanosphere, we will not employ trapping energies for the comparison but adiabatic ionization potentials (IP^{ad}), which have a common reference that is the vacuum energy, i.e. the energy of an electron at infinite distance from the system. As a matter of fact, trapping energies and IP^{ad} correlate: the smaller the adiabatic ionization potential, the larger is the trapping energy of the site under consideration.

In the bulk-like core of the spherical nanoparticle, we observe that the hole almost fully localizes (90%) on a three-fold coordinated O atom bound in axial position to the innermost Ti atom ($O_{3c}^{\text{core\_ax}}$). The IP^{ad} for this trapping site in the core of the **NS** is 7.68 eV. Then, if the hole has enough energy to overcome the diffusion barrier, it may migrate to the surface. On the nanosphere surface, various types of oxygen species exist, as represented Figure 4.2. The best trapping site for a hole is found to be a 2-fold coordinated O atom, which bridges a Ti_{5c} and a Ti_{6c} atoms ($IP^{ad} = 7.52$ eV), see O_{2c}^{5c-6c} in panel f in Figure 4.13. The energy necessary for the structural distortion (ΔE_{dist}) to obtain this stable trapping site is larger than the one for the

Table 4.6 – Trapping Energy (ΔE_{trap}) for an extra hole at different sites for the three anatase nanoparticles with B3LYP functional. The reference zero for ΔE_{trap} is obtained by removing one electron with no atomic relaxation. Their charge localization, distortion energy (ΔE_{dist}) and eigenvalue of the hole state (ε_{hole}) with respect to the valence band maximum are also given. Adiabatic Ionization Potential (IP^{ad}) of the most external, less bound, electron to the vacuum level is reported. No symmetry constrains are imposed in all the calculations. Energies are in eV. The sites nomenclature is defined graphically in Figure 4.2 or in the text.

Position	ΔE_{trap}	%hole	ΔE_{dist}	ϵ_{hole}	IP^{ad}
Hole addition in $\mathbf{NC}_S$					
Vertical					8.70
O_{2c}^{face}	−0.77	95%	1.75	2.32	7.93
O_{2c}^{corner}	−1.08	66%/33%	1.67	2.35	7.62
O_{2c}^{edge}	−0.54	71%/29%	1.82	2.06	8.16
$O_{3c}^{core\_ax}$	−0.97	91%	1.47	2.49	7.73
$O_{3c}^{core\_eq}$	−0.59	83%	1.30	1.88	8.11
Hole addition in $\mathbf{NC}_S$–**OH**					
Ti_{5c}–OH	-	70%/30%	2.21	2.75	7.72
Hole addition in $\mathbf{NC}_L$					
Vertical					8.64
O_{2c}^{corner}	−1.01	66%/33%	1.78	2.35	7.63
$O_{3c}^{core\_ax}$	−0.84	90%	1.48	2.32	7.80
Hole addition in **NS**					
Vertical					8.34
O_{2c}^{4c-6c}		89%/11%	1.78	1.96	7.74
O_{2c}^{5c-6c}		92%/8%	1.77	2.18	7.52
$O_{3c}^{core\_ax}$		90%	1.41	1.98	7.68
Ti_{3c}–OH		No trapping			
Ti_{4c}–OH		No trapping			
Hole addition in **NS**–**OH**					
Ti_{5c}–OH	-	85%/15%	2.41	2.02	7.81

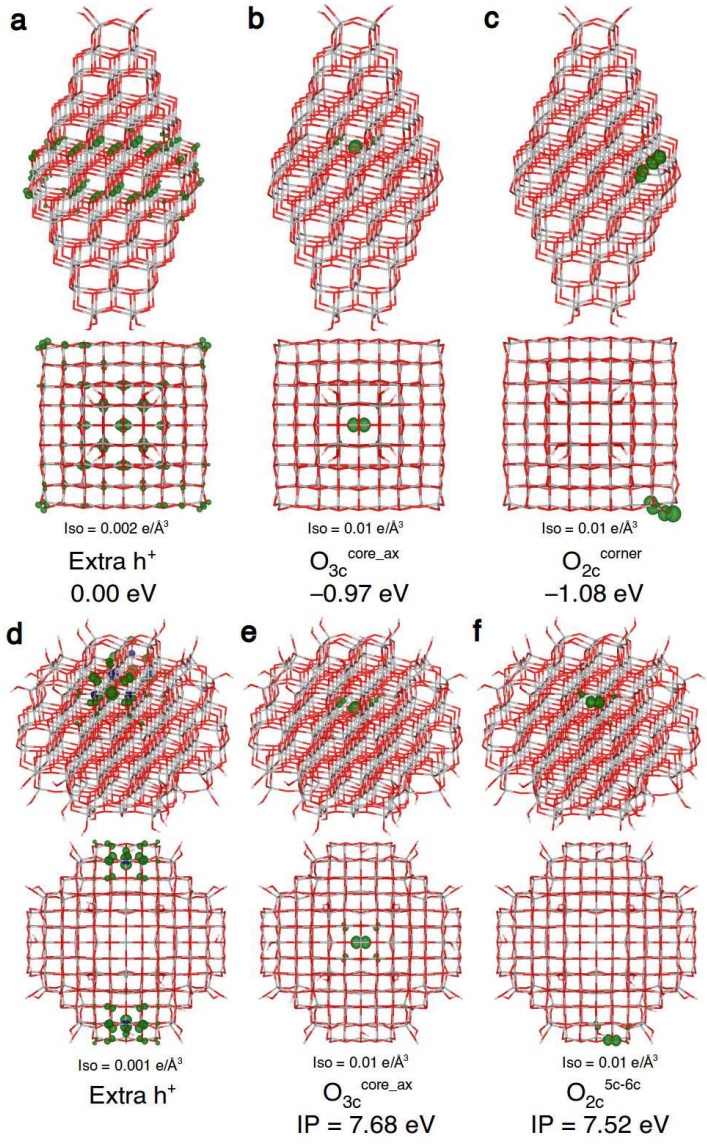

Figure 4.11 – Front and top views of the spin density 3D plots of an extra hole in $\mathbf{NC}_S$ nanocrystal (top panel) and **NS** nanosphere (bottom panel) for the principal trapping sites, as obtained with B3LYP functional. Below each structure the isovalue of corresponding 3D plot and the energy gain (ΔE_{trap} in Table 4.6) relative to the vertical addition of an extra positive charge are given. The sites nomenclature is defined graphically in Figure 4.2 or in the text.

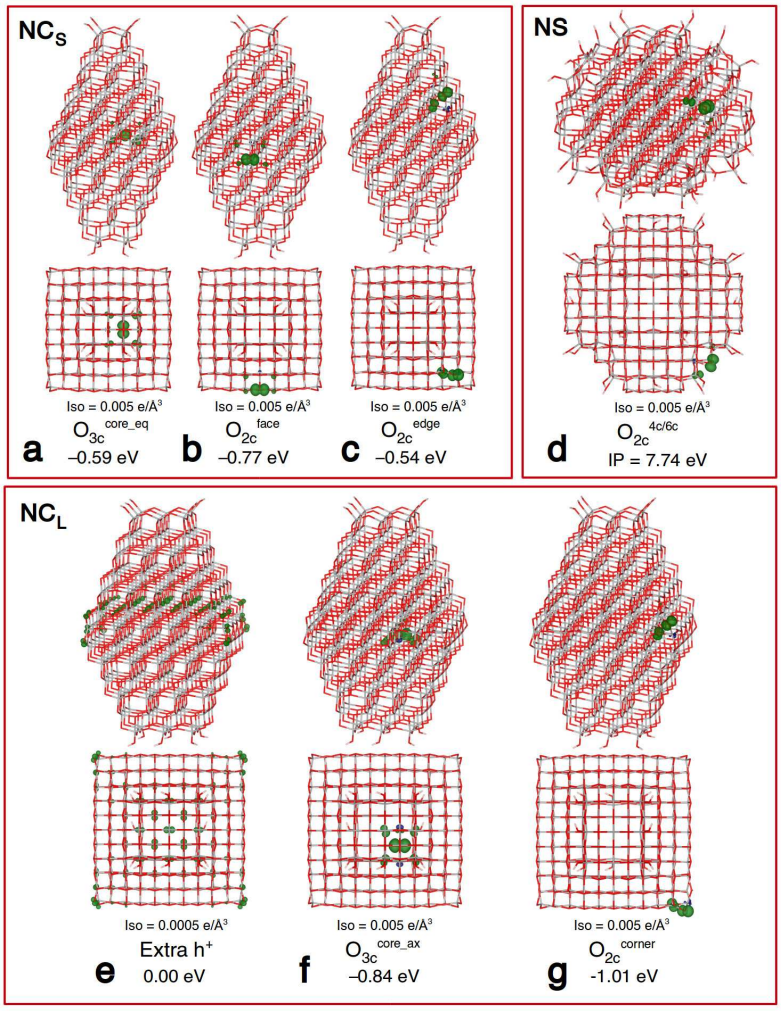

Figure 4.12 – Additional front and top views of the 3D plots of spin density of trapped holes in $\mathbf{NC}_S$ and $\mathbf{NC}_L$ nanocrystals (top panel left and bottom panel, respectively) and in **NS** nanosphere (top panel right). Below each structure the isovalue of each 3D plot and the energy gain (ΔE_{trap}) relative to the vertical addition of an excess charge are given. The sites nomenclature is defined graphically in Figure 4.2 or in the text.

O_{3c} site at the core of the nanoparticle (1.77 vs 1.41 eV). However, the energy gain evaluated with the energy level of the hole state (ϵ_{hole}) with respect to the valence band maximum is also larger (2.18 vs 1.98 eV), as reported in Table 4.6 and Figure 4.8. We consider also a second type of O_{2c} between a Ti_{4c} and a Ti_{6c} (see model d in Figure 4.12) which is found to be a competitive trapping site (IP = 7.74 eV) but less efficient than the O_{2c} between a Ti_{5c} and a Ti_{6c}.

Focusing the attention on the adiabatic IPs in Table 4.6, we can make a direct comparison between hole trapping sites in different nanoparticles ($\mathbf{NC}_S$, $\mathbf{NC}_L$ and **NS**), since, as mentioned above, the ionization potentials have a common reference, which is the vacuum level. We observe that the IP energies, considering all nanoparticles of various dimension and morphology, are in the range between 7.52 and 8.16 eV and the nanosphere seems to have a higher ability trap a hole. The nature of the most stable trapping sites on a faceted and on a spherical nanoparticle is different: for $\mathbf{NC}_S$ and $\mathbf{NC}_L$ it is an O_{2c} bound to a Ti_{4c} at the corner of the decahedron (O_{2c}^{corner}), whereas for **NS** it is an O_{2c} bridging a Ti_{5c} and a Ti_{6c} ion (O_{2c}^{5c-6c}).

Trapping centers

Analogously to the electron trapping centers, in the upper part of Figure 4.13 we report the bond distances and angles for the reference oxygen sites in the bulk (three-fold coordinated oxygen atom in Figure 4.13a), at the anatase (101) surface (two-fold coordinated O atom in Figure 4.13b) and at a corner of a nanocrystal (two-fold coordinated O atom in Figure 4.13c). In the middle and bottom panels, the hole trapping sites for nanocrystals and nanospheres, respectively, are shown. The highest structural distortion is found for the O_{2c} at a corner site in the nanocrystals: both Ti–O bonds are elongated by more than 0.1 Å, whereas the O–O distance is significantly shortened (from 2.45 to 2.22 Å). For all the other O_{2c} trapping sites, only Ti–O bond lenghts are elongated. In the case of O_{3c} species, upon hole trapping, Ti–O bonds are considerably longer (e.g. Ti–O_{ax} increases by about 0.3 Å) and the Ti–O–Ti angle decreases by 5°.

Hydroxyl groups

Lastly, we focus our attention on the OH group, which is likely to be common in aqueous environment and which might be a stable hole trapping site. However, despite the many attempts, the hydroxyl groups, already present on the surface of the nanosphere, i.e. Ti_{3c}–OH and Ti_{4c}–OH sites in Figure 4.2 and Table 4.6, could not trap an electron hole. Instead, an hydroxyl group bound to a fully coordinated titanium ion ($Ti_{5c}OH$) may be a stable hole trapping site, since it would be more electron rich than an OH bonded to a lower coordinated Ti. Nonetheless, on the surface of both faceted and spherical nanoparticle used there are no hydroxyl bound to Ti_{5c} sites, hence the addition of a dissociated water molecule is needed to obtain a Ti_{5c}–OH (see models in Figure 4.14).

As reported in Table 4.6, we observe that the hydroxyl bound to a five-coordinated titanium atoms is able to trap efficiently an extra hole both for a nanocrystal and for a nanosphere.

In particular, in the case of the nanocrystal ($\mathbf{NC}_S$), by comparison of the adiabatic IPs in Table 4.6, we have found that the additional hydroxyl group on a Ti_{5c} ($\mathbf{NC}_S$–**OH**) shows a trapping ability intermediate between that of an O_{2c} on a (101) surface (O_{2c}^{face}, 7.72 vs 7.93 eV) and that of the O_{2c} at a corner site (O_{2c}^{corner}, 7.72 vs 7.62 eV). The electron hole is mainly localized (70%) on a *p* orbital of the oxygen atom of the OH group and it is partially shared (30%) with a neighbor O_{3c} species, as evidenced by the 3D spin plot c in Figure 4.14.

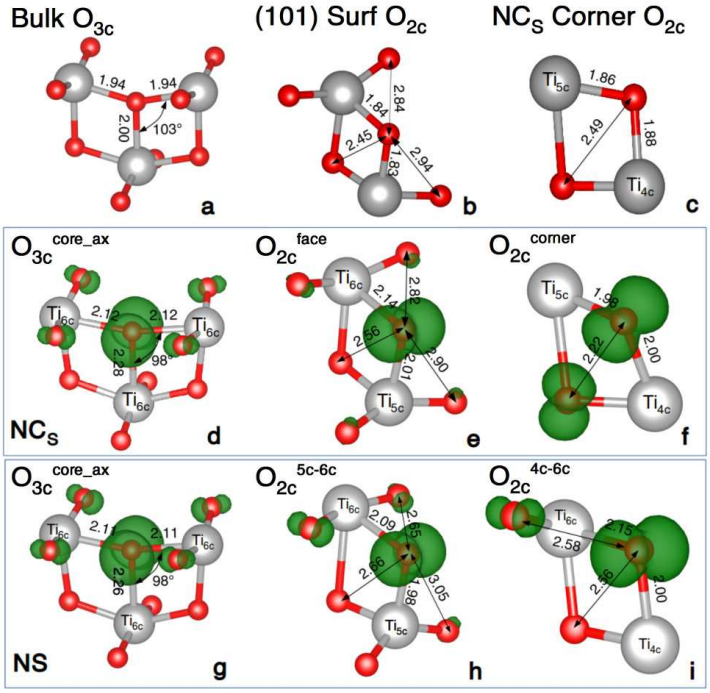

Figure 4.13 – Ball-and-stick representation and spin densities (isovalue = 0.01 a.u.) of the main trapping sites for an extra hole in $\mathbf{NC}_S$ (d, e, f) and **NS** (g, h, i), together with relevant bond lenghts and angles, as obtained with the B3LYP functional. As reference, the geometrical parameters for an a) O_{3c} of an anatase bulk; b) O_{2c} of an (101) anatase slab and c) O_{2c} at the corner of $\mathbf{NC}_S$ are shown in the top panel. The sites nomenclature is defined graphically in Figure 4.2 or in the text.

For the nanosphere, the trapping ability of the additional OH species (**NS–OH**) is found to be lower than that of any other oxygen species on the **NS**, because the IP is calculated to be 7.81 eV, which is 0.29 eV higher than the IP of the most stable trapping site (O_{2c}^{5c-6c}). In this case, the hole highly localizes on a p state of the O atom in the OH group (85%) with a small portion of the hole delocalized on a neighbor O_{3c} atom (15%), as clearly shown by the 3D spin plot h in Figure 4.14.

Upon hole trapping, the Ti–O bond lenght becomes longer (from 1.79 to 2.07 Å in $\mathbf{NC}_S$**–OH** and from 1.79 to 2.16 Å in **NS–OH**), while the OH bond undergoes a tiny elongation (from 0.974 to 0.991 Å in $\mathbf{NC}_S$**–OH** and from 0.973 to 0.986 Å in **NS–OH**). In the neutral nanoparticles the states of the lone pairs of the hydroxyl are not at the top of the oxygen 2p valence band (see panels a and e of Figure 4.14). Upon the removal of an electron, the hole is formed (see panels b and f in Figure 4.14) and a new empty level is formed in the middle of the band gap. Considering the projection of the DOS on the atoms of the OH bound to Ti_{5c} it is clear that the

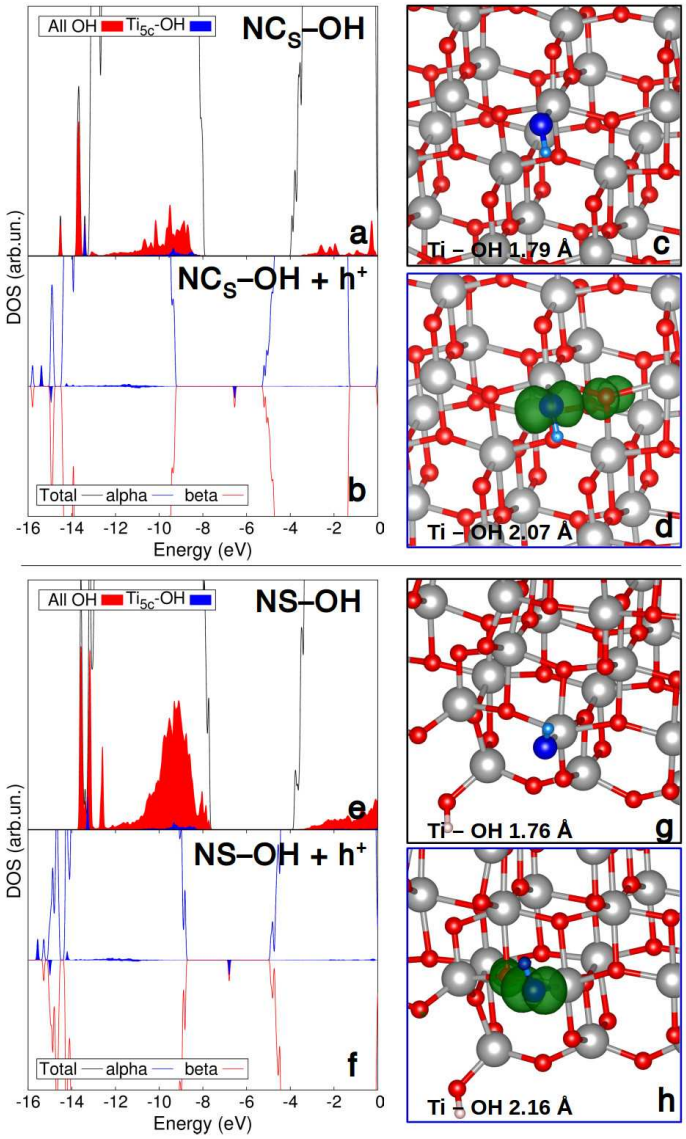

Figure 4.14 – Simulated total (DOS) and projected (PDOS) density of states on all the OH groups of the nanoparticle and on the specific trapping site, as calculated with the B3LYP functional, for the neutral $\mathbf{NC}_S$ and **NS** nanoparticles (a and e respectively) and for the same nanoparticles with an additional hole on the OH group (b and f). A 0.001 eV Gaussian broadening was used. The zero energy is set to the vacuum level. Ball-and-stick representation of a magnified portion of the neutral TiO_2 anatase faceted nanoparticle $\mathbf{NC}_S$ (c) and nanosphere **NS** (g) containing the extra OH bound to Ti_{5c}, highlighted in blue. Spin density 3D plots (isovalue = 0.005 a.u.) of the OH group when an electron is removed and the hole localizes on the hydroxyl group (d,h) are also given.

hole state is almost fully localized on the atoms of the hydroxyl.

Finally, if we compare the ionization potential energies for **NC**$_S$**–OH** and **NS–OH**, 7.72 vs 7.81 eV, we observe that these values are very close, because the chemical nature of the two Ti_{5c}–OH species in the differently shaped nanoparticles is very similar.

Comparison with experiments

Despite the many attempts, we could localize only deep hole traps, in line with the experimental measurements, where shallow hole traps were not observed. [23] The self-trapped hole at an O_{2c} site on the surface of both nanocrystals and nanospheres is the most stable. The calculated vertical electronic transition at this defect site is between 2.65 eV and 2.69 eV for faceted nanoparticles, in good agreement with the reported TA transition of 2.38 eV. [252] In the case of spherical nanoparticles, we computed a vertical transition from the VBM to the trap level of 2.59 eV, which is rather different from the experimental value of 1.9 eV by TA spectroscopy reported in literature. [253] This discrepancy may be related to the fact that these experiments were conducted on TiO_2 nanoparticles in an aqueous environment. Indeed, as we will discuss in detail in Section 4.5, the presence of water molecules close to the surface of the nanoparticle may enhance the trapping ability of the hydroxyl groups, through binding as a ligand to Ti–OH or H-bonding to the hydrogen of the OH.

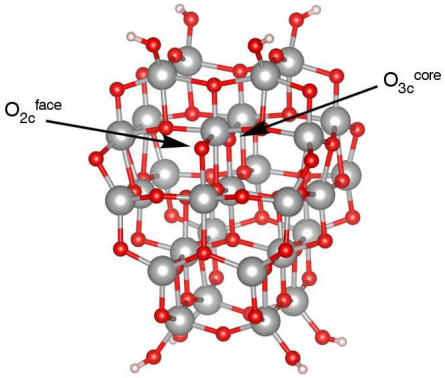

Figure 4.15 – Ball-and-Stick representation of the $Ti_{29}O_{58} \bullet 4\ H_2O$ cluster used for g- and A-tensor calculations. The oxygen atoms where the hole has been trapped are indicated by black arrows.

Neverthelss, the g- and A-tensor calculated for the self-trapped hole species (see Table 4.7) are in more than satisfactory quantitative agreement with the ones reported in the experimental literature. [80,248,249] This means that the computational models provide the correct degree of localization/delocalization of unpaired electrons. Note that the g-tensors have been calculated with the Gaussian09 code, as described in Section 4.2, using a smaller cluster, shown in Figure 4.15, carved from the faceted

Table 4.7 – g–tensor and hyperfine coupling constants (hpcc, in G) tensor with ^{17}O, decomposed as the Fermi contact term (a_{iso}) and the dipolar tensor (B) for an excess hole at the O_{2c}^{face} site in the $Ti_{29}O_{58}$ • 4 H_2O cluster, as calculated at the B3LYP/EPR–II level. Corresponding experimental data from literature for anatase nanoparticles are also given. The sites nomenclature is defined graphically in Figure 4.2 or in the text. Hyperfine coupling constants with ^{17}O for the various hole trapping sites in $\mathbf{NC}_S$ and **NS**, as calculated with the CRYSTAL14 code, are also given. The sites nomenclature is defined graphically in Figure 4.2 or in the text.

Position	g_{xx}	g_{yy}	g_{zz}	a_{iso}	B_{aa}	B_{bb}	B_{aa}
$Ti_{29}O_{58}$ • 4 H_2O cluster (Gaussian09)							
O_{3c}^{core}	2.004	2.015	2.019	−12	43	42	−85
O_{2c}^{surf}	2.006	2.017	2.020	−12	43	43	−86
Experimental							
Exp. O^-_{A1} [249]	2.004	2.019	2.019	±24	41	41	−82
Exp. O^-_{A2} [249]	2.004	2.014	2.014				
Exp. O^- [248]	2.003	2.015	2.027				
Exp. O^- [80]	2.007	2.014	2.024	±22	41	41	−82
$\mathbf{NC}_S$ (CRYSTAL14)							
O_{2c}^{face}				−36	45	45	−91
O_{2c}^{corner}				−30	−36	−36	72
O_{2c}^{edge}				−30	−38	−38	75
$O_{3c}^{core\_ax}$				−38	45	45	−90
$O_{3c}^{core\_eq}$				−36	42	42	−84
NS (CRYSTAL14)							
O_{2c}^{4c-6c}				−35	−87	43	44
O_{2c}^{5c-6c}				−35	44	-88	44
$O_{3c}^{core\_ax}$				−38	−89	44	44

nanocrystal and preliminary optimized with the CRYSTAL14 code. On the O_{2c}^{face} and O_{3c}^{core} sites, which are analogous to the ones of $\mathbf{NC}_S$ nanocrystal, an electron hole was then localized by Gaussian09 optimization and the EPR parameters were computed.

4.4.4 Distorsion due to the nanosize and trapping

In this section we will discuss the bond lenght distortions due to the nanoparticles size and how they may influence the energetics of the charge trapping process. As detailed in Section 3.3.3, in small faceted nanoparticles the close presence of surfaces, edges and corners affects the Ti–O and Ti–Ti bond distances with respect to the bulk values, even in the core of the nanocrystal. We shall recall that, with the present computational setup and the B3LYP functional, the Ti–O equatorial and axial bond distances in the relaxed bulk anatase TiO_2 are 1.94 and 2.00 Å, respectively, and the Ti–Ti equatorial distance is 3.79 Å.

In Figure 4.16, the compression/elongation of the equatorial Ti–O bond lenghts in several xy layers of $\mathbf{NC}_S$ are graphically shown by color-coding, together with relevant equatorial Ti–Ti distances. The values of these Ti–O and Ti–Ti distances are related to the electron trapping process since, as we have demonstrated in Section 4.4, it involves the d_{xy} orbitals. Note that these plots, as well as the ones in 4.17 have been generated with the procedure described in the Computational Details in Section 4.2.

Considering the first layer (Figure 4.16a), which corresponds to the central one of the **NC**, we can clearly observe that a Ti_{5c} atom at the border of the layer causes a shortening of the Ti–O bond underneath (red), which is counterbalanced by an elongation (blue) of the O–Ti_{6c} in the next inner bond. Similarly, following the Ti–O–Ti line towards the core, the subsequent Ti_{6c}–O distance is contracted, while the last O–Ti_{6c}^{core} is almost unaffected. On the whole, there is a compression of the innermost Ti–Ti distance to 3.72 Å, which is significantly shorter than the one in the bulk (3.79 Å). A shorter Ti–Ti distance reduces the possibility of the Ti–O bonds elongation, which is a necessary structural modification for the efficient trapping of an excess charge on titanium (electron) or on oxygen (hole) atoms. Furthermore, as shown in the previous sections, the extra charge has a tendency to localize on a Ti d_{xy} or on an O p_x (or p_y) orbital, hence the trapping process is very sensitive to equatorial distances. Therefore, we can argue that this short Ti–Ti distance provides a reason why no charge localization could be observed on the Ti_{6c}^{core} site of $\mathbf{NC}_S$ and the energy gain for hole trapping in $O_{3c}^{core\_eq}$ was lower than that computed for bulk anatase.

At the corner of the first layer, in correspondence to the Ti_{4c}^{corner} trapping site, we observe the highest shortening of the Ti–O bond (−0.16 Å) and Ti–Ti distance (to 3.65 Å). This high compression can explain the large distortion energy (ΔE_{dist}) and the low trapping energy calculated for this site and detailed in Section 4.4. Similarly, at the edge site in the fourth layer (Figure 4.16d, Ti_{5c}^{edge}) the neutral starting geometry is unfavorable for electron trapping because of a similar contraction of the Ti–Ti distance along the left-right direction (3.65 Å) and of two equatorial Ti_{5c}^{edge}–O bond lenghts out of three (red cylinders).

At the upper and lower borders of the second layer, there are O_{2c} species instead

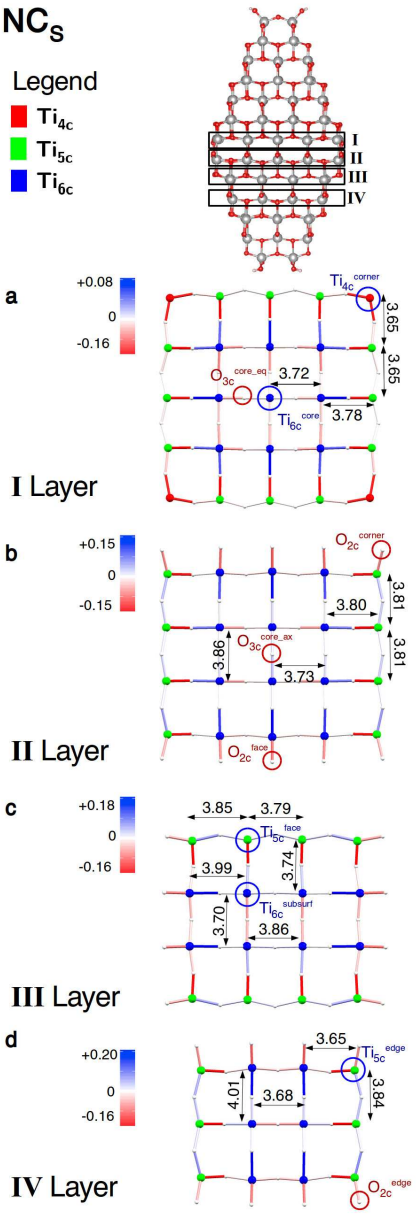

Figure 4.16 – Graphical representation of the elongation/compression of the bonds within four layers of the $\mathbf{NC}_S$ nanocrystal from the B3LYP bulk values for equatorial and axial distances, respectively. The elongation is given in shades of blue, the compression in shades of red, as indicated by the color scale close to each panel. Titanium atoms are colored according to their coordination patterns, following the color code on the upper left. Oxygen atoms are represented as small white balls. Atoms (labeled as in Figure 4.2 and 4.5) where the charge is highly localized are circled in blue (for electrons) or red (for holes). Distances between titanium atoms are in Å.

of Ti_{5c} ones (Figure 4.16b). In this case, along the up-down direction, the effect on the bulk-like distances in the core is opposite to the one of the first layer and the innermost Ti–Ti distance is significantly longer (3.86 Å) than in bulk anatase TiO_2. This is likely to be the reason why the hole is better trapped in $O_{3c}^{\text{core\_ax}}$, with higher energy gain with respect to $O_{3c}^{\text{core\_eq}}$ and the O_{3c} site in bulk anatase. In the same layer but in the other direction (left-right), the opposite tendency is observed with short Ti–Ti distance (3.73 Å) in the core of the nanocrystal. This is caused by the layer termination composed by Ti_{5c} atoms.

In the third layer (Figure 4.16c), an analogous but even improved behavior than in the second layer can be noticed, since the opposite facets are closer with shorter Ti–O–Ti chains from the borders to the inner part. As a matter of fact, in the up-down direction (Ti_{5c}–terminated) the distortions compress the innermost Ti–Ti distance to 3.70 Å, whilst the same distance in the left-right direction (O_{2c}–terminated) is 3.86 Å. Furthermore, Ti_{5c}–Ti_{5c} distances at the border are elongated, because the left-right lines terminate with O_{2c} species. This can explain why the Ti_{5c}^{face} is a good electron trapping site, since two out of three Ti–O distances in the equatorial plane are already elongated before electron trapping. Similarly, also the Ti_{6c}^{subsurf} site shows a good starting point for trapping an electron, because three Ti–O_{eq} bond lenghts out of four are stretched in the neutral geometry.

In Figure 4.17, a graphical representation of the polaronic distortions of the nanoparticle lattice for the electron (b and e) or hole (c and f) trapping on single sites sites in $\mathbf{NC}_S$ and **NS**, respectively, is given. A polaron is a quasi–particle which collectively describes the structural distortion (polaronic distortion) of a lattice due to the localization of an excess charge. The polaronic distortions related to shallow electron traps in $\mathbf{NC}_S$ and **NS** are also shown for comparison (a and d). In these 3D plots, the sticks representing the bonds are colored according to the relative elongation (blue)/contraction (red) with respect to the corresponding relaxed neutral geometry of the nanoparticle, whereas atoms are described by spheres of increasing diameter and darkness according to the amount of spin, i.e. excess electron or hole, localized on each atom.

As regards faceted nanoparticles, as already detailed in Section 4.4, the excess electron in $\text{Core}^{\text{deloc}}$ (see Figure 4.17a) is completely delocalized on the central three xy layers of the belt of the nanocrystal. Nonetheless, here we may also observe that the structural distortions are small (less than 0.02 Å in absolute value) but they involve a large part of the nanoparticle: in particular, all the bonds of the central layers and all the Ti–O bond lenghts along the vertical direction of the nanocrystal, with alternating elongation (blue) and contraction (red) effects. On the contrary, when the electron is trapped on a single site (see model b in Figure 4.17), the structural distortion is much more localized and affects only a very small region of the nanocrystal. The radius of this polaron is about 0.5 nm. Similarly, for the trapped hole (see model c in Figure 4.17), the polaronic distortion involves only a portion of the faceted nanoparticle close to the corner and the size of the polaron is below 1 nm in size.

As regards spherical nanoparticles, the delocalized electron (see model d in Figure 4.17) is slightly less delocalized than in the nanocrystal: the atomic spin density is not present in the outermost part of the three xy layers of the nanosphere involved in the hosting of the electron spin. In this case, the polaronic distortions are larger in

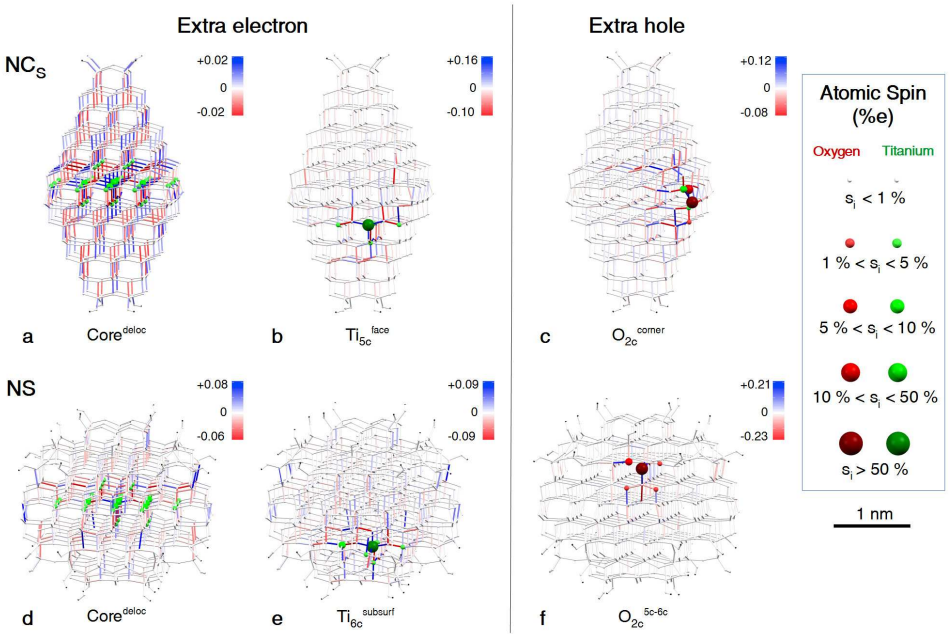

Figure 4.17 – Graphical representation of the elongation/compression of the bonds due to the polaronic distortion associated with the charge trapping in the $\mathbf{NC}_S$ nanocrystal and **NS** nanosphere. These 3D plots are obtained comparing the neutral B3LYP geometries with the ones with an excess trapped charge. The elongation is given in shades of blue, the compression in shades of red as indicated by the color scale close to each panel. Titanium and oxygen atoms are shown as spheres with a radius and color related to the degree of spin localization on each atom, according to the legend in the top right. The sites nomenclature is defined graphically in Figure 4.2 and 4.5 or in the text.

absolute value with respect to the nanocrystal, but confined only in the central three layers. When the electron is trapped on a single Ti center (see model e in Figure 4.17), only the next-neighbor titanium ions are involved in the trapping process and the structural distortion affects the bond distances within a radius of about 0.5 nm. Lastly, in the case of the trapped hole (see model f in Figure 4.17), the localization of the excess charge on the O_{2c} site is very high in terms of spin localization and in terms of polaronic distortion, since they involve only the first shell around the trapping oxygen atom, within a distance of less than 0.5 nm.

4.5 Effect of water on the hole trapping ability

As discussed above, a terminal hydroxyl group may trap an electron hole, even though its trapping ability is lower than that of a bridging oxygen on the surface of the nanoparticles. However, the presence of water layers may stabilize the hole trapped

at an OH group.

In order to elucidate the role of water on the charge carriers dynamics, we present a combined theoretical and experimental study in collaboration with research groups in Japan led by prof. Y. Matsumoto, which performed all the measurements of the water-dependent steady-state and transient infrared spectra of well-faceted and spherical TiO_2 samples. Firstly, the computed energetics and vibrational structure of adsorbed water at increasing coverage on decahedral and spherical TiO_2 nanoparticles are compared with pressure-controlled steady state infrared spectroscopy data in order to determine shape-dependent differences in the water adsorption modes. Secondly, the combination of this information with the calculated hole trapping abilities and experimental transient absorption (TA) spectra as a function of the water coverage allows to elucidate the role of additional water on hole trapping.

4.5.1 Vibrational analysis

Three different types of anatase TiO_2 nanoparticles were used for the experiments: decahedral anatase particles (DAPs), [257] octahedral anatase particles (OAPs), [258] and commercially available anatase nanoparticles (ST-01 of Ishihara Sangyo). High-resolution transmission electron microscopy (TEM) images of the three nanoparticles are given in Figure 4.18: DAPs (panel a) show both the most stable (101) and (001) anatase facets, whereas only the (101) one is observed in the TEM image of OAPs (panel b); on the contrary, ST-01 (panel c) particles do not have any facets with low Miller indices, but they present curved surfaces.

In Figure 4.18d, we show the diffuse reflectance infrared Fourier transform (DRIFT) spectra for the three nanoparticles as a function of water-vapour pressure. All of the three titania samples show three prominent absorption bands at 1500–1700, 2600–3650 and 3600–3750 cm^{-1}, which can be attributed to H_2O bending, hydrogen-bonded OH-stretching, and free OH-stretching bands, respectively. For free OH we intend the surface hydroxyls or water adsorbates that are not involved in hydrogen bonding. The H_2O bending band is derived from molecularly adsorbed water, whereas the latter two bands are contributed both from molecularly adsorbed water and surface OH groups. The water adsorbates responsible for the DRIFT spectra at $P \sim 0.01$ Pa are strongly bound species, [195] which we call hereafter A_0 species. Furthermore, through the analysis of the temperature dependence of adsorbate coverage under an adsorption-desorption equilibrium [195] at 0.01 Pa, we estimated that the adsorption energies of the A_0 species are in the range of 1.0–1.9 eV.

At $P = 100$ Pa, the surfaces of the three samples of nanoparticle are covered by 1 monolayer of additionally adsorbed water molecules. The difference spectra between 100 and 0.01 Pa are depicted in Fig. 4.18e. The observed spectral changes are reversible in terms of water-vapour pressure, demonstrating that the adsorbate responsible for the difference spectra is molecularly adsorbed water. Additionally, the estimated adsorption energy is $\sim$0.7 eV. We refer the water adsorbate responsible for the difference spectra to A_1 species. In this range of water pressure two spectral features are peculiar of ST-01 in comparison with DAP and OAP. First, A_1 species on ST-01 nanoparticles also show the OH-stretching band below $\sim$3100 cm^{-1} as in A_0 species. Second, a part of the free OH-stretching band around 3680 cm^{-1} of ST-01

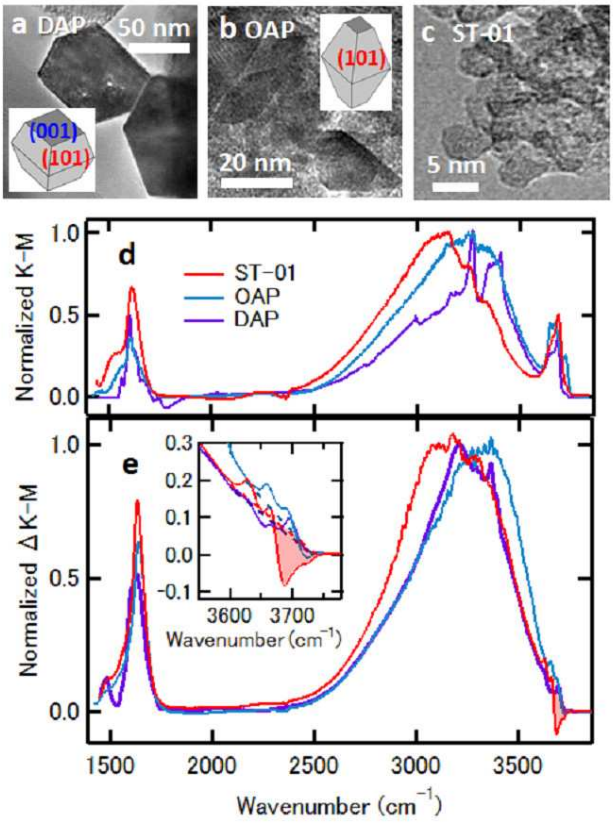

Figure 4.18 – Transmission electron microscope (TEM) images of DAP (a) and OAP (b) nanocrystals and ST-01 (c) highly curved nanoparticle. The corresponding diffuse reflectance infrared fourier transform (DRIFT) spectra for ST-01 (red), OAP (cyan), and DAP (purple) measured at water vapour pressure equal to 10^{-2} Pa are reported in panel (d). The Kubelka–Munk (K–M) is a measure of the intensity of adsorption and it is normalized at each peak of the hydrogen-bonded OH-stretching band. (e) Peak normalized difference spectra between 10^{2} and 10^{-2} Pa. In the inset of panel (e) an enlarged view of the difference spectra in the free OH-stretching band region is given.

is depleted upon water adsorption, whereas such a depletion in the free OH band does not occur in DAP and OAP. These findings suggest that surface species with a free OH on ST-01 nanoparticles are converted to other species with a significant red-shifted O–H stretching band below ∼3100 cm^{-1} upon hydrogen bonding with additional water. Since these changes associated with water adsorption occur on the surface of ST-01 but not on those of DAP and OAP, these red-shifted frequences are key to understand differences in the charge carriers dynamics as a function of the water coverage.

In order to clarify the observed infrared spectral features, we have performed hybrid

DFT calculations using the faceted and spherical anatase TiO_2 nanoparticle models.

We simulated faceted nanoparticles (DAP and OAP) with the nanocrystal model shown in Figure 4.19a, whilst spherical nanoparticles (ST-01) with that in Figure 4.19b. In particular, the model for nanocrystals is $(TiO_2)_{260} \bullet 6\ H_2O$ ($\mathbf{NC}_L$ in Section 3.3), whereas the model for the nanospheres is $(TiO_2)_{223} \bullet 18\ H_2O$ (**NS** in Figure 4.2). Note that, in order to avoid any spurious structural distortions during the optimization of water adsorbates, the nanosphere has been globally optimized with a DFTB-based simulated annealing analogous to that described in Section 3.5. After a subsequent B3LYP optimization run, the **NS** nanoparticle has been stabilized by −0.78 eV with respect to the "as-carved" **NS** employed in Sections 4.3 and 4.4. As discussed in Chapter 3, some intrinsic water is present on the surface of the nanoparticle models in dissociated form as terminal OH groups on Ti_{4c} (both in a and b) and Ti_{3c} (only in b).

As a further step, we investigate how an additional water would bind to the surface of these nanoparticles. On the faceted ones, water prevalently adsorbs molecularly on the Ti_{5c} of the (101) facets (by −0.91 eV) and very few water molecules dissociate on the four Ti_{4c} at the corners of the decahedron (red atoms in Figure 4.19), with a binding energy of −1.39 eV. Dissociative water adsorption also takes place on the anatase (001) facet, which is exposed by the DAP particles, resulting in two surface hydroxyls, with a binding energy of −2.68 eV (see model e in Figure 4.19).

On the spherical nanoparticles, a more complex scenario, depicted in Figure 4.20 is observed. A more detailed description of the single water adsorption on the TiO_2 nanosphere will be provided in Section 5.4 of the next chapter. Water is found to favorably dissociate on Ti_{4c} sites (binding energy from 1.1 to 2.0 eV) and to bind molecularly to Ti_{3c}–OH, Ti_{4c}–OH and Ti_{5c} sites (binding energy from 0.6 to 0.9 eV). Nonetheless, it is worth noting that some Ti_{5c} sites, whose vacant coordination position is axial, have a different coordination sphere than a Ti_{5c} site on regular (101) anatase surface, whose vacant coordination position is equatorial. On these specific Ti_{5c} sites water dissociation is found to be favored with respect to molecular adsorption. Lastly, further additional water may bind through H-bonding, either to the hydrogen of the Ti–OH groups or Ti–OH_2 or to surface bridging oxygen atoms (binding energy in the range between −0.5 to −0.7 eV).

The different types of water adsorption modes on the surface of the nanosphere can be assigned to the A_0 and A_1 families experimentally observed at low (0.01 Pa) and at higher water pressure (100 Pa), on the basis of the computed binding energy (BE) value: $|BE| > 0.7$ eV to A_0 family and $0.7\ eV \geq |BE| > 0.5$ eV to A_1 family, respectively.

The computed vibrational frequencies of several dissociated and molecular adsorbates are shown by lines in Figure 4.19c and 4.19d for the faceted and spherical nanoparticles, respectively. The detailed correspondence between each line and the vibrational mode of a specific adsorbate is reported in Figure 4.21 and Figure 4.22. Note that in the case of faceted nanoparticles, the reported lines correspond to the vibrational frequencies of the water mono- and bilayer on the (101) slab model together with the frequencies of water adsorbates on (001) surface (models e and f in Figure 4.19). In general, the calculated transitions are in very good agreement with the experimental spectra observed at 0.01 and 100 Pa for both ST-01 and DAP

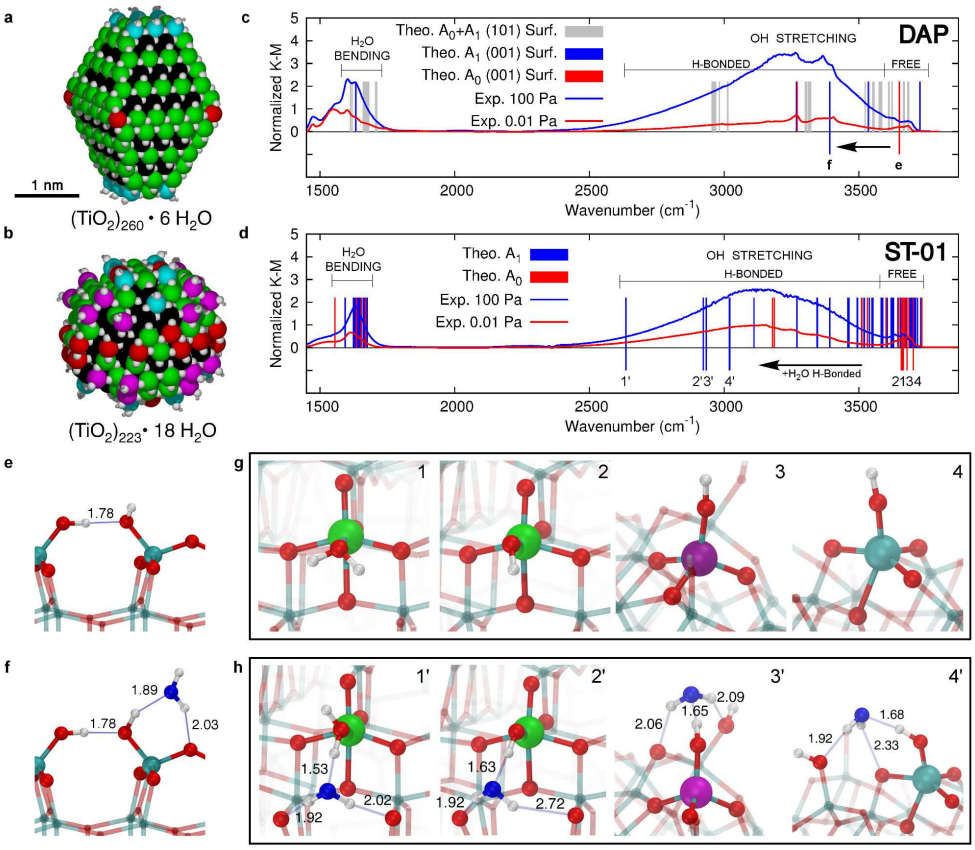

Figure 4.19 – (a,b) Space-filling representation of the faceted $(TiO_2)_{260}$ • 6 H_2O (a) and spherical $(TiO_2)_{223}$ • 18 H_2O (b) anatase TiO_2 nanoparticle models. Oxygen and hydrogen atoms are shown in white, titanium atoms are colored according to their coordination pattern: black for Ti_{6c}, green for Ti_{5c}, red for Ti_{4c}, magenta and cyan for Ti_{3c}–OH and Ti_{4c}–OH, respectively. In panel (c) is reported the comparison between the normalized experimental infrared spectrum of DAP nanocrystals at 0.01 and 100 Pa and the theoretical scaled frequencies of bending and O–H stretching for water adsorbates on the (001) and (101) anatase surface facets. The analogous comparison for water adsorbates on the spherical anatase nanoparticle model is given in panel (d). Black arrows in panel c and d highlight the redshift effect caused by hydrogen–bonded water (from red to blue lines) for some selected water adsorbates as depicted in panels e, f on the (001) facet of DAP and in panels g, h on the spherical anatase nanoparticle. The adsorption site and its next-neighbouring atoms are evidenced by larger spheres: Ti atoms are colored with the color-code mentioned above, H atoms are shown in white, lattice and hydroxyl O atoms in red, water O atoms in blue. Relevant hydrogen-bonds are represented by thin blue lines and distances are in Å.

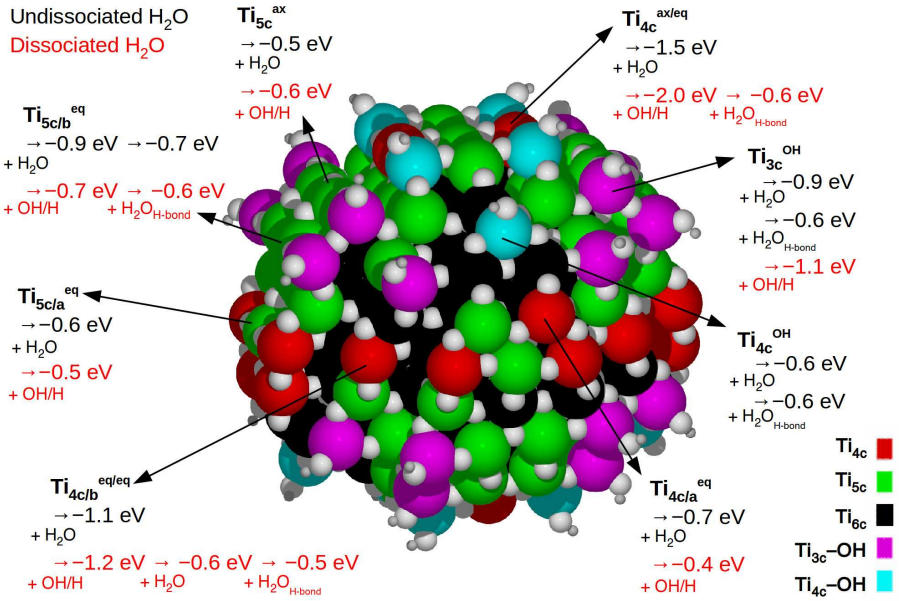

Figure 4.20 – Binding energy of water adsorbates on different sites on the surface of the **NS** model. The superscripts "ax" and "eq" stand for axial and equatorial, respectively, and they are related to the missing atoms in the coordination shell. The superscript "OH" is related to the presence on the Ti site of a hydroxyl group from intrinsic water. The labels "a" and "b" indicate atoms with a different second coordination sphere when the first is equal. Coordination number of each site is given by color coding.

nanoparticles.

Noteworthy, large red-shifts are computed when relatively strong H-bonding is established between the additional water and surface oxygen atoms or water adsorbates (H_2O or OH) on the surface of nanosphere. Specifically, after H-bonding with additional water, the stretching frequencies of free terminal hydroxyl at undercoordinated sites around 3680 cm^{-1} shift to wavenumbers below 3100 cm^{-1} (see black arrow in Figure 4.19d), in very good agreement with the difference infrared spectrum in Figure 4.18e, where the H-bonded band at ∼3100 cm^{-1} increases at the expenses of the free OH one at 3680 cm^{-1}. The water adsorbates characterized by the largest red-shift of the OH stretching frequency are depicted by ball-and-stick models before (1–4) and after (1'–4') hydrogen-bonding with an additional water molecule, in Figure 4.19g and h, respectively. On the nanosphere, the curved surface provides the local structures around terminal hydroxyls that allow the alignment of the $OH\cdots OH_2$ bond, which enhances the strenght of this H-bond. As commonly observed, [259] we noticed a clear correlation between H-bond distance and the extent of red-shift, which is shown for the current study in Figure 4.23. It is important to underline that the hydroxyl groups can only form strong H-bond with additional water molecules because the Ti–OH bond is not long enough to allow for large flexibility. Thus, they

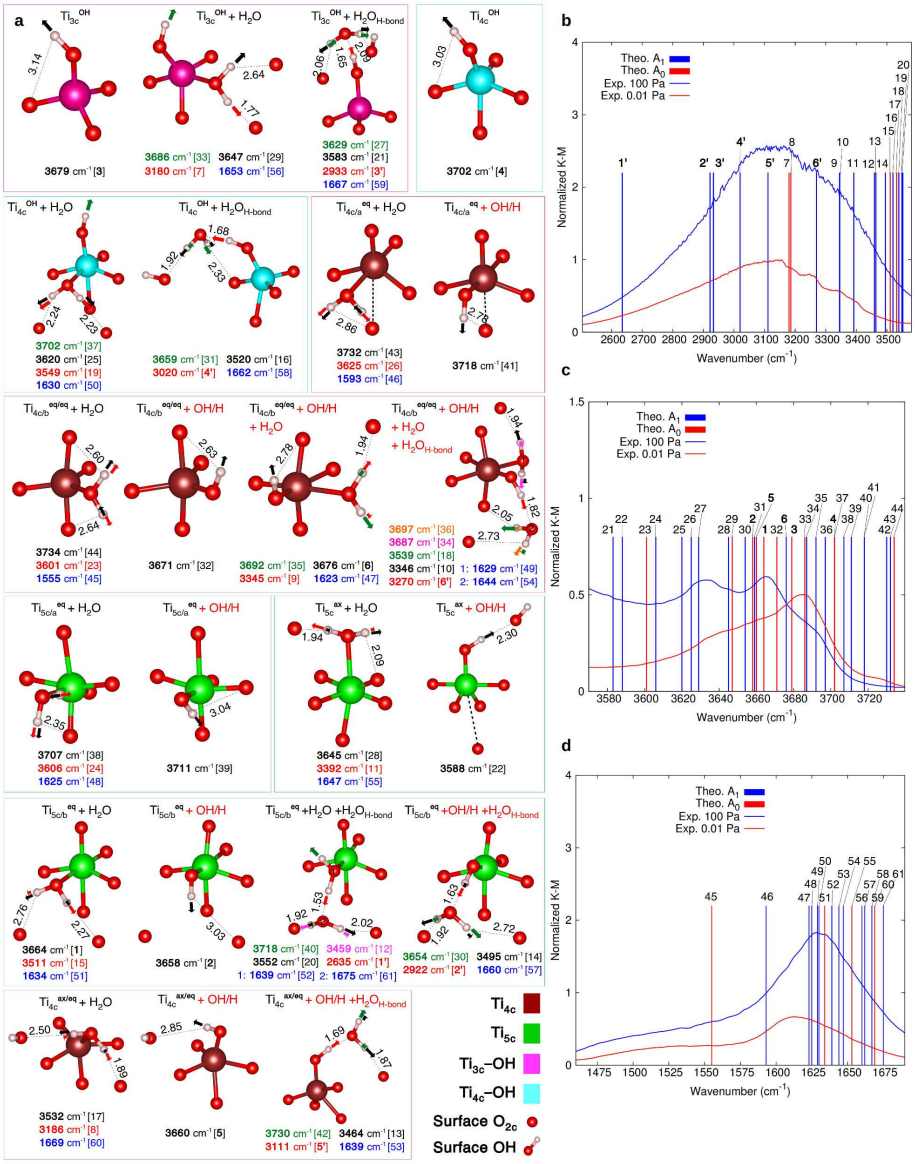

Figure 4.21 – Ball-and-stick models and wavenumber of O–H bond stretching and H_2O bending mode for water adsorbates on the different titanium sites of the spherical anatase nanoparticle model. The comparison between the experimental infrared spectrum of ST-01 at 0.01 and 100 Pa and the theoretical scaled frequencies of H-bonded OH stretching (b), free OH stretching (c) and H_2O bending (d) is also given. Numbers in bold refer to the free OH frequencies (1-6) that are significantly redshifted after H-bonding with additional water molecules (1-6). Ti atoms are colored according to the given color coding, H atoms are shown in white and O atoms in red.

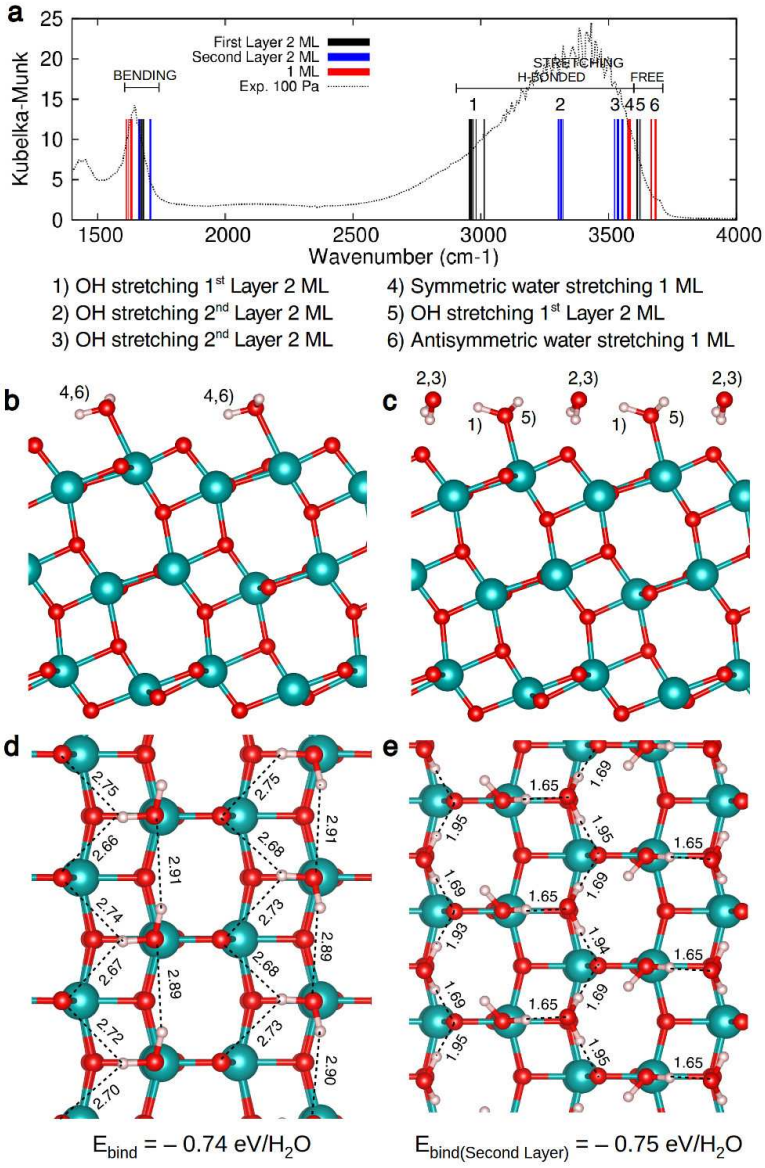

Figure 4.22 – Comparison between experimental infrared spectrum of OAP nanocrystal at 100 Pa and calculated scaled frequencies of the water adsorbates on a (101) anatase surface model. This is the most exposed surface on these anatase faceted nanoparticles. The frequencies have been assigned to stretching modes of the water monolayer (1 ML) or the first (1^{st}) of the second (2^{nd}) layer of the bilayer (2 ML). In bottom panels are reported the side and top view of the anatase (101) slab with a water monolayer (b and d) and bilayer (c and e) adsorbed on top. Absorption energies of the first and second water layer per water molecule are also given. Ti atoms are colored in cyan, H atoms are shown in white and O atoms in red. Distances in Å.

cannot establish H-bond with other surface hydroxyl groups, differently from the case of Ti–OH_2, where the bond is longer and more flexible.

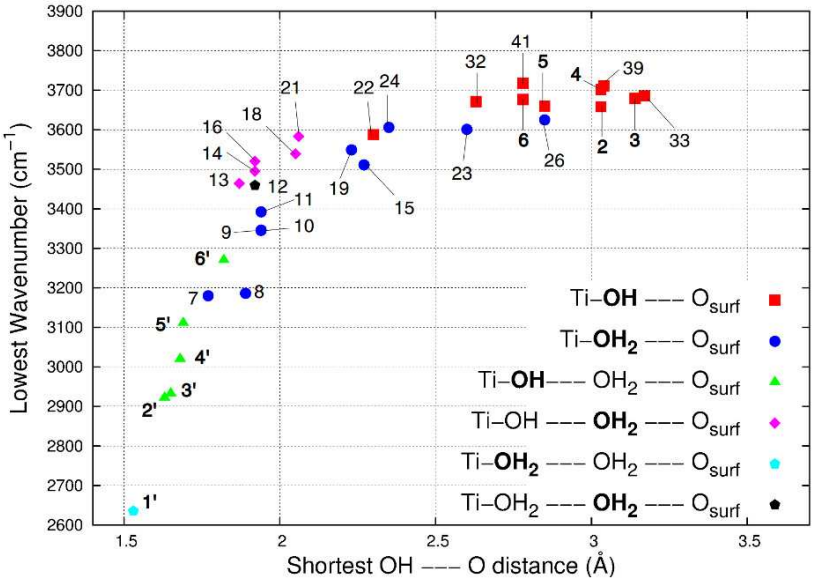

Figure 4.23 – Correlation between the lowest scaled stretching frequency of various water adsorbates on the nanosphere model and the shortest H-bond lenght the adsorbed water molecule (or OH) makes with vicinal oxygen atoms from the surface (O_{2c} or OH) or additional H_2O molecules. The atoms on which the vibrational mode is located are in bold in the legend. The numbers refer to the vibrational mode of each specific frequency, which are given in Figure 4.21.

On the contrary, even though free hydroxyls are present on a (001) facet of DAP as a consequence of the dissociative adsorption of water (see Figure 4.19e), the red-shift in the O–H bond stretching frequency upon water coordination (see Figure 4.19f) is much smaller than the one observed for nanospheres (see black arrow in Figure 4.19c) because the flat (001) surface forces the $OH\cdots OH_2$ H-bond to be bent, weakening the hydrogen bond. Therefore, calculations show that the hydroxyl groups whose frequency is significantly red-shifted upon H-bonding with additional water are present only on TiO_2 nanospheres.

4.5.2 Hole trapping mechanism

The dynamics of photoinduced charge carriers in the anatase TiO_2 samples were investigated by measuring time profiles of transient absorption (TA) as a function of the water pressure, as given in Figure 4.24. In fact, with this technique, it is possible to monitor photoelectrons with the IR probe, since extra electrons in the

conduction band and in shallow traps have a characteristic absorption band extending from near infrared to mid-infrared. [252, 260] Noteworthy, the intensity and the TA decay features of the faceted DAP and OAP nanoparticles are not affected by the increasing water pressure. On the contrary, the TA intensity for the round ST-01 nanoparticle significantly increases with water pressure, while the decay features were not sensitive to the pressure. These trends are made clear in Figure 4.24b, where the relative intensities of the decay are plotted against the water vapour pressure.

As discussed in the previous sections, photoinduced holes in anatase TiO_2 are trapped much faster than photogenerated electrons. [260, 261] Therefore, hole migration from the core to the surface of a nanoparticle, where they are preferentially trapped, is very fast. In the case that hole transport is accelerated because of the stabilization of hole at the surface, the electron-hole recombination in the core will decrease, hence the number of excess electrons in the core will increase. Therefore, the increase in the TA intensity of ST-01 at 4000 nm, where conduction band electrons mostly absorb, with increasing water vapor pressure implies that water adsorption improves the hole trapping ability at the surface of ST-01 nanoparticles. [195]

In the following, we refer this phenomenon to the water-assisted hole trapping effect. It is important to underline that this effect is reversible in terms of water-vapor pressure, indicating that no permanent changes in the structure of the nanoparticle are responsible for this effect. At this point, an important question to be answered concerns the reason why hole trapping probability of ST-01 is strongly enhanced by water adsorption, whereas no improvement with water adsorption has been observed for DAP and OAP faceted nanoparticles.

As detailed in the previous sections, there is a driving force for the hole to migrate from the bulk to the surface and we have found that the most stable surface-trapping site on a bare nanoparticle is a bridging O_{2c} atom. Furthermore, free hydroxyls have been found to be very poor hole trapping sites. Therefore, in vacuum conditions, where only surface hydroxyl groups from intrinsic water are present, holes are expected to be trapped at O_{2c} sites, either for faceted and spherical nanoparticles.

Increasing the water partial pressure, and consequently the coverage of water on the surface, the water-assisted hole trapping effect is not observed in the case of faceted nanoparticles (Figure 4.24b). There are several causes for that. First, on Ti_{5c} ions of the (101) facets water molecules do not dissociate but only adsorbs molecularly, as extensively reported in literature. [60,112–114,262,263] Molecular water molecules are not capable to trap an electron hole and hole-induced water dissociation is unlikely, since this process was found to be endothermic by 0.32 eV (Figure 4.25a,b), in line with a previous work. [125]

Second, molecularly adsorbed water on (101) facets was shown to be detrimental for hole trapping by O_{2c} species because they accept hydrogen-bonds from water molecules. [125] Therefore, the absence of any water-assisted effect indicates that hole trapping ability of O_{2c} is compensated by surface O_{3c}, which are also good trapping sites, being only 0.1 eV less efficient than an O_{2c} ion.

Third, water can be dissociatively adsorbed on (001) facets, which are widely exposed by DAP nanoparticles. Thus, we modelled water dissociation on the Ti_{5c} of the unreconstructed (001) surface slab, depicted in Figure 4.26a, as performed by previous theoretical works. [93, 121] Water exothermically dissociates and forms two

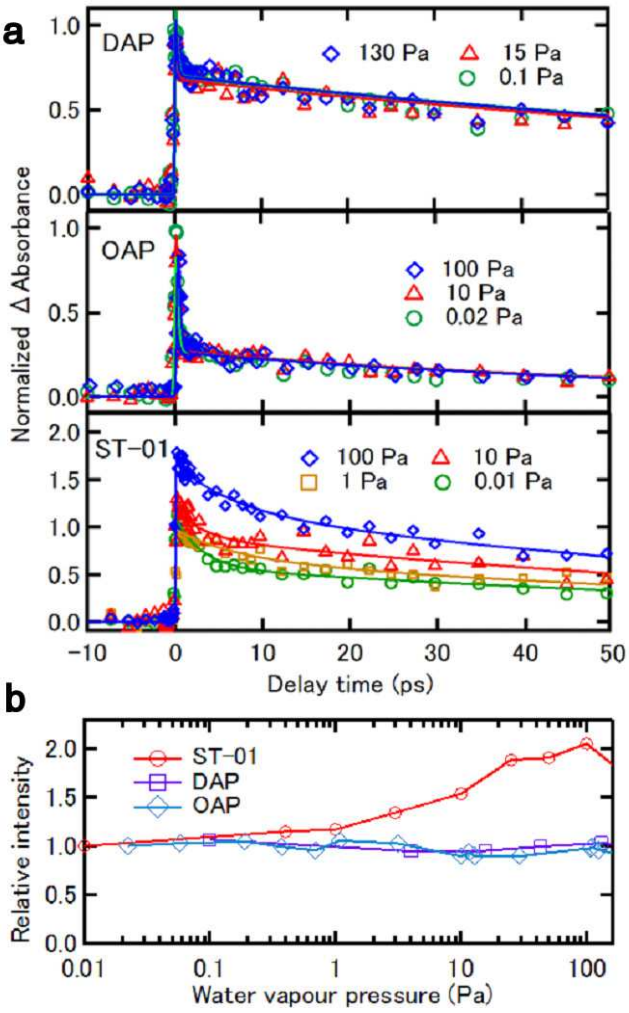

Figure 4.24 – (a) Time profiles of transient absorption of DAP and OAP nanocrystals and ST-01 highly curved nanoparticle excited with 400 nm pump and probed by 4000 nm probe light at various water pressures. Intensities are normalized at zero delay. (b) Intensities of the transient absorption profiles as a function of water-vapor pressure. Intensities of each sample are normalized at its lowest water vapor pressure.

facing hydroxyl groups (Figure 4.26b). The self-trapping of an electron hole at such hydroxyl groups requires the breaking of the hydrogen-bond between them, as shown by Figure 4.26c. Due to this positive energy contribution to the trapping energy, they are not good hole traps, being less stable by +0.34 eV with respect to a hole trapped on an O_{2c} of a (001) surface. The effect of additional water H-bonded to the hydroxyl is even more detrimental, since it increases the energy instability to +0.42 eV (see

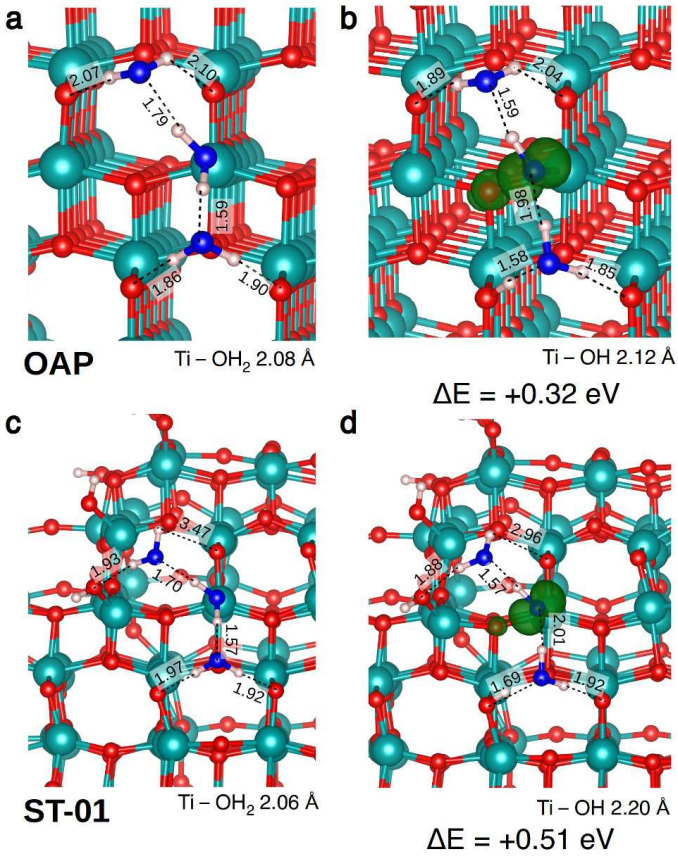

Figure 4.25 – Hole-induced water dissociation on a Ti_{5c} site on the (101) surface of the anatase TiO_2 nanocrystal (OAP in a, b) and nanosphere (ST-01 in c, d) models. In panels a and c are represented the two systems before dissociation, in which the central water molecule adsorbed on the Ti_{5c} site is molecularly adsorbed and the electron hole is trapped on the best trapping O_{2c} site of the nanoparticle, see Section 4.4.3. In panels b and d the electron hole is trapped on the hydroxyl group which results from the dissociation of water. The total energy difference for the whole process in the two cases is given. 3D spin density plots of the nanoparticles are reported with an isovalue of 0.01 a.u. Ti atoms are coloured in cyan, H atoms are shown in white and O atoms in red or in blue, in the case they belong to adsorbed water molecules. Relevant hydrogen bonds are depicted with black dashed lines and their bond lenghts are in Å.

Figure 4.26d).

Unlike faceted nanoparticles, the water-assisted effect is observed on spherical nanoparticles as a significant increase of intensity of slow component of the TA decay. In the following we will provide an explanation of that. First of all, water molecules dissociate on Ti_{3c}, Ti_{4c} and even some Ti_{5c} sites which miss an axial oxygen on the

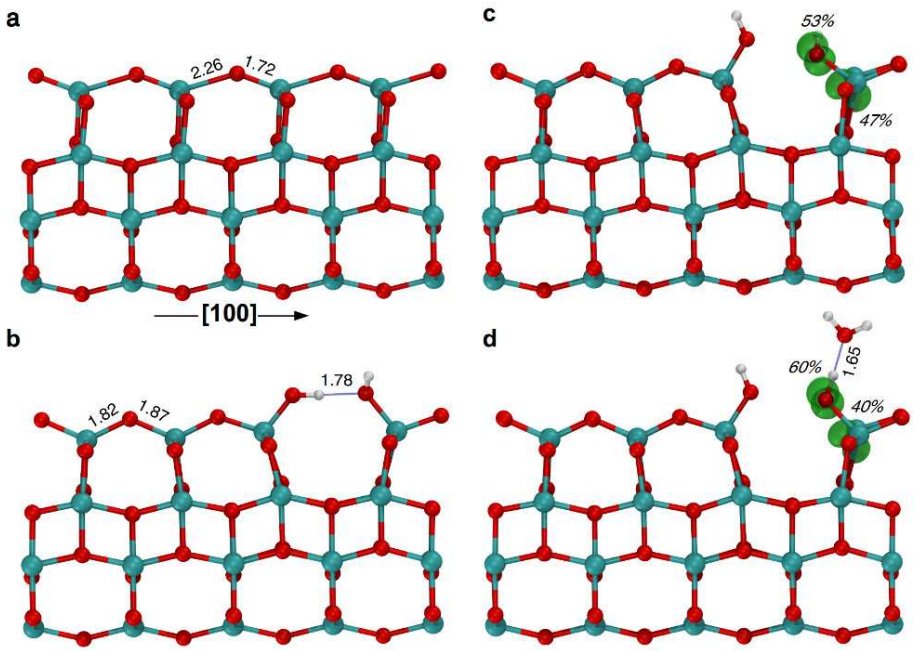

Figure 4.26 – (a) Ball-and-stick representation of the bare (001) surface, as obtained with DFT(B3LYP). (b) Structure of dissociated water on the anatase (001) surface. 3D spin density plot (isovalue = 0.01 a.u.) of the hole on anatase (001) surface, in the presence of only dissociated water (c) and with also an additional H-bonded water molecule (d). Relevant H-bonds are given in blue and distances are given in Å. The percentage values in italics are the atomic spins of the atoms which carry the hole. Red, cyan and white spheres indicate oxygen, titanium and hydrogen atoms, respectively.

nanosphere model. A considerable number of strongly bound isolated OH species are thus formed on the surface (A_0 species), which are capable to trap a hole, even though they are worse than an O_{2c} surface site (by +0.50 eV). Nevertheless, at this point the additional water (A_1 species) comes into play: additional water molecules assist the hole trapping process on OH species and enhance it, resulting in a larger hole trapping energy.

As shown in Figure 4.27, hybrid DFT calculations demonstrated that additional water may assist hole trapping in two ways: i) by binding as a further ligand to the low-coordinated Ti atom of the Ti_{3c}–OH or Ti_{4c}–OH hole trapping species and ii) by coordinating to the hydroxyl trapping species through rather strong hydrogen-bonding, which is responsible for the observed large red-shift in the OH stretching frequency in the DRIFT spectra.

As a matter of fact, the coordination of a water ligand to complete the coordination sphere of a Ti_{3c}–OH was found to enable its hole trapping ability, and in the case of a Ti_{4c}–OH to enhance it by −0.36 eV. The explanation is that the water ligand can

transfer some electronic charge to the titanium ion, resulting in a more electron rich OH species ($3a_1$ orbital of water $\rightarrow$ $d_{x^2-y^2}$ of titanium $\rightarrow$ $2p$ of the oxygen of the OH group) and this increases the OH trapping ability. This effect is demonstated by the energy shift of the empty (hole) state in the gap by +0.46 eV (compare Figure 4.27b with Figure 4.27c), showing a hole stabilization: the higher the hole energy level, the better the trapping.

Furthermore, a strong hydrogen-bonding of water to the hydrogen of the hydroxyl group favors hole trapping by about −0.15 eV, due to the formation of a bonding state between the σ_{OH} of the Ti–OH species and the $3a_1$ molecular orbital of H_2O (brown lobes in Figure 4.27d); this allows the electron transfer from H_2O to OH through the hydrogen-bond, as evidenced also by the elongation of the O–H bond distance by 0.06 Å. From the comparison between the projected density of states (PDOS) in Figure 4.27c with that in Figure 4.27d, we notice that the hydrogen-bonded water molecule lowers the energy of the OH states (red projections in the range between −15/−16 eV) close to the edge of the valence band. In the PDOS is clearly shown the position in the gap of the empty hole (h^+) state, which is fully localized on the O $2p$ state, since the red projection fills almost completely the hole peak. Thus, the electron transfer through the H-bond with the additional water molecule together with the elongation of terminal O–H bond stabilizes and localizes the hole on the oxygen atom of terminal hydroxyls.

Nevertheless, in order to induce successfull water-assisted hole trapping effect, another aspect of the H-bond with additional water must be considered. This crucial factor can be evidenced from the comparison of a surface hydroxyl on a nanosphere and on a DAP (001) facet, depicted in Figure 4.28b and Figure 4.28d, respectively. A surface OH group establishes a flexible hydrogen-bond network, that is highly influenced by hole trapping at the oxygen of the hydroxyl. Going from the neutral to the hole trapped charged system, that is from left to right of Figure 4.28 (b,c for nanosphere and d,e for (001) surface), two opposite behaviour are clearly observed: for nanospheres (blue curve in Fig. 4.28a), we notice an improved stabilization (ΔE) of the system upon hole trapping as a consequence of the strengthening of the hydrogen-bond net, as demonstrated by the shorter distances in Figure 4.28c with respect to Figure 4.28b; on the contrary, for DAP faceted nanoparticles, we observe a reduction of the stabilization by water because of the reduced number of hydrogen-bonds (one in Figure 4.28e, three in Figure 4.28d). In fact, the neutral state of the terminal OH on the (001) surface of DAP is stabilized through H-bonds with the neighboring OH and the additional water. Upon hole trapping, the terminal hydroxyl cannot donate anymore charge to the other OH bound to Ti, thus breaking this H-bond, but establishing a stronger and more directional hydrogen-bond with the additional water molecule (blue water in Figure 4.28). This strong H-bond lifts the water molecule from the surface towards the vacuum, with no chances of forming H-bonds with surface O_{2c} sites. Therefore, we highlighted a significant difference between spherical and faceted nanocrystallines in the local environments around the low-coordinated Ti–OH site. A favorable local structure is provided only by the highly curved surface of spherical nanoparticles, where an additional water molecule can establish strong H-bonds both to the substrate O_{2c} and to the terminal hydroxyl in the neutral state, and the robustness of this H-bond network is further improved in the charged state.

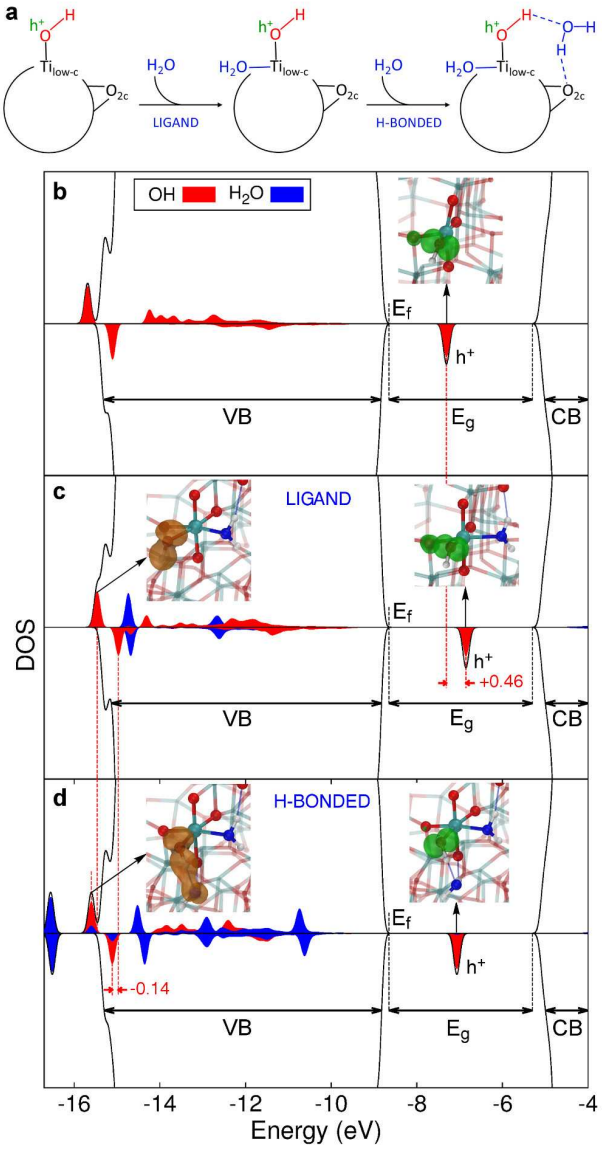

Figure 4.27 – (a) Scheme of the water adsorption on TiO_2 nanospheres and its effect on hole trapping ability. (b) Simulated total (DOS, black) and projected (PDOS, red and blue) density of states of the nanosphere with an excess hole in the $Ti_{4c}OH$ site and in the same site with an additional ligand water molecule (c), and with both an additional ligand and H-bonded water molecules (d). Dashed red lines are traced to highlight the energy shift (in eV) of the hole state (in b and c) and of the O–H bonding states (in c and d). In the insets on the right of (b), (c) and (d), the 3D spin density (in green, isovalue = 0.01 a.u.), representing the OH radical formed upon hole trapping, is given. In the left insets of (c) and (d) the alpha OH bonding orbital is represented with a $|\Psi|^2$ 3D plot (in orange, isovalue = 0.005 a.u). Next-neighbouring atoms are evidenced by larger spheres: Ti atoms are shown in cyan, H ones in white, lattice and OH O atoms in red, water O atoms in blue. Hydrogen bonds are shown by thin blue lines.

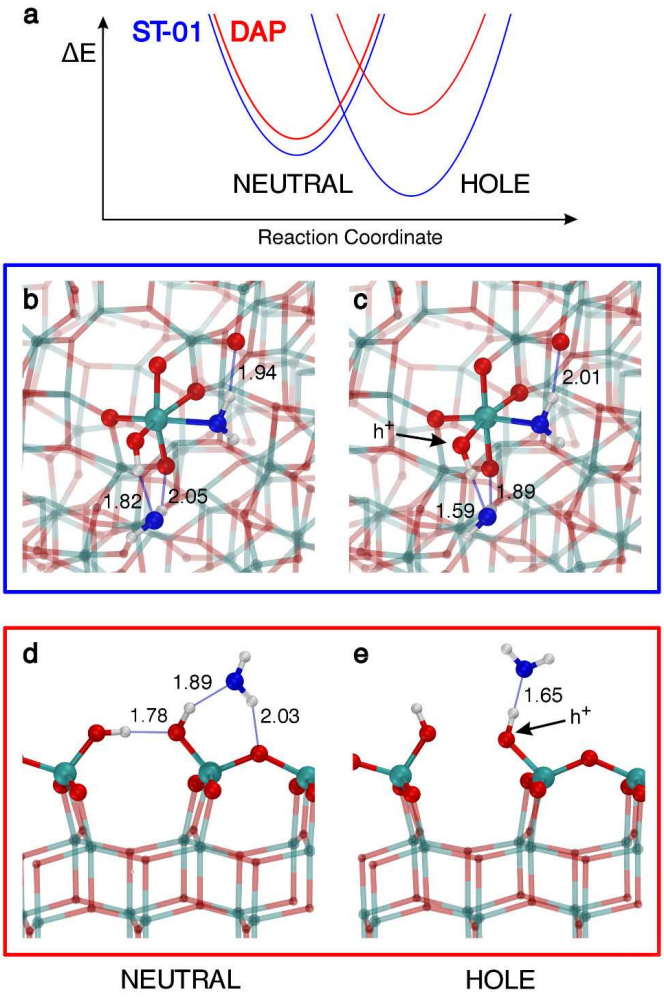

Figure 4.28 – (a) Schematic representation of the water stabilization energy (ΔE), due to H-bonds rearrangements, of the system before and after hole trapping for the spherical TiO_2 nanoparticle (ST-01, blue line) and the faceted one (DAP, red line). Ball-and-stick models of a hydroxyl on a Ti_{low-c} with an additional H-bonded water molecule on the spherical nanoparticle and the (001) surface before (b,d) and after (c,e) hole trapping at the OH group are also given. Next-neighboring atoms are evidenced by larger spheres: Ti atoms are coloured in cyan, H atoms in white, lattice and OH O atoms in red, water O atoms in blue. Relevant H-bonds are represented by thin blue lines and distances are in Å.

As a consequence, we show that for spherical nanoparticles (ST-01) there is an energy gain associated with the structural rearrangement upon hole trapping, whereas an energy loss is observed in the case of the (001) surface of faceted nanoparticles

(DAP).

4.6 Conclusions

In this chapter we presented a detailed study of the life path of energy carriers (excitons) and separated charge carriers (electron and holes), respectively, in realistic anatase TiO_2 nanoparticles by means of hybrid DFT (B3LYP), focusing on the effect of size, morphology (spherical vs faceted) and water environment. The use of a portion of exact exchange in the functional is crucial in order to account properly for the degree of localization/delocalization of the excess charges and the polaronic distortion accompanying their self-trapping at lattice sites.

In particular, we demonstrated that the photoinduced exciton self-trapping in the core of the nanoparticle is computed to be a favorable process for both morphologies and the full localization of the electron on a core Ti^{3+} ion and the hole on the O^- in axial position (Ti^{3+}–O^-) is the most stable configuration. If the exciton unbinds, the different situations, where the electron and the hole are localized in different positions, have similar energy. Nonetheless, for both shapes, there is a driving force for electron and hole migration towards the surface where they can be highly stabilized. Calculated photoluminescence emission energies for the self-trapped excitons in the core of **NC** and **NS** are in very good agreement with the available experimental literature.

Considering the behaviour of the separated charges, in the case of electrons in faceted nanoparticles, we observed both shallow trapping in the bulk-like part of the nanoparticles and deep trapping at five-fold surface or six-fold subsurface sites, in line with experimental findings, with a small but significant preference for electrons to migrate towards a surface trap from delocalized shallow traps in the central layers of the nanocrystal. Unexpectedly, we found that highly undercoordinated titanium ions at edge and corner sites are not capable of trapping. A similar scenario is observed for the excess electrons in spherical nanoparticles, but the electron localization is more effective in this case because of a less stable delocalized state on core titanium ions.

In the case of holes, only deep traps were observed and the O_{2c} surface species are the preferential sites for hole trapping. In particular, holes are preferential trapped by an O_{2c} ion at a corner site (Ti_{5c}–O–Ti_{4c}) in faceted nanoparticles and by a two-fold coordinated oxygen bridging a Ti_{5c} and a Ti_{6c} atom on the surface of spherical nanoparticles. Isolated OH groups have also been investigated as potential hole traps, but they were found to be less efficient by 0.1–0.3 eV than surface O_{2c}.

Calculated electron paramagnetic resonance (EPR) parameters and optical transitions for those electron/hole traps are in more than satisfactory agreement with experimental references. Furthermore, the computed trapping energies nicely correlate with the compression/elongation of the interatomic distances in the neutral geometry and the size of the polaron related to deep electron and hole traps is smaller than 1 nm.

As regards the effect of water on charge carriers dynamics, we performed a combined theoretical and experimental investigation, in collaboration with experimental groups in Japan, providing a comprehensive picture of the hole trapping mechanism

at the surface of differently shaped TiO_2 nanoparticles in the presence of gradually increasing water adsorbates. Through this two-dimensional approach, we proved that water adsorbates enhance the hole trapping ability of spherical nanoparticles, but do not affect that of faceted ones. On the low-coordinated titanium sites at the surface of spherical nanoparticles water molecules can easily dissociate forming superficial hydroxyl groups. The addition of further water molecules is found to play a fundamental role in improving the hole trapping ability of an OH group and, consequently, of the spherical nanoparticles either by binding as a ligand to the low-coordinated Ti_{4c}–OH or Ti_{3c}–OH site or by H-bonding directly to the OH group which traps the hole (see Figure 4.27a). Highly undercoordinated titanium sites are abundant on spherical nanoparticles, while they are very scarce on faceted ones. Additionally, the curved surface of spherical particles can provide local chemical environments around the terminal hydroxyl where robust hydrogen-bonds are formed with water adsorbate, resulting in considerably red-shifted O–H stretching bands. Therefore, there is a correlation between the number of red-shifted OH groups at the surface of nanosphere and the trapping ability of the nanoparticles: the higher is the number of red-shifted O–H stretching frequencies, the more abundant are good trapping sites.

To conclude, in the current chapter we provided new insights useful for the understanding of energy (excitons) and charge (electrons and holes) carriers in nanostructured TiO_2 with respect to the existing literature, where the attention is still mostly focused on bulk or extended surfaces. Here, we have shown in detail the effect of size, shape and water adsorption on the dynamics of charge carriers in TiO_2 nanoparticles. It is important to underline that the observations described above can be extended to other nanosystems of similar surface morphology. This study not only provides a molecular-level understanding of the photophysical processes in a metal oxide nanoparticle in vacuum and in presence of a water environment, but also suggest novel strategies for the surface engineering of photocatalysts.

5 Water Multilayers at the Interface with Anatase TiO_2 Nanoparticles

In this chapter,[†] the water/TiO_2 nanoparticle interface, which is extremely relevant for many modern technological applications, is investigated with a computational approach based on DFT and the less expensive self-consistent-charge density functional tight-binding (SCC-DFTB) methodology.

First, we develop and assess the accuracy of a novel SCC-DFTB approach for the description of the interactions between water and TiO_2. Then, using this new methodology, along with high-level hybrid DFT calculations, realistic TiO_2 nanosphere models at the interface with water layers are studied.

5.1 Introduction

The interaction between water and titanium dioxide nanoparticles plays an important role in many TiO_2-based technologies, [58] being normally performed in an aqueous medium or humid environment. [15, 21, 24, 25, 264] Even in the recent research field of TiO_2 materials for biomedicine, [31] the properties of this solid–liquid interface is of paramount importance, since the interaction with biomolecules and polymer coatings is in competition with water adsorption or may be mediated by it. [265–268].

In the last decade, the structure of water layers on the (101) anatase surface has been elucidated by several works based on ab initio Car-Parrinello molecular dynamics. [117–119] These works highlighted that water adsorption is governed by a complex and delicate interplay of many factors, such as the structural features of the surface and the relative strength of water-water and water-titania interactions. The molecular mode of water adsorption was always computed to be favored with respect to the dissociated one on the stoichiometric anatase (101) surface, in line with experimental observations. [112, 113].

[†]The results described in this Chapter have been reported in: D. Selli, G. Fazio, G. Seifert, C. Di Valentin, *J. Chem. Theory Comput.* **2017**, *13*, 3862–3873; G. Fazio, D. Selli, C. Di Valentin, "Fully dehydrated curved TiO_2 nanoparticles do not exist: modelling single water molecule, mono and multilayer coverage of realistic nanospheres", *in preparation.*

However, the fundamental building blocks of the modern technological applications are not extended surfaces but the TiO_2 nanoparticles, which may present peculiar wetting properties, [128] due to the size and shape effects and the characteristic surface structure described in Chapter 3 and 4. However, the dynamical study of realistic nanoparticles in a aqueous environment, with an appropriate time and size scale, is not feasible by means of density functional theory (DFT) calculations.

Self-consistent-charge density functional tight-binding (SCC-DFTB) methodology, as already discussed in Section 2.3, is a computationally efficient approach based on DFT, from which it retains much of the physics. [169, 269] As a matter of fact, this method has been shown to be about 2 to 3 orders of magnitude faster than standard DFT with a medium basis set size, [170, 270, 271] with no significant loss of accuracy in many biochemistry, organic and inorganic materials chemistry cases. [169,270,272–277] Thus, this approximate-DFT method can be applied to the accurate investigation of systems up to some thousands of atoms, as already demonstrated in Chapter 3. Importantly, unlike molecular mechanics (MM) methods, SCC-DFTB is also able to describe bond breaking and formation processes and, in analogy to DFT, all the electronic properties, such as electronic structure and optical spectrum. [169, 270, 271, 278].

As detailed in Section 2.3, the parametrization of the SCC-DFTB approach is limited to a small number of element and element-pair dependent parameters. Even though they are, in theory, meant to be transferable between different contexts, in practice, the accuracy of the results depends on the system and it is not universal. Therefore, it is crucial to evaluate the reliability of a certain parametrization scheme for a class of systems before exploiting it for more complex models: in the present case we will test it for the flat TiO_2 surface/water interaction and then use it for large TiO_2 nanoparticles/water interfaces.

Currently, two sets of parameters are publicly available for the study of Ti-containing compounds: [279]

- "tiorg-0-1": [197] this set is an extension to include the Ti–X pairs of the "mio-1-1" set, [169] developed for the main group elements and extensively benchmarked for organic molecules [272,274,280] and biological systems. [172,271,281] Using this set, the SCC-DFTB results have been found to agree with full DFT and experimental data for small $(TiO_2)_n$ molecules, bulk properties, surface energies and water adsorption on selected low-index surfaces of both anatase and rutile. [197, 282–285] Nonetheless, to the best of our knowledge, a clear benchmark of this set of parameters for the most exposed (101) anatase surface has not been published yet.

- "matsci-0-3": [187] this set has been parametrized specifically for materials science and solid-state simulations. Its reliability for bulk anatase and rutile and the chemical reactivity of (101) anatase and (110) rutile surfaces towards water (up to monolayer coverage) and simple organic molecules has been previously demonstrated. [187, 286]

However, the description of the adsorption and the dynamics of water multilayers on an oxide surface requires also a proper modeling of water part, i.e. of its local

structure and hydrogen bonding. To this end, the "mio-1-1 set" [169] has been already been largely tested for water or solvated models. [287–290] This parameter set has been shown to satisfactory reproduce the geometries of large water clusters, although it systematically underestimates hydrogen bonding distances and energies. The energetics and dynamics structure of water can be considerably improved with a-priori or empirical modifications of the original SCC-DFTB scheme. [291–295] On the contrary, the "matsci-0-3" set of parameter was not devised to describe the water/water interaction and no assessment on its performance is present in literature.

In the following, we have compared the static and dynamic behavior of the water/titania interface as obtained by the two available sets of DFTB parameters, with respect to DFT and experimental results from literature. [112, 117, 118, 296] Then, the successes and failures of both sets have been highlighted and, as a next step, a new set of parameters (called hereafter "matorg") has been defined as a combination of the best parameters from both sets. In particular, the "matsci-0-3" set has been found to better describe the titania/water interaction, while the "mio-1-1" set provides a more accurate evaluation of the water/water interaction, especially when an additional empirical correction [173] is included to better describe the hydrogen bonding.

The combined new set of parameters, that we have called "matorg+HBD" (MATORG+HBD), perform incredibly well for the description of water/water/(101) anatase TiO_2 interactions, when compared to high-level DFT-GGA calculations, but at an extremely reduced computational effort. Therefore, we employed this reliable tool for the static and dynamic study of a realistic TiO_2 spherical nanoparticle in contact with an increasing amount of water, from a single molecule adsorption to a full three-layer coverage. Moreover, the electronic and structural properties of the hydrated nanoparticle have been investigated at a full hybrid DFT level up to the monolayer coverage, providing highly accurate results to be compared with experimental references. Finally, molecular dynamics simulations of water multilayers on the TiO_2 nanoparticle have been performed with the MATORG+HBD approach in order to elucidate the dynamic structure of the hydration layers around a titanium dioxide nanosystem in an aqueous environment.

5.2 Computational Details

In this section, we will specify the computational methods, the models and the settings that have been used for the calculations presented in this Chapter. For a detailed discussion on the theoretical approaches see Chapter 2.

SCC–DFTB parameters

The SCC-DFTB approach has been used for the calculations of the water/TiO_2 interface within the DFTB+ simulation package. [186] First, we employed both the publicly available [279] Slater-Koster (SK) parameter sets for Ti-containing compounds, i.e. the "mio-1-1/tiorg-0-1" (TIORG) [197] and the "matsci-0-3" (MATSCI) [187].

Subsequently, we have combined the two sets of parameters in what we called "matorg" (MATORG) set as shown in Figure 5.1: all the SK files involving the Ti

atom (Ti–Ti.skf, Ti–O.skf, O–Ti.skf, Ti–H.skf and H–Ti.skf) were taken from the MATSCI set, whereas the SK files relevant for water systems (O–O.skf, O–H.skf, H–O.skf and H–H.skf) were extracted from the TIORG set. Note that the parameters for oxygen and hydrogen on-site and element-pair interactions are the same in the "mio-1-1/tiorg-0-1"(TIORG) and "mio-1-1" (MIO) [169] set, since the former is just an extension of the latter. Once that the Slater–Koster files have been combined, the phase of the integrals ($H^0_{\mu\nu}$ and $S_{\mu\nu}$ in Eq. 2.45), i.e. the sign of the Hamiltonian and overlap matrix elements as a function of the distance, has been checked to be equal to the one of the original MATSCI file. As graphically represented in Figure 5.1, just in the case of the O–H.skf and H–O.skf files the sign of the integrals between the TIORG and MATSCI SK file has been found to be different and changed accordingly to match the original sign of the MATSCI integrals in the new MATORG set.

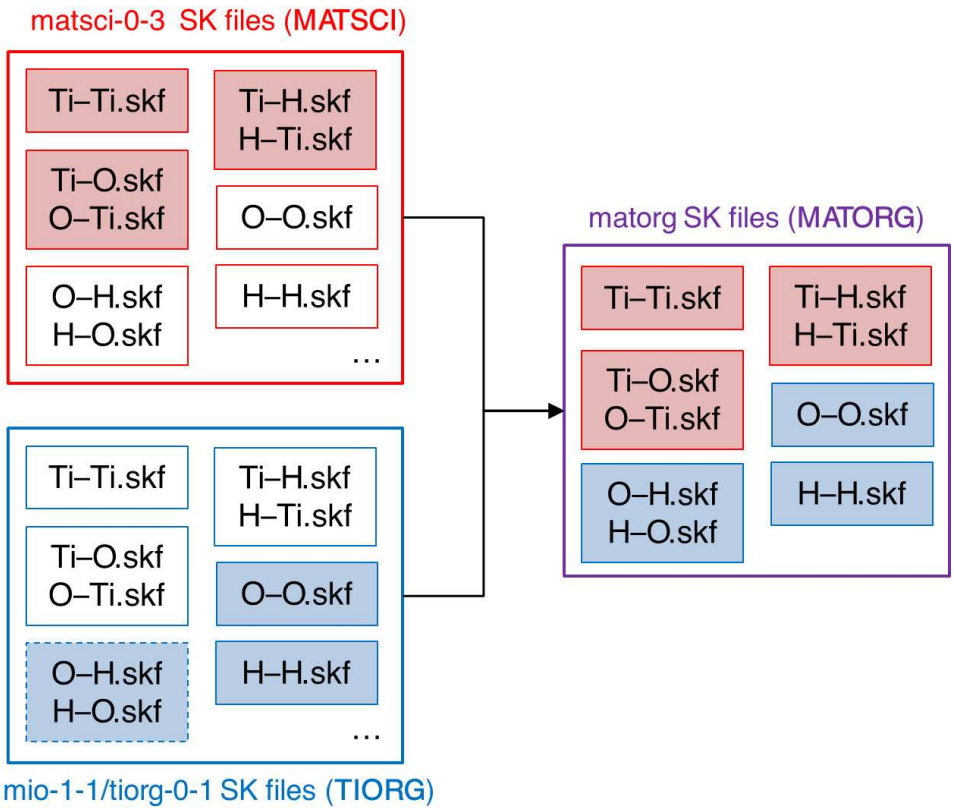

Figure 5.1 – Construction of the new MATORG parameters set from the MATSCI and TIORG Slater–Koster files. The dashed frame for the SK file indicates that the sign of the integrals is the opposite with respect to the MATSCI one.

Furthermore, we made use of the hydrogen bonding damped (HBD) modified γ function, as detailed in Section 2.3. The additional parameter ζ in the γ function has

been set to 4, in line with the original paper from Hu et al. [291], since it results in a more than satisfactory value of the hydrogen bond energy (see Table 5.1). From now on, we refer to this combined Slater-Koster file set with the HBD correction as MATORG+HBD.

Setup for the electronic structure calculations

For bulk anatase calculations, we employed a $16 \times 16 \times 16$ Monkhorst-Pack grid for k-point sampling. The lattice parameters of the optimized unit cell were obtained using the lattice optimization algorithm, as implemented in DFTB+. For the modeling of the (101) anatase surface, we used a three-triatomic-layer slab where the bottom layer has been kept fixed to the optimized bulk positions during the geometry relaxation. In order to investigate the static properties of this surface (coverage dependent water binding energies and equilibrium geometries), we used a 72 atoms 1×2 supercell model and a $2\times2\times1$ Monkhorst-Pack k-point mesh grid. In all the optimization runs within DFTB+, forces were relaxed to less than 10^{-4} a.u.

Reference DFT calculations were performed with the Quantum ESPRESSO simulation package, [297] using the standard PBE functional. [144] The anatase (101) surface models were analogous to the ones used for the density-functional tight-binding approach. Electron-ion interactions were described by ultrasoft pseudo-potential, the cut off in the plane-wave basis set was set to 30 Ry (300 Ry for the charge density) and the Brillouin zone sampling employed a $2 \times 2 \times 1$ Monkhorst-Pack k-point mesh grid. Forces were relaxed to less than 0.005 eV/Å. Periodic replicas were separated by 20 Å of vacuum in the direction normal to the surface to avoid any interactions between periodic images.

In the 1×2 supercell (101) anatase model there are four surface 5-fold coordinated cationic Ti (Ti_{5c}) atoms, which are active sites for water adsorption. Also undercoordinated 2-fold coordinated O (O_{2c}) atoms, connecting superficial Ti atoms, may be involved in the interaction with the water molecules by forming H-bonds or accepting the protons of the dissociated water molecules. The binding energy of n_{mol} molecules on the surface is defined as:

$$\Delta E_{ads} = E_{slab+n_{mol}} - (E_{slab} + n_{mol} E_{mol}) \tag{5.1}$$

where $E_{slab+n_{mol}}$ is the total energy of the global system with the slab and the adsorbed molecules, E_{slab} is the energy of the bare surface slab, n_{mol} is the number of molecules bound to the surface and E_{mol} is the total energy of a single molecule in the gas phase. In order to allow the comparison of the results for different water coverages, we also defined a per-molecule adsorption energy ΔE_{ads}^{mol} as follows:

$$\Delta E_{ads}^{mol} = \frac{\Delta E_{ads}}{n_{mol}} \tag{5.2}$$

Lastly, we evaluated the absolute error (ε) of the calculated SCC-DFTB values (v) with respect to the reference DFT ones (v_{ref}) simply as a difference between the two values:

$$\varepsilon = v - v_{ref} \tag{5.3}$$

All the DFT geometry optimizations and electronic structure evaluations on the TiO_2 nanoparticle model have been carried out with the CRYSTAL14 code, [185] employing the B3LYP functional and the same computational settings as in Section 3.2, as regards the basis set and the thresholds for the convergence of the SCF and the geometry optimization. Simulated total (DOS) and projected (PDOS) densities of states of the nanoparticles have been computed through the procedure detailed in Section 3.4.3, using a value of 0.001 eV for the σ of the Gaussian peaks in the convolution. The simulated EXAFS spectra, as well as the surface areas (S_{Conn}), have been calculated with the same procedures detailed in Chapter 3.

Nanoparticle models

In Section 5.4, we will use the anatase TiO_2 nanosphere model (**NS**) with a size of 2.2 nm and a stoichiometry of $(TiO_2)_{223} \bullet 10\ H_2O$, which has been described and widely analyzed in Chapter 3. For the DFT(B3LYP) and MATORG+HBD calculations on this model, the optimized structures with the corresponding methods were employed. The faceted anatase TiO_2 nanoparticle model (**NC**) used is the $(TiO_2)_{260} \bullet 6\ H_2O$, which has been refered to as $\mathbf{NC}_L$ in Chapter 3.

Starting geometries for the optimization of the adsorbed water monolayer have been constructed by saturating molecule by molecule the undercoordinated titanium atoms on the surface of the **NS** model. Instead, the initial geometry for the water multilayer on the **NS** model has been built with the PACKMOL code. [298] Using this program, a spherical water shell with an internal radius of 15 Å and external radius of 21 Å has been generated around the **NS** with an optimized water monolayer already adsorbed. The water shell has been filled with 824 non-overlapping water molecules, corresponding approximately to three water layers with a density of 0.0334 molecules/$Å^3$ (1 g/cm^3).

Molecular Dynamics setup and structural analysis tools

For the SCC-DFTB molecular dynamics of bulk water we adopted a multistep procedure. First, we have created a box containing 113 water molecules and performed a Born-Oppenheimer molecular dynamics simulation in the NPT ensemble in order to compute the correct volume of the box. A Nosé–Hoover chain thermostat and barostat have been employed to reach the equilibrium state at 1 atm and 300 K. This pre-equilibration simulation run was carried out for 10 ps and resulted in a box of 1.49 nm^3 and a corresponding density of water of 1.004 g/cm^3. Second, by means of a Born-Oppenheimer molecular dynamics simulation the system has been further equilibrated within the NVT ensemble at 300 K for 20 ps. Finally, the system has been let evolve in the constant NVE ensemble for other 20 ps, producing the data used to calculate the radial distribution functions (RDFs). The integration of the Newton's equations of motion were performed with the Velocity Verlet algorithm and a time step of 1.0 fs was used to ensure reversibility. This time step is relatively small compared to the typical time of the fastest motion, i.e. OH stretching ($\approx$ 10 fs), and it is commonly used for molecular dynamics simulation of water systems. [290, 291, 294]

A larger 1×3 supercell (101) anatase slab model (108 atoms) was employed for the molecular dynamics simulations of the water/TiO_2 surface interface. A Monkhorst-

Pack k-point mesh of 2 × 2 × 1 ensured the convergence of the electronic structure. We have investigated a monolayer (ML), a bilayer (BL) and a trilayer (TL) of water, composed by 6, 12 and 18 water molecules, respectively. In the case of the water/TiO_2 molecular dynamics, the Newton's equations of motion were integrated with the Velocity Verlet algorithm using a time step of 0.5 fs to ensure reversibility. The simulations were run in the NVT ensemble and a Nosé-Hoover chain thermostat ensured the equilibration to a constant temperature (160 K). This value has been chosen to avoid the desorption of superficial water molecules, as already done by some previous works. [117–119] After 5 ps of equilibration, the systems were allowed to evolve for other 20 ps.

Born-Oppenheimer MATORG+HBD molecular dynamics (MD) of the water multilayers on the **NS** model has been carried out within the canonical ensemble (NVT). The same integration algorithm and step used for the anatase (101)/water interface have been employed in the case of the nanoparticle. During the MD simulation, a constant temperature of 300 K has been kept by using the Nosé-Hoover thermostat. The system has been equilibrated for 5 ps and, then, a production run has been performed for 45 ps. No water molecules have been observed to desorb from the system into the vacuum.

The $g(d)$ function has been calculated by determining the MD-averaged number of water molecules within a distance d and $d + \Delta d$ away from the nanoparticle surface. The distance d is defined as the minimum value of the distance between the oxygen atom of water (O_w) and the superficial titanium atoms (Ti_{sup}). For a detailed definition of Ti_{sup} see Section 3.5.2. Note that for each value of d the $g(d)$ distribution is normalized for the volume of a spherical shell with a thichness Δd.

The θ angle is defined as the angle between the radial vector, i.e. the vector that connects the oxygen of the water molecule to the center of the nanoparticle, and the O–H bond vector. The radial vector is translated so that it has the same origin than the O–H bond vector. When an undissociated water molecule is considered, both O–H vectors are taken into account. Each point of the $P(\cos\theta)$ probability distribution is constructed by normalization of the number of times that the value of $\cos\theta$ is between $\cos\theta$ and $\cos\theta$+0.02 in the molecular dynamics simulation.

Transition State Search

The transition state for dissociation of an adsorbed water molecule on the 1 × 2 model has been evaluated with the Nudged Elastic Band method, [178] as described in detail in Section 2.4.3. This methodology is implemented in the Atomic Simulation Environment (ASE) toolkit, [188] which is capable to interface an external total energy calculator (the DFTB+ program in this case) with an internal NEB optimizer.

The NEB procedure was performed employing 20 intermediate images. At the end of the NEB calculation, we have computed the Hessian matrix for the transition structure to confirm that the structure was a saddle point on the potential energy surface. The reaction barrier for the dissociation process is defined as follows:

$$E^{\ddagger}_{\mathrm{diss}} = \mathrm{E_{TS}} - \mathrm{E_{slab+mol}} \tag{5.4}$$

where $\mathrm{E_{TS}}$ is the energy of the transition state structure and $\mathrm{E_{slab+mol}}$ is the total

energy of the optimized geometry of molecular water adsorbed on the titania surface slab.

5.3 Assessment of a DFTB-based method

In order to provide a correct description of the water/TiO_2 (101) anatase surface interface, the methodologies must appropriately describe the two separate components. First, we focused on the liquid component of the interface: water.

5.3.1 Water dimer and bulk water properties

We evaluated the strength of a single hydrogen bond ($\Delta E_{H\text{-}bond}$) as the binding energy of a dimer of water molecules. In Table 5.1 we report the values of $\Delta E_{H\text{-}bond}$ and the equilibrium oxygen-oxygen distances ($R_{O\text{–}O}$), as obtained with the SCC–DFTB approach using MATSCI, MIO and the combined MATORG+HBD sets of parameters. As a reference, we show also the corresponding values obtained with the post-Hartree-Fock CCSD method [299] and density functional theory with standard GGA and hybrid functionals. [300] Experimental values, measured by velocity map imaging [301] (for $\Delta E_{H\text{-}bond}$) and molecular beam electric resonance spectroscopy [302] (for $R_{O\text{–}O}$) are also given.

Table 5.1 – Hydrogen–bond energy ($\Delta E_{H\text{-}bond}$) and oxygen-oxygen distance ($R_{O\text{–}O}$) of the water dimer, as obtained with the considered SCC-DFTB methodologies (MATSCI, MIO and MATORG+HBD) and with high-level wavefunction and density functional methods (CCSD, PBE and B3LYP). Experimental values from velocity map imaging (for $\Delta E_{H\text{-}bond}$) and molecular beam electric resonance spectroscopy (for $R_{O\text{–}O}$). The absolute errors, reported in parenthesis, refers to the difference with the experimental values.

Method	Reference	$\Delta E_{H\text{-}bond}$	$R_{O\text{–}O}$
DFTB–MATSCI	This work	0.084 (−0.152)	2.863 (−0.109)
DFTB–MIO	This work	0.144 (−0.092)	2.862 (−0.110)
DFTB–MATORG+HBD	This work	0.199 (−0.037)	2.815 (−0.157)
CCSD	Ref. [299]	0.218	2.912
DFT(PBE)	Ref. [300]	0.222	2.889
DFT(B3LYP)	Ref. [300]	0.198	2.926
Exp.	Ref. [301] and [302]	0.236	2.972

As expected, the MATSCI set shows the highest error in the evaluation of the H–bond energy, because it was not conceived to describe this kind of system. A value of $\Delta E_{H\text{-}bond}$ in better agreement with the experimental references is obtained with the MIO set, even if still significantly underestimated. The inclusion of the hydrogen-bond damping function (HBD) [291] greatly heales the underestimation, providing a binding energy closer to the ab initio references and the experiment (see MATORG+HBD in Table 5.1). Nonetheless, the HBD correction causes a further shortening of the oxygen-oxygen distance by ∼0.05 Å with respect to the other DFTB approaches, which are also found to underestimate the hydrogen-bond lenght. Thus,

hydrogen bonds in water systems computed by DFTB are expected to be somewhat too short.

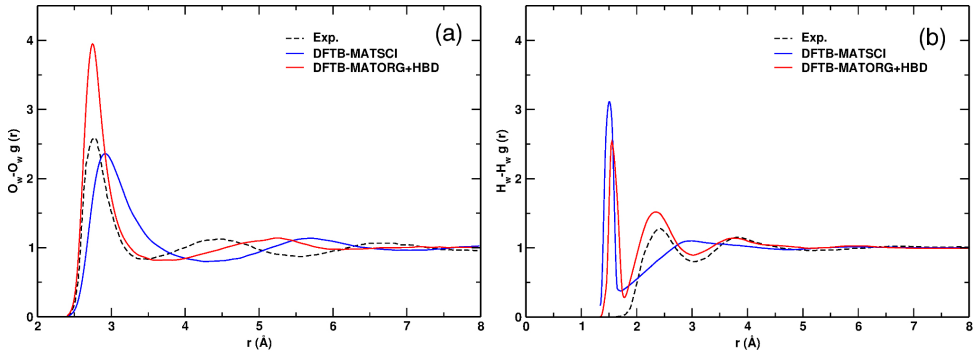

Figure 5.2 – Comparison of the (a) oxygen-oxygen (O_w–O_w) and (b) hydrogen-hydrogen (H_w–H_w) radial distribution functions (RDF) of bulk water: dashed black line, experimental measurement; blue line, DFTB–MATSCI; red line, DFTB–MATORG+HBD with the modified γ function for the H-bond.

However, an accurate description of the hydrogen–bond energy is not enough to assess the reliability of a method for water systems. Another fundamental point is the correct evaluation of the radial distribution function (RDF) of oxygen-oxygen (O_w–O_w) and hydrogen-hydrogen (H_w–H_w) atoms in bulk water. The radial distribution functions obtained with MATSCI and MATORG+HBD methods are shown in Figure 5.2 together with the experimental references.

The first intermolecular peaks in the experimental RDF are located at 2.77 and 2.31 Å, respectively for r(O_w–O_w) and r(H_w–H_w) distances. In the MATSCI RDFs (blue lines), these two intermolecular density maxima peak at significantly longer distances of 2.92 Å and 2.96 Å, respectively. For r(O_w–O_w) the shift is in the order ∼0.3 Å, which proves that water molecules of the first solvation shell are on average too far apart with the MATSCI method. In addition, the first water density depletion is very broad and its minimum is located at a too large distance, which is approximately the same of the second solvation shell in the experimental RDF. This means that there are too many water molecules in the first coordination shell and, consequently, the long-range bulk water structure is poorly described. Furthermore, the MATSCI H_w–H_w radial distribution function and the experimental one have extremely different shapes with the first intermolecular peak of the former shifted by 0.6 Å with respect to the experiment.

Contrarily, as previously reported, [291] using the MIO set, which is equivalent in this case to the MATORG set, and introducing the modified γ function by the MATORG+HBD method, there is a considerable improvement of the oxygen–oxygen RDF, shown as a red line in Figure 5.2a: although too high, the position of the first peak is shifted back to 2.75 Å, hence the RDF function partially overlaps with the experimental curve for distances lower than 3.30 Å; the density depletion minimum is closer to the experiment; the second intermolecular peak is located at 5.25 Å in better

agreement with the experimental data (4.55 Å). Finally, the hydrogen–hydrogen radial distribution function computed with the MATORG+HBD approach in Figure 5.2b reproduces the experimental shape and even the first intermolecular peak at 2.34 Å is consistent with experiments (2.31 Å).

The effect of the inclusion of the weak dispersion interaction on bulk water RDF has been evaluated by the a–posteriori Grimme's D3 method. [275] We observe that the first two intermolecular peaks in the distribution functions r(O_w-O_w) and r(H_w-H_w) are higher in value but their position is unaffected.

Additionally, we have computed the normalized velocity autocorrelation functions (C_{vv}) for oxygen and hydrogen to be compared with PBE Car-Parrinello molecular dynamics (CPMD) data. [303] These functions are calculated as the expectation value at time t of the product between the velocity at time 0 and time t:

$$C_{vv}(t) \equiv \langle \mathbf{v}(0)\mathbf{v}(t) \rangle \tag{5.5}$$

Both DFTB autocorrelation functions, given in Figure 5.3, decay approximately to zero within 500 fs. Nonetheless, the DFTB oxygen and hydrogen C_{vv} are different from CPMD ones in the first 200 fs, where they decay more rapidly. As previously reported, [292] this is related with the slightly weaker H-bonds modeled by the MATORG+HBD approach with respect to DFT(PBE) and experiment (see Table 5.1). This also influences the self-diffusion coefficient of water, which is higher (0.65±0.02 Å^2/ps) but still comparable to the experimental (0.23±0.04 Å^2/ps) [304] and CPMD (0.1 Å^2/ps) ones. [303]

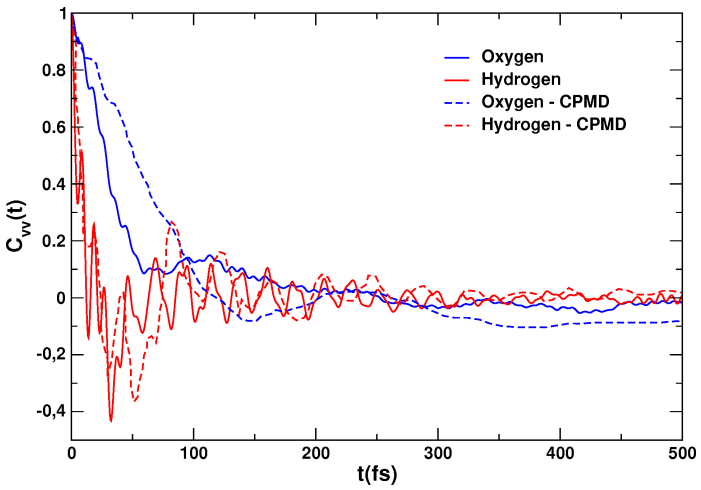

Figure 5.3 – Comparison of the oxygen (blue, solid line) and hydrogen (red, solid line) velocity autocorrelation function (C_{vv}) calculated with DFTB-MATORG+HBD with the oxygen (blue, dashed line) and hydrogen (red, dashed line) C_{vv} calculated with CPMD from Ref. [303]

To sum up this part devoted to the assessment of the ability of MATORG+HBD

to describe water, we demonstrated that this method overcomes the limits of the pre-existing MATSCI set, providing satisfactory results both for the hydrogen-bonding energy and for the bulk water structure and dynamics.

5.3.2 Bulk anatase TiO_2

As a next step, we assess the DFTB set of parameters for the description of bulk anatase by comparing the DFTB structural parameters with the DFT and experimental ones, which are reported in Table 5.2.

Table 5.2 – Bulk TiO_2 Anatase a and c parameters and c/a ratio as calculated with the DFTB and DFT methods and from the experiments. The absolute errors (in parenthesis) refer to the experimental data.

Method	Reference	a (Å)	c (Å)	c/a (Å)
DFTB-TIORG	This work	3.848(+0.066)	9.355(−0.147)	2.431(−0.081)
DFTB-MATSCI	This work	3.810(+0.028)	9.732(+0.230)	2.554(+0.042)
DFTB-MATORG+HBD	This work	3.796(+0.014)	9.790(+0.288)	2.579(+0.067)
DFT(PBE)	This work	3.789(+0.007)	9.612(+0.110)	2.537(+0.025)
DFT(PBE)	Ref. [81]	3.786(+0.004)	9.737(+0.235)	2.572(+0.060)
DFT(B3LYP)	Ref. [204]	3.783(+0.001)	9.805(+0.303)	2.592(+0.080)
Exp.	Ref. [61]	3.782	9.502	2.512

Essentially, all the DFTB values are in very good agreement with both DFT and experimental data. The MATSCI set provides a very accurate a value, but overestimates the lattice parameter c and thus also the c/a ratio, although less than DFT(B3LYP) method. The TIORG parametrization is an exception, since it gives a small underestimation of the c lattice vector and, consequently, a lower c/a ratio. We recall that the MATORG+HBD set only differs from the MATSCI one for the oxygen on-site and pair interactions, since they are taken from the MIO set. Favorably, in spite of this difference, bulk parameters from MATORG+HBD are as good as those from MATSCI. Note that the HBD correction does not have any effect here, since no hydrogen atoms are present.

5.3.3 Water/(101) anatase interface

Adsorption Energy

In this section, we discuss the adsorption energy per molecule (ΔE_{ads}^{mol}) for low and high water coverages on the anatase TiO_2 (101) surface, in both the molecular and dissociated state, i.e. when all the water molecules in the model are undissociated or dissociated, respectively. The values from all the DFTB approaches are compared to DFT(PBE) results and experimental data in Table 5.3.

Only with the TIORG set, all the binding energies for the water adsorption on the (101) surface at any coverage and dissociation degree are overestimated. At monolayer coverage water dissociation is even favored, at odds with many experimental [113,114,

Table 5.3 – Adsorption energies per water molecule (ΔE_{ads}^{mol}) on the (101) anatase slab in the molecular (H_2O) and dissociated (OH,H) mode at low ($\theta = 0.25$) and full ($\theta = 1$) coverage, as obtained with DFT and DFTB methods. The range of adsorption energy of the water monolayer on the (101) surface from Temperature Programmed Desorption (TPD) experiments is also given. The absolute error reported in parenthesis for DFTB data is calculated with respect to the PBE values from the present work.

Method	Reference	Coverage, θ	ΔE_{ads}^{mol}, H_2O (eV)	ΔE_{ads}^{mol}, OH,H (eV)
DFTB–TIORG	This work	0.25	−0.86 (+0.19)	−0.83 (+0.51)
		1	−0.80 (+0.18)	−0.98 (+0.55)
DFTB–MATSCI	This work	0.25	−0.79 (+0.12)	−0.34 (+0.02)
		1	−0.70 (−0.08)	−0.38 (−0.05)
DFTB–MATORG	This work	0.25	−1.08 (+0.41)	−0.54 (+0.22)
		1	−0.96 (+0.34)	−0.58 (+0.15)
DFTB–MATORG+HBD	This work	0.25	−0.80 (+0.13)	−0.31 (−0.01)
		1	−0.71 (+0.09)	−0.40 (−0.03)
DFT(PBE)	This work	0.25	−0.67	−0.32
		1	−0.62	−0.43
DFT(PBE)	Ref. [112]	0.25	−0.74	−0.23
		1	−0.72	−0.44
Exp. (TPD)	Refs. [262, 263]	1	−0.5/−0.7	

262, 263] and theoretical [60, 112] reports. With all the other parametrization sets, this fundamental qualitative feature is always well-reproduced. Given these results, we ceased to further investigate the reliability of the TIORG set for this specific water/TiO_2 benchmark system.

We observe that, in line with DFT calculations, as the water coverage increases, the binding energy per molecule with all DFTB methods decreases for the molecular adsorption mode, whereas it slightly increases for the dissociated one. Nevertheless, molecular adsorption energies are in general overestimated by DFTB approaches, particularly in the case of uncorrected MATORG, with errors up to 0.41 eV. The inclusion of the HBD corrected γ function (MATORG+HBD) solves this serious issue, reducing the absolute errors to less than 0.13 eV, in line with MATSCI results.

Equilibrium Structures

The equilibrium structure of the molecular and of the dissociated water molecule on the (101) anatase surface, as computed with DFT(PBE) in the low coverage regime ($\theta = 0.25$), is represented in Figure 5.4. In Table 5.4 bond distances and α angle values (defined as the angle between the O atom of the water molecule, the Ti surface atom, bonded to H_2O, and its nearest O_{2c} atom, H_2O–Ti–O_{2c}, see Figure 5.5) are reported for the DFTB and DFT methodologies.

Molecular water binds to the 5-fold coordinated Ti atom with a bond lenght of about 2.3 Å (see A in Figure 5.4 and Table 5.4). Hydrogen atoms form two identical

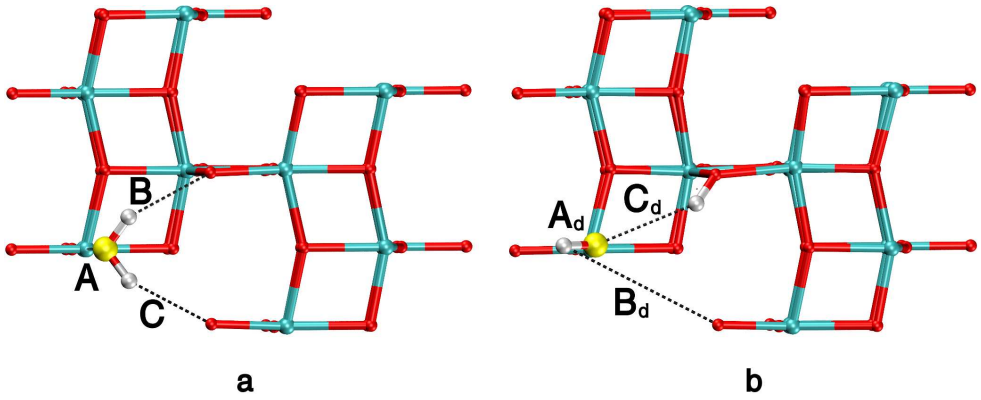

Figure 5.4 – Molecular, H_2O (a) and dissociated, OH,H (b) equilibrium geometries in the low coverage regime, $\theta = 0.25$, as obtained with DFT(PBE) calculations. Values of bond distances are reported in the Table 5.4.

hydrogen bonds, with a lenght of about 2.3 Å, with the neighboring bridging O_{2c} atoms (defined as B and C in Figure 5.4 and Table 5.4). From the data in Table 5.4, one can clearly conclude that both DFTB parametrization sets correctly describe the structure of a single water molecule adsorbed on the TiO_2 (101) anatase surface, with the MATORG+HBD being better for Ti–OH_2 bond distance. Nevertheless, the bond angle α is larger for both the DFTB methods than the DFT one. Since Ti–OH_2 bond lenghts are approximately the same in the two methods, the water molecule is closer to the surface in the case of the DFTB geometry with respect to the DFT one.

As regards the dissociative mode of adsorption of water (right panel of Figure 5.4 and bottom panels of Table 5.4), one of the hydrogen atoms of the water molecule binds to a bridging oxygen site (O_{2c}), whereas the residual OH binds to the Ti_{5c} site. The Ti–OH equilibrium distance (A_d in Table 5.4 and Figure 5.4) is just slightly overestimated by the two DFTB methods, while the two interatomic distances describing the H-bonds (B_d and C_d in Table 5.4 and Figure 5.4) are in satisfactory agreement with the DFT references.

Similar considerations can be drawn at the full coverage regime ($\theta = 1$), whose geometrical parameters of molecular and dissociated water molecules on the anatase surface are given in Figure 5.6 and Table 5.5. Indeed, Ti–O bond lenghts are well-described, whereas there is some discrepancies between DFTB and DFT reference for the hydrogen bonding distances. In particular, in the molecular mode of adsorption, according to the DFT(PBE) calculations, water molecules of the monolayer form two asymmetric H-bond with the two neighbour O_{2c} atoms. However, this fine detail is not properly described by any of the considered DFTB approach.

To conclude this section, we demonstrated that both MATSCI and MATORG-HBD sets of parameters provide an accurate picture of the energetic and structural features of single and monolayer water adsorption on the anatase surface. Therefore, both methods are expected to provide a correct description of the water monolayer/TiO_2

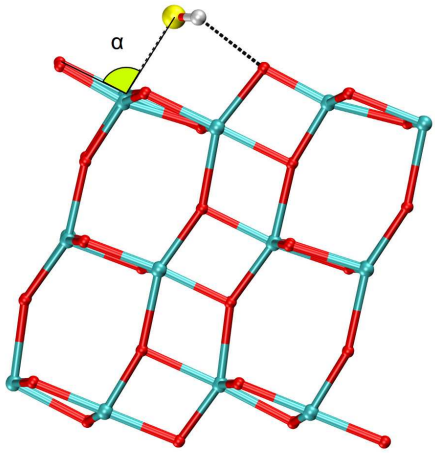

Figure 5.5 – Definition of the bond angle α between the water molecule and the (101) anatase slab.

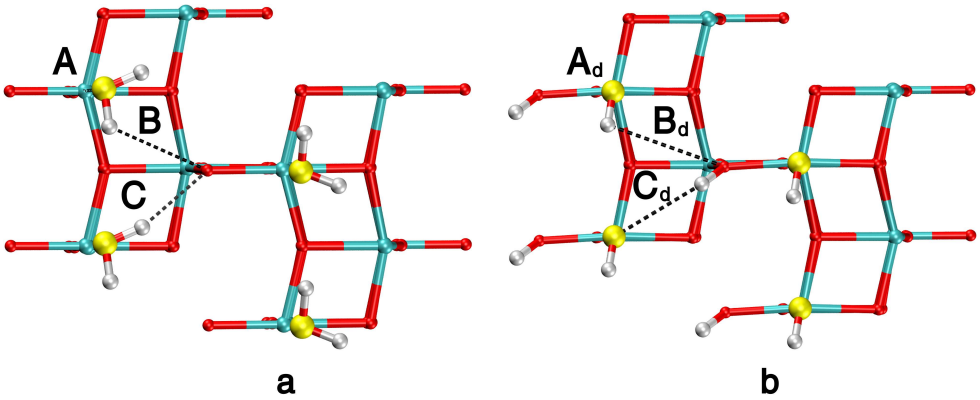

Figure 5.6 – Molecular, H_2O (a) and dissociated, OH,H (b) equilibrium geometries in the full water coverage regime, $\theta = 0.25$, as obtained with DFT(PBE) calculations. Values of bond distances are reported in Table 5.5.

interface dynamical properties. However, MATORG+HBD set should outperform MATSCI when two or more layers of water molecules are deposited on the surface slab, since water/water interactions are way better described by MATORG+HBD, as detailed in the previous section.

Table 5.4 – Geometrical parameters of the equilibrium structures of H_2O (*Molecular Adsorption*, top panel) and OH, H (*Dissociative Adsorption*, bottom panel) at a single water molecule coverage ($\theta = 0.25$) on the (101) TiO_2 anatase slab, as obtained with DFTB and DFT methods. In the dissociative mode of adsorption, we define H as the hydrogen atom of the OH group bound to the Ti atom, whereas H* is the hydrogen atom bound to the bridging O_{2c} atom. The interatomic distances and the angle α are graphically defined in Figure 5.4 and 5.5, respectively. The absolute error reported in parenthesis for DFTB data is computed with respect to the PBE values from the present work.

Molecular Adsorption

Method	Reference	$Ti_{5c}-OH_2$ A(Å)	$H\cdots O_{2c}$ B = C (Å)	$\alpha(^\circ)$
DFTB-MATSCI	This work	2.37 (+0.06)	2.33 (−0.01)	101.6°
DFTB-MATORG+HBD	This work	2.31 (+0.00)	2.26 (−0.08)	105.5°
DFT(PBE)	This work	2.31	2.34	96.2°
DFT(PBE)	Ref. [112]	2.28	1.96	

Dissociative Adsorption

Method	Reference	$Ti_{5c}-OH$ A_d(Å)	$H\cdots O_{2c}$ B_d (Å)	$H^*\cdots OH$ C_d (Å)
DFTB-MATSCI	This work	1.90 (+0.07)	4.14 (−0.17)	2.80 (+0.14)
DFTB-MATORG+HBD	This work	1.89 (+0.06)	3.92 (−0.22)	2.92 (+0.26)
DFT(PBE)	This work	1.83	4.31	2.66
DFT(PBE)	Ref. [112]	1.85	-	2.39

5.3.4 Molecular dynamics of water multilayers on (101) anatase

As a further step in the assessment of the performances of the novel DFTB approach, here we discuss the results obtained by performing molecular dynamics (MD) simulations of the (101) anatase surface with a growing amount of water layers using the MATORG+HBD set. The results will be compared to previous works based on Car-Parrinello (PBE) molecular dynamics simulations [118] and other DFT (PBE) structural investigations. [296]

Monolayer

We will start by considering the water monolayer (ML) in its most stable geometry, i.e. the fully undissociated one shown in Figure 5.7a.

In Figure 5.8a we report the distribution $p(z)$ and time evolution $z(t)$ of vertical distances between the oxygen atoms of the water molecules and the Ti_{5c} plane of the surface, as extracted from the MD simulation run of the water monolayer. As one would expect from the good static description of the full coverage (see Section 5.3.3), the $p(z)$ distribution is in satisfactory agreement with Car-Parrinello (PBE)

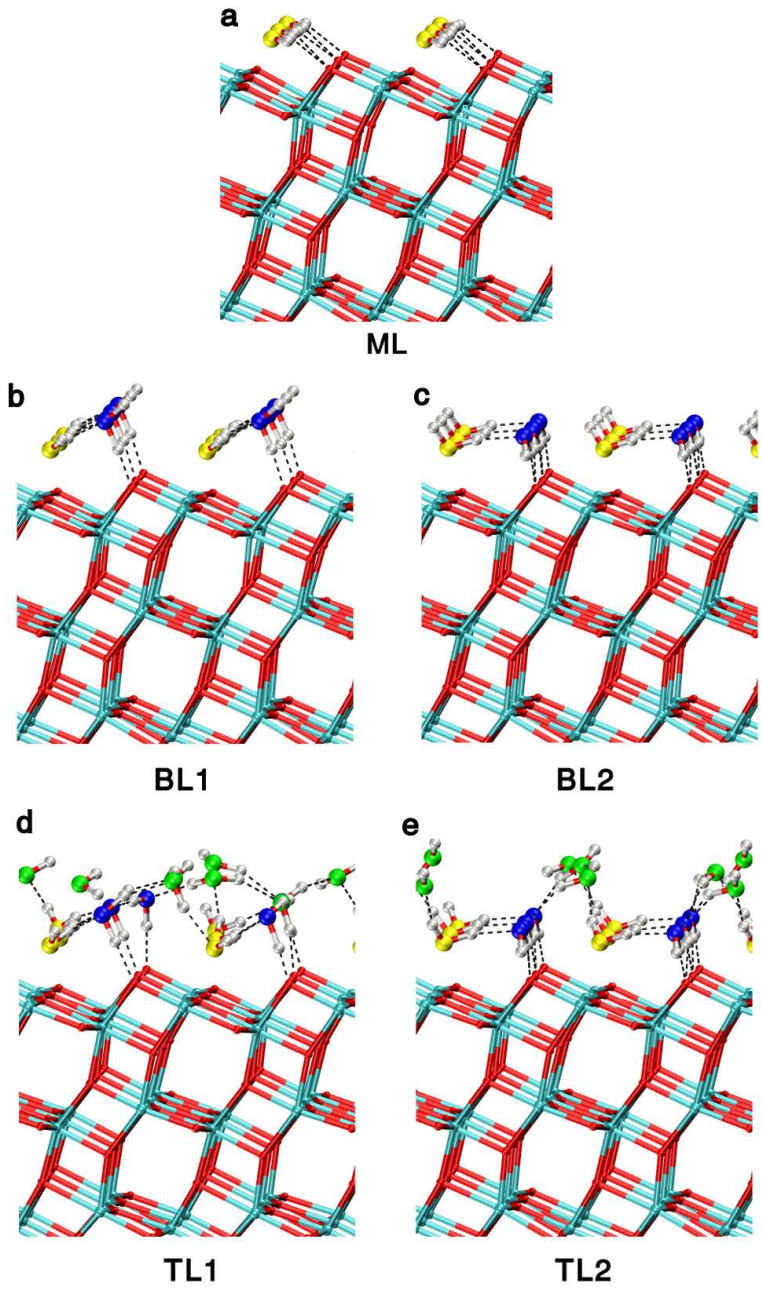

Figure 5.7 – MATORG+HBD structures for a monolayer (ML, a), bilayers (BL1, b and BL2, c) and trilayers (TL1, d and TL2, e) of water on the (101) TiO_2 anatase surface. Dashed lines correspond to H-bonds. The structures reported come from the 0 K geometry optimization of the last snapshots of the molecular dynamics trajectories.

Table 5.5 – Geometrical parameters for the equilibrium structures of H_2O (*Molecular Adsorption*, top panel) and OH, H (*Dissociative Adsorption*, bottom panel) for the adsorption of a full water monolayer ($\theta = 1$) on the (101) TiO_2 anatase slab, as obtained with DFTB and DFT methods. In the dissociative mode of adsorption, we define H as the hydrogen atom of the OH group bound to the Ti atom, whereas H* is the hydrogen atom bound to the bridging O_{2c} atom. The interatomic distances and the angle α are graphically defined in Figure 5.4 and 5.5, respectively. The absolute error reported in parenthesis for DFTB data is computed with respect to the PBE values from the present work.

Molecular Adsorption

Method	Reference	$Ti_{5c}-OH_2$ A(Å)	$H\cdots O_{2c}$ B (Å)	$H\cdots O_{2c}$ C (Å)	$\alpha(^\circ)$
DFTB-MATSCI	This work	2.46 (+0.08)	2.11 (−0.89)	2.11 (−0.23)	104.8°
DFTB-MATORG+HBD	This work	2.41 (+0.03)	2.14 (−0.86)	2.15 (−0.19)	105.2°
DFT(PBE)	This work	2.38	3.00	2.34	93.0°

Dissociative Adsorption

Method	Reference	$Ti_{5c}-OH$ A_d(Å)	$H\cdots O_{2c}$ B_d (Å)	$H^*\cdots OH$ C_d (Å)
DFTB-MATSCI	This work	1.91 (+0.05)	3.48 (−0.17)	2.65 (−0.06)
DFTB-MATORG+HBD	This work	1.92 (+0.06)	3.94 (+0.64)	3.10 (+0.39)
DFT(PBE)	This work	1.86	3.30	2.71

molecular dynamics data. [118] Specifically, the width of the $p(z)$ peak is very similar to the reference, although it is slighlty shifted by 0.1 Å to shorter distances. This is due to the fact that, even if DFTB methods correctly reproduce the Ti–OH_2 bond distance, the α angle (H_2O–Ti–O_{2c}, see Figure 5.5) is broader than in DFT(PBE) calculations, as already discussed in Section 5.3.3 and reported in Table 5.5: 105.2° with MATORG+HBD vs 93.0° with PBE and only small oscillations around this value are recorded during the MD simulation. This more pronounced tilting in the DFTB case is further confirmed by the better overlap of the analogous DFTB and DFT distributions of the Euclidean Ti–OH_2 distances, shown in Figure 5.8b, in place of the vertical distances $p(z)$.

As shown by the breadth of the oscillations of the time evolution $z(t)$ in the right side of Figure 5.8a, each water molecule librates around its equilibrium position during the MATORG+HBD molecular dynamics run, similarly to what obtained with CPMD simulations. [118]

In addition, the binding energy per molecule (ΔE_{ads}^{mol} in Table 5.6) for the water monolayer (ML), as calculated with the MATORG+HBD method, is 0.70 eV, in a very good quantitative agreement with the DFT(PBE) data. [117]

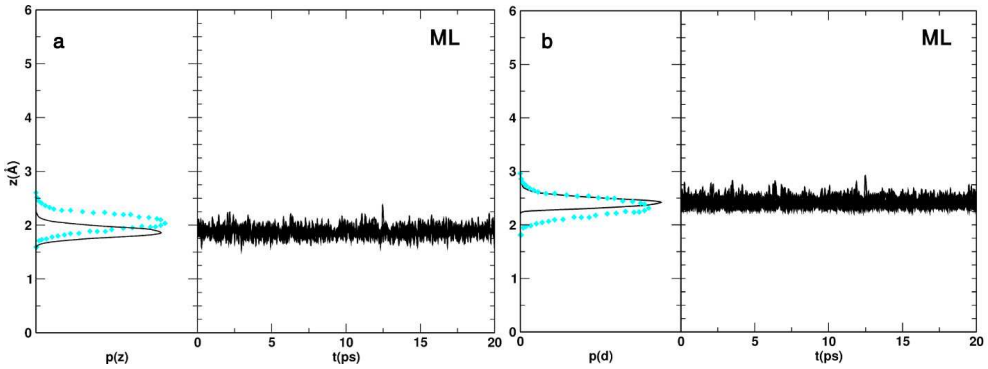

Figure 5.8 – (a) MATORG+HBD distribution $p(z)$ and time evolution $z(t)$ of the distances between the water molecules (oxygen atoms) of the water monolayer and the titania surface (Ti_{5c} atoms). (b) Analogous distribution and time evolution for the Euclidean Ti–O distance. The DFT Car-Parrinello corresponding distribution $p(z)$ is reported in cyan diamonds. [118]

Table 5.6 – Adsorption energy per molecule (ΔE_{ads}^{mol}) of the water monolayer (ML), bilayer (BL1 and BL2) and trilayer (TL1 and TL2) on the (101) TiO_2 anatase 1×3 slab model, as obtained with DFT and DFTB approaches after an optimization run of the last snapshot of the MD simulation. The adsorption energy is defined as the total energy difference between the equilibrium structure of the water/titania interface and the isolated systems, i.e. six isolated water molecules and the optimized slab with one water layer less.

Water configuration	ΔE_{ads}^{mol} DFTB-MATORG+HBD	ΔE_{ads}^{mol} DFT(PBE)*	ΔE_{ads}^{mol} DFT(PBE)†
ML	−0.70	−0.62	−0.69
BL1	−0.73	−0.67	−0.65
BL2	−0.84	−0.66	-
TL1	−0.53	−0.53	−0.56
TL2	−0.51	−0.45	-

* This work
† from Ref. [117]

Bilayer

In the case of the water bilayer (BL), the situation is more complex, since several configurations are possible. Here, we considered two different configurations in line with previous studies [117, 118, 296]. These two bilayers, labeled BL1 and BL2, are shown in Figure 5.7b,c.

In the BL1 configuration each molecule of the first water layer is bound to Ti_{5c} atoms and establishes two hydrogen bonds with two molecules of the second layer. In turn, the second layer molecules form only one H-bond with an O_{2c} of the TiO_2 surface, with the other hydrogen atom pointing towards the vacuum.

In the BL2 configuration, the first layer water molecules are also bound to the Ti_{5c} atom of the surface, but only one hydrogen bond is formed with the second layer molecules, which, in this case, establish two H-bonds with the superficial O_{2c}. On the whole, the number of H-bonds is equal in the two cases. As a matter of fact, with our DFT–PBE setup, we found that the two configurations are essentially isoenergetic: the adsorption energy of the second layer for the BL1 case is −0.67 eV per molecule, whereas it is −0.66 eV for the BL2 (see Table 5.6). Analogous results are reported in ref. [117].

In order to provide a comprehensive picture, we carried out molecular dynamics runs starting from both BL1 and BL2 configurations. The $p(z)$ distribution and $z(t)$ time evolution of the vertical z component of the distance between the oxygen atoms of the H_2O molecules and the Ti_{5c} atoms plane are shown in Figure 5.9, together with the results from PBE CPMD simulations.

Focusing the attention on the plots for the BL1 bilayer, there is a very good match between the DFT and MATORG+HBD $p(z)$ distribution, both for the position of the peaks and for their broadening: within PBE simulation, the first layer of molecules is centered at 2.15 Å (2.11 Å for DFTB), whereas the second one oscillates around the distance of 2.98 Å (3.08 Å for DFTB). Furthermore, even the value of the α angle (H_2O–Ti–O_{2c}) of first layer water molecules with the slab, as defined in Figure 5.5, is perfectly reproduced, being around 90° for both DFTB and DFT.

In the case of BL2 plots in Figure 5.9, we can observe that in the MATORG+HBD $p(z)$ the water molecules of the second layer are closer to the surface than in the BL1 case, since the second maximum in the distribution is peaked at shorter distances (2.69 Å and 3.08 Å for BL1 and BL2, respectively).

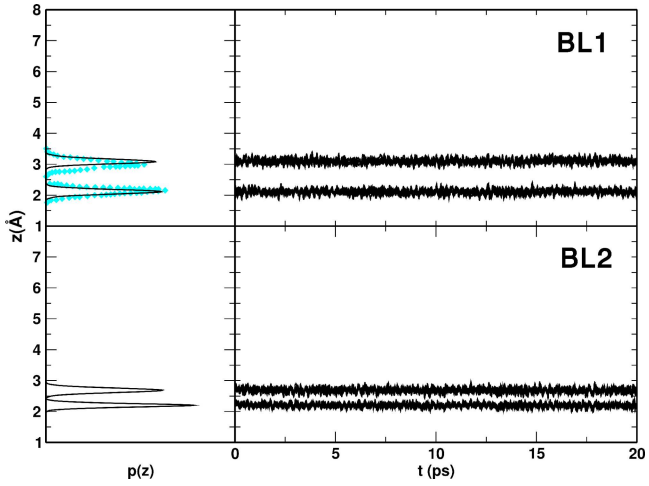

Figure 5.9 – MATORG+HBD distribution $p(z)$ and time evolution $z(t)$ of the distances between the water molecules (oxygen atoms) of the BL1 and BL2 water bilayer, defined in Figure 5.7, and the titania surface (Ti_{5c} atoms). The DFT Car-Parrinello corresponding distribution $p(z)$ is reported in cyan diamonds. [118]

Although the bilayer structures and dynamics as obtained by DFTB match the DFT ones, the binding energies per molecule (ΔE_{ads}^{mol} in Table 5.6) for both configurations are slightly overestimated in the DFTB case, with the BL2 bilayer slightly favored with respect to BL1, differently from DFT(PBE) results where they are isoenergetic. This effect may be caused by a greater stability of the water molecules in the second layer of BL2 when the DFTB method is used with respect to DFT(PBE) calculations. In fact, in the case of DFTB, these water molecules are found to establish stronger and shorter H-bonds with the O_{2c} atoms of the surface, as clearly shown for a single water molecule in Figure 5.10.

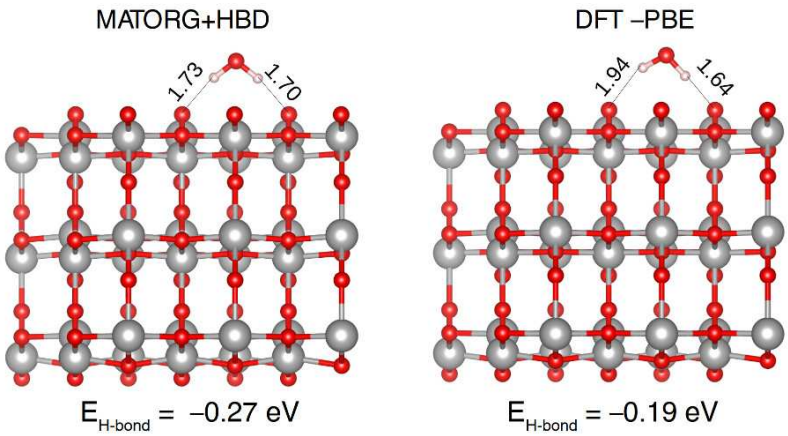

Figure 5.10 – MATORG+HBD and DFT(PBE) (101) anatase slab with a single water molecule in the same position as the second layer water molecules of the BL2 bilayer. Relevant hydrogen bond distances are also given. The strength of the hydrogen bond has been evaluated with single-point calculations of these structure and the isolated systems.

Even though there are few fine differences between DFTB and DFT results, the qualitative picture is analogous, i.e. the first two layers are vertically ordered and adapt to the TiO_2 surface lattice.

Trilayer

The trilayer of water molecules (TL) cannot be uniquely defined since many valid configurations are conceivable. Therefore, we devised two representative starting configurations, on the basis of what observed above for the water bilayers. These are the TL1 and TL2 configurations shown in Figure 5.7d,e, where the first two water layers are in the same positions of the BL1 and BL2 models, respectively.

In Figure 5.11 we report the distribution $p(z)$ of the distances along the z coordinate and their evolution during the MD simulation $z(t)$ for both configurations to be compared with the available DFT(PBE) CPMD references. [118] The agreement between the two MATORG+HBD and DFT(PBE) data is rather good. As a matter

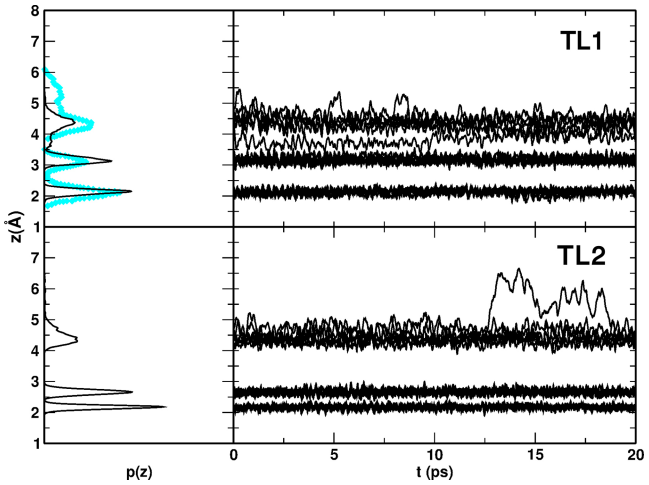

Figure 5.11 – MATORG+HBD distribution $p(z)$ and time evolution $z(t)$ of the distances between the water molecules (oxygen atoms) of the TL1 and TL2 water trilayer, defined in Figure 5.7, and the titania surface (Ti_{5c} atoms). The DFT Car-Parrinello corresponding distribution $p(z)$ is reported in cyan diamonds. [118]

of fact, there is a good overlap between the DFTB curve of the TL1 trilayer, shown in the top panel of Figure 5.11, and the DFT one: the first two layers in the DFTB distribution are vertically ordered and do not change their position for the whole simulation time, whereas the third layer is less bound and interacts with the second layer of water molecules. Another proof that the third layer is less bound is given by the time evolution *z(t)*: at about 12 ps, one water molecule even leaves temporarily the trilayer. The range of vertical distances explored by the third layer is between $3.6 < z < 5.1$ Å with DFTB, hence it is closer to the surface than with DFT–PBE simulations, where the trilayer oscillates between $\sim 4.0 < z < \sim 6.0$ Å .

The binding energies per molecule (ΔE_{ads}^{mol} in Table 5.6) for the TL1 and TL2 trilayers is in very good agreement with the DFT(PBE) data. Furthermore, in line with the DFT results, also with MATORG+HBD the TL1 configuration is found to be more energetically favorable.

In Figure 5.12 the corresponding $p(z)$ and $z(t)$ for the ML (top panel), BLs (middle panels) and TLs (bottom panels) as extracted from the molecular dynamics simulations with the MATSCI parametrization set are given. As already anticipated by the results for bulk water and water adsorption with the MATSCI set, there is a very good match with the DFT reference only for the monolayer configuration, whereas there is a poor overlap for the bilayer and trilayer configurations, because the interactions between water molecules, underestimated by MATSCI, become more relevant.

From the present analysis of water multilayers on an anatase TiO_2 surface, the main factors governing the water/titania interface, which are correctly addressed by DFTB, can be highlighted.

Above all, the balance between water/surface and water/water interactions is

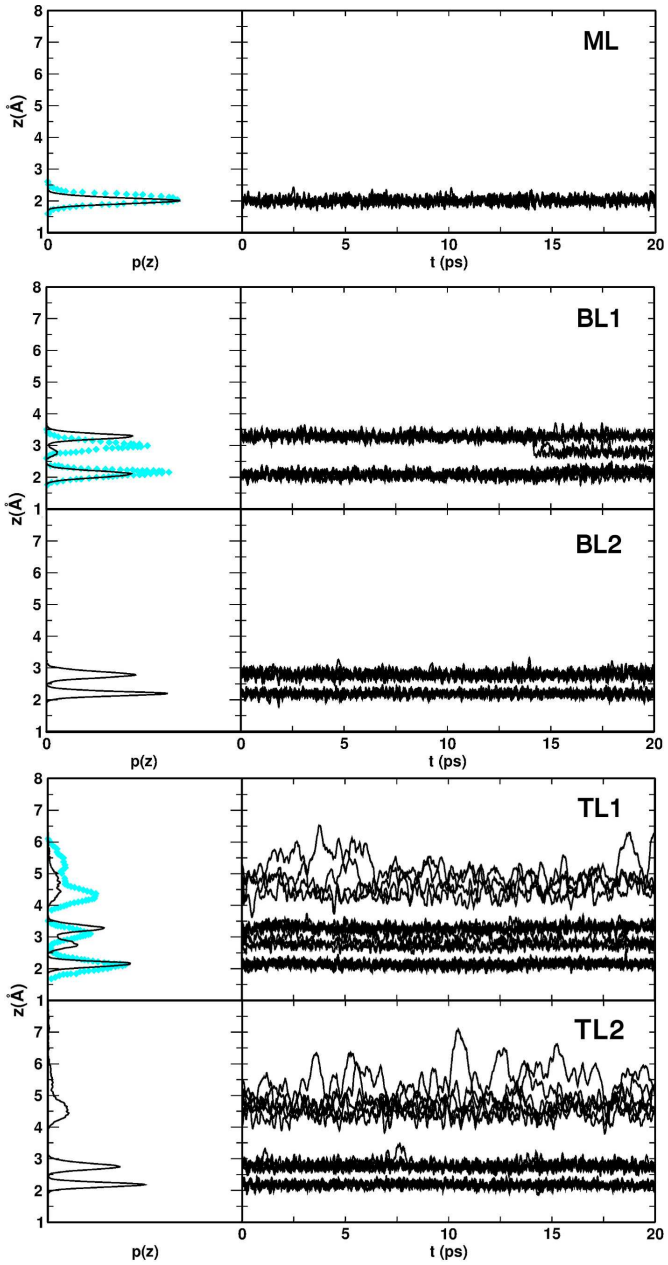

Figure 5.12 – MATSCI Distribution $p(z)$ and time evolution $z(t)$ of the perpendicular distances between the water molecule (oxygen atoms) and the titania surface (Ti_{5c} atoms) for the monolayer (ML), bilayers (BL1 and BL2) and trilayers (TL1 and TL2) of water molecules. The DFT Car-Parrinello corresponding distribution $p(z)$ is reported in cyan diamonds. [118]

clearly a crucial aspect in the multilayer water adsorption. As evidenced by the decrease of binding energy between the BLs and TLs, the pure water/water interaction is found to be always weaker than the water/surface one, in line with a previous DFT study. [117]

In addition, while the position of the water molecules along the z axis are always fixed with a certain degree of oscillation (*vertical* order) in all the configurations considered (ML, BLs and TLs), the order in the xy plane (*in-plane* order) is present only for the first and second layer of molecules, since the third one is found to be more free to move, in agreement with another DFT study. [118] The in-plane order is caused by the strong coordination of the first layer water molecules with the surface Ti_{5c} atoms, which keeps the molecules separated and prevents lateral interactions. This strong bonding situation still holds for the water molecules of the second layer, which are hydrogen-bonded to the surface O_{2c} atoms, but not for the third layer that does not directly interact with surface atoms anymore. Lastly, we noticed that the strength of the Ti–OH_2 bond in the first water layer increases at coverages higher than 1 ML, as also reported in ref. [118]. This effect has been proven by the decreasing Ti_{5c}water average distance (ML = 2.43 Å, BL = 2.29 Å, TL = 2.28 Å), as extracted from the MATORG+HBD molecular dynamics runs.

Thus, the use of a modified hydrogen bonding damping (HBD) function in the combined MATORG set allows for the proper description of the balance between water/water and water/titania interactions, resulting in a good agreement with the DFT reference for the $p(z)$ distributions and water layers binding energies, reported in Figure 5.8, 5.9 and 5.11 and Table 5.6, respectively.

As already performed for static calculations in Section 5.3.3, we tested the effect of the inclusion of a–posteriori dispersion corrections in the D3 flavor, as developed by S. Grimme. [275] We observed that binding energies systematically increase by about 0.2 eV, but the qualitative description of the water/titania interface is not improved. As an example, the issue concerning the relative stability between BL1 and BL2 bilayers still persists.

5.3.5 Energy barrier for water dissociation

In this final part, we discuss the energy barrier associated to the dissociation of a single molecule of water on a Ti_{5c} site of the anatase TiO_2 (101) surface (coverage $\theta = 0.25$) as obtained with DFTB methods, which have been recently proven to be reliable in the prediction of reaction barriers. [305] The results have been compared with the energy barriers obtained with DFT methods (see Table 5.7). Note that in the case of DFT–B3LYP-D* the barrier has been calculated in this work by using the computational settings detailed in Ref. [306].

We observed that the barrier for the dissociation process is generally overestimated by both DFTB methods considered, in particular with the MATSCI set of parameters. Nevertheless, the MATORG+HBD approach partially solves this issue, providing results in better agreement with the DFT references. Furthermore, one should notice that the reaction barrier for water dissociation, as found with DFT(B3LYP-D*), [306] is higher than the PBE+U reference, with an energy barrier closer to the one obtained with MATORG+HBD. In any case, such high barriers ($\Delta E^{\dagger}_{diss} \gg 0.5$ eV) would not

Table 5.7 – Energy barrier for the dissociation of a single water molecule on the anatase TiO_2 1×2 model ($\Delta E^{\ddagger}_{diss}$) and total energy difference between molecular and dissociated water adsorption (ΔE_{diss}).

Method	Reference	$\Delta E^{\ddagger}_{diss}$	ΔE_{diss}
DFTB–MATSCI	this work	1.12	0.41
DFTB–MATORG+HBD	this work	0.96	0.49
DFT(PBE+U)	Ref. [115]	0.52	0.40
DFT(B3LYP-D*)	Ref. [306]	0.81	0.36

allow for spontaneous water dissociation in a reasonably long molecular dynamics simulation time.

Table 5.8 – Geometrical parameters, as defined graphically in Figure 5.13, for the transition state structure of water dissociation on the (101) anatase slab model with the DFTB methods and in the DFT reference.

Method	Reference	A	B	C
DFTB–MATSCI	this work	1.34	1.44	2.27
DFTB–MATORG+HBD	this work	1.15	1.48	2.25
DFT(B3LYP-D*)	Ref. [306]	1.18	1.35	2.06

Finally, in Figure 5.13 and Table 5.8 we report the transition state structure and its geometrical parameters as computed with DFTB and DFT methods. The use of the MATORG set instead of MATSCI and the inclusion of the HBD correction greatly improves the description of the transition state geometry in comparison to the DFT reference. However, the MATORG+HBD transition state is found to be somewhat later than with DFT(B3LYP-D*), i.e. the distance between the oxygen atom of water and the leaving hydrogen atom (B in Table 5.8) is longer than in the DFT reference.

To conclude this section devoted to the assessment of the novel MATORG+HBD set of DFTB parameters, we demonstrated the applicability of SCC-DFTB for the description of the structural, energetic and dynamical properties of the water-multilayers/TiO_2 interface, but only when a proper combination of DFTB parameters and corrections is used. On the basis of this proven reliability, we applied this method to perform computationally efficient molecular dynamics of large and realistic models of TiO_2 nano-systems into a solvent surrounding, as it will be discussed in the next section.

5.4 Water/anatase TiO_2 spherical nanoparticle interface

In the following, we will discuss a static and dynamic investigation of the water/anatase TiO_2 nanoparticle interface. Specifically, we will consider the adsorption of single water molecules, a water monolayer and a multilayer of water molecules on a

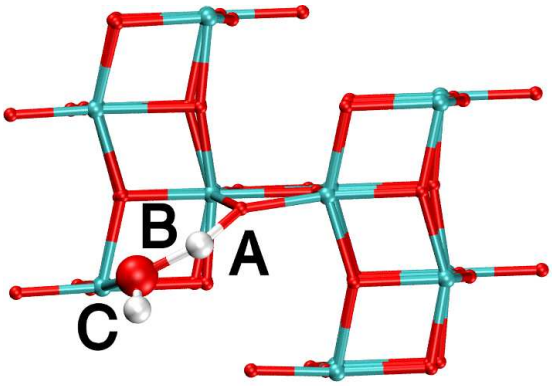

Figure 5.13 – MATORG+HBD optimized structure of the transition state for the process of water dissociation (coverage $\theta = 0.25$). Values of bond distances are reported in the Table 5.8.

spherical TiO_2 nanoparticle model.

Up to monolayer coverage, we employed both the DFT(B3LYP) and SCC-DFTB with the MATORG+HBD parameters for the static description of the energetics and the structural and electronic properties. At this stage, the MATORG+HBD methodology has been further assessed by the comparison with the DFT(B3LYP) results.

Finally, a MATORG+HBD molecular dynamics simulation of a multilayer of water adsorbed on the nanoparticle has been performed and analyzed with the aim to describe the dynamic properties of this important solid–liquid interface.

5.4.1 Single site coverage

A spherical TiO_2 nanoparticle, such as the **NS** nanosphere used in this study (see Section 5.2 for more details on the model), presents a large variety of different undercoordinated surface Ti atoms, which are the preferential water adsorption sites. First of all, as was deeply discussed in Section 3.5.2, in the **NS** system there are four main categories of Ti sites: Ti_{5c}, Ti_{4c}, $Ti_{4c}OH$ and $Ti_{3c}OH$.

In addition, these four main categories may be subdivided in several subcategories, which account for the different chemical environment of each specific site. For instance, Ti_{5c} can be differentiated by their vacant coordination position, that can be axial or equatorial. Otherwise, they can be characterized by the presence of bridging O_{2c} species or hydroxyl groups that are close enough to accept an hydrogen bond. In this way, it is possible to distinguish 18 significantly inequivalent undercoordinated surface sites on the **NS** model, as shown in Figure 5.14.

For the binding of a single water molecule on each of the 18 sites, two adsorption modes have been considered: undissociated water ("Undiss.") and dissociated water with the hydrogen fragment on the closest bridging O_{2c} oxygen ("Diss."). In the case

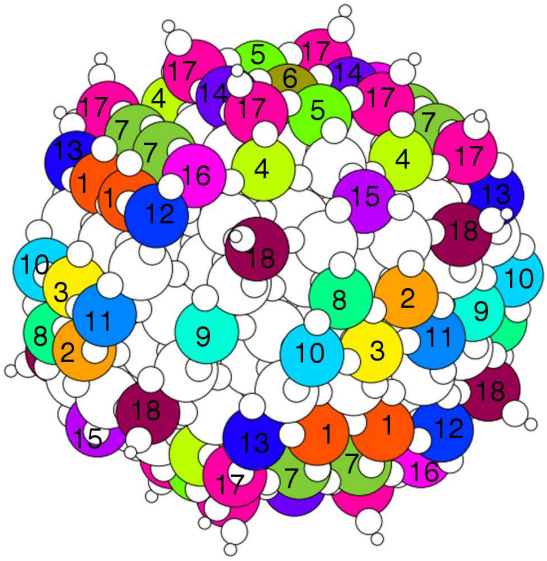

Figure 5.14 – Position of the inequivalent undercoordinated titanium sites on the surface of the **NS** model. The numbering corresponds to the labels in Table 5.9.

of $Ti_{5c}(2)$ and $Ti_{4c}(12)$ sites, the resulting O_{2c}–H cleaved one Ti–O_{2c} bond during the DFT(B3LYP) geometry optimization, resulting in the formation of a terminal Ti–OH, similarly to what has been reported for the dissociative water adsorption on anatase (001) surfaces. [93, 112, 121] Interestingly, this binding mode is more stable than dissociative adsorption without Ti–O_{2c} cleavage by −0.4 eV. However, this peculiar behaviour will not be considered from now on, because the Ti–O_{2c} bond is restored upon adsorption of another water molecule at the same Ti site.

The binding energies for water on each site, as obtained with DFT(B3LYP) and MATORG+HBD methods, are reported in Table 5.9. The DFTB approach is able to accurately reproduce the DFT(B3LYP) adsorption energies for molecular water with a mean absolute error (MAE) of 0.12 eV, whereas it provides not as good performances for dissociated water, being most of the values underestimated. The cause of this underestimation may be related to a rigidity of the DFTB parametrization, which cannot describe the higher distortion of the Ti–O bonds that is induced by water dissociation, contrarily to DFT(B3LYP). These general tendencies can be clearly observed in Figure 5.15, where the MATORG+HBD binding energies are plotted against the DFT(B3LYP) ones.

The distribution of the binding energies for undissociated water, together with the computed energy difference between the dissociative and molecular adsorption modes, is graphically represented in Figure 5.16. Interestingly, we demonstrated that on the surface of a spherical nanoparticle there is a wide variety of water adsorption sites that are characterized by a different preferential binding mode and adsorption energy. This is in line with several experimental works, which postulate, on the surface of

Table 5.9 – Comparison between the binding energies (ΔE_{ads}^{mol}, in eV) for a water molecule on each specific site of the **NS** nanoparticle model with the MATORG+HBD and the DFT(B3LYP) method. Both the undissociated (Undiss.) and the dissociated (Diss.) adsorption mode are considered. The preferred adsorption mode for each site is highlighted in bold. The mean absolute error (MAE, in eV) of DFTB with respect to DFT for undissociated and dissociated water is also given.

Site	Label	Occurrence	MATORG+HBD		DFT(B3LYP)	
			Undiss.	Diss.	Undiss	Diss.
	1	8	**−0.72**	−0.04	**−0.97**	−0.97
	2	4	**−0.68**	−0.43	−0.65	**−1.05**
	3	4	**−0.67**	−0.28	−0.76	**−0.99**
Ti_{5c}	4	8	**−1.00**	−0.15	**−0.92**	−0.86
	5	4	**−0.41**	−0.20	−0.55	**−0.59**
	6	2	**−0.34**	1.71	**−0.44**	0.51
	7	8	**−0.56**	−0.08	**−0.61**	−0.54
	8	4	**−0.63**	−0.24	−0.61	**−0.84**
	9	4	−0.98	**−1.30**	−0.61	**−1.58**
	10	4	−0.99	**−1.16**	−1.03	**−1.32**
	11	4	−0.94	**−1.45**	−1.17	**−1.86**
Ti_{4c}	12	4	−1.11	**−1.18**	−1.22	**−1.78**
	13	4	−0.97	**−1.39**	−1.27	**−1.80**
	14	4	**−1.17**	−0.69	−1.57	**−1.73**
	15	4	**−0.95**	−0.83	−0.96	**−1.05**
	16	4	−1.25	**−1.27**	−1.22	**−0.54**
Ti_{4c}(OH)	17	12	**−0.40**	0.17	**−0.56**	0.46
Ti_{3c}(OH)	17	8	**−0.63**	0.39	**−0.63**	−0.53
MAE			0.12	0.67		

curved TiO_2 nanoparticle samples, the existence of many inequivalent sites capable of binding. [54,307–310] Interestingly, water dissociation is favored over most of the sites of the TiO_2 nanosphere, which is an evidence of the higher reactivity of spherical TiO_2 nanoparticles in comparison to faceted ones, where water only molecularly adsorbs on the mostly exposed (101) surfaces.

5.4.2 Monolayer coverage

Overall, the number of water molecules that are needed to build a water monolayer is given by the amount of effective vacant positions of coordination on all the Ti surface sites. This number corresponds to 134 molecules for the $(TiO_2)_{223} \bullet 10\ H_2O$ nanosphere model, as it can be derived by the occurrence of each site and its corresponding coordination number in Table 5.9.

On the surface of the nanosphere, the water molecules may be all undissociated, all dissociated or in an intermediate configuration where a portion of them is dissociated and the remaining ones are undissociated. In order to discriminate between these

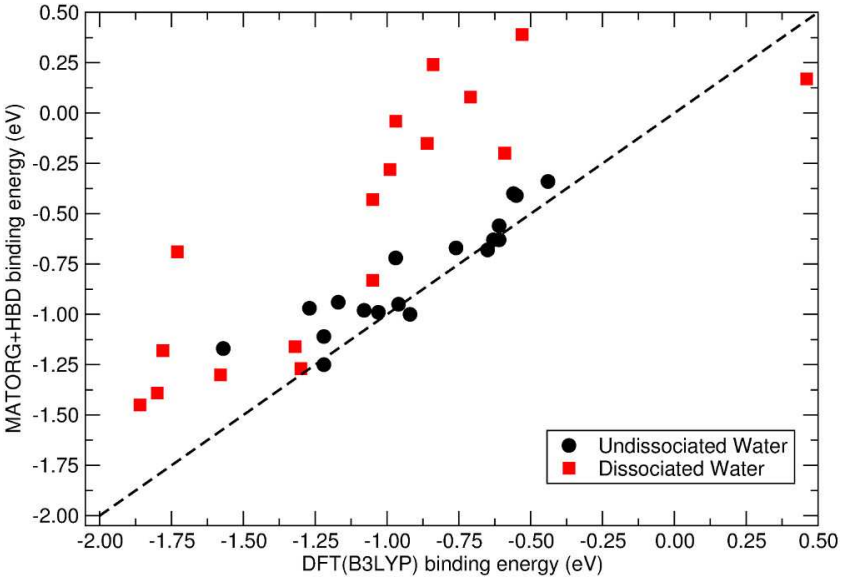

Figure 5.15 – Correlation between the binding energy of undissociated (black circles) and dissociated (red squares) water molecules as obtained with DFT(B3LYP) and MATORG+HBD. The xy bisector is shown as a black dashed line.

situations, we define the extent of the dissociation reaction (α) as follows:

$$\alpha = \frac{n_{OH,H}}{n_{tot}}, \quad n_{tot} = n_{H_2O} + n_{OH,H} \tag{5.6}$$

where $n_{OH,H}$ and n_{H_2O} are the number of dissociated and undissociated water molecules in the water monolayer, respectively.

The results for the DFT(B3LYP) binding energies (ΔE_{ads}^{mol} in Table 5.9) for each site may suggest that water would be almost completely dissociated on the surface of the nanosphere. Nonetheless, one should consider that a high degree of dissociated water molecules implies the formation of a large quantity of bridging O_{2c}–H species and a strong distortion of the surface. In other words, the relative stability of the dissociative or molecular adsorption modes of water is expected to be coverage-dependent.

In order to verify this hypothesis, we devised three main models of the water monolayer on the **NS** nanoparticle model: all undissociated ($\alpha = 0.00$, Figure 5.17a); a portion of water molecules (28 out of 134) dissociated and the remaining ones undissociated ($\alpha = 0.21$, Figure 5.17b); a portion of water molecules (40 out of 134) dissociated and the remaining ones undissociated ($\alpha = 0.30$, Figure 5.17c). The sites where water molecules have been dissociated were selected on the basis of the DFT(B3LYP) binding energies in Table 5.9: in the case of $\alpha = 0.21$, all the sites with a $\Delta E_{ads}^{mol} < -1.25$ eV; in the case of $\alpha = 0.30$, all the sites with a $\Delta E_{ads}^{mol} < -1.05$ eV. For the less expensive MATORG+HBD computational approach, also other dissociation degrees have been considered, up to a number of 68 dissociated water molecules out

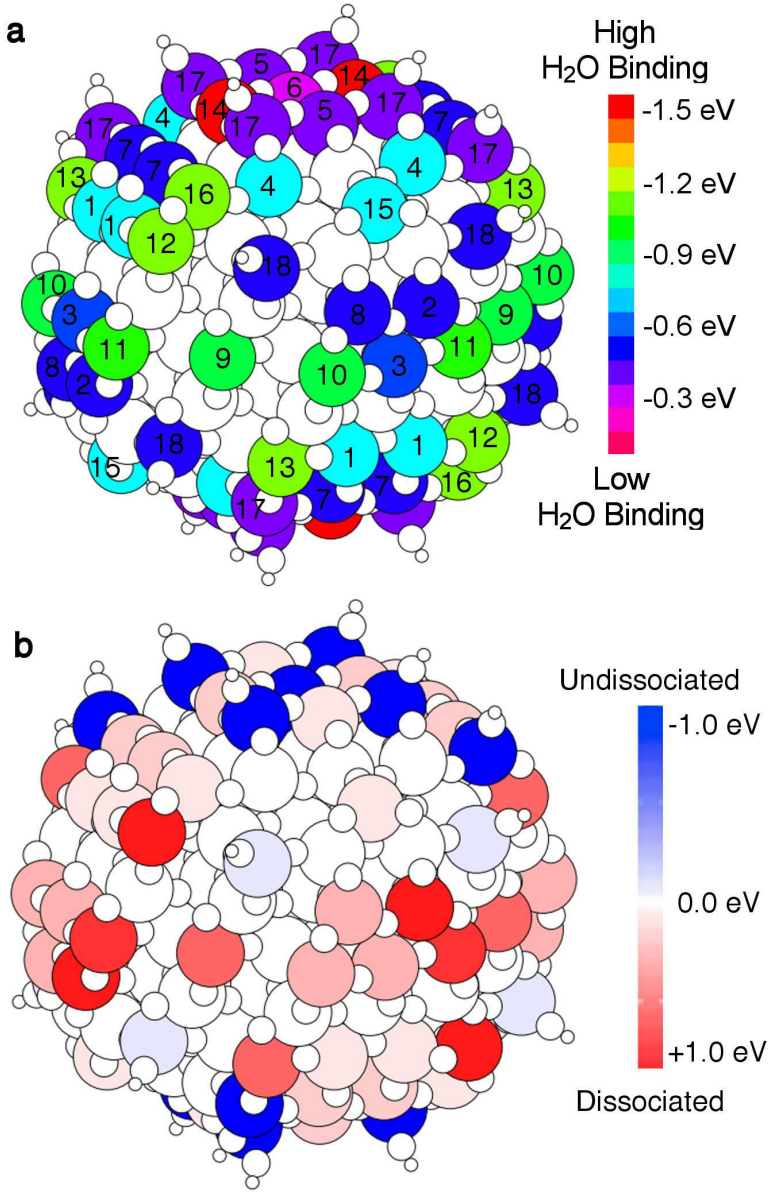

Figure 5.16 – Pictorial representation of the distribution of (a) binding energies (ΔE_{ads}^{mol} in Table 5.9) for undissociated water molecules and (b) energy difference between undissociated and dissociated adsorption for each undercoordinated sites of the **NS** model as obtained with DFT(B3LYP).

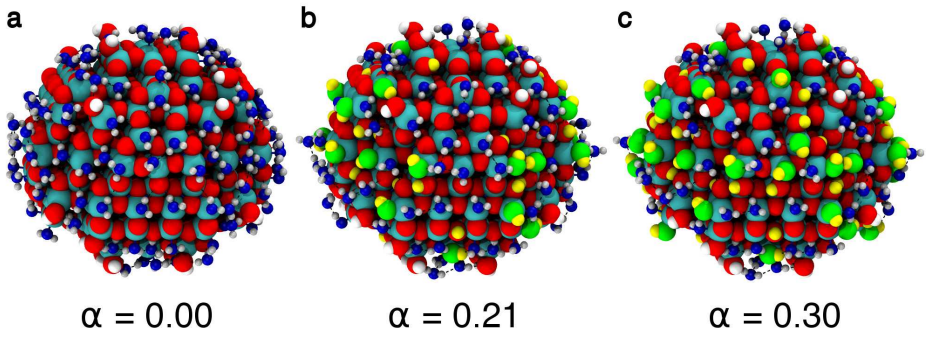

Figure 5.17 – Optimized structures of the water monolayer with a different extent of dissociation (α) on the **NS** model, as obtained with DFT(B3LYP): (a) all undissociated (α = 0.00), (b) 28 water molecules out of 134 dissociated (α = 0.21), (c) 40 water molecules out of 134 dissociated (α = 0.30). Oxygen atoms from undissociated water molecules are shown in blue. Titanium, oxygen and hydrogen atoms of the nanoparticle are shown as cyan, red and white spheres, respectively. Hydrogen and oxygen atoms from dissociated water molecules are given in yellow and green, respectively. Hydrogen bonds are shown as dashed black lines.

of 134.

Table 5.10 – Binding Energy per molecule (ΔE_{ads}^{mol}, in eV) for the water monolayer on the **NS** and **NC** models with a different degree of dissociation, expressed in terms of fraction of dissociated molecules and α, as obtained with MATORG+HBD and DFT(B3LYP) methods. The values for the most stable configuration are highlighted in bold.

Fraction of dissociated H_2O	α	ΔE_{ads}^{mol} MATORG+HBD	ΔE_{ads}^{mol} DFT(B3LYP)
		NS	
0/134	0.00	−0.708	−0.814
28/134	**0.21**	**−0.743**	**−0.878**
36/134	0.27	−0.729	
40/134	0.30	−0.727	−0.867
48/134	0.36	−0.706	
68/134	0.51	−0.646	
		NC	
4/126	0.03		−0.744

The binding energies per molecule for the water monolayer with different degrees of dissociation, as obtained by DFT(B3LYP) and MATORG+HBD, are given in Table 5.10. Note that the energy differences may seem small when one compares the results for different α, but the ΔE_{ads}^{mol} are averaged on hundreds of water molecules, so that a difference of 0.01 eV in binding energy per molecule accounts for more than 1 eV

on the whole.

Indeed, the configuration in which the water monolayer is more stable is the one in which 28 out of 134 water molecules are dissociated. In addition, the same result is obtained by both MATORG+HBD and DFT(B3LYP) approaches. These findings clearly demonstrate that: i) overall, the best configuration in the full coverage regime is the one where water is dissociated only on the more reactive Ti_{4c} sites; ii) even though MATORG+HBD has been shown to be not particularly accurate for water dissociation energy on single sites (see Table 5.9), it gives a correct qualitative and even quantitative description of a water monolayer adsorption on a TiO_2 nanoparticle. Furthermore, one can notice that there is a smooth decrease of the binding energy as a function of the dissociation degree α (see MATORG+HBD results in Table 5.10).

Another important result is that the average binding energy of water on a TiO_2 nanosphere is considerably larger than that of a faceted nanoparticle by -0.13 eV per molecule (compare **NS** and **NC** model in Table 5.9). This is a computational evidence of the observed higher chemical reactivity of curved TiO_2 nanosystems with respect to well-faceted ones. [31] Furthermore, from a chemical point of view, the spherical nanoparticle contains a large number of acidic Ti sites, which can bind an hydroxyl anion and release a H^+, and basic O_{2c} species, which can accept a proton. Overall, the extent of dissociation α for the most stable configuration gives a measure of the acid/base reactivity of the nanoparticle. Therefore, the faceted TiO_2 nanoparticle shows a significantly lower acid/base reactivity than the spherical one, since water dissociates only on the few corner sites of the **NC** model (see Section 4.5.1 for more details).

Table 5.11 – Connolly surface areas (S_{Conn} in nm^2) and surface energies (γ_{Conn} in J/m^2) for the faceted (**NC**) and spherical (**NS**) TiO_2 nanoparticle models with and without an adsorbed monolayer of water molecules, as obtained with DFT(B3LYP). In the case of the spherical nanoparticle, the considered monolayer is the most stable one with 28 out of 134 dissociated water molecules. The Connolly radius is set to 3.0 Å.

	NC	**NC** + H_2O ML	**NS**	**NS** + H_2O ML
S_{Conn}	23.8		22.1	
γ_{Conn}	0.59	−0.04	0.72	−0.13

The larger energy gain associated with water adsorption for spherical anatase nanoparticles with respect to faceted ones is connected with the computed surface energies, reported in Table 5.11. In vacuum, the faceted nanoparticle shows a surface energy lower than the nanosphere (0.59 vs 0.72 J/m^2), since it exposes highly stable (101) surfaces. In a water environment, a reversal of the relative stability is observed: the TiO_2 nanosphere is more stabilized by water than the faceted nanoparticle, resulting in a more negative surface energy (-0.13 vs -0.04 J/m^2). In other words, we provide computational evidences that, in the presence of water molecules, spherical TiO_2 nanoparticles would be more stable than faceted nanoparticles.

Note that a negative surface energy implies that the surface is more stable than the bulk and this cannot happen for a single component system, e.g. TiO_2 only. However, in the case of a multi-component system, such as TiO_2 and water, this may happen,

as demonstrated by Nørskov et al. for alumina surfaces in aqueous surroundings. [311]

Table 5.12 – Surface densities (in nm^{-2}) of terminal (OH) and bridging ($O_{2c}H$) hydroxyl groups and of water molecules directly bound to a titanium atom (H_2O–Ti) or H-bonded to the surface (H_2O_{HB}) in the DFT(B3LYP) optimized water monolayer on the **NS** model with a different extent of dissociation (α). The values corresponding to the most stable configuration are highlighted in bold.

α	OH	$O_{2c}H$	H_2O–Ti	H_2O_{HB}
0.00	0.9	0.0	4.9	1.1
0.21	**2.2**	**1.3**	**4.0**	**0.8**
0.30	2.7	1.8	3.6	0.7

The surface composition of water species on the hydrated **NS** model, reported in Table 5.12, is consistent with the data from experimental literature, which reports a mixed molecular and dissociative adsorption for water on curved TiO_2 nanoparticles. [307–310, 312] Considering the experimental data for nanoparticles with a size similar to **NS**, the agreement is even quantitative: for instance, the sum of the computed density of terminal and bridging OH is 3.5 nm^{-2}, which is in satisfactory agreement with a measured density of 4.5 nm^{-2}. [312] The surface density of undissociated water molecules cannot be easily compared with the experimental values since, in the measurements, it is hard to determine whether only a monolayer is adsorbed or, instead, more water layers are present on the surface.

Water adsorption causes also an increase in crystallinity in the structure of the whole spherical TiO_2 nanoparticle, as it can be noticed from the simulated EXAFS in Figure 5.18. In fact, the distribution of the Ti–O distances reported in the EXAFS spectrum of the bare **NS** model (see Figure 5.18b) shows a significant distortion from bulk interatomic distances in Figure 5.18a, as widely discussed in Section 3.5.2. In contrast, a bulk-like structure is recovered after the adsorption of a water monolayer (see Figure 5.18c) which presents a sharpening of the peak centered at 1.95 Å in the first coordination shell (Ti–O) and a small number of broad peaks close to the bulk values in the second coordination shell (Ti$\cdots$Ti and Ti$\cdots$O). This water-driven recovering of the crystallinity is related with the restoring of the full six-fold coordination of the surface Ti sites. A similar result has been already reported in a previous molecular mechanics study on the water/TiO_2 nanoparticle interface. [98]

The presence of water is expected to influence also the electronic structure of the the TiO_2 nanoparticle. In this regard, the electronic density of states (DOS) for the bare **NS** model and for the same system with an adsorbed water monolayer are shown in Figure 5.19, along with the projections on molecular water (H_2O), hydroxyls (OH), bridging oxygen atoms (O_{2c}) and O_{2c} species with a bound proton ($O_{2c}H$). The O–H bonding states of water are located between −16 and −14 eV, whereas the states of the lone pairs partially overlap with the valence band of the TiO_2 nanoparticle between −13 and −7 eV.

Upon the addition of an undissociated water monolayer to the bare **NS** nanoparticle model a clear effect can be noticed: the valence band edge is shifted by 1.32 eV towards more positive energies (compare Figure 5.19b with Figure 5.19a); similarly,

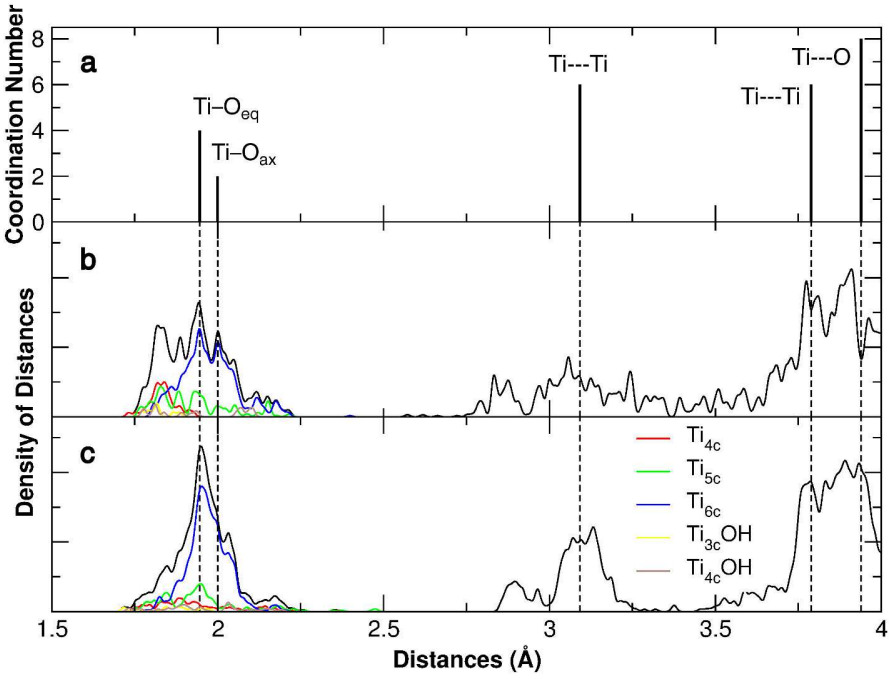

Figure 5.18 – Simulated EXAFS spectra as obtained with DFT(B3LYP) for bulk anatase (top panel, a) and for the **NS** model as it is (middle panel, b) and with a full monolayer of water molecules ($\alpha = 0.21$) adsorbed on it (bottom panel, c).

the conduction band edge shifts to higher energies but the extent of the shift is lower, causing an overall reduction of the band gap by 0.14 eV. This energy shift is caused by the interaction of the valence and conduction electronic states with water dipoles, which are mainly oriented with the negative sign close to the surface (for more details on the orientation of water see Section 5.4.3).

The water dissociation process induces an almost rigid back-shift of the valence and conduction band edges, as one can notice by comparing Figure 5.19c,d with Figure 5.19b. This effect occurs because valence states are stabilized by the protons adsorbed on the O_{2c} species, as it can be clearly observed by the more negative energy of the projection onto $O_{2c}H$ species (in green) with respect to the projections onto O_{2c} atoms (in violet). Very interestingly, also the energy level of the free O_{2c} species are shifted to more negative energies, even if they are not directly involved in the binding of a H atom. This implies that the O_{2c} species become less basic, i.e. less prone to bind a proton, the more water is dissociated.

In Table 5.13 the position of the band edges with respect to the vacuum for the bare and hydrated **NS** are tabulated, along with the HOMO–LUMO ($\Delta E_{H\text{-}L}$) and Kohn-Sham (E_{gKS}) energy gaps (for a definition of these quantities see Section 3.5.3). As discussed in Chapter 3, the HOMO–LUMO gap may be influenced by the presence of localized surface states close to the band edges. In order to elucidate the effect of

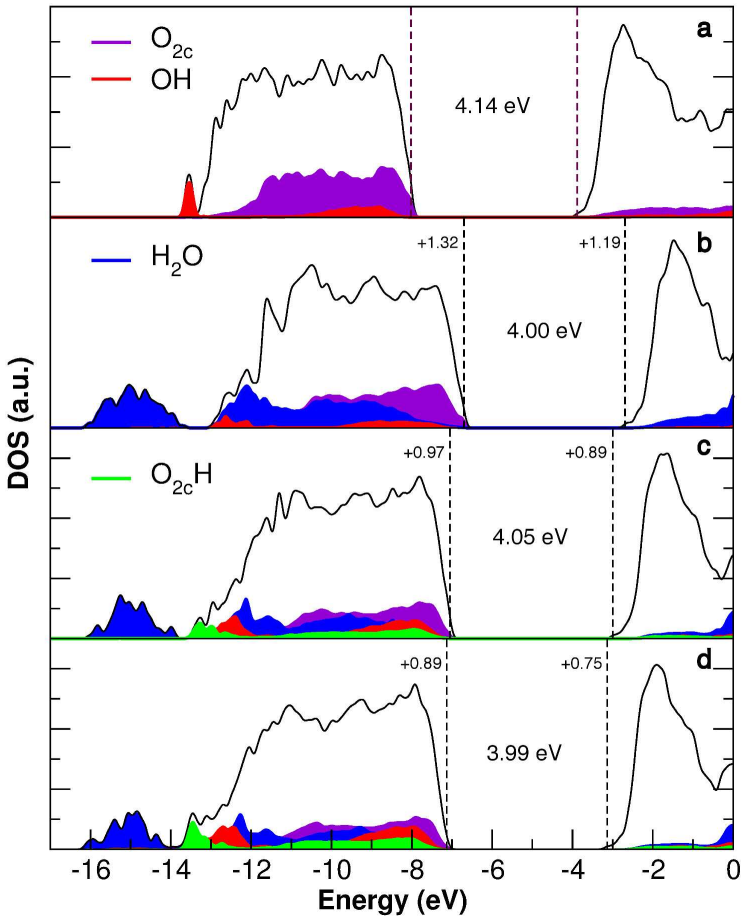

Figure 5.19 – Density of states and projected density of states for the bare **NS** (a), **NS** with a monolayer of undissociated water molecules ($\alpha = 0.00$, b) and with a monolayer of partially dissociated ($\alpha = 0.21$ for c and 0.30 for d) water molecules. In each panel, the band gap and the energy shift (in eV) of the valence and conduction band edges with respect to the bare **NS** model are given.

water on the band-like states, we report also the E_{gKS} gap, which is the difference between the highest occupied and lowest unoccupied delocalized Kohn-Sham state.

Noticeably, the $\Delta E_{H\text{-}L}$ and E_{gKS} energy gaps become very similar upon water monolayer adsorption and they perfectly match in the case of the most stable monolayer with a dissociation degree of 0.21. Thus, it appears that the interaction with the water monolayer shifts back into the valence band those localized surface states, which are instead at the valence band edge of the bare **NS**. It is worth noting that the E_{gKS} energy gap in presence of water is much closer to the DFT(B3LYP) bulk value (3.81 eV, see Table 3.12) than in the bare **NS** model.

Table 5.13 – DFT(B3LYP) Kohn-Sham energy values, with respect to the vacuum level, of the top of the valence band (Top VB) and of the bottom of the conduction band (Bottom VB) for the bare and hydrated **NS** model with different degrees of water dissociation (α). Energy differences between HOMO and LUMO levels ($\Delta E_{H\text{-}L}$) and Kohn-Sham energy gap (E_{gKS}) are also reported.

	Bare **NS**	$\alpha = 0.00$	$\alpha = 0.21$	$\alpha = 0.30$
TOP VB	−8.02	−6.70	−7.05	−7.13
BOTTOM CB	−3.88	−2.69	−3.00	−3.14
$\Delta E_{H\text{-}L}$	4.14	4.00	4.05	3.99
E_{gKS}	4.31	4.04	4.05	4.04

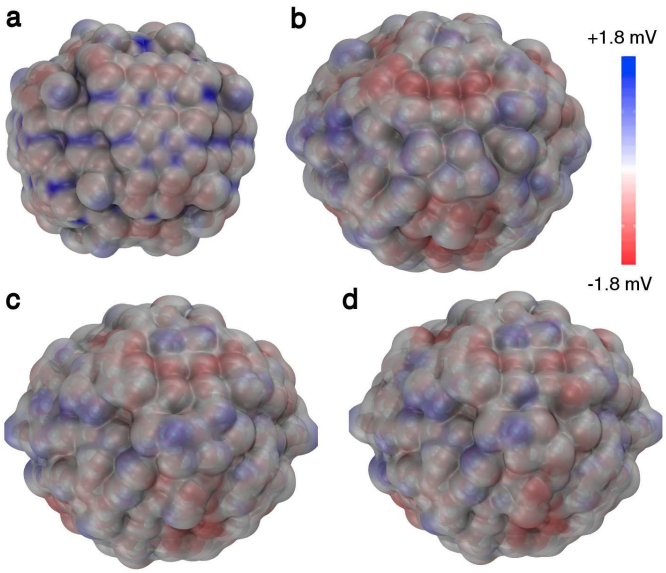

Figure 5.20 – Molecular electrostatic potential (MEP) projected on the charge density isosurface (isovalue = 0.0001 a.u.) for the bare **NS** model (a), **NS** with a monolayer of undissociated water (b) and partially dissociated one with $\alpha = 0.21$ and 0.30 for c and d, respectively. Blue areas are positively charged, red areas are negatively charged.

Finally, the molecular electrostatic potentials (MEP), projected on a charge density isosurface, for the bare (a) and hydrated (b, c, d) **NS** are shown in Figure 5.20. One can observe that for the bare **NS** (Figure 5.20a) bright blue spots are present, which correspond to the positive potential generated by the Ti cations. Upon adsorption of the undissociated water monolayer, these blue spots disappear and some other regions, corresponding to groups of O_{2c} species, become negatively charged (red areas in Figure 5.20b). This effect is mitigated by water dissociation, because of the adsorption of the H atoms, leading to an overall discharging of the O_{2c} atoms, which become less

prone to accept a proton from the water surroundings.

5.4.3 Multilayer coverage

The study of the dynamical properties of a water multilayer can provide useful information on the behaviour of a TiO_2 nanoparticle in a water environment. However, this task is not feasible at the DFT level, hence we employed only the computationally efficient MATORG+HBD approach.

The starting configuration for the water multilayer on the **NS** model has been constructed by adding a 6 Å-thick spherical shell of 824 H_2O molecules to the geometry of the most stable water monolayer ($\alpha = 0.21$), as obtained with the MATORG+HBD approach.

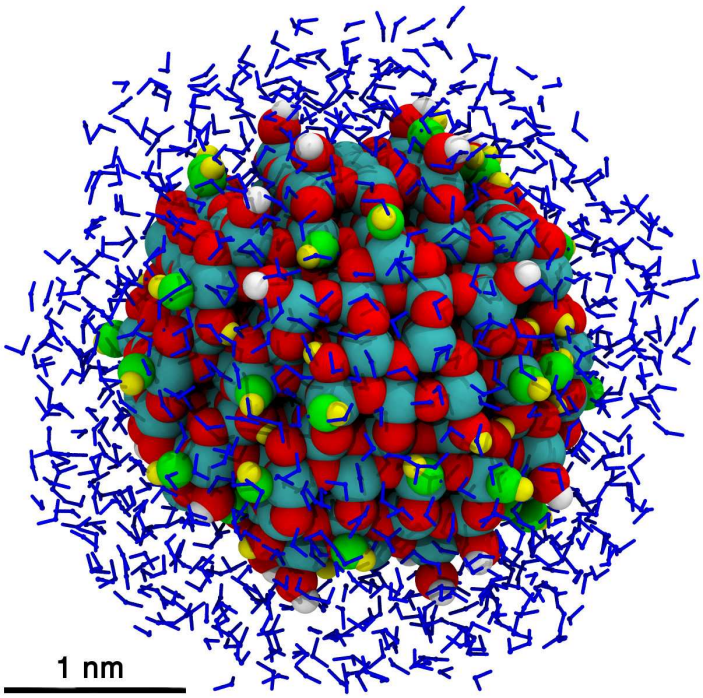

Figure 5.21 – Last snapshot of the MATORG+HBD molecular dynamics simulation of the NS model with a water multilayer, i.e. a monolayer of water ($\alpha = 0.21$) and an additional spherical shell of 824 H_2O molecules, for an overall stoichiometry of $(TiO_2)_{223} \bullet$ 978 H_2O. Titanium, oxygen and hydrogen atoms of the nanoparticle are shown as cyan, red and white spheres, respectively. Oxygen and hydrogen atoms of hydroxyl groups coming from dissociated water molecules are given in green and yellow, respectively; undissociated water molecules are shown as blue sticks.

Subsequently, the geometry has been relaxed to an energy minimum. It is worth noting that in the equilibrium structure water molecules have collapsed onto the

nanoparticle, reducing significantly the initial water shell thickness. The optimized structure has been used as initial configuration for the MATORG+HBD molecular dynamics run, whose final snapshot is represented in Figure 5.21. During the simulation time, no significant reactivity has been observed, except for a single recombination between a hydrogen adsorbed on a O_{2c} and a hydroxyl, leading to the formation of a water molecule.

Being the nanoparticle not perfectly spherical, the radial distribution function (RDF) from the center of mass is not a meaningful quantity to describe the structure of the multilayer, because it would be affected by the shape of the system. For instance, a peak in the RDF may appear split in two because in a certain direction the nanoparticle is elongated and in another direction is compressed. For this reason, we have analyzed the structure of the water multilayers in terms of MD-averaged distribution function $g(d)$ of the minimum distance d between the oxygen of a water molecule of the multilayer (O_w) and the superficial titanium atoms of the nanoparticle (Ti_{sup}). Note that, as it is defined in Section 5.2, the $g(d)$ function is analogous to the radial distribution function, since the value of $g(d)$ is related to water density at each distance and would tend to 1 for bulk water.

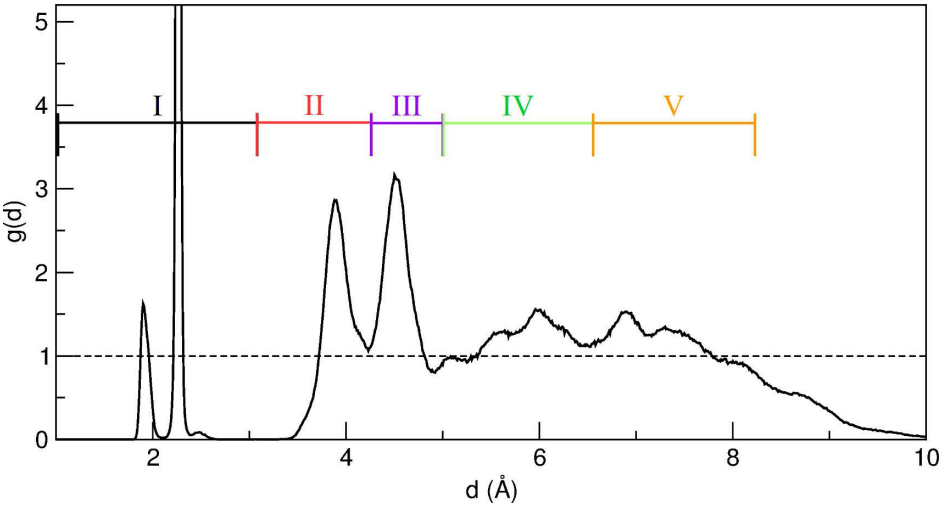

Figure 5.22 – Distribution function $g(d)$ of the distances d between the oxygen atoms of water molecules and the closest titanium atom of the surface, as extracted from the MATORG+HBD molecular dynamics run on the **NS** model with an adsorbed water multilayer. Roman numbers from I to V indicate the different water layers. A dashed black line is traced for $g(d) = 1$, which corresponds to bulk water density.

The distribution function $g(d)$, as derived from the MATORG+HBD molecular dynamics trajectory, is reported in Figure 5.22. First of all, the MD-averaged distance of water molecules from the surface extends from about 2 Å to 10 Å. At ∼10 Å the $g(d)$ is almost zero because of the finiteness of the model, hence we will consider the $g(d)$ to be meaningful up to about 8 Å. We can notice six clear density maxima in

the $g(d)$ function and the region around the peaks is assigned to a solvation layer, as graphically shown in Figure 5.22: the first two peaks at short O_w–Ti_{sup} distances are included in the first solvation layer (*Layer I*), whereas the other four peaks are considered to be included in *Layer II*, *III*, *IV* and *V*, respectively.

The two peaks in *Layer I* are centered at 1.90 and 2.27 Å and are related to dissociated and molecular water directly adsorbed on surface titanium atoms. The second peak is particularly high (up to a $g(d)$ of 28) and sharp, because many undissociated water molecules share a similar bond lenght.

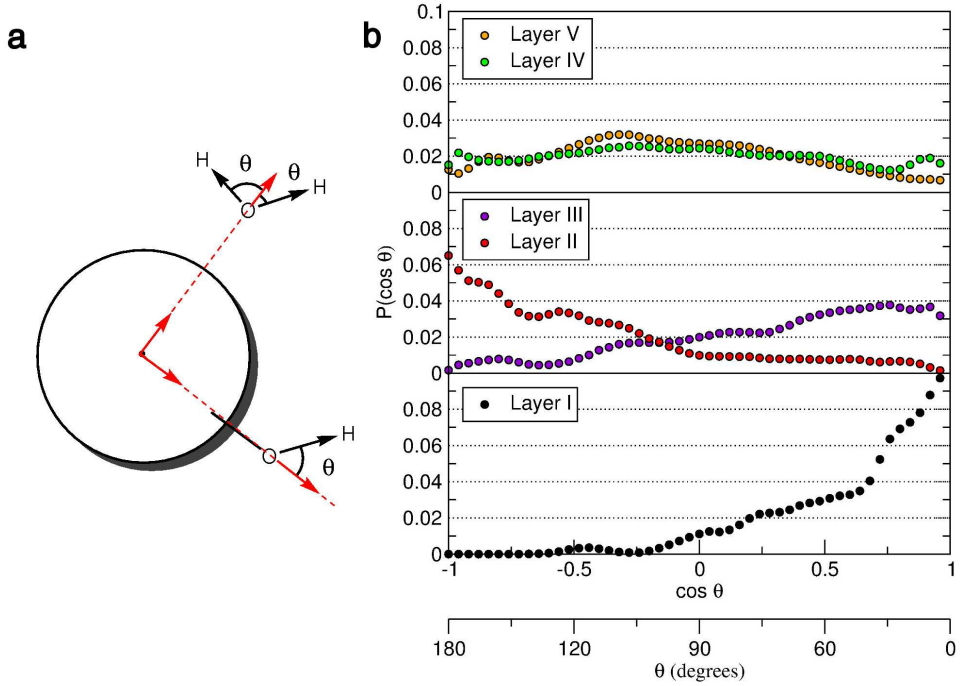

Figure 5.23 – (a) Graphical definition of the angle θ, i.e. the angle between the O–H bond vector (in black) and the vector connecting the water oxygen atom with the center of the **NS** model (radial vector, in red). The radial vector is translated so that it has the same origin than the O–H bond vector. A cos θ equals to 1 means that the O–H bond is directed outwards, whereas a value close to -1 means that the O–H bond is oriented towards the center of the nanosphere. (b) Probability distributions $P(\cos\theta)$ of the angle θ for the water molecules of the multilayer adsorbed on the **NS** model within *Layer I* (bottom panel, in black), *Layer II* and *III* (as red and violet points, respectively, in middle panel) and *Layer IV* and *V* (as green and orange points, respectively, in top panel).

In order to better understand the structure of the water multilayer, we report in Figure 5.23 the probability $P(\cos\theta)$ of the various O–H bond orientation within each of the five layers (see Section 5.2 for the definition of this quantity). Being θ the angle between the radial vector and the O–H bond, a value of 1 for the $\cos\theta$ implies that the O–H bond is directed outwards, whereas a value close to -1 means that the O–H

bond is oriented towards the center of the nanosphere. Note that in the case that an undissociated water molecule is considered, both θ angles are taken into account in the probability distribution.

In *Layer I*, the O–H bonds are preferentially oriented outwards. In such a way, the hydrogen atom of the adsorbed water molecules or hydroxyls can form H-bond with the outer layers, as it is clearly evidenced in Figure 5.24, where water adsorbates of *Layer I* are shown with a black oxygen atom. Interestingly, both O–H bonds of the undissociated water molecules are directed outwards, since no other maximum in the $P(\cos\theta)$ probability distribution is observed.

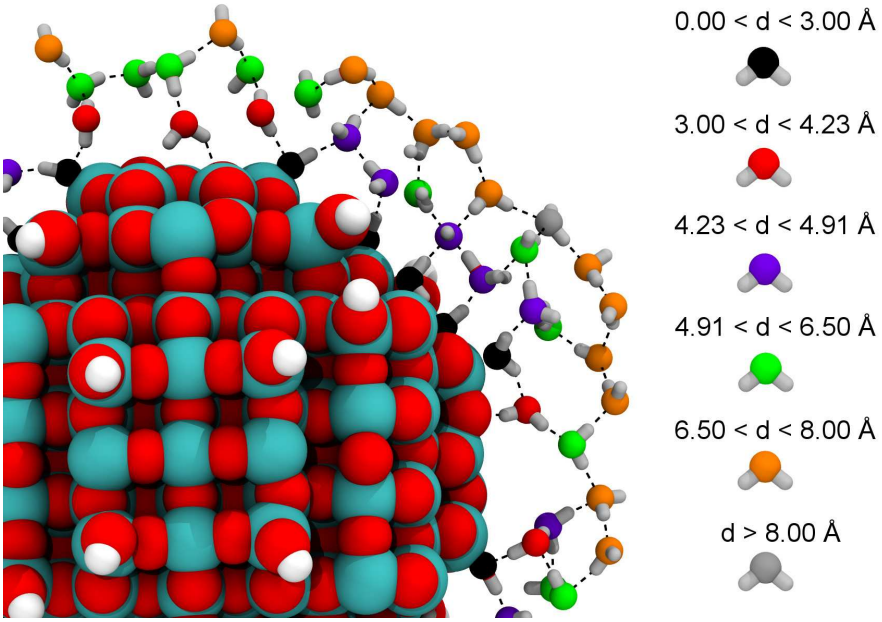

Figure 5.24 – Top view of a cross-section of the water multilayer on the **NS** model, as obtained from the last snapshot of the MATORG+HBD molecular dynamics simulations. Oxygen atoms of the adsorbed water molecules and hydroxyls are colored according to their distance from the closest titanium atom, as described in the legend on the right. Titanium, oxygen and hydrogen atoms of the nanoparticle are shown as cyan, red and white spheres, respectively. Hydrogen bonds are represented as dashed black lines.

Between 3 and 5 Å in the $g(d)$ function, we can observe the second and the third solvation layers (*Layer II* and *III*), which present two peaks centered at 3.89 Å and 4.50 Å. The probability of the different orientations of the O–H bond for these two layers is shown in middle panel of Figure 5.23. In this case, the $P(\cos\theta)$ is more evenly distributed, which means that water is oriented more randomly than in the first layer. Nonetheless, O–H bonds of H_2O molecules within *Layer II* are more likely to be oriented inwards, whereas the ones of *Layer III* are preferentially directed outwards. In fact, as clearly depicted in Figure 5.24, the second solvation layer (red

molecules) is mainly composed of water molecules which donate H-bonds to surface O_{2c}, adsorbed water or hydroxyl groups. On the contrary, water in *Layer III* (violet molecules) mostly accepts H-bonds from water adsorbates in the first solvation layer. Thus, in the third solvation layer the hydrogen atoms of the O–H bond are free to establish hydrogen bonds with the water overlayers.

Between 5 and 8 Å, the $g(d)$ distribution function is more complex and two main broad peaks are located at about 6 and 7 Å. The orientation of water molecules in these range of distances may provide a clue to understand the origin of these features. In fact, there is almost an equal probability of any orientation of the O–H bond for the water molecules within the fourth and fifth solvation layer (*Layer IV* and *Layer V*), as reported in top panels of Figure 5.23. Thus, water in these two layers does not present a long range order, even though in this region there is a water density slightly higher than in the bulk. However, these features may be caused by a spurious effect due to the finiteness of the model and further checks with a larger system are necessary to have a definite answer.

To sum up, three structured hydration layers have been clearly observed in the solvation shell of a TiO_2 spherical nanoparticle model: the first layer (black molecules in Figure 5.24) is composed by water molecules anchored to the surface titanium sites as undissociated water or OH groups; then, the second layer (red molecules in Figure 5.24) is more mobile and contains water molecules H-bonded via the hydrogen atom to surface O_{2c}, adsorbed water or hydroxyls; finally, the third layer (violet molecules in Figure 5.24) includes water molecules that accept hydrogen bonding from water adsorbates, either OH groups and H_2O. Water overlayers, i.e. the fourth and fifth layers, may be only weakly affected by the presence of the TiO_2 nanoparticle.

As a final comment, the $g(d)$ function between 3 and 5 Å is found to be about 2 on average, which indicates that in this region the water density is doubled with respect to that of bulk water. This is in line with the experimentally observed increased density of water by a factor of 2 in the inner water layers of a hydrated TiO_2 nanoparticle sample. [313]

5.5 Conclusions

The first-principles investigation of the properties of large TiO_2 models in aqueous surroundings is a very demanding task, that is yet not feasible at a full DFT level of theory, especially if one is interested in the dynamic properties of this important solid–liquid interface. Self-consistent field density functional tight-binding (SCC-DFTB) can be a valid option to tackle this challenging task, being a fast DFT-based algorithm, which has been proven to be accurate for a wide range of systems in materials science and (bio)chemistry. Since the computational effort within SCC-DFTB is much lower than in DFT, it allows for the simulation of large models up to several thousands of atoms. However, the accuracy of this approach is dependent on the validity of the DFTB parameters for the system under study.

Thus, we have first focused on the assessment of the reliability of SCC-DFTB for the study of the structural, energetic and dynamical properties of the titania/water-multilayers interface. When a proper combination of the already existing DFTB

parametrization sets for Ti-containing compounds, together with specific corrections for water systems, is employed, SCC-DFTB is capable to accurately describe the prototypical anatase (101)/water interface. Specifically, we combined the parameters commonly used for solid-state systems (matsci-0-3, MATSCI) with the ones largely tested for organic systems and water (mio-1-1, MIO) in a novel DFTB-based methodology which we have called MATORG+HBD.

First of all, we have assessed the ability of this new approach to model the two separated components of the interface: water/water interactions, as evaluated by water dimer H-bond energy and the bulk water radial distribution function, are in fair agreement with DFT and experimental references, as well as bulk TiO_2 lattice parameters. As regards the interface, the structural and energetic description of water adsorption on the (101) anatase surface was found to be in line with high-level DFT calculations. Thanks to this good balance between water/water and water/titania interactions, the MATORG+HBD methodology has been shown to be successful also for the dynamic description of the interface, when compared to DFT-based Car-Parrinello molecular dynamics simulations. Furthermore, this DFTB method was also found to give a satisfactory description of the transition state for water dissociation, even though the energy barrier is slightly overestimated with respect to hybrid DFT calculations. Overall, we found that our combined approach is able to reproduce the main features of the titania/water-multilayers interface with a DFT-like accuracy but at a particularly low computational cost.

Given this proven reliability of SCC-DFTB for water/water/titania interactions, we applied this method, in parallel with hybrid DFT, to model the interface between water and a realistic TiO_2 spherical nanoparticle with an average diameter of 2.2 nm. In particular, we have first investigated the adsorption of a single water molecule on different sites and a full water monolayer on the surface of the TiO_2 nanosphere. This nanoparticle model presents a large variety of inequivalent surface Ti atoms, which are the preferential water adsorption sites.

At single-site water coverage, the binding energies on these Ti sites, as obtained with hybrid DFT, can vary in a wide range between -0.4 and -1.9 eV. Dissociative adsorption is computed to be favored over molecular one for all the four-fold coordinated Ti sites and, rather surprisingly, also for several five-fold cordinates ones. Computed MATORG+HBD adsorption energies for undissociated water molecules are in very good agreement with hybrid DFT data, whereas the energies associated with water dissociation are systematically underestimated.

At monolayer coverage, in spite of the observed preference for dissociation at single-site coverage, the most stable configuration is the one where only $\sim$20% of the molecules are dissociated for either hybrid DFT and MATORG+HBD. Upon water monolayer adsorption, a recrystallization of the nanoparticle has been evidenced by the simulated EXAFS spectra. Furthermore, the monolayer of water molecules causes a considerable shift (> 1 eV) of the valence and conduction band edges towards higher energies. This effect is stronger for the valence band than for the conduction one, resulting in a small but significant reduction of the band gap with respect to the vacuum. The water dissociation process is found to partially shift back the band edges, due to the increase of adsorbed hydrogen species. On the whole, the average binding energy for the full monolayer on a spherical TiO_2 nanoparticle is considerably

higher than on a faceted one. As a consequence, the surface energy of a hydrated nanosphere is lower than the one of a hydrated nanocrystal.

Finally, the multilayer coverage has been investigated by MATORG+HBD molecular dynamics simulations. We observed the formation of five hydration layers within a distance from the surface of 8 Å. The first layer (up to 3 Å) is composed by a mix of molecular and dissociated water molecules directly adsorbed to the Ti site, whereas the second and the third ones (between 3 and 5 Å) include water molecules that donate and accept, respectively, hydrogen bonding with the oxygen species on the surface. Lastly, the fourth and fifth layers (between 5 and 8 Å) do not show any significant long-range order, even though their density is still higher than that of bulk water.

In conclusion, with the present computational study we provided an accurate picture of the thermodynamic, structural and electronic properties of the water/nano-TiO_2 interface. These insights into the molecular-level features of this interface, which is relevant for many energy-related and biomedical applications, can be extremely useful for an efficient design of TiO_2-based functional nanomaterials.

6 Summary and Conclusions

Titanium dioxide (TiO_2) is one of the most investigated materials for the direct conversion of light photons into electricity (photovoltaics) and chemical energy (photocatalysis). Although TiO_2 nanoparticles are commonly used as building blocks for photoapplications, most of the theoretical studies on titanium dioxide are still focused on bulk or extended surface TiO_2 models.

In this thesis, we pushed the boundaries of the state of the art of theoretical studies on TiO_2 by devising a computational toolbox for the modelling of realistic titanium dioxide nanoparticles in vacuum and in aqueous environment with hybrid density functional theory (DFT) and approximate-DFT, namely density-functional tight-binding (DFTB).

First, we prepared and refined stoichiometric and chemically stable models of anatase TiO_2 nanoparticles of both well-faceted and spherical shape. The range of size considered is from 1.5 to 4.4 nm, approaching the feasible limit for hybrid DFT calculations and the dimensions of real titania nanoparticles used in practical applications. In order to fully relax the less ordered structure of spherical nanoparticles, we performed a simulated high temperature annealing at the DFTB level, which allowed reaching a stable global minimum geometry. A detailed analysis of the models evidences the main features of faceted and spherical nanoparticles: nanocrystals are particularly rich in Ti_{5c} species, whereas nanospheres expose many highly reactive four-fold coordinated Ti atoms; spherical nanoparticles present higher surface-to-bulk ratio, larger surface energy and lower crystallinity than well-faceted ones. We also computed the electronic structure of these realistic metal oxide systems in terms of simulated density of states, energy gaps and frontier orbitals. Overall, this work highlights size and shape dependencies of structural and electronic properties of TiO_2 nanomaterials to exploit for different uses and applications.

Secondly, we acquired a first-principles electronic and atomistic description of the photoinduced processes in real-size TiO_2 nanoparticles of different shape by hybrid DFT calculations. This level of theory is required to partially correct for the self-interaction error and correctly localize photoexcited charge carriers in TiO_2. We modelled the overall process from electron/hole pair formation, to its separation and migration to the surface, which is found to be energetically favourable, proving that there is a tendency for electrons and holes to travel from the core of the nanoparticle to the surface sites. We determined the role played by low coordinated sites and by the

surface curvature on the charge trapping: corners and edges of the nanocrystals are poor electron traps but excellent hole traps; curved surfaces on nanospheres promote the migration of the electrons and holes from the core to subsurface/surface sites. We validated the models of photoexcited TiO_2 nanoparticles by an extensive comparison with available experimental data from electron paramagnetic resonance (EPR) and optical transitions experiments.

We exploited these models of photoexcited TiO_2 for a collaborative study where infrared and transient absorption measurements were used to investigate the effect of water adsorption on the photoexcited charge carriers dynamics. For this, we developed a strategy to simulate the coverage-dependent vibrational frequencies of water adsorbates on the surface of well-faceted and spherical titania nanoparticles. The computed vibrational structures are consistent with the experiments and allow for the identification of water adsorption modes on nanospheres and nanocrystals. We theoretically determined the stability of hole traps as a function of surface water coverage, proving a key role played by water on the hole trapping process in the case of spherical nanoparticles but not of well-faceted ones. These findings pave the way to novel strategies in the engineering of nanophotocatalysts morphology for improved performances in photoapplications.

Finally, we devised a computational approach for the investigation of the complex water/TiO_2 interface at a quantum mechanical level. We demonstrated the applicability of a computationally efficient DFTB methodology, based on the combination of the best available parameters, for the study of the interaction between TiO_2 and water multilayers. We proved this method to describe bulk TiO_2, water/water interactions and the static/dynamic behavior of a prototypical water/(101) anatase interface with an accuracy comparable to DFT. Because of the relatively low computational cost of this approach, we applied it to the study of large and realistic TiO_2 systems in an aqueous environment. Starting from the investigation of single water molecule adsorption, we increased the water coverage to the mono and then to the multilayer regime (up to a thickness of about 1 nm) on a 2.2 nm spherical TiO_2 nanoparticle. Up to the monolayer coverage, we compared DFTB results with hybrid DFT and found that only 20% of the water molecules dissociate. We determined structure, density and dipoles orientation for the multilayer coverage through DFTB molecular dynamics simulations at 300 K.

In conclusion, with the present work we have made a step forward in the understanding of the size- and shape-dependent structural, electronic and (photo)chemical properties of bare and hydrated titanium dioxide nanomaterials. Moreover, we have developed a computational framework for future investigations on more complex TiO_2-based systems, interfaces and composites.

Bibliography

[1] REN21, Renewable Energy Policy Network for the 21st Century, Paris, France (2017).
[2] Trends in Atmospheric Carbon Dioxide, `https://www.esrl.noaa.gov/gmd/ccgg/trends/full.html`, accessed: 2017-11-13.
[3] World's carbon dioxide concentration teetering on the point of no return, `https://www.theguardian.com/environment/2016/may/11/worlds-carbon-dioxide-concentration-teetering-on-the-point-of-no-return`, accessed: 2017-11-14.
[4] The consequences of climate change, `https://climate.nasa.gov/effects/`, accessed: 2017-11-13.
[5] A. J. Nozik and J. Miller, Chem. Rev. **110**, 6443 (2010).
[6] T. R. Cook, D. K. Dogutan, S. Y. Reece, Y. Surendranath, T. S. Teets, and D. G. Nocera, Chem. Rev. **110**, 6474 (2010).
[7] R. Feynman, Eng. Sci. **4**, 23 (1960).
[8] F. Caruso, T. Hyeon, and V. M. Rotello, Chem. Soc. Rev. **41**, 2537 (2012).
[9] M. Kapilashrami, Y. Zhang, Y.-S. Liu, A. Hagfeldt, and J. Guo, Chem. Rev. **114**, 9662 (2014).
[10] B. O'Regan and M. Grätzel, Nature **353**, 737 (1991).
[11] J. S. Manser, J. A. Christians, and P. V. Kamat, Chem. Rev. **116**, 12956 (2016).
[12] W. S. Yang, B.-W. Park, E. H. Jung, N. J. Jeon, Y. C. Kim, D. U. Lee, S. S. Shin, J. Seo, E. K. Kim, J. H. Noh, and S. I. Seok, Science **356**, 1376 (2017).
[13] M. Grätzel, Nature **414**, 338 (2001).
[14] O. Carp, C. L. Huisman, and A. Reller, Prog. Solid State Chem. **32**, 33 (2004).
[15] M. Ni, M. K. Leung, D. Y. Leung, and K. Sumathy, Renew. Sust. En. Rev. **11**, 401 (2007).
[16] Y. Lan, Y. Lu, and Z. Ren, Nano En. **2**, 1031 (2013).
[17] H. Fu, T. Xu, S. Zhu, and Y. Zhu, Environ. Sci. Technol. **42**, 8064 (2008).
[18] O. Khaselev and J. A. Turner, Science **280**, 425 (1998).
[19] R. J. Barnes, R. Molina, J. Xu, P. J. Dobson, and I. P. Thompson, J. Nanopart. Res. **15**, 1432 (2013).
[20] A. Fujishima and K. Honda, Nature **238**, 37 (1972).
[21] Y. Ma, X. Wang, Y. Jia, X. Chen, H. Han, and C. Li, Chem. Rev. **114**, 9987 (2014).
[22] Y. Bai, I. Mora-Ser, F. De Angelis, J. Bisquert, and P. Wang, Chem. Rev. **114**, 10095 (2014).
[23] J. Schneider, M. Matsuoka, M. Takeuchi, J. Zhang, Y. Horiuchi, M. Anpo, and D. W. Bahnemann, Chem. Rev. **114**, 9919 (2014).
[24] N. M. Dimitrijevic, B. K. Vijayan, O. G. Poluektov, T. Rajh, K. A. Gray, H. He, and P. Zapol, J. Am. Chem. Soc. **133**, 3964 (2011).
[25] S. Malato, P. Fernández-Ibáñez, M. Maldonado, J. Blanco, and W. Gernjak, Catal.

Today **147**, 1 (2009).
[26] J. Lyu, L. Zhu, and C. Burda, ChemCatChem **5**, 3114 (2013).
[27] J.-J. Yin, J. Liu, M. Ehrenshaft, J. E. Roberts, P. P. Fu, R. P. Mason, and B. Zhao, Toxicol. Appl. Pharmacol. **263**, 81 (2012).
[28] T. L. Doane and C. Burda, Chem. Soc. Rev. **41**, 2885 (2012).
[29] L. Sang, Y. Zhao, and C. Burda, Chem. Rev. **114**, 9283 (2014).
[30] M. Landmann, E. Rauls, and W. G. Schmidt, J. Phys. Condens. Matter **24**, 195503 (2012).
[31] T. Rajh, N. M. Dimitrijevic, M. Bissonnette, T. Koritarov, and V. Konda, Chem. Rev. **114**, 10177 (2014).
[32] L. Kavan, M. Grätzel, S. E. Gilbert, C. Klemenz, and H. J. Scheel, J. Am. Chem. Soc. **118**, 6716 (1996).
[33] L. Liu, H. Zhao, J. Andino, and Y. Li, ACS Catal. **2**, 1817 (2012).
[34] M. Cargnello, T. R. Gordon, and C. B. Murray, Chem. Rev. **114**, 9319 (2014).
[35] R. C. Mehrotra and A. Singh, Chem. Soc. Rev. **25**, 1 (1996).
[36] W. Zhang, Z. Zhu, and C. Y. Cheng, Hydrometallurgy **108**, 177 (2011).
[37] G. Liu, H. G. Yang, J. Pan, Y. Q. Yang, G. Q. M. Lu, and H.-M. Cheng, Chem. Rev. **114**, 9559 (2014).
[38] J. Tang, F. Redl, Y. Zhu, T. Siegrist, L. E. Brus, and M. L. Steigerwald, Nano Lett. **5**, 543 (2005).
[39] C. Chen, R. Hu, K. Mai, Z. Ren, H. Wang, G. Qian, and Z. Wang, Cryst. Growth Des. **11**, 5221 (2011).
[40] J. Li and D. Xu, Chem. Commun. **46**, 2301 (2010).
[41] H. G. Yang, C. H. Sun, S. Z. Qiao, J. Zou, G. Liu, S. C. Smith, H. M. Cheng, and G. Q. Lu, Nature **453**, 638 (2008).
[42] J. Zhang, B. Wu, L. Huang, P. Liu, X. Wang, Z. Lu, G. Xu, E. Zhang, H. Wang, Z. Kong, J. Xi, and Z. Ji, J. Alloys Compd. **661**, 441 (2016).
[43] S. Yang, B. X. Yang, L. Wu, Y. H. Li, P. Liu, H. Zhao, Y. Y. Yu, X. Q. Gong, and H. G. Yang, Nat. Commun. **5**, 5355 (2014).
[44] T. Paunesku, T. Rajh, G. Wiederrecht, J. Maser, S. Vogt, N. Stojicevic, M. Protic, B. Lai, J. Oryhon, M. Thurnauer, and G. Woloschak, Nat. Mater. **2**, 343 (2003).
[45] T. Tachikawa, Y. Asanoi, K. Kawai, S. Tojo, A. Sugimoto, M. Fujitsuka, and T. Majima, Chem. Eur. J. **14**, 1492 (2008).
[46] T. Rajh, J. M. Nedeljkovic, L. X. Chen, O. Poluektov, and M. C. Thurnauer, J. Phys. Chem. B **103**, 3515 (1999).
[47] N. Serpone, D. Lawless, R. Khairutdinov, and E. Pelizzetti, J. Phys. Chem. **99**, 16655 (1995).
[48] T. Paunesku, T. Rajh, G. Wiederrecht, J. Maser, S. Vogt, N. Stojicevic, M. Protic, B. Lai, J. Oryhon, M. Thurnauer, and G. Woloschak, Nat. Mater. **2**, 343 (2003).
[49] T. Rajh, Z. Saponjic, J. Q. Liu, N. M. Dimitrijevic, N. F. Scherer, M. Vega-Arroyo, P. Zapol, L. A. Curtiss, and M. C. Thurnauer, Nano Lett. **4**, 1017 (2004).
[50] T. Paunesku, S. Vogt, B. Lai, J. Maser, N. Stojicevic, K. T. Thurn, C. Osipo, H. Liu, D. Legnini, Z. Wang, C. Lee, and G. E. Woloschak, Nano Lett. **7**, 596 (2007).
[51] T. Tachikawa, Y. Asanoi, K. Kawai, S. Tojo, A. Sugimoto, M. Fujitsuka, and T. Majima, Chem. Eur. J. **14**, 1492 (2008).
[52] K. T. Thurn, T. Paunesku, A. Wu, E. M. B. Brown, B. Lai, S. Vogt, J. Maser, M. Aslam, V. Dravid, R. Bergan, and G. E. Woloschak, Small **5**, 1318 (2009).
[53] H. Zhang and F. Banfield, J. Mater. Chem. **8**, 2073 (1998).
[54] G. Li, L. Li, J. Boerio-Goates, and B. F. Woodfield, J. Am. Chem. Soc. **127**, 8659 (2005).

[55] D. Reyes-Coronado, G. Rodríguez-Gattorno, M. E. Espinosa-Pesqueira, C. Cab, R. de Coss, and G. Oskam, Nanotechnology **19**, 145605 (2008).
[56] N. M. Dimitrijevic, Z. V. Saponjic, B. M. Rabatic, O. G. Poluektov, and T. Rajh, J. Phys. Chem. C **111**, 14597 (2007).
[57] P. J. Hardman, G. N. Raikar, C. A. Muryn, G. Vanderlaan, P. L. Wincott, G. Thornton, D. W. Bullett, and P. Dale, Phys. Rev. B **49**, 7170 (1994).
[58] U. Diebold, Surf. Sci. Rep. **48**, 53 (2003).
[59] N. A. Deskins, R. Rousseau, and M. Dupuis, J. Phys. Chem. C **114**, 5891 (2010).
[60] F. De Angelis, C. Di Valentin, S. Fantacci, A. Vittadini, and A. Selloni, Chem. Rev. **114**, 9708 (2014).
[61] J. K. Burdett, T. Hughbanks, G. J. Miller, J. W. Richardson, and J. V. Smith, J. Am. Chem. Soc. **109**, 3639 (1987).
[62] R. Asahi, Y. Taga, W. Mannstadt, and A. J. Freeman, Phys. Rev. B **61**, 7459 (2000).
[63] H. Tang, F. Lévy, H. Berger, and P. E. Schmid, Phys. Rev. B **52**, 7771 (1995).
[64] Y. F. Zhang, W. Lin, Y. Li, K. N. Ding, and J. Q. Li, J. Phys. Chem. B **109**, 19270 (2005).
[65] P. Deak, B. Aradi, and T. Frauenheim, Phys. Rev. B **83**, 155207 (2011).
[66] G. Mattioli, P. Alippi, F. Filippone, R. Caminiti, and A. A. Bonapasta, J. Phys. Chem. C **114**, 21694 (2010).
[67] L. Chiodo, J. M. García-Lastra, A. Iacomino, S. Ossicini, J. Zhao, H. Petek, and A. Rubio, Phys. Rev. B **82**, 045207 (2010).
[68] M. van Schilfgaarde, T. Kotani, and S. Faleev, Phys. Rev. Lett. **96**, 226402 (2006).
[69] W. Kang and M. S. Hybertsen, Phys. Rev. B **82**, 085203 (2011).
[70] C. E. Patrick and F. Giustino, J. Phys. Condens. Matter **24**, 202201 (2012).
[71] D. O. Scanlon, C. W. Dunnill, J. Buckeridge, S. A. Shevlin, A. J. Logsdail, S. M. Woodley, C. R. A. Catlow, M. J. Powell, R. G. Palgrave, I. P. Parkin, G. W. Watson, T. W. Keal, P. Sherwood, A. Walsh, and A. A. Sokol, Nat. Mater. **12**, 798 (2013).
[72] Y. Zhao, B. J. Lynch, and D. G. Truhlar, J. Phys. Chem. A **108**, 2715 (2004).
[73] C. Di Valentin and A. Selloni, J. Phys. Chem. Lett. **2**, 2223 (2011).
[74] I. G. Austin and N. F. Mott, Adv. Phys. **18**, 41 (1969).
[75] N. A. Deskins and M. Dupuis, Phys. Rev. B **75**, 195212 (2007).
[76] B. J. Morgan and G. W. Watson, Phys. Rev. B **80**, 233102 (2009).
[77] P. Deák, B. Aradi, and T. Frauenheim, Phys. Rev. B **86**, 195206 (2012).
[78] T. Yamamoto and T. Ohno, Phys. Chem. Chem. Phys. **14**, 589 (2012).
[79] N. A. Deskins and M. Dupuis, J. Phys. Chem. C **113**, 346 (2009).
[80] O. I. Micic, Y. Zhang, K. R. Cromack, A. D. Trifunac, and M. C. Thurnauer, J. Phys. Chem. **97**, 7277 (1993).
[81] M. Lazzeri, A. Vittadini, and A. Selloni, Phys. Rev. B **63**, 155409 (2001).
[82] C. Arrouvel, M. Digne, M. Breysse, H. Toulhoat, and P. Raybaud, J. Catal. **222**, 152 (2004).
[83] A. S. Barnard and P. Zapol, Phys. Rev. B **70**, 235403 (2004).
[84] Z. Zhao, Z. Li, and Z. Zou, J. Phys. Condens. Matter **22**, 175008 (2010).
[85] T. R. Esch, I. Gadaczek, and T. Bredow, Appl. Surf. Sci. **288**, 275 (2014).
[86] L. Mino, A. M. Ferrari, V. Lacivita, G. Spoto, S. Bordiga, and A. Zecchina, J. Phys. Chem. C **115**, 7694 (2011).
[87] S. Selçuk and A. Selloni, Nat. Mat. **15**, 1107 (2016).
[88] G. Z. Wulff, Kristallogr. Mineral **34**, 449 (1901).
[89] A. S. Barnard and L. A. Curtiss, Nano Lett. **5**, 1261 (2005).
[90] A. S. Barnard, P. Zapol, and L. A. Curtiss, J. Chem. Theory Comput. **1**, 107 (2005).
[91] M. Lazzeri and A. Selloni, Phys. Rev. Lett. **87**, 266105/1 (2001).

[92] Y. Liang, S. Gan, S. A. Chambers, and E. I. Altman, Phys. Rev. B **63**, 235402 (2001).
[93] X.-Q. Gong and A. Selloni, J. Phys. Chem. B **109**, 19560 (2005).
[94] P. K. Naicker, P. T. Cummings, H. Zhang, and J. F. Banfield, J. Phys. Chem. B **109**, 15243 (2005).
[95] D. R. Collins, W. Smith, N. M. Harrison, and T. R. Forester, J. Mater. Chem. **7**, 2543 (1997).
[96] V. N. Koparde and P. T. Cummings, J. Phys. Chem. B **109**, 24280 (2005).
[97] M. Alimohammadi and K. A. Fichthorn, Nano Lett. **9**, 4198 (2009).
[98] V. N. Koparde and P. T. Cummings, J. Phys. Chem. C **111**, 6920 (2007).
[99] M. Raju, A. C. T. Van Duin, and K. A. Fichthorn, Nano Lett. **14**, 1836 (2014).
[100] S.-y. Kim, A. C. T. V. Duin, and J. D. Kubicki, J. Mater. Res. **28**, 513 (2013).
[101] A. Hagfeldt, H. Siegbahn, S. E. Lindquist, and S. Lunell, Int. J. Quantum Chem. **44**, 477 (1992).
[102] T. Bredow and K. Jug, J. Phys. Chem. **99**, 285 (1995).
[103] K. D. Schierbaum and W. X. Xu, Int. J. Quantum Chem. **57**, 1121 (1996).
[104] D. R. Hummer, J. D. Kubicki, P. R. C. Kent, J. E. Post, and P. J. Heaney, J. Phys. Chem. C **113**, 4240 (2009).
[105] F. Nunzi, E. Mosconi, L. Storchi, E. Ronca, A. Selloni, M. Grätzel, and F. De Angelis, Energy Environ. Sci. **6**, 1221 (2013).
[106] Y. F. Li and Z. P. Liu, J. Am. Chem. Soc. **133**, 15743 (2011).
[107] G. Mattioli, A. Amore Bonapasta, D. Bovi, and P. Giannozzi, J. Phys. Chem. B **118**, 29928 (2014).
[108] F. Nunzi, L. Storchi, M. Manca, R. Giannuzzi, G. Gigli, and F. D. Angelis, ACS Appl. Mater. Interfaces **6**, 2471 (2014).
[109] O. Lamiel-Garcia, K. C. Ko, J. Y. Lee, S. T. Bromley, and F. J. Illas, J. Chem. Theory Comput. **13**, 17851793 (2014).
[110] M. Matsui and M. Akaogi, Mol. Simul. **6**, 239 (1991).
[111] C. H. Sun, L. M. Liu, A. Selloni, G. Q. Lu, and S. C. Smith, Mater. Chem. **20**, 10319 (2010).
[112] A. Vittadini, A. Selloni, F. P. Rotzinger, and M. Grätzel, Phys. Rev. Lett. **81**, 2954 (1998).
[113] G. S. Herman, Z. Dohnlek, N. Ruzycki, and U. Diebold, J. Phys. Chem. B **107**, 2788 (2003).
[114] Y. He, A. Tilocca, O. Dulub, A. Selloni, and U. Diebold, Nat. Mater. **8**, 585 (2009).
[115] U. Aschauer, Y. He, H. Cheng, S.-C. Li, U. Diebold, and A. Selloni, J. Phys. Chem. C **114**, 1278 (2010).
[116] M. Sumita, C. Hu, and Y. Tateyama, J. Phys. Chem. C **114**, 18529 (2010).
[117] A. Tilocca and A. Selloni, Langmuir **20**, 8379 (2004).
[118] A. Tilocca and A. Selloni, J. Phys. Chem. B **116**, 9114 (2012).
[119] U. J. Aschauer, A. Tilocca, and A. Selloni, Int. J. Quantum Chem. **115**, 1250 (2015).
[120] G. Mattioli, F. Filippone, R. Caminiti, and A. A. Bonapasta, J. Phys. Chem. C **112**, 13579 (2008).
[121] S. Selçuk and A. Selloni, J. Phys. Chem. C **117**, 6358 (2013).
[122] J. Rossmeisl, Z. W. Qu, H. Zhu, G. J. Kroes, and J. K. Nørskov, J. Electroanal. Chem. **607**, 83 (2007).
[123] A. Valds, Z. W. Qu, G. J. Kroes, J. Rossmeisl, and J. K. Nørskov, J. Phys. Chem. C **112**, 9872 (2008).
[124] Y.-F. Li, Z.-P. Liu, L. Liu, and W. Gao, J. Am. Chem. Soc. **132**, 13008 (2010).
[125] J. Chen, Y.-F. Li, P. Sit, and A. Selloni, J. Am. Chem. Soc. **135**, 18774 (2013).
[126] C. D. Valentin, J. Phys. Condens. Matter **28**, 074002 (2016).

[127] S. Y. Kim, N. Kumar, P. Persson, J. Sofo, A. C. T. Van Duin, and J. D. Kubicki, Langmuir **29**, 7838 (2013).
[128] E. G. Brandt, L. Agosta, and A. P. Lyubartsev, Nanoscale **8**, 13385 (2016).
[129] W. Koch and M. C. Holthausen, *A Chemist's Guide to Density Functional Theory* (Wiley - VCH, Weinheim - New York, 2nd edition, 2001).
[130] T. Koopmans, Physica **1**, 104 (1934).
[131] F. Bloch, Zeitschrift fur Physik **52**, 555 (1929).
[132] H. J. Monkhorst and J. D. Pack, Phys. Rev. B **13**, 5188 (1976).
[133] M. R. V. Jørgensen, V. R. Hathwar, N. Bindzus, N. Wahlberg, Y.-S. Chen, J. Overgaard, and B. B. Iversen, IUCrJ **1**, 267 (2014).
[134] L. H. Thomas, Proc. Cambridge Philos. Soc. **23**, 542 (1927).
[135] E. Fermi, Z. Phys. **48**, 73 (1928).
[136] P. Hohenberg and W. Kohn, Phys. Rev. **136**, B864 (1964).
[137] W. Kohn and L. J. Sham, Phys. Rev. **140**, A1133 (1965).
[138] R. G. Parr and W. Yang, Annu. Rev. Phys. Chem. **46**, 701 (1995).
[139] P. A. M. Dirac, Math. Proc. Camb. Philos. Soc. **26**, 376 (1930).
[140] D. M. Ceperley and B. J. Alder, Phys. Rev. Lett. **45**, 566 (1980).
[141] S. H. Vosko, L. Wilk, and M. Nusair, Can. J. Phys. **58**, 1200 (1980).
[142] V. N. Staroverov, G. E. Scuseria, J. Tao, and J. P. Perdew, The Journal of Chemical Physics **119**, 12129 (2003).
[143] A. D. Boese, J. M. L. Martin, and N. C. Handy, J. Chem. Phys. **119**, 3005 (2003).
[144] J. P. Perdew, K. Burke, and M. Ernzerhof, Phys. Rev. Lett. **77**, 3865 (1996).
[145] C. Lee, W. Yang, and R. G. Parr, Phys. Rev. B **37**, 785 (1988).
[146] F. Jensen, *Introduction to Computational Chemistry* (John Wiley & Sons, West Sussex, 2006).
[147] A. D. Becke, J. Chem. Phys. **98**, 5648 (1993).
[148] F. Corà, M. Alfredsson, G. Mallia, D. S. Middlemiss, W. C. Mackrodt, R. Dovesi, and R. Orlando, in *Principles and Applications of Density Functional Theory in Inorganic Chemistry II* (Springer Berlin Heidelberg, Berlin, Heidelberg, 2004), pp. 171–232.
[149] J. Muscat, A. Wander, and N. Harrison, Chem. Phys. Lett. **342**, 397 (2001).
[150] F. Labat, P. Baranek, and C. Adamo, J. Chem. Theory Comput. **4**, 341 (2008).
[151] J. Heyd and G. E. Scuseria, J. Chem. Phys. **121**, 1187 (2004).
[152] J. P. Perdew and M. Levy, Phys. Rev. Lett. **51**, 1884 (1983).
[153] J. P. Perdew and M. Levy, Phys. Rev. B **56**, 16021 (1997).
[154] S. Kümmel and L. Kronik, Rev. Mod. Phys. **80**, 3 (2008).
[155] J. Paier, M. Marsman, K. Hummer, G. Kresse, I. C. Gerber, and J. G. Ángyán, J. Chem. Phys. **124**, 154709 (2006).
[156] J. Paier, M. Marsman, K. Hummer, G. Kresse, I. C. Gerber, and J. G. Ángyán, J. Chem. Phys. **125**, 249901 (2006).
[157] V. N. Staroverov, G. E. Scuseria, J. Tao, and J. P. Perdew, J. Chem. Phys. **119**, 12129 (2003).
[158] J. Tao and J. P. Perdew, J. Chem. Phys. **122**, 114102 (2005).
[159] F. Furche and R. Ahlrichs, J. Chem. Phys. **117**, 7433 (2002).
[160] L. Hedin, Phys. Rev. **139**, A796 (1965).
[161] E. E. Salpeter and H. A. Bethe, Phys. Rev. **84**, 1232 (1951).
[162] F. Gallino, G. Pacchioni, and C. Di Valentin, J. Chem. Phys. **133**, 144512 (2010).
[163] C. G. Van de Walle and J. Neugebauer, J. Appl. Phys. **95**, 3851 (2004).
[164] S. Lany and A. Zunger, Phys. Rev. B **78**, 235104 (2008).
[165] G. Seifert and J.-O. Joswig, Wiley Interdiscip. Rev. Comput. Mol. Sci. **2**, 456 (2012).
[166] E. Hückel, Zeitschrift für Physik **70**, 204 (1931).

[167] J. C. Slater and G. F. Koster, Phys. Rev. **94**, 1498 (1954).
[168] D. J. Chadi, Phys. Rev. Lett. **43**, 43 (1979).
[169] M. Elstner, D. Porezag, G. Jungnickel, J. Elsner, M. Haugk, T. Frauenheim, S. Suhai, and G. Seifert, Phys. Rev. B **58**, 7260 (1998).
[170] M. Elstner and G. Seifert, Philos. Trans. Royal Soc. A **372**, 20120483 (2014).
[171] M. Elstner, D. Porezag, G. Jungnickel, J. Elsner, M. Haugk, T. Frauenheim, S. Suhai, and G. Seifert, Phys. Rev. B **58**, 7260 (1998).
[172] M. Elstner, Theor. Chem. Acc. **116**, 316 (2006).
[173] H. Hu, Z. Lu, M. Elstner, J. Hermans, and W. Yang, J. Phys. Chem. A **111**, 5685 (2007).
[174] Potential energy surfaces, Model chemistries, Asking the right questions, `http://www.chem.wayne.edu/~hbs/chm6440/PES.html`, accessed: 2017-09-19.
[175] C. G. Broyden, IMA J. Appl. Math. **6**, 76 (1970).
[176] C. G. Broyden, IMA J. Appl. Math. **6**, 222 (1970).
[177] S. Kirkpatrick, C. D. Gelatt, and M. P. Vecchi, Science **220**, 671 (1983).
[178] G. Henkelman, B. P. Uberuaga, and H. Jnsson, J. Chem. Phys. **113**, 9901 (2000).
[179] M. P. Allen and D. J. Tildesley, *Computer Simulation of Liquids* (Clarendon Press, Oxford, 1960).
[180] L. Verlet, Phys. Rev. **159**, 98 (1967).
[181] X. Li, J. M. Millam, and H. B. Schlegel, J. Chem. Phys. **113**, 10062 (2000).
[182] R. Car and M. Parrinello, Phys. Rev. Lett. **55**, 2471 (1985).
[183] W. G. Hoover, Phys. Rev. A **31**, 1695 (1985).
[184] G. J. Martyna, M. L. Klein, and M. Tuckerman, J. Chem. Phys. **97**, 2635 (1992).
[185] R. Dovesi, R. Orlando, A. Erba, C. M. Zicovich-Wilson, B. Civalleri, S. Casassa, L. Maschio, M. Ferrabone, M. De La Pierre, P. D'Arco, Y. Nol, M. Caus, M. Rrat, and B. Kirtman, Int. J. Quantum Chem. **114**, 1287 (2014).
[186] B. Aradi, B. Hourahine, and T. Frauenheim, J. Phys. Chem. A **111**, 5678 (2007).
[187] R. Luschtinetz, J. Frenzel, T. Milek, and G. Seifert, J. Phys. Chem. C **113**, 5730 (2009).
[188] A. H. Larsen, J. J. Mortensen, J. Blomqvist, I. E. Castelli, R. Christensen, M. Duak, J. Friis, M. N. Groves, B. Hammer, C. Hargus, E. D. Hermes, P. C. Jennings, P. B. Jensen, J. Kermode, J. R. Kitchin, E. L. Kolsbjerg, J. Kubal, K. Kaasbjerg, S. Lysgaard, J. B. Maronsson, T. Maxson, T. Olsen, L. Pastewka, A. Peterson, C. Rostgaard, J. Schitz, O. Schtt, M. Strange, K. S. Thygesen, T. Vegge, L. Vilhelmsen, M. Walter, Z. Zeng, and K. W. Jacobsen, J.Phys. Condens. Matter **29**, 273002 (2017).
[189] M. Connolly, Science **221**, 709 (1983).
[190] M. L. Connolly, J. Appl. Cryst. **16**, 548 (1983).
[191] L. X. Chen, T. Rajh, Z. Wang, and M. C. Thurnauer, J. Phys. Chem. B **101**, 10688 (1997).
[192] P. Deák, B. Aradi, and T. Frauenheim, Phys. Rev. B **83**, 155207 (2011).
[193] T. Stein, H. Eisenberg, L. Kronik, and R. Baer, Phys. Rev. Lett. **105**, 266802 (2010).
[194] E. J. Baerends, O. V. Gritsenko, and R. van Meer, Phys. Chem. Chem. Phys. **15**, 16408 (2013).
[195] K. Shirai, T. Sugimoto, K. Watanabe, M. Haruta, H. Kurata, and Y. Matsumoto, Nano Lett. **16**, 1323 (2016).
[196] G. Seifert, D. Porezag, and T. Frauenheim, Int. J. Quantum Chem. **58**, 185 (1996).
[197] G. Dolgonos, B. Aradi, N. H. Moreira, and T. Frauenheim, J. Chem. Theory. Comput. **6**, 266 (2010).
[198] H. Fox, K. E. Newman, W. F. Schneider, and S. A. Corcelli, J. Chem. Theory. Comput. **6**, 499 (2010).

[199] V. C. Fuertes, C. F. A. Negre, M. B. Oviedo, F. P. Bonaf, F. Y. Oliva, and C. G. Snchez, J. Phys. Condens. Matter **25**, 115304 (2013).
[200] Y. Liu and R. O. Claus, J. Am. Chem. Soc. **119**, 5273 (1997).
[201] Y. Zhu, C. Ding, G. Ma, and Z. Du, J. Sol. State. Chem. **139**, 124 (1998).
[202] V. Luca, J. Phys. Chem. C **113**, 6367 (2009).
[203] D. P. Colombo, K. A. Roussel, J. Saeh, D. E. Skinner, J. J. Cavaleri, and R. M. Bowman, Chem. Phys. Lett. **232**, 207 (1995).
[204] F. Labat, P. Baranek, C. Domain, C. Minot, and C. Adamo, J. Chem. Phys. **126**, 154703 (2007).
[205] L. E. Brus, J. Chem. Phys. **80**, 4403 (1984).
[206] K. M. Reddy, S. V. Manorama, and A. R. Reddy, Mater. Chem. Phys. **78**, 239 (2003).
[207] S. W. Koch, M. Kira, G. Khitrova, and H. M. Gibbs, Nat. Mat. **5**, 523 (2006).
[208] H. Tang, H. Berger, P. Schmid, F. Lvy, and G. Burri, Solid State Commun. **87**, 847 (1993).
[209] G. H. Wannier, Phys. Rev. **52**, 191 (1937).
[210] N. F. Mott and A. M. Stoneham, J. Phys. C **10**, 3391 (1977).
[211] M. A. El-Sayed, Acc. Chem. Res. **37**, 326 (2004).
[212] C. Richter and C. A. Schmuttenmaer, Nat. Nanotech. **5**, 769 (2010).
[213] J. Tang, J. R. Durrant, and D. R. Klug, J. Am. Chem. Soc. **130**, 13885 (2008).
[214] E. G. Panarelli, S. Livraghi, S. Maurelli, V. Polliotto, M. Chiesa, and E. Giamello, J. Photochem. Photobiol. A **322**, 27 (2016).
[215] A. Litke, Y. Su, I. Tranca, T. Weber, E. J. M. Hensen, and J. P. Hofmann, J. Phys. Chem. C **121**, 7514 (2017).
[216] C. Di Valentin, G. Pacchioni, and A. Selloni, Phys. Rev. Lett. **97**, 166803 (2006).
[217] C. Di Valentin, G. Pacchioni, and A. Selloni, J. Phys. Chem. C **113**, 20543 (2009).
[218] N. A. Deskins, R. Rousseau, and M. Dupuis, J. Phys. Chem. C **113**, 14583 (2009).
[219] S. Kerisit, N. A. Deskins, K. M. Rosso, and M. Dupuis, J. Phys. Chem. C **112**, 7678 (2008).
[220] F. Pascale, C. M. Zicovich-Wilson, F. López Gejo, B. Civalleri, R. Orlando, and R. Dovesi, J. Comput. Chem. **25**, 888 (2004).
[221] C. M. Zicovich-Wilson, F. Pascale, C. Roetti, V. R. Saunders, R. Orlando, and R. Dovesi, J. Comput. Chem. **25**, 1873 (2004).
[222] T. Shimanouchi, *Tables of molecular vibrational frequencies* (National Bureau of Standards, Washington D.C., 1972), Vol. 1, pp. 1–160.
[223] M. J. Frisch, G. W. Trucks, H. B. Schlegel, G. E. Scuseria, M. A. Robb, J. R. Cheeseman, G. Scalmani, V. Barone, B. Mennucci, G. A. Petersson, H. Nakatsuji, M. Caricato, X. Li, H. P. Hratchian, A. F. Izmaylov, J. Bloino, G. Zheng, J. L. Sonnenberg, M. Hada, M. Ehara, K. Toyota, R. Fukuda, J. Hasegawa, M. Ishida, T. Nakajima, Y., O. Kitao, H. Nakai, T. Vreven, J. A. Montgomery, Jr., J. E. Peralta, F. Ogliaro, M. Bearpark, J. J. Heyd, E. Brothers, K. N. Kudin, V. N. Staroverov, R. Kobayashi, J. Normand, K. Raghavachari, A. Rendell, J. C. Burant, S. S. Iyengar, J. Tomasi, M. Cossi, N. Rega, J. M. Millam, M. Klene, J. E. Knox, J. B. Cross, V. Bakken, C. Adamo, J. Jaramillo, R. Gomperts, R. E. Stratmann, O. Yazyev, A. J. Austin, R. Cammi, C. Pomelli, J. W. Ochterski, R. L. Martin, K. Morokuma, V. G. Zakrzewski, G. A. Voth, P. Salvador, J. J. Dannenberg, S. Dapprich, A. D. Daniels, Ö. Farkas, J. B. Foresman, J. V. Ortiz, J. Cioslowski, and D. J. Fox, Gaussian 09 Revision E.01, Gaussian Inc. Wallingford CT 2009.
[224] D. K. Buck and A. A. Collins, *POV-Ray - The Persistence of Vision Raytracer* (accessed 2017-11-13, http://www.povray.org/, 2010).
[225] C. F. Macrae, I. J. Bruno, J. A. Chisholm, P. R. Edgington, P. McCabe, E. Pidcock,

L. Rodriguez-Monge, R. Taylor, J. van de Streek, and P. A. Wood, J. Appl. Cryst. **41**, 466 (2008).
[226] M. A. Watanabe and T. Hayashi, J. Lumin. **112**, 88 (2005).
[227] H. Tang, K. Prasad, R. Sanjinès, P. E. Schmid, and F. Lévy, J. Appl. Phys. **75**, 2042 (1994).
[228] H. Tang, H. Berger, P. E. Schmid, and F. Levy, Solid State Commun. **92**, 267 (1994).
[229] H. Najafov, S. Tokita, S. Ohshio, A. Kato, and H. Saitoh, Jap. J. Appl. Phys. **245**, (2005).
[230] T. Sekiya, S. Kamei, and S. Kurita, J. Lumin. **89**, 1140 (2000).
[231] H. Bieber, P. Gilliot, M. Gallart, N. Keller, V. Keller, S. Bégin-Colin, C. Pighini, and N. Millot, Catal. Today **122**, 101 (2007).
[232] W. F. Zhang, M. S. Zhang, Z. Yin, and Q. Chen, Appl. Phys. B **70**, 261 (2000).
[233] L. Cavigli, F. Bogani, A. Vinattieri, V. Faso, G. Baldi, L. Cavigli, F. Bogani, A. Vinattieri, V. Faso, and G. Baldi, J. Appl. Phys. **106**, 053516 (2009).
[234] L. Cavigli, F. Bogani, A. Vinattieri, L. Cortese, M. Colocci, V. Faso, and G. Baldi, Solid State Sci. **12**, 1877 (2010).
[235] B. D. Pan, N. Zhao, and Q. Wang, Adv. Mat. **17**, 1991 (2005).
[236] A. M. Peiro, X. Dome, and A. Ayllo, Chem. Mater. **13**, 2567 (2001).
[237] K. Ding, Z. Miao, Z. Liu, Z. Zhang, B. Han, G. An, and S. Miao, J. Am. Chem. Soc. **129**, 6362 (2007).
[238] Y. Obara, H. Ito, T. Ito, N. Kurahashi, S. Thürmer, H. Tanaka, and T. Katayama, Struct. Dyn. **4**, 044033 (2017).
[239] D. A. Panayotov and J. T. Yates Jr, Chem. Phys. Lett. **436**, 204 (2007).
[240] A. Yamakata, T.-a. Ishibashi, and H. Onishi, Chem. Phys. Lett. **333**, 271 (2001).
[241] J. R. Durrant, J. Photochem. Photobiol. A **148**, 5 (2002).
[242] S. T. Martin, H. Herrmann, W. Choi, and M. R. Hoffmann, J. Chem. Soc., Faraday Trans. **90**, 3315 (1994).
[243] G. Boschloo and D. Fitzmaurice, J. Phys. Chem. B **4**, 2228 (1999).
[244] N. Beermann, G. Boschloo, and A. Hagfeldt, J. Photochem. Photobiol. A **152**, 213 (2002).
[245] S. H. Szczepankiewicz, J. A. Moss, and M. R. Hoffmann, J. Phys. Chem. B **91125**, 2922 (2002).
[246] T. Berger, M. Sterrer, O. Diwald, and E. Knözinger, ChemPhysChem **6**, 2104 (2005).
[247] T. Berger, M. Sterrer, S. Stankic, J. Bernardi, O. Diwald, and E. Knözinger, Mater. Sci. Eng. C **25**, 664 (2005).
[248] M. Chiesa, M. C. Paganini, S. Livraghi, and E. Giamello, Phys. Chem. Chem. Phys. **15**, 9435 (2013).
[249] V. Brezová, Z. Barbieriková, M. Zukalová, D. Dvoranová, and L. Kavan, Catal. Today **230**, 112 (2014).
[250] L. J. Antila, F. G. Santomauro, L. Hammarstrom, D. L. A. Fernandes, and J. Sà, Chem. Commun. **51**, 10914 (2015).
[251] S. Moser, L. Moreschini, J. Jacimovic, O. S. Barisic, H. Berger, A. Magrez, Y. J. Chang, K. S. Kim, A. Bostwick, E. Rotenberg, L. Forrò, and M. Grioni, Phys. Rev. Lett. **110**, 196403 (2013).
[252] T. Yoshihara, R. Katoh, A. Furube, Y. Tamaki, M. Murai, K. Hara, S. Murata, H. Arakawa, and M. Tachiya, J. Phys. Chem. B **108**, 3817 (2004).
[253] I. A. Shkrob and M. C. Sauer, J. Phys. Chem. B **108**, 12497 (2004).
[254] M. H. Rittmann-frank, C. J. Milne, J. Rittmann, M. Reinhard, T. J. Penfold, and M. Chergui, Angew. Chem. **0702**, 5858 (2014).
[255] J. Zhang, T. F. Hughes, M. Steigerwald, L. Brus, and R. A. Friesner, J. Am. Chem.

Soc. **134**, 12028 (2012).
[256] S. Maurelli, S. Livraghi, M. Chiesa, E. Giamello, S. Van Doorslaer, C. Di Valentin, and G. Pacchioni, Inorg. Chem. **50**, 2385 (2011).
[257] Z. Wei, E. Kowalska, and B. Ohtani, Chem. Lett. **43**, 346 (2014).
[258] F. Amano, O. O. Prieto-Mahaney, Y. Terada, T. Yasumoto, T. Shibayama, and B. Ohtani, Chem. Mater. **21**, 2601 (2009).
[259] M. Rozenberg, G. Shoham, I. Reva, and R. Fausto, Phys. Chem. Chem. Phys. **7**, 2376 (2005).
[260] Q. Shen, K. Katayama, T. Sawada, M. Yamaguchi, Y. Kumagai, and T. Toyoda, Chem. Phys. Lett. **419**, 464 (2006).
[261] X. Yang and N. Tamai, Phys. Chem. Chem. Phys. **3**, 3393 (2001).
[262] E. Makoto, K. Shohachi, K. Shuichi, and S. Tetsuro, Bull. Chem. Soc. Jpn. **51**, 3144 (1978).
[263] D. D. Beck, J. M. White, and C. T. Ratcliffe, J. Phys. Chem. **90**, 3123 (1986).
[264] S. U. M. Khan, M. Al-Shahry, and W. B. Ingler, Science **297**, 2243 (2002).
[265] D. Selli and C. D. Valentin, J. Phys. Chem. C **120**, 29190 (2016).
[266] O. Cohavi, S. Corni, F. De Rienzo, R. Di Felice, K. E. Gottschalk, M. Hoefling, D. Kokh, E. Molinari, G. Schreiber, A. Vaskevich, and R. C. Wade, J. Mol. Recognit. **23**, 259 (2010).
[267] A. A. Skelton, T. Liang, and T. R. Walsh, ACS Appl. Mater. Interfaces **1**, 1482 (2009).
[268] L. Agosta, G. Zollo, C. Arcangeli, F. Buonocore, F. Gala, and M. Celino, Phys. Chem. Chem. Phys. **17**, 1556 (2015).
[269] G. Seifert, J. Phys. Chem. A **111**, 5609 (2007).
[270] T. Frauenheim, G. Seifert, M. Elstner, T. Niehaus, C. Khler, M. Amkreutz, M. Sternberg, Z. Hajnal, A. D. Carlo, and S. Suhai, J. Phys. Condens. Matter **14**, 3015 (2002).
[271] M. Elstner, T. Frauenheim, and S. Suhai, J. Mol. Struct. THEOCHEM **632**, 29 (2003).
[272] Q. Cui, M. Elstner, E. Kaxiras, T. Frauenheim, and M. Karplus, J. Phys. Chem. B **105**, 569 (2001).
[273] T. Krüger, M. Elstner, P. Schiffels, and T. Frauenheim, J. Chem. Phys. **122**, 114110 (2005).
[274] P. Melix, A. F. Oliveira, R. Rüger, and T. Heine, Theor. Chem. Acc. **135**, 232 (2016).
[275] J. G. Brandenburg and S. Grimme, J. Phys. Chem. Lett. **5**, 1785 (2014).
[276] G. Zheng, S. Irle, and K. Morokuma, Chem. Phys. Lett. **412**, 210 (2005).
[277] B. Grundkötter-Stock, V. Bezugly, J. Kunstmann, G. Cuniberti, T. Frauenheim, and T. A. Niehaus, J. Chem. Theory Comput. **8**, 1153 (2012).
[278] Q. Cui and M. Elstner, Phys. Chem. Chem. Phys. **16**, 14368 (2014).
[279] DFTB+ website, `https://www.dftbplus.org/`, accessed: 2017-10-13.
[280] K. W. Sattelmeyer, J. Tirado-Rives, and W. L. Jorgensen, J. Phys. Chem. A **110**, 13551 (2006).
[281] M. Gaus, Q. Cui, and M. Elstner, Wiley Interdiscip. Rev. Comput. Mol. Sci. **4**, 49 (2014).
[282] W. Heckel, B. a. M. Elsner, C. Schulz, and S. Müller, J. Phys. Chem. C **118**, 10771 (2014).
[283] H. Fox and K. Newman, J. Chem. Theory Comput. **6**, 499 (2010).
[284] A. R. R. Neto and H. W. Leite Alves, Phys. Status Solidi C **7**, 308 (2010).
[285] S. Hu, P. A. Bopp, L. Österlund, P. Broqvist, and K. Hermansson, J. Phys. Chem. C **118**, 14876 (2014).
[286] S. Gemming, A. N. Enyashin, J. Frenzel, and G. Seifert, Int. J. Mater. Res. **101**, 758 (2010).
[287] S. Xu, S. Irle, D. G. Musaev, and M. C. Lin, J. Phys. Chem. A **109**, 9563 (2005).

[288] S. Bulusu, S. Yoo, and E. Apra, J. Phys. Chem. Lett. A **110**, 11781 (2006).
[289] C. S. Lin, R. Q. Zhang, S. T. Lee, M. Elstner, T. Frauenheim, and L. J. Wan, J. Phys. Chem. B **109**, 14183 (2005).
[290] R. Liang, J. M. J. Swanson, and G. A. Voth, J. Chem. Theory Comput. **10**, 451 (2014).
[291] H. Hu, Z. Lu, M. Elstner, J. Hermans, and W. Yang, J. Phys. Chem A **111**, 5685 (2007).
[292] C. M. Maupin, B. Aradi, and G. A. Voth, J. Phys. Chem. B **114**, 6922 (2010).
[293] P. Miro and C. J. Cramer, Phys. Chem. Chem. Phys. **15**, 1837 (2013).
[294] T. H. Choi, R. Liang, C. M. Maupin, and G. A. Voth, J. Phys. Chem. B **117**, 5165 (2013).
[295] T. H. Choi, Chem. Phys. Lett. **543**, 45 (2012).
[296] Z. Zhao, Z. Li, and Z. Zou, J. Phys. Chem. C **116**, 11054 (2012).
[297] P. Giannozzi, S. Baroni, N. Bonini, M. Calandra, R. Car, C. Cavazzoni, D. Ceresoli, G. L. Chiarotti, M. Cococcioni, I. Dabo, A. D. Corso, S. de Gironcoli, S. Fabris, G. Fratesi, R. Gebauer, U. Gerstmann, C. Gougoussis, A. Kokalj, M. Lazzeri, L. Martin-Samos, N. Marzari, F. Mauri, R. Mazzarello, S. Paolini, A. Pasquarello, L. Paulatto, C. Sbraccia, S. Scandolo, G. Sclauzero, A. P. Seitsonen, A. Smogunov, P. Umari, and R. M. Wentzcovitch, J. Phys. Condens. Matter **21**, 395502 (2009).
[298] L. Martínez, R. Andrade, E. G. Birgin, and J. M. Martínez, J. Comput. Chem. **30**, 2157 (2009).
[299] G. S. Tschumper, M. L. Leininger, B. C. Hoffman, E. F. Valeev, H. F. Schaefer, and M. Quack, J. Chem. Phys. **116**, 690 (2002).
[300] X. Xu and W. A. Goddard, J. Phys. Chem. A **108**, 2305 (2004).
[301] L. A. Curtiss, D. J. Frurip, and M. Blander, J. Chem. Phys. **71**, 2703 (1979).
[302] J. A. Odutola and T. R. Dyke, J. Chem. Phys. **72**, 5062 (1980).
[303] T. D. Kühne, M. Krack, and M. Parrinello, J. Chem. Theory Comput. **5**, 235 (2009).
[304] K. Krynicki, C. D. Green, and D. W. Sawyer, Faraday Discuss. Chem. Soc. **66**, 199 (1978).
[305] M. Gruden, L. Andjeklovi, A. K. Jissy, S. Stepanovi, M. Zlatar, Q. Cui, and M. Elstner, J. Comput. Chem. **38**, 2171 (2017).
[306] L. Ferrighi, M. Datteo, G. Fazio, and C. Di Valentin, J. Am. Chem. Soc. **138**, 7365 (2016).
[307] A. Y. Nosaka, T. Fujiwara, H. Yagi, H. Akutsu, and Y. Nosaka, J. Phys. Chem. B **108**, 9121 (2004).
[308] S. Benkoula, O. Sublemontier, M. Patanen, C. Nicolas, F. Sirotti, A. Naitabdi, F. Gaie-Levrel, E. Antonsson, D. Aureau, F.-X. Ouf, S.-I. Wada, A. Etcheberry, K. Ueda, and C. Miron, Sci. Rep. **5**, 15088 (2015).
[309] C.-y. Wang, H. Groenzin, and M. J. Shultz, Langmuir **19**, 7330 (2003).
[310] K. I. Hadjiivanov and D. G. Klissurski, Chem. Soc. Rev. **25**, 61 (1996).
[311] Z. Łodziana, N.-Y. Topsøe, and J. K. Nørskov, Nat. Mat. **3**, 289 (2004).
[312] D. W. Bahnemann, M. Hilgendorff, and R. Memming, J. Phys. Chem. B **101**, 4265 (1997).
[313] J. Boerio-Goates, G. Li, L. Li, T. F. Walker, T. Parry, and B. F. Woodfield, Nano Lett. **6**, 750 (2006).

List of Publications

- *Fully dehydrated curved TiO_2 nanoparticles do not exist: modelling single water molecule, mono and multilayer coverage of realistic nanospheres*
  G. Fazio, D. Selli, G. Seifert, C. Di Valentin
  in preparation (2018)

- *Water-assisted hole trapping at highly curved surface of nano-TiO_2 photocatalyst*
  G. Fazio, K. Shirai, T. Sugimoto, D. Selli, L. Ferraro, K. Watanabe, B. Ohtani, H. Kurata, C. Di Valentin, Y. Matsumoto
  J. Am. Chem. Soc., 140, 1415–1422 (2018)

- *Modelling Realistic TiO_2 Nanospheres: a Benchmark Study of SCC-DFTB against Hybrid DFT*
  D. Selli, G. Fazio, C. Di Valentin
  J. Chem. Phys., 147, 164701 (2017)

- *Water Multilayers on TiO_2 (101) Anatase Surface: Assessment of a DFTB-Based Method*
  D. Selli, G. Fazio, G. Seifert, C. Di Valentin
  J. Chem. Comput. Theory, 13, 3862–3873 (2017)

- *Photoexcited Carriers Recombination and Trapping in Spherical vs Faceted TiO_2 Nanoparticles*
  G. Fazio, L. Ferrighi, C. Di Valentin
  Nano Energy, 27, 673–689 (2016)

- *Spherical versus Faceted Anatase TiO_2 Nanoparticles: A Model Study of Structural and Electronic Properties*
  G. Fazio, L. Ferrighi, C. Di Valentin
  J. Phys. Chem. C, 119, 20735–20746 (2015)

During my studies I also authored:

- *Surface-charge dependent orientation of water at the interface of a gold electrode: a cluster study*
  G. Fazio, G. Seifert, M. Rapacioli, N. Tarrat, J.-O. Joswig
  Z. Phys. Chem., minor revisions (2018)

- *π Magnetism of Carbon Monovacancy in Graphene by Hybrid Density Functional Calculations*
  C. Ronchi, M. Datteo, D. Perilli, L. Ferrighi, G. Fazio, D. Selli, C. Di Valentin
  J. Phys. Chem. C, 121, 8653–8661 (2017)

- *Computational Electrochemistry of Doped Graphene as Electrocatalytic Material in Fuel Cells*
  G. Fazio, L. Ferrighi, D. Perilli, C. Di Valentin
  Int. J. Quantum. Chem., 116, 1623–1640 (2016)

- *Catalysis Under Cover: enhanced reactivity at the interface between (doped) graphene and anatase TiO_2*
  L. Ferrighi, M. Datteo, G. Fazio, C. Di Valentin
  J. Am. Chem. Soc., 138, 7365–7376 (2016)

- *Theoretical Studies of Oxygen Reactivity with Free-Standing, Metal- Or Semiconductor-Supported Boron Doped Graphene*
  L. Ferrighi, G. Fazio, C. Di Valentin
  ChemSusChem, 10, 1061–1077 (2016)

- *Charge Carriers Separation at the Graphene / (101) Anatase TiO_2 Interface*
  L. Ferrighi, G. Fazio, C. Di Valentin
  Adv. Mat. Inter., 3, 1500624 (2016)

School participations, Oral presentations

Schools

1. MPI-CEC Summer School 2015 in Methods in Molecular Research: Theory and Spectroscopy, Gelsenkirchen, Germany (August 2015)
2. INSTM School of Nanomedicine, Bari, Italy (December 2015)
3. SMART Winter School 2016 - Space-Time Multiscale Approaches in Research and Technology, Pisa, Italy (January 2016)
4. Introduction to Modern FORTRAN, Milan, Italy (May 2016)
5. PRACE Autumn School in Modern HPC for Scientist and Engineers, Hagenberg im Mühlkreis, Austria (September 2016)
6. NSF/CECAM School in Computational Materials Science, Lausanne, Switzerland (July 2017)

Presentations

1. Giornate dell'Elettrochimica Italiana, Bertinoro (FC), Italy (20/9/2015); *Modeling doped graphene for the electrocatalysis of the oxygen reduction reaction (ORR)*, Oral Contribution
2. Seminar in Prof. G. Seifert Group, TU Dresden, Germany (26/10/2016); *Photoexcited Carriers Recombination and Trapping in Spherical vs Faceted TiO_2 Nanoparticles*
3. 2018 MRS Spring Meeting, Phoenix, USA (04/04/2018); *Photoexcited Carriers Recombination and Trapping in Realistic Spherical vs Faceted TiO_2 Nanoparticles in Vacuum and Aqueous Environment*, Oral Contribution